A Dissertation

entitled

Mathematical Modeling and Analysis of a Variable Displacement Hydraulic Bent Axis Pump Linked to High Pressure and Low Pressure Accumulators

by

Mohammad Abuhaiba

Submitted as partial fulfillment of the requirements for the

Doctor of Philosophy degree in Engineering

_____

Adviser: Dr. Walter W. Olson

_____

College of Graduate Studies

The University of Toledo

May 2009

The University of Toledo

College of Engineering

I HEREBY RECOMMEND THAT THE DISSERTATION PREPARED UNDER MY SUPERVISION BY Mohammad Abuhaiba

ENTITLED Mathematical Modeling and Analysis of a Variable Displacement Hydraulic Bent Axis Pump Linked to High Pressure and Low Pressure Accumulators

BE ACCEPTED IN PARTIAL FULFILLMENT OF THE REQUIREMENTS FOR THE DOCTOR OF PHILOSOPHY DEGREE IN MECHANICAL ENGINEERING

_____

Dissertation Advisor: Dr. Walter W. Olson

Recommendation concurred by

_____

Dr. Mohammad Elahinia

_____

Dr. Maria R. Coleman

_____

Dr. Sorin Cioc

_____

Dr. Efstratios Nikolaidis

Committee

On

Final Examination

_____

Dean, College of Engineering

An Abstract of

Mathematical Modeling and Analysis of a Variable Displacement Hydraulic Bent Axis Pump Linked to High Pressure and Low Pressure Accumulators

Mohammad Abuhaiba

Submitted as partial fulfillment of the requirements for the

Doctor of Philosophy degree in Engineering

The University of Toledo

May 2009

Working prototypes of a Hydraulic Hybrid Vehicle (HHV) are already under testing and investigation. One of the problems reported from testing is that the noise levels emitted by the hydraulic system are not acceptable. Therefore, there is a need to perform extensive research to improve the HHV systems in terms of noise and performance. The pump is the main source of noise in HHV systems. However, the lack of space, the high pressure and the dynamics of components within the pump have prevented either direct observation or measurement of potential noise causing mechanisms within the pump structure. As a result, there are several theories as to the source of the noise from the pump units but little concrete information to further isolate and reduce the noise generation.

Currently, the industry use “cut and try” methods in order to study the noise issue. This necessities the development of a theoretical tool that will enable us to avoid the costly (time and money) cut and try procedure already employed in the current efforts.

This work creates a dynamic and geometric model of a bent axis pump for this purpose. Elements of the model include finding the variation of pressure, flow rate, and dynamic forces acting on the pump components and case as a function of angular rotations of both the main shaft and the yoke.

The model was constructed using Mathematica™ software and verified against test data. In turn, this study identifies and analyzes the dominant forces in both the time and frequency domains. The solution of the theoretical model using Mathematica™ is verified by a dynamic model created using ADAMS/View software.

The kinematic model was able to predict the variations of the angular velocities and accelerations and the velocities and the accelerations of the center of gravity of the entire pump's parts starting from the main shaft up to the yoke.

This work presents all equations necessary to solve for the piston pressure and pump flow rate as a function of main shaft and yoke rotations. These equations were tested, and verified at a constant angular speed of the main shaft and yoke angles ranging from 5° to 40°. Results indicate that the model can predict the variations of pressure profile and flow rate as well as the forces acting on the pump's case both in the time and frequency domains. Conclusions and recommendations are at the end of this research effort. The harmonics of the reaction forces acting on the pump case occur at frequencies of 25, 50, 100, 200, 220, 250, 350, and 450 Hz respectively.

DEDICATION

I dedicate this work to my mother, my father, my wife Rana, and my children: Shyamaa', Ahmad, Anas, and Noor, without their caring and warm support it would not have been possible. My family members were continually supporting me although they are in desperate need to such support. Without the support, love, and patience of the beloved people to my heart this work would not have been possible.

ACKNOWLEDGMENTS

I would like to express the warmest appreciation to my advisor, Dr. Walter W. Olson. Dr. Olson has the attitude and the substance of a genius: he continually and realistically conveyed a spirit of adventure about research and scholarship, and an excitement regarding teaching. Without his guidance and persistent help, this dissertation would not have been possible.

Special thanks to the distinguished faculty members who served on my committee: Dr. Mohammad Elahinia, Dr. Maria R. Coleman, Dr. Sorin Cioc, and Dr. Efstratios Nikolaidis, for their critical suggestions and advice. In addition, I would like to thank Dr. Mohammad Samir Hefzy for his continuous encouragement and support. I am also grateful to my brother Dr. Ibrahim Abuhaiba for his support, encouragement, and useful suggestions. Moreover, I would like to thank Dr. Matt Witte for his support.

I am also grateful for the support and friendship of the members of the hydraulic hybrid vehicle group. Special thanks to my friends who cheered me on from the beginning.

TABLE OF CONTENTS

LIST OF TABLES

LIST OF FIGURES

NOMENCLATURE

"$a_1a_2a_3$"	Inertial coordinate system ("A" frame)
${}_Aa_{c2}$	The acceleration of the CG of the second cross
${}_Aa_{CR}(\theta, \phi)$	Acceleration of the CG of the connecting rod
${}_Aa_{im1}$	Acceleration of the CG of the first intermediate shaft of the CVJ
${}_Aa_{os}$	The acceleration of the CG of the barrel-output shaft assembly
${}_Aa_p$	The acceleration of the CG of the piston
ABN	Air Born Noise
A_c	Cylinder cross sectional area
A_{ce}	Exit cross sectional area of the cylinder
${}_AF_{ACtoY66}$	The reaction force from the actuating link to the yoke
${}_AF_{B1toMS}$	Reaction force from the ball bearing to the main shaft
${}_AF_{B2toMS}$	Reaction force from the thrust bearing to the main shaft
${}_AF_{CtoRAM90}$	The frictional force from the ram cylinder interface at point 90
${}_AF_{CtoY67}$	Reaction force on case from yoke at yoke axis of rotation (Suction port)
${}_AF_{CtoY68}$	Reaction force on case from yoke at yoke axis of rotation (discharge port)
${}_AF_{HPAtoY79}$	The reaction force from the fluid inside the hose between the HPA and the discharge exit at the yoke axis of rotation at point 79
${}_AF_{LPAtoY78}$	The reaction force from the fluid inside the hose between the LPA and the suction exit at the yoke axis of rotation at point 78
${}_AF_{MStoCR,i}$	Reaction force from the main shaft to the i^{th} connecting rod
${}_AF_{PtoCRi}$	The reaction from the i^{th} piston to the i^{th} connecting rod

${}_{A}F_{PtoRAM}$	The cylinder pressure force on the ram
${}_{A}F_{RAMtoAC90}$	The reaction force from the pin of the ram at point 90
${}_{A}I_{AC}$	Moment of inertia of the actuating link around axis system that is attached to its CG and parallel to the principal axes of the part
${}_{A}M_{ACtoY66}$	The frictional moment from the actuating link to the yoke
${}_{A}M_{B1toMS}$	The ball bearing frictional moment on the main shaft
${}_{A}M_{B2toMS}$	The thrust roller bearing frictional moment on the main shaft
${}_{A}M_{CtoY67}$	The friction moment at the axis of rotation of the yoke at point 67
${}_{A}M_{CtoY68}$	The friction moment at the axis of rotation the yoke at point 68
${}_{A}M_{MStoCR,i}$	The friction moments generated on the i^{th} spherical joint between the main shaft and the i^{th} connecting rod
${}_{A}M_{PtoCRi}$	The frictional moment from the i^{th} piston to the i^{th} connecting rod
${}_{A}M_{RAMtoAC90}$	Friction moment from the pin of the ram at point 90
A_p	Cross sectional area of the piston
$A_{r,i}(\phi)$	The overlap area of the i^{th} region at any angular position of the barrel
${}_{A}r_1$	Position vector of the ball bearing reaction at point (1) (Figure **3-4**) with respect to the left end of the main shaft
${}_{A}r_2$	Position vector of the thrust bearing reaction at point 2 of main shaft (Figure **3-4**) with respect to the left end of the main shaft
${}_{A}r_{29}$	Position vector of point (29) on the second cross with respect to the center of rotation of the yoke
${}_{A}r_{30}$	Position vector of point (30) on the second cross with respect to the center of rotation of the yoke

A_{RAM}	Cross sectional area of the ram
${}_{A}r_{CR,i}$	Position vector of the i^{th} spherical joint between the main shaft and the i^{th} connecting rod with respect to the left end of the main shaft
${}_{A}r_{CtoY67}$	The position vector of the reaction force from the yoke to the case at the axis of rotation of the yoke at point 67
${}_{A}r_{CtoY68}$	The position vector of the reaction force from the yoke to the case at the axis of rotation of the yoke at point 68
${}_{A}r_{EB}$	Position vector of spherical joint between piston and connecting rod with respect to spherical joint between main shaft and connecting rod
${}_{A}r_{HPAtoY79}$	Position vector of the reaction force from the fluid, that is inside the hose between the HPA and the discharge exit at the yoke axis of rotation at point 79 with respect to the axes of rotation of the yoke
${}_{A}r_{LPAtoY78}$	Position vector of the reaction force from the fluid inside the hose between the LPA and the suction exit at the yoke axis of rotation at point 78 with respect to the axes of rotation of the yoke
${}_{A}r_{RAMtoAC90}$	Position vector of the reaction force from ram on actuating link at point 90 as measured from common point between the yoke and actuating link
${}_{A}r_{Wms}$	Position vector of the CG of main shaft with respect its left end
$A_{s,i}$	The i^{th} solid area between successive cylinders
${}_{A}T_{in}$	Input torque to the main shaft
${}_{A}V_{B}$	Velocity of point B (Figure 3-9)
${}_{A}V_{CR}(\theta, \phi)$	Velocity of the CG of the connecting rod
${}_{A}V_{p}$	Velocity of the CG of the piston

${}_{A}W_{AC}$	Weight of the actuating link
${}_{A}W_{C1}$	Weight of the first cross of the CVJ
${}_{A}W_{C2}$	Weight of the second cross of the CVJ
${}_{A}W_{CR}$	Weight of the connecting rod
${}_{A}W_{im1}$	Weight of the first intermediate shaft of the CVJ
${}_{A}W_{im2}$	Weight of the second intermediate shaft the CVJ
${}_{A}W_{MS}$	Weight of the main shaft
${}_{A}W_{OIL,i}$	Weight of the i^{th} oil control volume
${}_{A}W_{os}$	Weight of the barrel-output shaft assembly
${}_{A}W_{P}$	Weight of the piston
${}_{A}W_{RAM}$	Weight of the ram
${}_{A}W_{vp}$	Weight of the valve plate-yoke assembly
B	Bulk Modulus of the hydraulic oil
"$b_1b_2b_3$"	Moving coordinate system attached to the main shaft ("B" frame)
BDC	Bottom Dead Center
${}_{B}I_{ms}$	Principal moment of inertia of main shaft with respect
${}_{B}r_{3}$	Position vector of the pin of the first cross at point 3 of the main shaft with respect to the left end of the main shaft
${}_{B}r_{4}$	Position vector of the pin of the first cross at point 4 of the main shaft with respect to the left end of the main shaft
${}_{B}\omega_{MS}$	Angular velocity of main shaft, rad/s
"$c_1c_2c_3$"	Moving coordinate system attached to the first intermediate shaft
${}_{C}a_{im1}$	Acceleration of the CG of the first intermediate shaft of the CVJ

${}_{C}a_{im2}$	Acceleration of the CG of the second intermediate shaft,
C_d	Orifice discharge coefficient at the i^{th} overlap area
${}_{C}F_{IM2toIM125}$	Sliding force reaction from second intermediate to first intermediate shaft
CG	Center of gravity
${}_{C}I_{im1}$	Principal moment of inertia of the first intermediate shaft of the CVJ
${}_{C}I_{im2}$	Principal moment of inertia of the second intermediate shaft of the CVJ
${}_{C}M_{IM2toIM125}$	Reaction couple from second intermediate shaft to first intermediate shaft
C_{o1}	The static load rating of the ball bearing of the main shaft
C_{o2}	The static load rating of the thrust roller bearing of the main shaft
C_{o4}	The static load rating of the thrust ball bearing at the barrel
C_p	One half the radial clearance between the piston and the cylinder
${}_{C}r_{23}$	Position vector of point (23) on the first intermediate shaft as measured from the center of the first cross
${}_{C}r_{24}$	Position vector of point (24) on the first intermediate shaft as measured from the center of the first cross
${}_{C}r_{27}$	Position vector of point (27) on the second cross or second intermediate shaft as measured from the center of the first cross
${}_{C}r_{28}$	Position vector of point (28) on the second cross or second intermediate shaft as measured from the center of the first cross
${}_{C}r_{im1}$	Position vector of CG of first intermediate shaft relative to CG of first cross
${}_{C}r_{im2}$	Position vector of CG of second intermediate shaft relative to CG of first cross

${}_C V_{c2}$	Velocity of the CG of the second cross
${}_C V_{im1}$	Velocity of CG of the first intermediate shaft
${}_C V_{im2}$	Velocity of CG of the second intermediate shaft
${}_C V_{im2/im1}$	Velocity of CG of second intermediate shaft with respect to first intermediate shaft
CVJ	Constant velocity joint
cw, ccw	Clockwise, counter clockwise
${}_C \alpha_{im1}$	Angular acceleration of the first intermediate shaft of the CVJ, rad/s^2
${}_C \omega_{im1}$	Angular velocity of the first intermediate shaft of the CVJ, rad/s
D_1	Outside diameter of the ball bearing at the main shaft, mm
d_1	Bore diameter of the ball bearing at the main shaft, mm
"$d_1 d_2 d_3$"	Moving coordinate system attached to the output shaft of the CVJ
d_2	Bore diameter of the thrust bearing at the main shaft, mm
D_2	Outside diameter of the thrust bearing at the main shaft, mm
d_3	Bore diameter of the needle bearing at the barrel, mm
D_3	Outside diameter of the needle bearing at the barrel, mm
d_4	Bore diameter of the thrust ball bearing at the barrel, mm
D_4	Outside diameter of the thrust ball bearing at the barrel, mm
DF	Distance from center of spherical joint between piston and connecting rod and the bottom end of the cylindrical cavity for a zero yoke angle (Figure 3-15)
${}_D F_{B3FtoB}$	Reaction force from the first journal bearing to the barrel at the end of the barrel (point 58)

${}_{D}F_{B3StoB}$	Reaction force from the second journal bearing to the barrel at the end of the barrel (point 58)
${}_{D}F_{B4toB}$	Reaction force from the thrust bearing to the barrel at point 65
${}_{D}F_{BStoVP,i}$	Reaction force between discharge/suction port of the valve plate and the i^{th} solid area located between each successive cylinders at points 69 to 77
${}_{D}F_{BtoP,i}$	Reaction force from the i^{th} oil film between the barrel and piston to the piston at points 31 to 39
${}_{D}F_{OILtoB,i}$	The force from the i^{th} oil column in the cylinder at points 49 to 57
${}_{D}F_{OILtoP,i}$	The force from the i^{th} oil control volume in the cylinder to the i^{th} piston at points 40 to 48
${}_{D}F_{OILtoVP,i}$	Force due to pressure on discharge or suction orifice at points 80 to 88
${}_{D}F_{VPtoBinD}$	Hydrodynamic force due to the oil film between the valve plate and the barrel at point 60 at the discharge side
${}_{D}F_{VPtoBinS}$	Hydrodynamic force due to the oil film between the valve plate and the barrel at point 61 at the suction side
${}_{D}F_{VPtoBoutD}$	Hydrodynamic force due to the oil film between the valve plate and the barrel at point 59 at the discharge side
${}_{D}F_{VPtoBoutS}$	Hydrodynamic force due to the oil film between the valve plate and the barrel at point 62 at the suction side
DG	Distance from upper end of actuating link (D) to its CG
${}_{D}I_{os}$	Moment of inertia of output shaft of the barrel-output shaft assembly
${}_{D}I_{p}$	Principal moment of inertia of the
d_{m1}	Pitch circle diameter of the ball bearing at the main shaft, mm

d_{m2}	Pitch circle diameter of the thrust bearing at the main shaft, mm
d_{m4}	Pitch circle diameter of the thrust ball bearing at the barrel, mm
${}_{D}M_{B3toB}$	Frictional moment on the barrel form the journal bearing at point 58
${}_{D}M_{B4toB}$	Frictional moment on the barrel from the thrust ball bearing at the end of the barrel at point 65
${}_{D}M_{VPtoB}$	Frictional moment due to fluid film between the barrel and the valve plate
${}_{D}r_{30+i}$	i^{th} position vector of the reaction force from oil film between the i^{th} piston and the barrel at points 31 to 39 as observed from yoke axis of rotation
${}_{D}r_{B3FtoB}$	Position vector of the reaction force from the first needle bearing at the end of the barrel (point 58) as observed from the yoke axis of rotation
${}_{D}r_{B3StoB}$	Position vector of the reaction force from the second needle bearing at the end of the barrel (point 58) as observed from the yoke axis of rotation
${}_{D}r_{B4toB}$	Position vector of the reaction force from the thrust ball bearing at the end of the barrel (point 65) as observed from the yoke axis of rotation
${}_{D}r_{BStoVPi}$	Position vector of the reaction force between the discharge/suction port of the valve plate and the solid area located between each successive cylinders at points 69 to 77 as observed from the yoke axis of rotation
${}_{D}r_{BtoP}$	Position vector of reaction force from the barrel to the piston as measured from the common point between the piston and the connecting rod
${}_{D}r_{I}$	The position vector of the center of the second cross with respect to the center of rotation of the yoke
${}_{D}r_{inD}$	Position vector of hydrodynamic force at inner land of the discharge port
${}_{D}r_{inS}$	Position vector of the hydrodynamic force at the inner land of suction port

${}_D r_{OILtoB,i}$	Position vector of the force from oil column in cylinders at points 49 to 57
${}_D r_{OILtoVPD,i}$	The i^{th} position vector of the force due to the pressure on the discharge or suction orifice at points 80 to 88
${}_D r_{OS}$	Position vector of the CG of the barrel-output shaft assembly with respect to the center of rotation of the yoke
${}_D r_{OUTD}$	Position vector of hydrodynamic force at outer land of the discharge port
${}_D r_{OUTS}$	Position vector of the hydrodynamic force at the outer land of suction port
${}_D r_{WP}$	Position vector of the CG of the piston as measured from the center of the spherical joint between the piston and the connecting rod
${}_D V_{os}$	The velocity of the CG of the barrel-output shaft assembly
${}_D v_{pb,i}$	Axial velocity of the i^{th} piston with respect to the barrel
${}_D \alpha_{ms}$	Angular acceleration of the piston, rad/s^2
${}_D \omega_{os}$	Angular velocity of barrel-output shaft assembly, rad/s
${}_D \omega_{p}$	Angular velocity of the piston, rad/s
EF	Distance from the center of rotation of the yoke and the bottom end of the cylindrical cavity for a zero yoke angle (Figure 3-15)
f_1	An index taking into account the magnitude of the load at a roller bearing
$f_1 f_2 f_3$	Moving coordinate system attached to the first cross of the CVJ
F_{a1}	Axial load component of the ball bearing reaction at the main shaft
F_{a2}	Axial load component of the thrust bearing reaction at the main shaft
f_{a2}	Index, depending on the axial load F_{a2} and the lubricating condition
F_{a4}	Axial load component of the thrust ball bearing reaction at the barrel
f_{a4}	Index, depending on the axial load F_{a4} and the lubricating condition

${}_{F}F_{IM1toC123}$	Reaction from the first intermediate shaft to the first cross at point 23
${}_{F}F_{IM1toC124}$	Reaction from the first intermediate shaft to the first cross at point 24
${}_{F}F_{MStoC13}$	Reaction force from the main shaft to the pin of first cross at point (3)
${}_{F}F_{MStoC14}$	Reaction force from the main shaft to the pin of first cross at point (4)
${}_{F}I_{c1}$	Principal moment of inertia of first cross of the CVJ
${}_{F}M_{IM1toC123}$	Frictional moment from first intermediate shaft to first cross at point (23)
${}_{F}M_{IM1toC124}$	Frictional moment from first intermediate shaft to first cross at point (24)
${}_{F}M_{MStoC13}$	Frictional moment at the pin of the first cross (point 3)
${}_{F}M_{MStoC14}$	Frictional moment at the pin of the first cross (point 4)
f_{o1}, f_{o2}, f_{o4}	Index for bearing type and lubrication type for ball bearing at main shaft, thrust bearing at main shaft, and thrust ball bearing at barrel respectively
F_{r1}	Radial load component of the ball bearing reaction at the main shaft
F_{r2}	Radial load component of the thrust bearing reaction at the main shaft
${}_{F}r_{23}$	Position vector of point (23) on the first cross with respect to its center
${}_{F}r_{24}$	Position vector of point (24) on the first cross with respect to its center
${}_{F}r_{3}$	Position vector of point 3 on first cross of the CVJ with respect to its center
F_{r4}	Radial load component of the thrust ball bearing reaction at the barrel
${}_{F}r_{4}$	Position vector of point 3 on first cross of the CVJ with respect to its center
${}_{F}\alpha_{c1}$	Angular acceleration of first cross of the CVJ, rad/s^2
${}_{F}\omega_{c1}$	Angular velocity of the first cross of the constant velocity joint, rad/s
g	Acceleration of gravity
h	Fluid film thickness between valve plate and the barrel
${}_{H}a_{vp}$	Acceleration of the CG of the valve plate-yoke assembly

h_g	Half width of groove after discharge/suction port of the valve plate
HHV	Hydraulic Hybrid Vehicle
${}_H I_{vp}$	Moment of inertia of the valve plate-yoke assembly
HPA	High pressure accumulator
${}_H r_{ACtoY66}$	Position vector of the reaction force from the actuating link at point 66 with respect to the center of rotation of the yoke
${}_H r_{vp}$	Position vector of the CG of the valve plate-yoke assembly with respect to the center of rotation of the yoke
${}_H V_{vp}$	Velocity of the CG of the valve plate-yoke assembly
${}_H \alpha_{vp}$	Angular acceleration of the valve plate-yoke assembly, rad/s^2
${}_H \omega_{vp}$	Angular velocity of the valve plate-yoke assembly, rad/s
"$i_1 i_2 i_3$"	Moving coordinate system attached to the second cross of the joint
${}_I F_{IM2toC227}$	Reaction force from the second intermediate shaft to the second cross at the pin point (27)
${}_I F_{IM2toC228}$	Reaction force from the second intermediate shaft to the second cross at the pin point (28)
${}_I F_{OStoC229}$	Reaction force from the output shaft to the second cross at point (29)
${}_I F_{OStoC230}$	Reaction force from the output shaft to the second cross at point (30)
${}_I I_{c2}$	Principal moment of inertia of the second cross of the CVJ
${}_I M_{IM2toC227}$	Frictional moment from second intermediate shaft to second cross at point (27)
${}_I M_{IM2toC228}$	Frictional moment from second intermediate shaft to second cross at point (28)

${}_{I}M_{OStoC229}$	Frictional moments from the output shaft to the second cross at point (29)
${}_{I}M_{OStoC230}$	Frictional moment from the output shaft to the second cross at point (30)
IP	Distance from CG of second intermediate shaft to center of second cross
${}_{I}r_{27}$	Position vector of point (27) on the second cross with respect to its center
${}_{I}r_{28}$	Position vector of point (28) on the second cross with respect to its center
${}_{I}r_{29}$	Position vector of point (29) on the second cross with respect to its center
${}_{I}r_{30}$	Position vector of point (30) on the second cross with respect to its center
${}_{J}I_{CR}$	Principal moment of inertia of the connecting rod
L_{45}	Length of notch groove base (Figure 3-20)
Lac	Length of actuating link
L_{C1}	Minimum cylindrical length of the oil control volume at any angular position of the yoke (Figure 3-14)
L_{C2}	Length of the convergent part of the cylindrical cavity (Figure 3-14)
L_{CIMo}	Contact length between first and second intermediate shafts at zero yoke angle
L_{Co}	Length of oil cylindrical cavity at zero yoke angle (Figure 3-15)
L_{CR}	Length of the connecting rod
L_{im}	Distance between the centers of the two cardan joints of the CVJ
L_{IM1}	Distance from the center of the first cross to the far edge of the first intermediate shaft along the "c_3" direction
L_{is}	Length of input shaft of the CVJ (Figure 3-9)
$LM_{CS,i}$	The i^{th} net rate of change of the linear momentum through the control surface of the i^{th} oil control volume

LM_{cv}	The i^{th} net rate of change of the linear momentum of the content of the control volume of the i^{th} oil column
L_{min}	Distance from the barrel-valve plate interface to the CG of the oil control volume at TDC for any angular rotation of the yoke angle (Figure 3-14)
L_p	Length of piston that is in the cylinder when axial displacement is zero
L_{p1}	Distance from the spherical joint between the piston and the connecting rod to the piston's face
LPA	Low pressure accumulator
L_{PtoCR}	Distance from the left face of the piston to the common point between the piston and the connecting rod
L_v	Distance from barrel-valve plate interface to CG of the oil control volume at any yoke angle, θ and any main shaft angular rotation, ϕ (Figure 3-14)
L_{YtoVP}	Distance along the "d_3" direction from the yoke axis of rotation to the barrel valve plate interface
M_{1m}, M_{2m}, M_{4m}	Mechanical friction torque of: ball bearing at the main shaft, thrust bearing at the main shaft, and the thrust ball bearing at the barrel respectively
M_{1v}, M_{2v}, M_{4v}	Viscous friction torque of: ball bearing at the main shaft, thrust bearing at the main shaft, and the thrust ball bearing at the barrel respectively
M_{2a} , M_{4a}	Mechanical friction torque of thrust bearing at main shaft and the thrust ball bearing at the end of the barrel due to axial load
M_{AC}	Mass of the actuating link
M_{c1}	Mass of the first cross
M_{c2}	Mass of the second cross

M_{CR}	Mass of the connecting rod
M_H	Mass of gas in the HPA
MHH	Mild hydraulic hybrid
M_{im1}	Mass of the first intermediate shaft
M_{im2}	Mass of the second intermediate shaft
M_L	Mass of gas in the LPA
M_{MS}	Mass of the main shaft
$M_{OIL,i}$	Mass of oil in the i^{th} cylinder
M_{os}	Mass of the barrel-output shaft assembly
M_p	Mass of piston
M_{RAM}	Mass of the ram
M_{vp}	Mass of the valve plate-yoke assembly
n_{ms}	Angular velocity of the main shaft, rpm
N_{rated}	Rated speed of pump, rpm
P	Pressure at radius R
P/M	Pump/Motor
P_{11}	Load that governs the load-depending frictional moment M_{1m}, M_{2m}, and M_{4m}, which takes into account the fact that these frictional moments change with the load angle
$P_b(\phi)$	Boundary pressure at the valve plate (either P_D or P_S)
P_D	Discharge pressure at the valve plate
$P_H(t)$	Gas pressure in the HPA
$P_L(t)$	Gas pressure in the LPA

P_{lossH}	Pressure losses between the discharge port and the HPA
P_{lossL}	Pressure losses between the suction port and the LPA
P_{maxH}	Maximum gas pressure in the HPA
P_{maxL}	Maximum gas pressure in the LPA
P_{minH}	Minimum gas pressure in the HPA
P_{minL}	Minimum gas pressure in the LPA
P_{o1}	Equivalent load determined for operating load at ball bearing of main shaft
P_{OILi}	Pressure of the i^{th} cylinder
P_{PH}	Pre-charge pressure in the HPA
P_{PL}	Pre-charge pressure in the LPA
P_{RAM}	Fluid pressure at the ram
P_s	Suction pressure at the valve plate
Q_A	Actual flow rate
$Q_{DS,i}(t)$	Discharge/suction flow rate at the overlap area
$Q_i(t)$	Net flow rate from the i^{th} cylinder
$Q_{L,i}(t)$	Leakage flow rate from the i^{th} cylinder
Q_T	Theoretical flow rate
Q_{TTD}	Total theoretical oil flow rate of the pump at the discharge port
r	Pitch circle radius at the barrel side
R	Pitch circle radius at the main shaft side
R_1	Radius of the outer land of the port plate (Figure 2-5)
R_2	Outside radius of the discharge/suction port (Figure 2-5)
R_3	Inside radius of the discharge/suction port (Figure 2-5)

R_4 Radius of the inner land of the port plate (Figure 2-5)

r_{AC} Radius of pin between the yoke and the actuating link

r_{C1} Distance from the center of the first or the center of the second cross to point 3 on the first cross or point 29 on the second cross

r_{C2} Distance from the center of the first or second cross to point 23 on the first cross or point 27 on the second cross

r_{CP1} Radius of the cross section of pin 3-4 that is attached to the input shaft at the first cross or the output shaft at the second cross

r_{CP2} Radius of the cross section of pin 23-24 that is attached to the first or second intermediate shafts at point 23

r_{CP3} Radius of the cross section of pin 23-24 that is attached to the first or second intermediate shafts at point 24

R_{CRL} Radius of the left end of the connecting rod

R_{CRR} Radius of the right end of the connecting rod

R_{inD} Radius of point of application of the normal hydraulic force between the barrel and the valve for the inner land at the discharge side

R_{inS} Radius of point of application of the normal hydraulic force between the barrel and the valve for the inner land at the suction side

R_N Gas constant of nitrogen, J/kg°K

R_{outD} Radius of point of application of the normal hydraulic force between the barrel and the valve for the outer land at the discharge side

R_{outS} Radius of point of application of the normal hydraulic force between the barrel and the valve for the outer land at the suction side

r_p	The piston radius
r_Y	Radius of the yoke's pin at its axis of rotation
R_y	Distance from center of rotation of yoke to center of first or second cross
SBN	Structure Born Noise
$Shear_{in}$	Shear moment at the inner land due to discharge and suction ports
$Shear_{out,D}$	Shear moment at the outer land due to discharge and suction ports
T	Operating oil temperature, ^oC
T_1	Rotation matrix of the "$b_1b_2b_3$" frame of reference with respect to "$a_1a_2a_3$"
T_2	Rotation matrix resulting from rotating "$a_1a_2a_3$" frame of reference about a_1 axis by an angle of θ to get "$a_1'a_2'a_3'$"
T_3	Rotation matrix resulting from rotating "$a_1'a_2'a_3'$" frame of reference about a_3' axis by an angle of δ to get "$c_1c_2c_3$"
T_6	Rotation matrix of the "$h_1h_2h_3$" frame of reference with respect to "$a_1a_2a_3$"
T_{c1}	Rotation matrix of the "$f_1f_2f_3$" frame of reference with respect to "$a_1a_2a_3$"
T_{c2}	Rotation matrix of the "$i_1i_2i_3$" frame of reference with respect to "$a_1a_2a_3$"
TDC	Top Dead Center
T_g	Temperature of gas in the HPA or LPA at pre-charge, ^oK
T_{im1}	Rotation matrix of the "$c_1c_2c_3$" frame of reference with respect to "$a_1a_2a_3$"
T_{os}	Rotation matrix of the output shaft "$d_1d_2d_3$" with respect to the A frame
V_{CRLi}	Absolute value of the sliding velocity between the left end of the connecting rod and the cup at the main shaft
V_{CRRi}	Absolute value of the sliding velocity between the right end of the

	connecting rod and the piston
V_{fixed}	Volume of oil at end of the cylinder cavity (conical portion) (Figure 3-14)
$V_H(t)$	Instantaneous gas volume in the HPA
V_{i+39}	Velocity of flow at the piston contact for the i^{th} control volume
V_{i+79}	Velocity of flow just before the exit of the cylinder of i^{th} control volume
$V_L(t)$	Instantaneous gas volume in the LPA
V_{maxH}	Maximum gas volume in the HPA
V_{maxL}	Maximum gas volume in the LPA
V_{min}	Minimum cylinder volume at zero piston displacement (at TDC) which is a function of the yoke angle, θ
$V_{OIL,i}$	Volume of oil in the i^{th} cylinder
V_{PH}	Pre-charge gas volume in the HPA
V_{PL}	Pre-charge gas volume in the LPA
$Z(\theta,\phi)$	Piston's displacement with respect to barrel as measured from the TDC
${}_B\alpha_{ms}$	Angular acceleration of main shaft, rad/s^2
${}_I\alpha_{c2}$	Angular acceleration of the second cross of the CVJ, rad/s
${}_I\omega_{c2}$	Angular velocity of the second cross of the CVJ, rad/s
β	Angle between intermediate and main shaft / output shafts
α_o	Nominal contact angle of the thrust bearing at the main shaft
δ	Angular rotation of the intermediate shaft about its axis of rotation
ε	Inclination angle of the cylinder along which the ram slides
ϕ	Angular rotation of the main shaft about its axis of rotation

γ_o	Connecting rod angle with the horizontal at a zero yoke angle
$\phi_1, \ldots \phi_{16}$	Angular positions of overlap areas between the exit of one cylinder and the suction/discharge port
φ_o	Connecting rod angle with the horizontal at any angular rotation of the yoke at the TDC (Figure 3-15)
$\eta_{v,i}$	The volumetric efficiency of the pump at the i^{th} cylinder as read from the pump map as a function of pressure and angular speed of the barrel
μ	Coefficient of dynamic viscosity
μ_{ACtoY}	Friction coefficient at the pin between the yoke and the actuating link
μ_{B3toB}	Friction coefficient at the interface between the journal bearing and the barrel at point 58
μ_{C1}	Friction coefficient at the pins of the first or second cross
μ_{CRLi}	Friction coefficient at the right end of the i^{th} connecting rod
μ_{CRLi}	Friction coefficient at the left end of the i^{th} connecting rod
$\mu_{CtoRAM90}$	Friction coefficient between the ram and the cylinder walls at point 90
μ_{im}	Friction coefficient between the first and second intermediate shafts
μ_Y	Friction coefficient at the right/left pins of the yoke at its axis of rotation
$\lambda_1, \ldots \lambda_{12}$	Angular positions of solid areas between successive cylinders that are under either suction or discharge pressures
θ	Angular rotation of the yoke about its axis of rotation
ρ	Oil density
θ_L	Angular rotation of the line of action of the reaction force from the

	LPA/HPA from the negative "a_3" direction
τ	Tangential stress
υ	Operating kinematic viscosity of the hydraulic oil, mm^2/s
ψ	Angular rotation of the output shaft about its axis of rotation
ζ	Kidney angle of the valve plate
ζ_1	Angular position of the center line of the circular end of the discharge port with respect to the TDC (Figure **3-32**)
ζ_C	Angle between the center lines of the circular ends of the bottom of the cylindrical cavity (Figure **3-32**)
ζ_D	Angle between two successive cylinders

CHAPTER 1:INTRODUCTION

In hydraulic power systems, variable displacement pumps save power, increase the productivity, or control the motion of a load precisely, safely and in an economic manner. The displacement-varying mechanism and power-to-weight ratio of variable-geometry axial piston pumps make them most suitable for control of high power levels.

1.1 Background for the Research

The bent axis pump is preferred in hydraulic hybrid vehicles because of its high performance and efficiency. It is also capable of operating at variable conditions of flow, pressure, speed, and torque.

Although many researchers in the literature have considered modeling bent axis pump, they only considered models for pumps rotating at constant angular velocity of the main shaft of the pump. In real driving conditions, the velocity of the vehicle changes continuously. Therefore, there is a strong need to consider the transient response of the pump, i.e. at a variable angular velocity of the main shaft and a variable angular velocity of the yoke.

Some working prototypes of a Hydraulic Hybrid Vehicle (HHV) are already under testing and investigation. However, it was found that noise levels emitted by HHV systems are not acceptable; therefore, additional research has to be conducted to improve the HHV systems in terms of noise and performance. The pump is the main source of

noise in HHV systems. Currently, industry uses “cut and try” methods in order to study the noise issue. A theoretical tool will enable us to avoid the costly (time and money) cut and try procedure already employed in the current efforts.

The derived dynamic mathematical model permits methodical study of the variation of pressure head, flow rate, and dynamic forces acting on the pump casing as a function of angular rotations of both the main shaft and the yoke, given the variable input torque and the variable angular motion of the main shaft of the pump. The mathematical model predicts the steady state and transient responses of the forces acting on the pump casing due to the interaction with the moving internal parts of the pump. Subsequently, using vibration and acoustic finite element analysis of the pump enables us to find the effect of these forces on noise level variations created by the pump.

In addition to the material mentioned above, the ability of a variable displacement pump to respond to a constant signal is a critical factor in assessing the dynamic performance of the circuit in which the pump is located. Hence, a comprehensive dynamic response model of the pump is necessary in order to realize new techniques for control.

1.2 Problem Statement

The objective of this research is to find the dominating factors that create the noise in the bent axis pump. The pump will be working within the circuit of a hydraulic hybrid vehicle. Knowing the sources of noise enables taking the appropriate decisions in terms of design, control strategy, and the implementation of anti-noise techniques and procedures either to the pump or to the hydraulic system in order to reduce the noise level to acceptable levels.

The application and extension of the results presented in this study would significantly assist in the analysis of the structures that connects to the pump within a hydraulic system. Knowing the constraints at all joints in the pump structure and the forces in the time and frequency domain as obtained from the current study, a transient finite element model could be implemented for both the pump's case and the pump's internal parts. Moreover, a vibration analysis could be implemented on the structure to which the pump is mounted. This allows an effective design and development of the mounts, which tie to the pump. Furthermore, an acoustic finite element analysis of the pump may be performed to find the effect of the different forces that act on the pump case on noise level variations created by the pump.

1.3 Work Outline

Chapter 2 will present a literature review. The key components of a Hydraulic Hybrid Vehicle are described and explained in detail including: the pump, the high and low pressure accumulators, the oil conditioning system, the hydraulic power steering system, the potential changes to the battery, alternator, and starter system, and the hydraulic fittings and hoses. It also introduces Mild Hydraulic Hybrid vehicles and Full Hydraulic Hybrid vehicles.

Moreover, chapter 2 fully describes the bent axis piston pump/motor including definitions of some performance parameters such as volumetric efficiency, mechanical efficiency, and overall efficiency. It also explains pump noise and cavitation as performance parameters and types of noise. Likewise, it clarifies and defines in some detail pump noise level limits and control.

The principal forces acting on the bearing surface between the valve plate and cylinder block are considered. The effect of the valve plate shape on the fluid film between the valve plate and the cylinder block has been investigated under real working conditions.

This study presents mathematical modeling of bent-axis hydraulic piston pumps and motors including: steady state modeling and performance of a variable displacement pump, the mathematical expressions for the torque applied to the swash plate considering the different loss components, theoretical flow rate and leakage flow rates. The feasibility of using a nonlinear gas spring in the pump controller is also investigated. In addition, bent-axis piston pump modeling using neural networks are mentioned.

In addition, the theoretical mechanism for driving the tapered pistons of a bent axis pump is introduced. Besides, Friction losses analyses of a bent-axis type hydraulic piston pump. Furthermore, noise reduction techniques and control have been introduced.

Chapter 3 considers in detail a comprehensive theoretical dynamic modeling and analysis of the internal pump parts are. A kinematic analysis for each part of the pump determines velocities, accelerations, angular velocities, and angular. Then, the equations of motion of each part as well as the whole system have been determined using Newtonian mechanics.

Chapter 4 shows the implementation and simulation of the mathematical model using Mathematica^{TM} software to study the steady state and transient responses of the forces acting on the pump casing. In addition, the study validates the model against the commercially available ADAMS/View software. Chapter 5 summarizes the work and outlines the conclusions and future work.

CHAPTER 2:LITERATURE REVIEW

2.1 Hydraulic Hybrid Vehicles

One major benefit of a hydraulic vehicle is the ability to capture a large percentage of the energy normally lost in vehicle braking. In urban stop-and-go driving, as much as half of all the energy available at the vehicle wheels is lost in braking and a hydraulic design can capture and reuse a large portion of this otherwise wasted energy. The specific fuel economy improvement associated with a hydraulic hybrid vehicle is dependent upon vehicle driving cycle. In turn, there will always be a larger improvement for those vehicles with a high amount of stop-and-go driving. Therefore, hydraulic hybrid technology has perhaps the greatest commercial potential for a wide range of medium-duty vehicles such as urban delivery trucks [1].

Hydraulic hybrid vehicles can be classified into two main categories: parallel hydraulic hybrid vehicles and series hydraulic hybrid vehicles.

Parallel Hydraulic Hybrid Vehicle (PHH)

A parallel hydraulic hybrid vehicle has both a conventional vehicle power train and a hydraulic secondary storage system. A PHH system captures and stores a large fraction of the energy normally wasted in vehicle braking and uses this energy to help propel the vehicle during the next vehicle acceleration. Figure 2-1 shows the hydraulic circuit diagram of PHH vehicle. In a parallel hydraulic hybrid system, the engine and the

hydraulic pump/motor are mechanically coupled to the same drive shaft. This system has the potential to decrease the fuel consumption in the range of 20% to 40%. Higher efficiencies are limited because the engine must follow the speed of the tires through the transmission.

In pumping mode, hydraulic fluid is pumped into an accumulator under pressure. This requires power from the drive shaft of the vehicle provided either by the ICE or by braking. The accumulator holds the pressurized fluid until it is needed. In motor mode, the hydraulic P/M uses the pressurized fluid to drive the vehicle. In this way, the hydraulic P/M returns power to the vehicle [2].

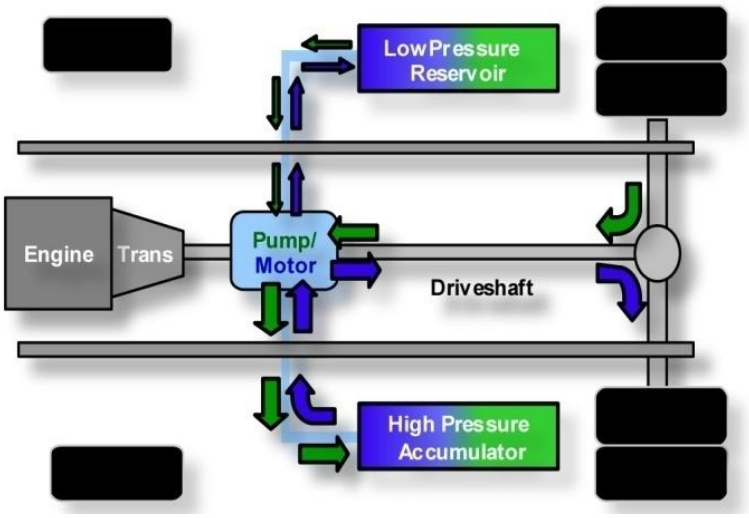

Figure 2-1: Basic hydraulic circuit diagram of a parallel hydraulic hybrid vehicle [2-4]

One issue with a PHH vehicle is whether the engine would ever be shut off to save fuel in those modes where engine power is not required or where the hydraulic launch-assist alone is able to provide sufficient power. Therefore, a PHH vehicle can be designed to work according to either an engine-on strategy, or an engine-off strategy. In an engine-on strategy, the driver would only shut down the engine when the he turns the engine off,

usually at the end of a trip. On the other hand, in an engine-off strategy, the engine operation will be shut down whenever the vehicle is not moving [1].

Series Hydraulic Hybrids (SHH)

In a series hydraulic hybrid, there is no direct link between the internal combustion engine and the driveline components of the vehicle (Figure 2-2). Since the internal combustion engine is now separated from the road, the SHH design permits much greater use of engine-off strategies and maximizes the operation of the engine at or near its peak efficiency [1]. An SHH is capable of more than 70% improvement in fuel savings. The engine is operated to pump hydraulic fluid at pressure to the HPA. When operating conditions are such that there is sufficient pressure in the HPA, the ICE is placed in an off condition. When it is necessary to operate the engine again, a small amount of fluid is directed to the P/M to restart the engine, and this unit returns to motoring mode. The rear P/M operates the drive train of the vehicle. In motoring mode, it takes high-pressure hydraulic fluid from the accumulator to drive the axle. When braking, the axle drives the unit in pumping mode to re-pressurize the HPA [2].

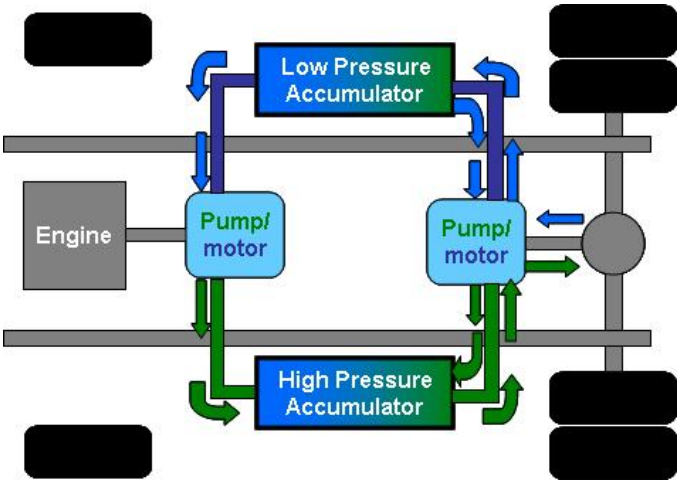

Figure 2-2: A series hydraulic hybrid configuration [2-4]

2.2 Description of Bent Axis Piston Pump/Motor

Piston pumps are the most expensive of the hydraulic pumps. They also provide the highest level of overall performance. They can operate at high speeds to provide a high power-to-weight ratio. They can operate at the highest-pressure levels (up to 5000 psi). Due to very close-fitting pistons, they have the highest volumetric efficiencies among the other types of pumps [5]. Piston P/M can be classified as in-line piston P/M (swash plate) or bent axis type.

2.2.1 Bent axial piston pump

Figure 2-3 shows a bent axis piston pump, which contains a cylinder block rotating with the drive shaft. The centerline of the cylinder block is set at an offset angle relative to the centerline of the drive shaft. The cylinder block contains a number of pistons arranged along a circle. Ball and socket joints connect the piston rods to the drive shaft flange. The pistons are forced in and out of their bores as the distance between the drive shaft flange and cylinder block changes. A universal link connects the block to the drive shaft to provide alignment and positive drive.

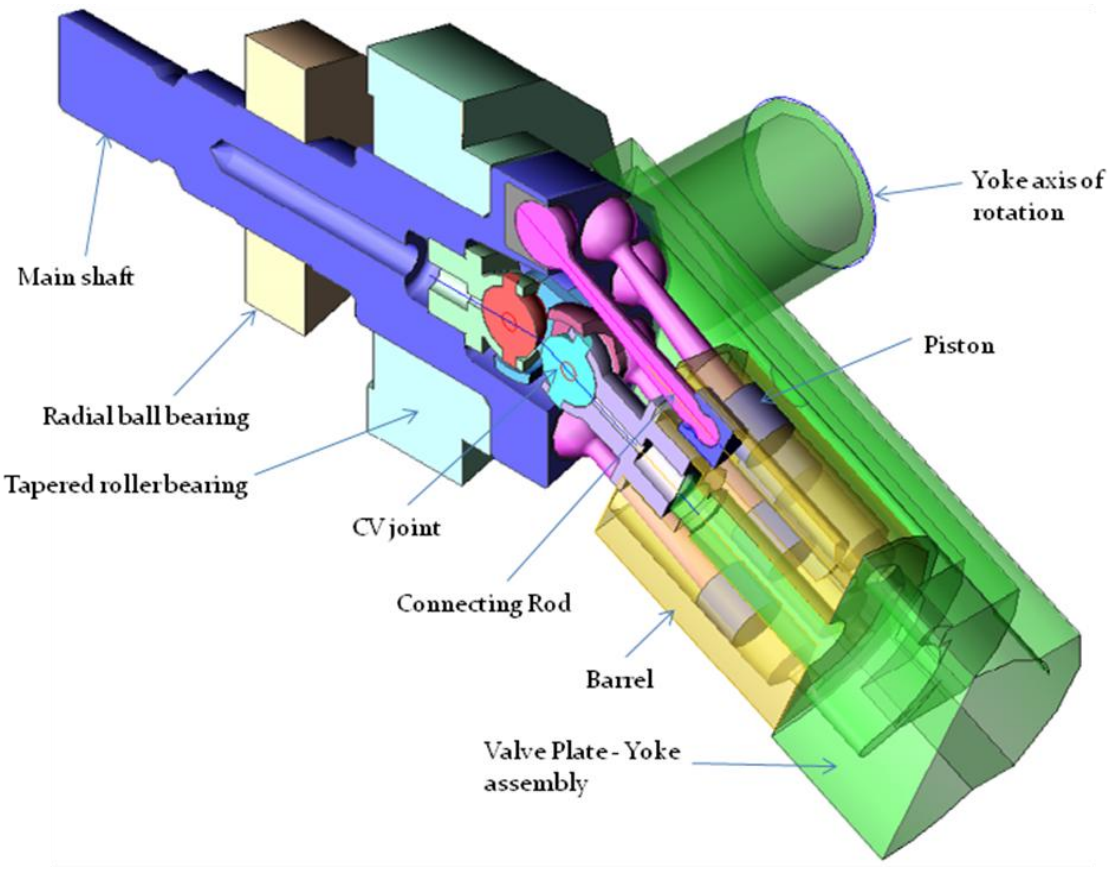

Figure 2-3: Basic components of a bent axis pump

2.2.2 Inline piston pump (swash plate)

Figure 2-4 shows the basic design of an inline piston pump. The cylinder bears against a valve plate. Ports in the plate alternatively connect the cylinders to the inlet, and to the discharge ports. The switch from inlet to discharge occurs when a piston is at its most extended position (BDC). The switch from discharge back to inlet occurs 180^{o} later when the piston reaches its greatest penetration into the cylinder block (TDC) [6].

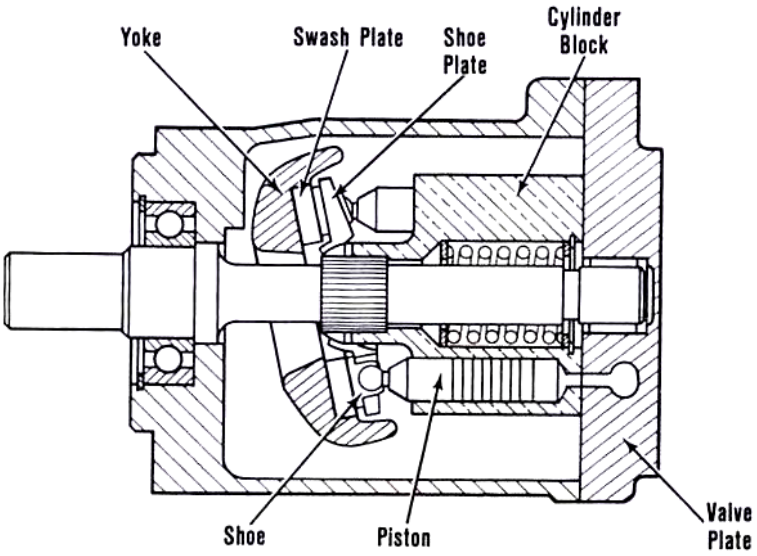

Figure 2-4: Inline piston pump [6]

2.2.3 Pump/Motor basic parameters

2.2.3.1 Volumetric efficiency

The volumetric displacement of the P/M varies with the offset angle θ. No flow results when the cylinder block centerline is parallel to the drive shaft centerline. θ can vary from zero degrees to a maximum of about 50º.

Internal leakage between the inlet and outlet reduces the volumetric efficiencies of a hydraulic pump/motor. Volumetric efficiency of the pump indicates the amount of leakage that takes place within the pump and can be written as [5]

$$\eta_{v,pump} = \frac{Q_A}{Q_T} \tag{2.1}$$

The volumetric efficiency of a hydraulic motor is the inverse of that for a pump. This is because a pump does not produce as much flow as it should theoretically, whereas a motor uses more flow than it should theoretically due to leakage. In turn, the volumetric efficiency of a motor is given by

$$\eta_v = \frac{Q_T}{Q_A} \tag{2.2}$$

2.2.3.2 Mechanical efficiency

Mechanical efficiency indicates the amount of energy losses that occur for reasons other than leakage. This includes friction in bearings and between other mating parts. It also includes energy losses due to fluid turbulence. Therefore, the mechanical efficiency of a pump is expressed as [5]

$$\eta_{m,pump} = \frac{\text{pump output power assuming no leakage}}{\text{actual power delevired to pump}} = \frac{pQ_T}{T_A N} \tag{2.3}$$

One can also compute the mechanical efficiency of a pump in terms of torques as given by

$$\eta_{m,pump} = \frac{\text{theoretical torque required to operate pump}}{\text{actual torque delevired to pump}} = \frac{T_T}{T_A} \tag{2.4}$$

The mechanical efficiency of a hydraulic motor is the inverse of that for a pump. Because of friction, a pump requires a greater torque than it should theoretically whereas a motor produces less torque than it should theoretically.

$$\eta_{m,motor} = \frac{\text{actual torque delevired by motor}}{\text{torque motor should theoretically deliver}} = \frac{T_A}{T_T} \tag{2.5}$$

Where

p = pump discharge pressure

T_A = actual torque delivered to pump

The theoretical torque varies proportionally to both the pressure and the volumetric displacement:

$$T_T = \frac{V_D \times p}{2\pi} \quad \textbf{(2.6)}$$

The theoretical power (which is the power a frictionless hydraulic motor would develop) is given by

$$\text{Theoretical power (W)} = T_T \text{ (N.m)} \times N \text{ (rad/s)} \quad \textbf{(2.7)}$$

The actual torque is given by

$$T_A = \frac{\text{actual power delivered to/by pump/motor(W)}}{\omega(rad/s)}$$
$$\omega = \frac{2\pi}{60} N(rpm) \quad \textbf{(2.8)}$$

2.2.3.3 The overall efficiency of P/M

The overall efficiency (η_o) considers all energy losses and is defined as [5]

$$\eta_o = \frac{\text{actual power delivered by pump/motor}}{\text{actual power delivered to pump/motor}} = \eta_v \times \eta_m \quad \textbf{(2.9)}$$

2.2.4 Pump noise

More than 95% of noise problems in hydraulically actuated machines are due to pumps and motors. Valves are the other major hydraulic noise source [6].

Pumps are good generators but poor radiators of noise. The noise we hear is not just the sound coming directly from the pump. It includes the vibration and fluid pulsations produced by the pump as well. Pumps are compact, and because of their relatively small size, they are poor radiators of noise, especially at lower frequencies. Therefore, pump-induced vibrations or pulsations can cause them to radiate audible noise greater than that coming from the pump [5].

Pump speed has a strong effect on noise, whereas pressure and pump size have about equal but smaller effects. To achieve the lowest noise levels, the lowest practical speed (1000 or 2000 rpm) is selected [5].

Pump noise is created as the internal rotating components abruptly increase the fluid pressure from inlet to outlet. The abruptness of the pressure increases plays a big role in the intensity of the pump noise. Thus, the noise level at which a pump operates depends greatly on the design of the pump. Noise can be classified into three types [6]: audible noise referred to as Air Born Noise (ABN), vibrations referred to as Structure Born Noise (SBN), and fluid pulsations referred to as Fluid Born Noise (FBN).

Pumps commonly generate as much as 1000 times more energy in the form of SBN or FBN noise than they do in the form of ABN. These forms act on other machine elements and frequently end up generating more noise than that coming directly from the pump.

Machines generally have a number of noise sources. Effective noise control depends on identifying one or two of the strongest noises. Separating noise by energy path and frequency helps identify these leading noises. Once we find how they travel from their source to our ear, their control is generally assured [6].

Chen et al. studied the dynamic analysis of a swash-plate water hydraulic motor in a modern water hydraulic system. They modeled a swash-plate mechanism as a system with 3 masses and 14 degrees of freedom. They presented numerical simulation analysis of the dynamic response of the model due to pressure pulsation and compared with experimental testing. They obtained and studied a series of the dynamic vibration characteristics of the water hydraulic piston motor by the numerical simulation. The model simulates the vibration signal of the casing in the hydraulic motor. According to the authors, the

waveform and frequency of the simulated signal is similar to the experimental signal. In addition, they found that the simulated signals in other directions show that the vibration signals in all the directions mainly consist of the hydraulic pump and motor rotational frequencies.

2.2.5 Noise level limits

The strength of a sound wave, which depends on the pressure amplitude, is described by its intensity. Sound intensity is defined as the rate at which sound energy is transmitted through a unit area. This energy transfer rate is expressed in units of decibels (dB). Decibels give the relative magnitudes of two intensities by comparing the one under consideration to the intensity of a sound at the threshold of hearing [5].

Intensity and loudness are not the same. Loudness depends on each person's sense of hearing. The intensity of a sound, which represents the amount of energy possessed by the sound, can be measured and thus does not depend on the person hearing it [5].

One decibel equals approximately the smallest change in intensity that most people can detect. Zero dB designates the weakest sound intensity that the human ear can hear. Sound intensities of 120dB or greater produce pain and may cause permanent loss of hearing [5].

The sound level in dB is obtained by taking the logarithm to the base 10 of the ratio of the intensity under consideration to the threshold of hearing intensity [5].

$$I(dB) = 10\log\frac{I}{I_{hear.threshold}} \qquad \textbf{(2.10)}$$

Where

I = the intensity of a sound under consideration in units of W/m^2

$I_{hear\ threshold}$ = the intensity of a sound at the threshold of hearing in units of W/m^2

The amount that the intensity of sound increases in units of dB if the intensity in W/m^2 increases by a given factor is given by

$$dB_{increase} = 10\log\frac{I_{final}}{I_{initial}} \quad \textbf{(2.11)}$$

The occupational Safety and Health Administration (OSHA) stipulates that 90 dB is the maximum sound level that a person may be exposed to during an 8hr period in the workplace [5]. Higher noise levels are allowable if the exposure durations were shorter. For each 5-dB (A) increase in noise, the allowable duration was cut to half. Similarly, if longer exposure time occurred, the level was decreased by the same rate.

Table 2-1 shows the allowable noise exposure levels. The total exposure time at various noise levels is given by [6]

$$C_T = \frac{C_1}{T_1} + \frac{C_2}{T_2} + ... + \frac{C_n}{T_n} \le 1 \quad \textbf{(2.12)}$$

Where

n = number of exposure levels

$C_1, C_2 \ldots C_n$ = total time at the given levels

$T_1, T_2 \ldots T_n$ = total time allowed at the given levels

Noise reduction can be accomplished in different ways as follows [5]:

1. Make changes to the source of noise. Problems may include misaligned pump/motor couplings, improperly installed pump/motor mounting plates, pump cavitation, and excess pump speed or pressure.
2. Modify components connected to the primary source of the noise. An example is the clamping of hydraulic piping at specifically located supports.

3. Use sound absorption materials in nearby screens or partitions. This practice will reduce the reflection of sound waves to other areas of the building where noise can be a problem.
4. Refer to the methods mentioned in chapter 1, section 1.3.4 (Noise Reduction and Control).

Table 2-1: OSHA Allowable Noise Exposures [6]

Noise level dB(A)	Exposure per day hr	Noise level dB(A)	Exposure per day hr
90	8	102	1.5
92	6	105	1
95	4	110	0.5
97	3	115 max	0.25
100	2		

2.2.6 Pump cavitation

Cavitation occurs when pump suction lift is excessive and the pump inlet pressure falls below the vapor pressure of the fluid (usually about 5-psi suction). As a result, air or vapor bubbles, which form in the low-pressure inlet region of the pump, collapse when they reach the high-pressure discharge region. This produces high fluid velocity and impact forces, which can erode the metallic components and shorten pump life.

2.3 Design of Valve Plate and Forces Acting on It

With reference to Figure 2-5, the interface between valve plate and cylinder block is the most important sliding part in axial piston pumps, because the cylinder block rapidly

rotates on the fixed valve plate, and the pistons in the cylinders during approximately half a revolution perform the suction and discharge action of working oil through the kidney ports. In addition, the pressure distribution on the valve plate varies momentarily. Therefore, optimal force balance is required to reduce the leakage flow rates and friction.

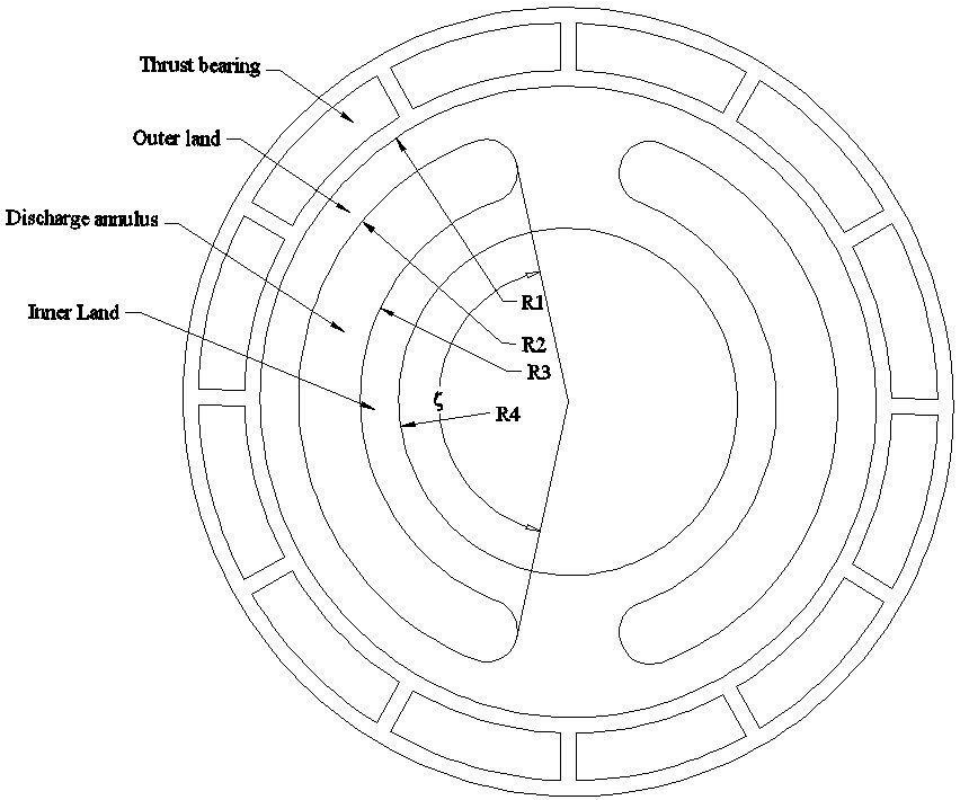

Figure 2-5: Geometric parameters of the valve plate

Figure 2-6 shows that there are two principal axial forces acting on the bearing surface between valve plate and cylinder block. One of these forces is a pushing force associated with the highly pressurized pistons tending to push the cylinder block via the highly pressurized oil to the valve plate. This is because the highly pressurized fluid on the discharge port of the valve plate acts on the cylinder block walls by a frictional force in the direction of the oil stream leaving the cylindrical cavity. On the other hand, on the suction port of the valve plate, the oil enters the cylindrical cavity resulting in a frictional

force that pulls the cylindrical block from the valve plate. Therefore, the net frictional force, which is the difference between the two forces at the discharge and suction ports, acts in the direction of pushing the cylindrical block towards the valve plate.

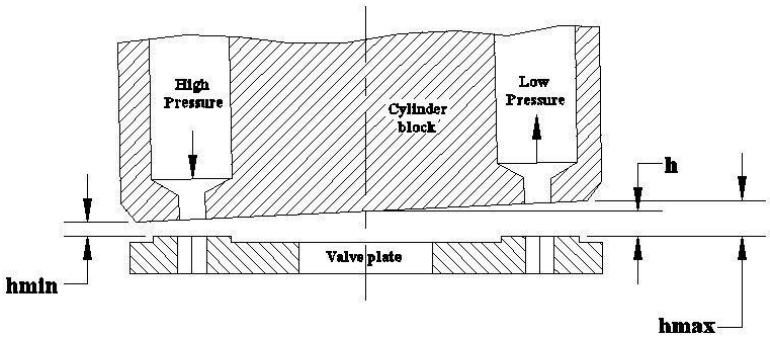

Figure 2-6: Principal forces in the interface between the barrel and the valve plate

The other force is a separating force associated with the pressure in the highly pressurized kidney port and across its lands tending to separate the cylinder block with the valve plate. If the pushing force due to the pistons under high pressure is too big, the faces will be subjected to high friction, rapid wear, overheating, and therefore reducing mechanical efficiency. If the separating force due to the pressure distribution on the seal lands is too big, the cylinder block will be forced away from the valve plate leading to excessive leakage losses [7].

Franco [8] derived equations for the forces that act on the port plate of a swash plate pump based on the following assumptions:

1 Fluid flow in the clearance between the barrel and port plate is laminar.

2 Forces due to pressure drop peripherally between the inlet and discharge ports were ignored.

3 Hydrodynamic friction forces created by the rotary motion of the barrel were neglected.

4 Leakage flow is assumed to spread in the radial direction between the lands.

5 Constant coefficient of dynamic viscosity.

6 The centrifugal forces of the fluid in the clearance between the port plate and the barrel were neglected.

7 The velocity distribution in the clearance is based on the conditions that the maximum relative velocity happens at the middle of the clearance and zero at the walls.

Manring [9] examined the control and containment forces and moments acting on the swash plate of an axial-piston pump. Swash-plate control and containment devices must resist the moments and forces that attempt to dislocate the swash plate from its proper position. He derived the needed forces and moments for insuring proper swash-plate motion.

Manring [10] examined the control and containment forces acting on the swash plate of an axial piston pump by including the analysis of a secondary swash-plate angle. He derived the needed forces and moments for insuring proper swash plate motion. He also studied the dynamic characteristics of the control and containment forces by deriving instantaneous and average equations of motion for the swash plate. Manring showed that the primary advantage of implementing a secondary swash-plate angle is that it can reduce the overall control effort of the pump. On the other hand, the disadvantages of using the secondary swash-plate angle are associated with additional containment requirements for the swash plate.

Manring [11] identified the physical contributors of the phenomenon of tipping of the cylinder block. He specified certain design guidelines that may be used to prevent the failure of cylinder block tipping. He begins with the mechanical analysis of the machine and presents a tipping criterion based upon the centroidal location of the force reaction between the cylinder block and the valve plate. He then derived the effective pressurized area within a single piston bore. In addition, he examined the pressure within a single piston bore using an approximate pressure profile in order to specify a design criterion. The design criterion ensures that the pressures within the system never cause the cylinder block to tip. By satisfying this criterion, he found that the worst tipping conditions exists when the system pressures are zero.

Bergada et al. [12] had analyzed the pressure distribution, leakage, force, and torque between the barrel and the port plate of an axial piston pump. They developed a detailed set of new equations, which takes into account important parameters such as tilt, clearance and rotational speed, and timing groove. Additionally, they derived the pressure distribution for different operating conditions, together with a complementary numerical analysis of the original differential equations. They evaluated overall mean force and torques over the barrel and showed that the torque over the XX axis is much smaller than the torque over the YY axis (Figure 2-7). They then conducted a detailed dynamic analysis and found that the torque fluctuation over the YY axis is typically 8% of the torque total magnitude. They were also able to predict a double peak in each torque fluctuation resulting from the more exact modeling the pressure distribution characteristic of the piston/port plate/timing groove during motion.

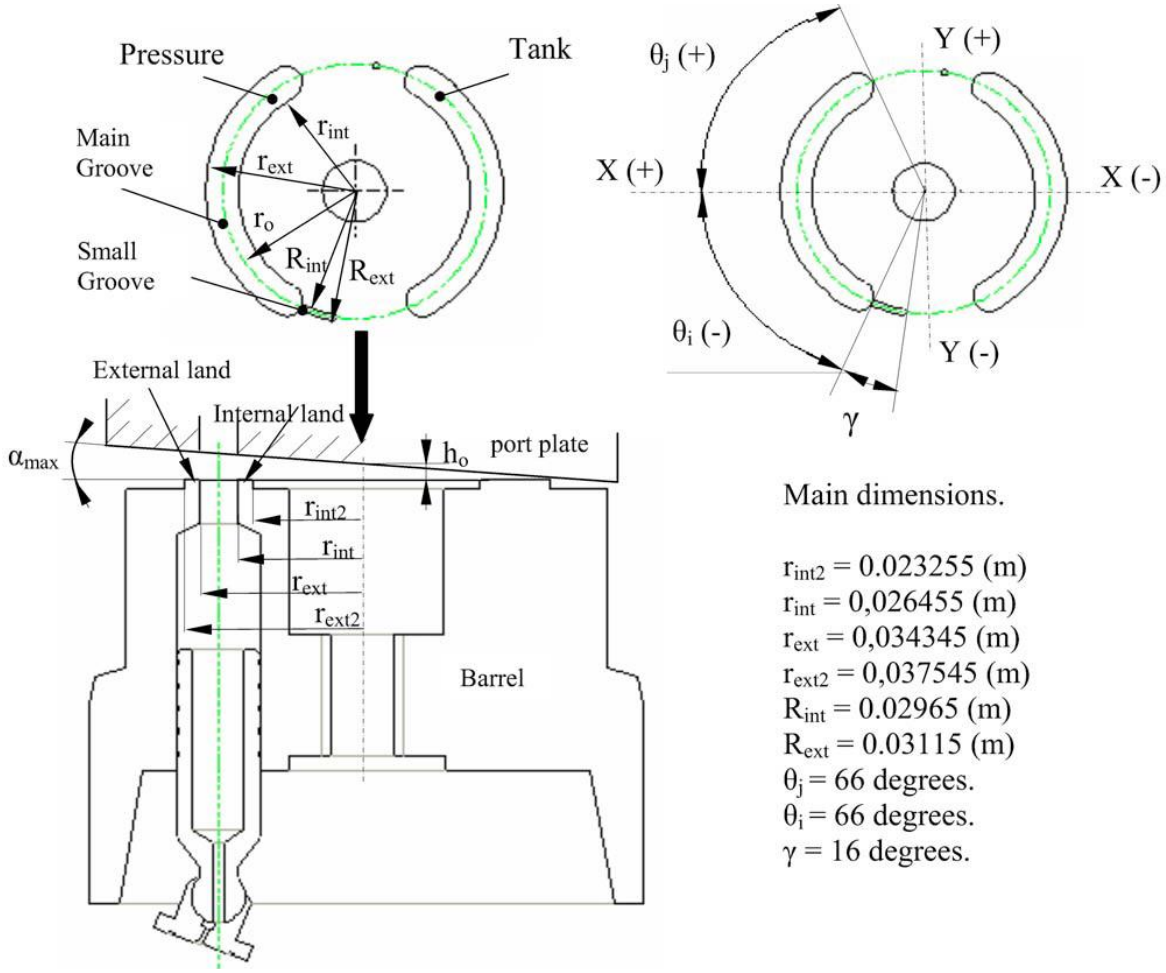

Figure 2-7: Barrel/port plate configuration[12]

For radial flow in a system, the temperature of the fluid increases as the pressure drop across the system. Therefore, Mckeown et al. [13] had derived an analysis for the forces acting on valve plate for a system in which both radial and tangential flows occur. Given the input conditions of pressure, temperature, and a reference viscosity, they presented a numerical method to solve for the corresponding temperature, pressure drop, leakage flow rate, and the viscosity at any point in the fluid film between the barrel and the valve plate. He then defined three force coefficients to calculate the hydrostatic force between the valve plate and the rotating barrel. This analysis was conducted for two cases. For the first case, it was assumed that no heat from the fluid is lost to the boundaries. For the other

case, they considered the effect of heat losses from the fluid as it passed through the sealing gap.

Casoli et al. [14] presented a numerical model for the simulation of a swash-plate axial piston pump, focusing on the characterization of fluid properties. First, they gave a quick overview on a previously developed pump model. Then, they presented four different models of the fluid, which take into account cavitation. These models aim at characterizing the unsteady and erratic cavitation features in a simplified manner in order to apply the models to the simulation of hydraulic components. In the second part of the paper, they showed an application of these models to an axial piston pump. They got a few results and compared them with available test data.

Kim et al. [7] conducted a study to investigate the effect of the valve plate shape on the fluid film between the valve plate and the cylinder block under real working conditions. They designed three valve plates with different shapes. One of the valve plates was without bearing pad, a second one with a bearing pad and the third one was a spherical valve plate. The leakage flow rates and the shaft torque were also investigated in order to clarify the performance difference between the three types. The spherical valve plate estimated good fluid film patterns and good performance more than the other valve plates in oil hydraulic axial piston pumps in overall pressure range. The discharge pressure pulsation, the leakage flow rates and the total efficiency are strongly related to the changing pattern of the fluid film on the valve plate. Kim et al. [7] also reached the following conclusions:

1. As the barrel is tilted from the center of the valve plate, the fluid film in the discharge region is smaller than that in the suction region.

2. The fluid film on the valve plate is continuously changed in value and location during one revolution of the cylinder block as can be seen in Figure 2-6. The shaking of the cylinder block is attributed to the discharge pressure pulsation. The clearance of the spline and the bearing causes the tilting of the cylinder block. The size of the shaking and the tilting increases with increased discharge pressure. The spherical valve plate was able to reduce both the shaking and the tilting of the cylinder block over all driving conditions due to spherical contact.
3. In case of the plane valve plate without bearing pad, the possibility of contacts between valve plate and cylinder block is really increasing in high discharge pressure condition. Therefore, high friction, severe wear and hence the frictional loss will be increased.
4. For both the spherical valve plate and plane valve plate with bearing pad, the difference of fluid film between discharge region and suction region was noticeably reduced compared with that of the plane valve plate without bearing pad.
5. Overall, the minimum fluid film thickness slightly increased as rotational speed increased.
6. The minimum fluid film linearly decreased as discharge pressure increases. The minimum fluid film of the plane valve plate without bearing pad decreased more steeply than the other valve plates in high-pressure range.

In general, the leakage flow rates increase as discharge pressure increases. The leakage flow rates of the spherical valve plate show the lowest value compared with the other two valve plates in the range above 20 MPa. The leakage flow rates of the plane valve plate

without bearing pad sharply increase compared with those of the plane valve plate with bearing pad in high-pressure range above 25MPa due to the increase of fluid film.

Manring [15] examined the volumetric efficiency of an axial-piston pump as it relates to the compressibility losses of the fluid. He compared a standard valve-plate design which utilizes slots to a trapped-volume design which eliminates the slots altogether. He found analytically that the standard valve-plate design introduces a volumetric loss, which may be accounted for by the uncontrolled expansion and compression of the fluid that occurs through the slots themselves. In addition, he suggested that the operating efficiency could be improved by utilizing a trapped volume design.

Zloto et al. [16] applied the Reynolds equation, commonly applied in the theory of lubrication, in the numerical analysis (finite element method) of pressure distribution of an oil film on the valve plate in the variable height gap of an axial piston pump. They used an adaptive mesh refinement based on residual estimations of solution errors in order to obtain high accuracy of the results. They found that the geometric and work parameters of the kinematic pair (cylinder block/valve plate) have a substantial impact on the pressure distributions in the variable height gap. With an increase in the angular velocity of the cylinder block or oil viscosity, the values of the oil film over-and under-pressure “peaks” increase linearly. They also reported that Maximal over-and under-pressure “peaks” occur for the smallest values of the bias angle. Upon an increase in bias angle the values of the over-and under-pressure “peaks” decrease. Additionally, the maximal values of the over-and under-pressure “peaks” occur for the minimal gap height. Upon an increase in the minimal value of the gap height the values of the over-and under-pressure “peaks” decrease.

2.4 Modeling of Bent-Axis hydraulic Piston Pumps and Motors

Schoenau et al. [17] presented a mathematical model of a variable displacement swash plate pump modulated by a hydraulic control signal. The model was based on the assumptions that the main input shaft is rotating at a fixed angular velocity, and negligible stiction due to the constant piston motion. They derived an expression for the torque applied to the swash plate that consists of four components: piston inertia effects, pressure force effects, piston shear effect, and shoe plate force effect. Neglecting stiction, an expression for the damping torque acting on the yoke due to viscous friction was introduced. This torque varies linearly with the angular velocity of the yoke via a proportionality constant determined experimentally.

In finding the pressure force effects, Schoenau et al. [17] had considered the pressure variations through one complete revolution of the swash plate. Because the valve ports have relief notches to avoid step changes in pressure in the transition regions, they considered the resulting overlap, which produces six distinct pressure regions for each revolution of the piston barrel (see Figure 2-8).

In region 1, the cylinder is completely open to the discharge port and so the cylinder pressure is equal to the discharge pressure. In region 2, the cylinder is open to both the discharge port and the relief notch before the suction port. In region 3, the cylinder is open only to the relief notch before the suction port. In region 4, the cylinder is completely open to the suction port and so the cylinder pressure is equal to the suction pressure. In region 5, the cylinder is open to both the suction port and the relief notch before the discharge port. In region 6, the cylinder is open only to the relief notch before the discharge port.

Applying the continuity and momentum equations to each region resulted in expressions for the pressure and flow variation with the barrel rotational angle. The leakage flow rate is the sum of the flow rate between the cylinders and the pistons, the flow out through the slippers, and the leakage between the cylinder barrel and the valve plate. The leakage flow rate was found to be proportional to the pressure [17].

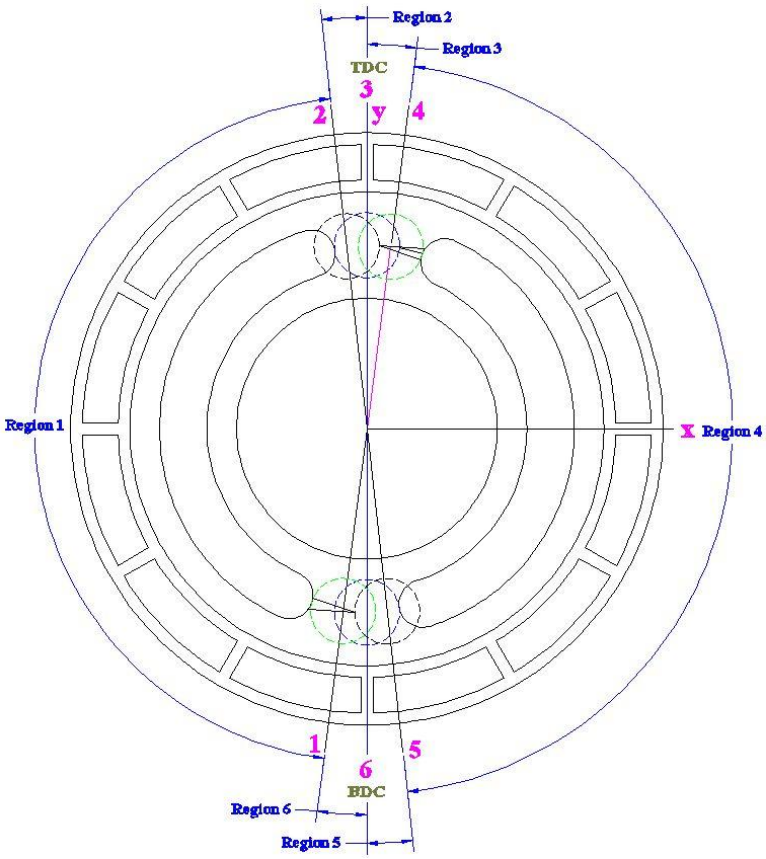

Figure 2-8: Pressure regions according to Schoenau et al. [17]

Bartos [18] presented a mathematical modeling for bent-axis hydraulic piston motor with multiple pistons. In his model, he derived an equation for the instantaneous theoretical torque generated by the fluid pressure forces at the pistons. This equation only expresses the torque generated by the pressure forces and does not model the net torque

output of the motor because losses due to viscous forces and Coulomb friction were not considered. Mathematical relations that involve two non-dimensional constants then approximated the equation. Moreover, he derived the torque losses. These losses include: the torque due to viscous forces of the fluid in the clearance between the barrel and the valve plate, the resisting torque created by viscous forces in the clearance between the barrel and the motor housing, coulomb friction torque at the motor bearings, shaft torques resulting from Coulomb friction from internal oil seals, and piston motion within the barrel. The net motor output torque to the load is therefore equivalent to the pressure torque at the pistons less the torque losses and the torque expended to accelerate the motor parts. Likewise, the theoretical flow rate through the motor, ignoring leakage effects was found. This flow rate was also approximated by mathematical relationships that involve two non-dimensional constants that have the same values as those for the torque expression. Besides, the leakage flow rates were also derived that include: the leakage past the hydraulic motor pistons from the pressure and return ports to the case drain, the fluid leakage between the valve plate and the cylinder block, and the total cross port leakage (leakage flow between motor ports across the valve plate to barrel sealing surface).

Karkoub et al. [19] derived a neural network model to predict the steady-state and dynamic behavior of a bent-axis piston pump with the objective to reduce the power loss at high pressures. The model uses data obtained from an experimental setup. The neural network model has a feed forward architecture and uses the Levenberg Marquardt optimization technique in the training process. According to the authors, the model was able to predict the behavior of the pump accurately.

Canbulut et al. [20] employed a neural network to analyze axial piston pump of hydrostatic circular recessed bearing. The system mainly consists of cylinder block, piston, slipper, ball-joint and swash plate. The neural model of the system has three layers, which are input layer with one neuron, hidden layer with ten neurons and output layer with three neurons. According to the authors, the proposed neural network was able to predict static and dynamic parameters of the bearing system in real time.

Gad et al. [21] investigated the static and dynamic behavior of a variable displacement bent axis axial piston pump with power controller theoretically and experimentally. A mathematical model was deduced to predict the performance of the pump and its controller. The steady-state characteristics and pump transient response were predicted theoretically and evaluated experimentally. The authors indicated that the theoretical results showed good agreement with the experimental results in the steady state and transient modes of operation. According to the authors, the study of the pump performance showed that the pump does not present the hyperbolic power curve, which represents the constant power curve.

The feasibility of using a nonlinear gas spring in the pump controller was also investigated. The proposed controller includes a gas charged accumulator to replace the used mechanical springs in the feedback path. A nonlinear mathematical model of the proposed controller was developed and treated by using SIMULINK. The static characteristics of the proposed controller showed that, the P-Q relation is near to the required hyperbola in case of slow variation load pressure, isothermal compression process. In case of real polytrophic gas process in the accumulator, the resulting P-Q

relation deviates from the required hyperbolic curve. During short time period, the gas temperature reaches its original steady-state value due to the good thermal conductivity of the metallic materials of the accumulator house. Then the operating point displaces to be on the P-Q curve corresponding to the isothermal process. The mathematical model describing the pump dynamic behavior was based on the following assumptions [21]:

- The fluid pressure at the suction and return lines is zero gauge pressure.
- The pressure losses in the short pipelines are neglected.
- The pump rotates at constant speed.
- The oil temperature and viscosity are constant.
- The inertia force of oil column in the cylinder is negligible.
- Half the number of pistons is exposed to high pressure and the leakage originates at these cylinders.
- The pressure forces acting on the valve plate were neglected.

The proposed controller, equipped with the hydraulic accumulator, results in a better utilization of available power compared with the actual one specially at the commencement power control at the higher operating pressure range. The transient response of the pump, to step throttling of exit line, is calculated. The transient pressure oscillations and settling time are considerably reduced, but the maximum over shoot is increased [21].

Zhang et al. [22] proposed the modeling of a damping mechanism with an open-loop reduced order model for the swash plate dynamics of an axial piston pump. They derived an analytical expression for the damping mechanism. They also validated the proposed reduced order model by comparing with a complete nonlinear simulation of the pump

dynamics over the entire range of operating conditions. The model should potentially help in the development of improved control design of swash plate for hydraulic axial-piston pumps.

In a study conducted by Kim et al. [23], the theoretical mechanism for driving the tapered pistons of a bent axis pump is studied by use of the geometric method. The driving area of the tapered pistons was defined by measuring the strain of a cylinder forced against a tapered piston using an electric strain gage and a slip ring as can be seen in Figure 2-9. The forces applied to tapered pistons are also investigated with the change of discharge pressure and the rotational speed. It was concluded that the cylinder block is driven by one tapered piston in a limited area and the driving area is changed due to space angle of the tapered pistons and the swivel angle of the barrel. The force applied to tapered pistons increases as the discharge pressure and the rotational speed increase.

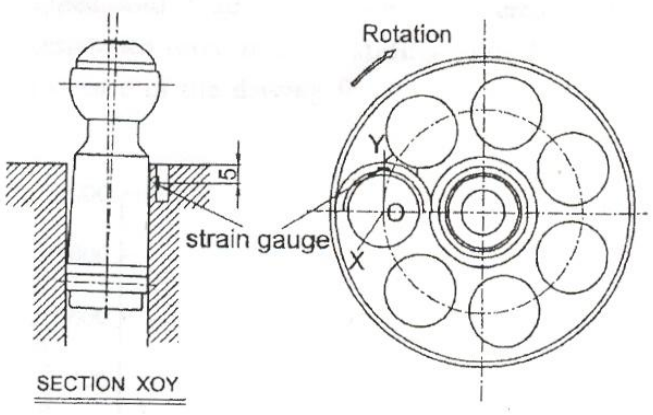

Figure 2-9: Driving mechanism experimental setup [23]

Bael et al. [24] studied the theoretical mechanism for the bent-axis type axial piston pump by using the geometrical method. They determined the theoretical equations for the driving range of the tapered piston. They found out that, the cylinder block is driven by

one tapered piston in a limited range and that the core parameters such as the tilting angle of the piston and the ahead delay angle influence performance of the bent-axis type axial piston pump.

Hong et al. [25] presented a study on the friction losses of a bent-axis Type Hydraulic Piston Pump to find out which design factors influence its torque efficiency most significantly. The friction coefficients of the pump parts such as piston heads, spherical joints, shaft bearings, and valve plate were experimentally identified. Applying the experimental data to the equations of motion for pistons as well as to the theoretical friction models for the pump parts, the frictional torques produced by them was computed. The accuracy of the computed results was confirmed by comparison with the practical input torque of the pump. They found that the viscous friction forces on the valve plate and input shaft bearing are the primary sources of the friction losses of the bent-axis type pump, while the friction forces and moments on the piston are of little significance. According to the study, the diameters of the valve plate and the shaft bearing should be minimized in order to increase the torque efficiency of the object pump at high input shaft speed [25].

The total friction torques generated by the piston heads, spherical joints, valve plate and bearing add to around 10.9% of the theoretical input torque at a rotational speed of 10, 000 rpm and a load pressure of 300 bars. The computed total input torques is slightly smaller than the measured ones. The object pump indicated a practical torque efficiency of about 85% at a rotational speed of 4, 000 rpm and 75% at 8, 000 rpm for the load pressure of 136 bars [25].

Nie et al. [26] formulated the characteristic equation of the hydrostatic slipper bearing with an annular orifice damper, where the effects of various geometric factors are reflected. They investigated the reaction force of the bearing in water hydraulic axial piston motor (WHAPM). Moreover, they examined the effects from the friction within the cylinder bore, the dynamics of the piston, and the centrifugal force of the piston–slipper assembly. Results of the theoretical analyses indicated that the friction coefficient, the swash plate angle, and the inertia and centrifugal loads would have significant influences on the reaction force. Furthermore, an appropriate swash plate angle can help eliminate the fluctuation of the reaction force. Besides, the load-carrying capacity of the hydrostatic slipper bearing is more sensitive to the damping length than to the supporting length of the piston. Moreover, a short damping length can help improve the load-carrying capacity. Experimental studies of the slipper pads sliding against the swash plates are also conducted at a custom-manufactured test apparatus. The experimental results indicated that the hydrostatic slipper bearing with an annular orifice damper would decrease the possibility of the severe wear between the slipper pad and the swash plate in comparison with the hydrostatic clamping ratio bearing in the WHAPM.

Watton, J. [27] introduced a non-dimensional approach to the explicit characterization of the non-linear steady state performance of an axial piston motor. The motor is driven by a servo valve and it is shown how the flow characteristics, including losses, may be sufficiently represented by a well-established single equation that may then be used to produce directly usable design equations for speed, efficiency, and power transfer. The new equations allow direct determination of the conditions for maximum efficiency and

power transfer, which leads to determine the effect of flow and torque losses for both open-loop and closed-loop operation. The approach was validated by experimental results. The derived equations, though applicable over a wide range of conditions, become more accurate at high speeds and particularly with closed-loop control at higher load pressures. The flow equations for closed-loop control at very high load pressures where the servo valve current saturates are not applicable. Optimum drive performance in the sense of maximum power transfer and efficiency may be possible but at a very low drive speed and a low drive efficiency.

2.5 Noise Reduction and Control

The reduction in source flow ripple in hydraulic systems is the most effective method of reducing pump-generated pressure ripple and system noise.

According to Watton [27] and Johansson [28, 29], the noise and vibrations created by the pump have mainly two different origins. First, the cylinder pressures acting on the piston will create piston forces inside the pump. Second, the pump generates flow ripple, which in a system will be transformed to pressure ripple and noise. Pump generated flow ripple can be divided into two different parts. The first part is the kinematic flow ripple, which is due to the limited number of pistons, which portion the flow into the delivery line. The second part is the compressible flow ripple, which becomes evident as the fluid is exposed to large alternating pressures.

Manring [30] examined the idealized and actual flow-ripple of an axial-piston swash-plate type hydrostatic pump. He considered two cases. First, the idealized case in which the leakage is considered zero and the fluid is assumed incompressible. Both the ripple height and the pulse frequency of the ripple are described for a pump with an even and an

odd number of pistons. In the other case, the actual flow-ripple of the pump is examined by considering the pump leakage and the fluid compressibility. From an idealized point of view, Manring showed quantitatively that an eight-piston design is less attractive than a nine or seven-piston design. From a flow ripple point of view, Manring indicated numerically that a pump designed with an even number of pistons might be as feasible as one that is designed with an odd number of pistons.

Helgestad et al. [31] outlined a scheme whereby the delivery port opened relatively late in the cycle and allowed a one-way valve in the port plate to open when the cylinder reached the delivery pressure. Ideally, this would produce optimal cylinder pre-compression for every pump operating condition. The valve would close each time that it communicated with a low-pressure cylinder and then open again as each cylinder reached the delivery pressure. Because of this, the valve might only have a limited life; a nine-piston pump operating at 1500 rpm for example would cause the valve to switch 810000 times/hour. Furthermore, at higher pump speeds, the frequency response of the valve may limit its switching performance.

A possible solution to the FBN problem is the incorporation of an auxiliary source of flow ripple which, when combined with the pump flow ripple, produces destructive interference. However, a mechanical method of achieving this would be difficult due to the short duration of the cylinder reverse flows. Likewise, the anti-noise mechanism would need to respond precisely to transient changes in the mean delivery pressure, displacement, and speed. Otherwise, the device itself might create a significant unwanted FBN. Rebel [32] attempted FBN cancellation by introducing a high-frequency flow fluctuation using a fast-response servo-valve and an auxiliary pump. Initially, open-loop

control was used with a single sinusoidal control of the valve used to cancel a specific harmonic. He carried out cancellation tests on a radial three-piston pump, operating at a maximum speed of 2000 rpm and achieved a measure of success. He found that the servo-valve could cause a 9dB reduction in the pump FBN at the pump fundamental frequency. Under closed-loop control, with the pump pressure ripple signal used for feedback, a larger reduction of 17dB was achieved through cancellation of a number of the lower-pump flow ripple harmonics. However, Rebel concluded that the system was not commercially feasible; the cancellation of higher-frequency components above 50Hz was limited by the frequency response of the servo-valve. Also, bleeding off and adding fluid reduced the overall system efficiency. Furthermore, the cost of the servo valve would probably be analogous with that of the piston pump.

The delivery delay needed for optimal pre-compression depends on the fluid properties, pump speed and displacement, and pressure difference between suction and delivery. To achieve optimal or near-optimal pre-compression over a wide range of operating conditions, a variable timing mechanism was proposed by several researchers that actuates the angular position of the port plate [33-35] in response to changes in these characteristics. However, the concept is limited in its effectiveness because any delay in the opening of the delivery port is also applied to the suction port. With large delays, the end of the delivery port can extend over the piston TDC position, leading to transfer of fluid back to the suction port and a consequent reduction in the pump volumetric efficiency. In addition, a delayed opening of the suction port is likely to cause cavitation in the cylinder at the start of the suction stroke.

Martin et al. [35] and Boltyanski et al. [36] attempted to separate the timing of the suction and delivery ports by using independent mechanisms acting at the start of both ports. However, the main problem with these mechanisms is the high cost of their implementation. In addition, the servomechanisms controlling the variable timing elements become extremely complex in order to reveal the necessary pressure, flow and speed compensation characteristic.

An alternative approach to variable timing is to use mechanisms that pre-compress the cylinder contents to the delivery pressure in time for communication with a fixed delivery port. Pre-compression filter volume (PCFV) has been developed by Boyer [37] and Pettersson [38]. Very careful design of the arrangement is required for adequate flow ripple attenuation over a wide range of operating conditions. In particular, the volume of the PCFV and the diameter and length of the connecting channel from the PCFV to the port plate are critical factors in achieving good performance. Now, results from the PCFV mechanism have only been published for fixed-displacement pumps.

Bartos [39] presented a Mathematical Model describing the torque and flow ripple effects of a bent-axis hydraulic piston motor. This paper describes how the resultant torque and flow ripple can be reduced by properly phasing the hydraulic motors when multiple motors are used to drive a device. The total instantaneous torque with minimum torque and flow ripple generated by the hydraulic motors is equivalent to the instantaneous torque generated by a single motor with a displacement equal to the displacement of one motor multiplied by the number of motors. In the mean time, number of pistons equal to the number of pistons of one motor multiplied by twice the number of motors if the motor has an odd number of pistons. The corresponding equivalent displacement for an even

number of pistons equals to the displacement of one motor multiplied by the number of motors, while the equivalent number of pistons equals to the number of pistons of one motor multiplied by the number of motors.

Harrison et al. [40] indicated that the main feature of the axial piston pump delivery flow ripple is the short-duration reverse flow into the cylinder at the beginning of the delivery phase caused by under-compression of the cylinder fluid as the cylinder passes from the suction port to the delivery port. Conventionally, a pressure relief groove machined on the face of the port plate prior to the opening of the delivery kidney slot reduces the severity of the cylinder reverse flow. This extends the period over which reverse flow occurs, thereby reducing the magnitude of higher frequency flow ripple harmonics. However, the size and timing of this feature are highly dependent upon the delivery and suction pressures and upon the pump displacement and speed. Pressure relief grooves have no mechanism to respond to such changes, and so they are optimized for best performance over a limited range of operating conditions. Consequently, pumps with relief grooves can generate a significant increase in FBN when operating away from the design point.

Kim et al. [41] simultaneously measured pressure variations in a cylinder at the discharge region and the pump noise for different values of the discharge pressures and rotational speeds during the pump working. They used three types of valve plates to investigate the effects of the pre-compression and the V-notch in the valve plate. They found that the pressure variations in the cylinder increase as the discharge pressure and the rotational speed increase. In addition, the pump noise is deeply related to the pressure variations in the cylinder and the pressure pulsations in the discharge line. Furthermore,

the pressure variations in the cylinder and the pressure pulsations in the discharge line can be reduced by optimizing the design of the pre-compression angle and the V-notch in the valve plate, which consequently may result in the reduction of the pump noise.

Mandal et al. [42] presented a model that puts special emphasis on analyzing the effect of volume variation of the silencing grooves. They carried out the analysis for a swash plate pump with leading-side manifolds. Therefore, they indicated optimal dimensions for these grooves through a constant-speed parametric analysis at fixed load. With the goal to minimize the pressure and flow ripples, they also developed a mathematical model that attempts an explicit solution of pressure within each silencing groove.

Kumar et al. [43] presented static and dynamic characteristics of a piston pump slipper with a groove. They have applied three-dimensional Navier Stokes equations in cylindrical coordinates to the slipper/plate gap, including the groove. They presented pressure, leakage, force, and torque variations when groove dimensions and position are being modified. They also considered the effect of slipper tangential velocity and turning speed. They found a good agreement between theoretical analysis and experimental results. In their analysis, they assumed laminar and incompressible flow under all conditions and that the slipper is parallel to the plate. In addition, they gave design instructions to optimize slipper/groove performance.

Harrison et al. [40] presented a timing mechanism which is speed, flow and pressure sensing to reduce axial piston pump delivery flow ripple. The mechanism consists of a series of heavily damped check valves (HDCV) built-in the delivery port of the pump valve plate. Fixed-speed tests have shown that the mechanism can significantly reduce axial-piston pump’s delivery flow ripple over a wide range of delivery pressures and pump

displacements. Moreover, the reduction in pressure ripple achieved with the mechanism led to reductions in overall Air Born Noise (ABN) levels of up to 6 dB in a simple system. A simulation model has been produced to predict the behavior of the prototype mechanism. According to the authors, the model achieved good agreement with the measured delivery flow ripple. The final HDCV prototype achieved reductions in delivery flow ripple and casing ABN for delivery pressures between 100 and 250bar, and for pump displacements between 20 and 100%. The level of damping applied to the valve is important. With too much damping, the valve response will be slow and the pump could become noisy during transient changes in operating conditions. With too little damping, the valve element will switch rapidly and hence may have a limited life and may be an additional noise source; it could also result in damage to the pump. In each condition, the HDCV prototype appears to cause more gradual cylinder compression. For the maximum flow conditions, the first harmonic is significantly reduced with the higher harmonics relatively unaffected. However, for the 20% flow conditions, the flow ripple is significantly reduced for the first four harmonics. In high-flow conditions, the improvements are less exciting. The introduction of the HDCVs led to a reduction in measured sound pressure level (SPL) of between one and 6 dB (A). As with the reductions in flow ripple, the largest SPL reductions occurred at lower pump displacements. Overall, the simulation model underestimates the HDCV damping at low frequencies in contrast with the overestimation at higher frequencies.

Johansson et al. [28, 29] introduced an overview of a design feature called the “cross-angle”. Cross-angle is a bias angle (2º to 4º) of the swash plate around the axis that is perpendicular to the normal displacement angle (see Figure 2-10). Because of the cross-

angle, the time delay (pre-compression) before linking up to the discharge kidney changes with the displacement angle. The physical principle of a cross-angle is similar to the revolving valve plate, but instead of rotating the valve plate, the dead centers are moved as the displacement angle changes.

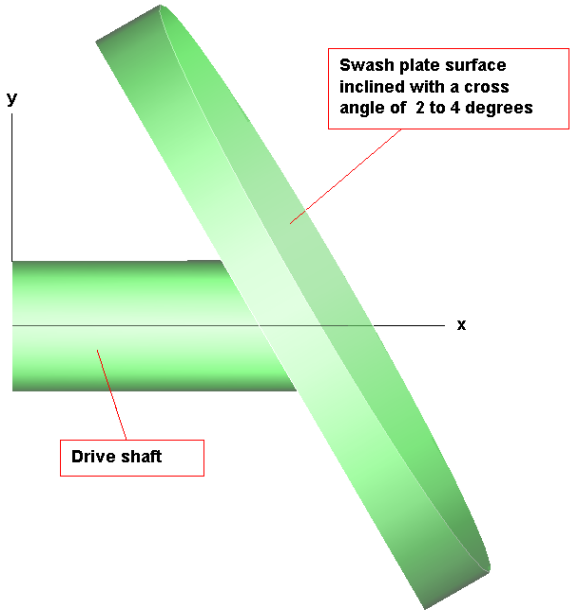

Figure 2-10: Cross angle

In a study conducted by Kim et al. [44], a parallel line is introduced to the hydraulic pipeline for the hydraulic system with a bent axis piston pump as a method to reduce the pressure ripples. It was confirmed by experiment and by simulation that the hydraulic pipeline with a parallel line can considerably reduce the amount of pressure ripples by using the phase difference of pressure waves caused by the length difference between the main line and the parallel line.

CHAPTER 3: THEORITICAL ANALYSIS

All vectors dealt with in this analysis should be referenced to either the inertial coordinate frame "$a_1a_2a_3$" or any other moving coordinate frame. A letter at its lower left corner should precede the vector. This letter indicates that the vector is expressed with respect to the indicated frame of reference. For example, the vector ${}_DV$ is a vector V that is expressed with respect to the moving coordinate frame D.

3.1 The Frictional Moments at the Rolling Bearings

Figure 3-1 shows the basic components of a ball roller bearing, which include the inner race, the rollers, the outer race, and the cage. The resistance to rotation of a rolling bearing is composed of rolling, sliding, and lubrication frictions.

Rolling contact friction occurs when the rolling elements roll over the raceways. It results in part from elastic hysteresis and partially from the associated sliding resistance. The rolling contact friction is proportional to the size of the contact areas and the size of the contact angle between rolling elements and raceways.

Sliding friction occurs at the guiding surfaces of the cage, between the rollers for bearings without a cage, at the roller faces and the raceway lips. Lubricant friction is the result of the internal friction of the lubricant between the working surfaces as well as its churning and working action that occurs with excess lubricant at high speeds.

The total resistance to running of a rolling bearing is very small compared with the transmitted forces. However, the friction determines the heat generated in a bearing, thus influencing the operating temperature of the bearing parts and the lubricant.

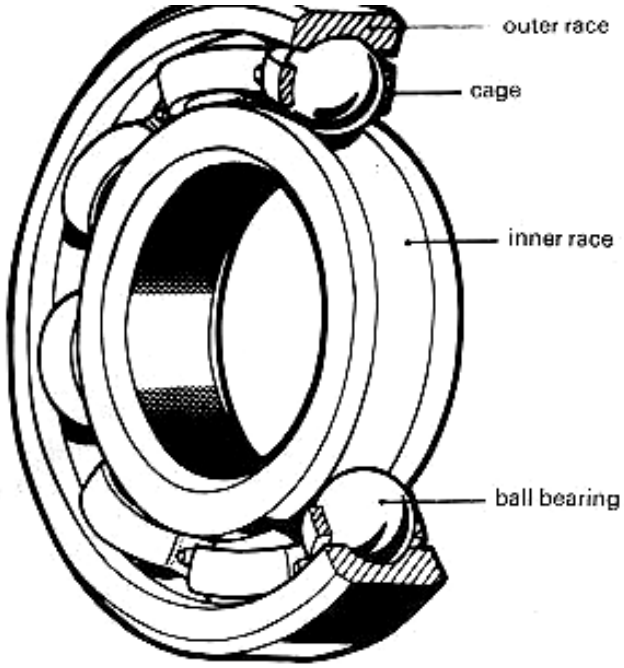

Figure 3-1: Basic components of a roller bearing [45]

The frictional moment of a roller bearing depends on the load, the speed, and the lubrication viscosity. Under normal operating conditions, the entire frictional moment of a roller bearing, which accommodates both radial and axial loads is given by

$$M = M_v + M_m + M_a \quad \textbf{(3.1)}$$

Where

M = total frictional moment of the bearing (N.m)

M_v = load independent component of the frictional moment (N.m)

M_m = radial load dependent component of the frictional moment (N.m)

M_a = axial load dependent component of the frictional moment (N.m)

3.1.1 The load-independent component Mv

This depends on the operating viscosity ν of the lubricant and on the speed of the rotating shaft. The bearing friction through the bearing temperature in turn influences the operating viscosity. In addition, the bearing size d_m and the width of the rolling contact areas, which varies noticeably from type to type, have an effect on M_v. The load independent component M_v of the frictional moment is determined in accordance with the empirical formula given by [25]

$$M_v = \begin{cases} 10^{-10} f_o (\nu n_{ms})^{2/3} d_m^3, \nu n_{ms} \geq 2000 \\ 160 \times 10^{-10} f_o d_m^3, \nu n_{ms} < 2000 \end{cases} \quad \textbf{(3.2)}$$

f_o = index for bearing type and lubrication type [45]

The pitch circle diameter of the bearing, d_m is given by

$$d_m = \frac{D+d}{2} \quad \textbf{(3.3)}$$

Where

d = bore diameter of the bearing in mm

D = Outside diameter of the bearing in mm

ν = operating viscosity (mm^2/s) of the oil

The oil used in the pump assumed here is Mobile 1 synthetic ATF, which has viscosity values as shown in Figure 3-2. For the operating temperature range (20°C to 40°C), the kinematic viscosity could be assumed to vary exponentially with the operating temperature with reasonable accuracy according to the relationship

$$\nu = 92.31 e^{-0.025T} \quad \textbf{(3.4)}$$

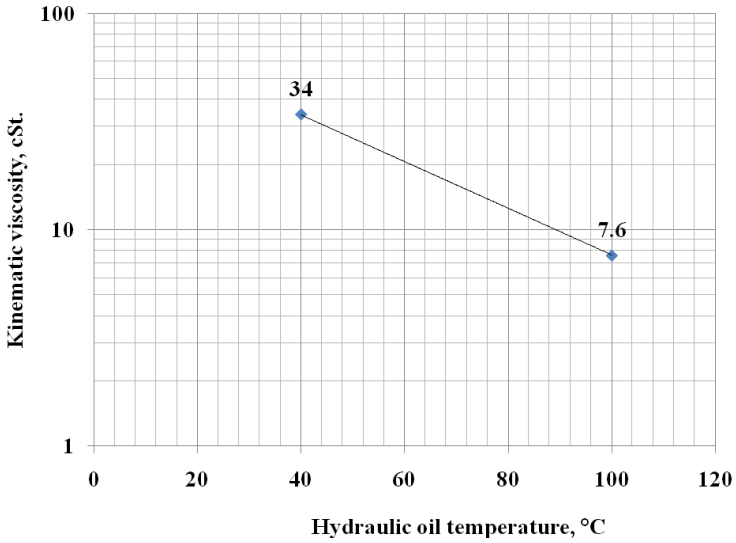

Figure 3-2: Kinematic viscosity of Mobile 1 synthetic ATF hydraulic oil vs. temperature

The index f_o is indicated in Table 3-1 for oil bath lubrication where the oil level in the stationary bearing reaches the center of the bottommost rolling element. For fixed d_m, f_o increases with the size of the balls or with the length of the rollers, i.e. it also increases indirectly with the size of the bearing cross-section. If radial bearings run on a vertical shaft under radial load, twice the value given in Table 3-1 has to be assumed; the same applies to a large cooling-oil flow rate or an excessive amount of grease.

Table 3-1: Indexes f_o, f_1, P_1 for the calculation of rolling bearings frictional moment [45]

Bearing type	**f_o**	**f_1**	**P_1**
Deep groove ball bearings	1.5-2	$0.005 - 0.009\left(\frac{P_o}{C_o}\right)^{0.5}$	$\max\left(F_r, 3.3\,F_a - 0.1\,F_r\right)$
Tapered roller bearings	3-6	0.0004	$\max\left(2Y\,F_a, F_r\right)$
Needle roller bearings	5-5.5	0.0005	F_r
Thrust ball bearings	1.5	$0.0012\left(\frac{F_a}{C_o}\right)^{0.33}$	F_a

3.1.2 The Radial load dependent frictional moment component M_m

This results from the rolling friction and from the sliding friction at the lips. Under normal operating conditions, M_m hardly varies with speed but it does vary with the size of the contact area and consequently with the rolling element/raceway curvature ratio and the loading of the bearing. The radial load dependent frictional moment is given by

$$M_m = \frac{f_1 P_1 d_m}{1000} \tag{3.5}$$

f_1 is an index taking into account the magnitude of load and is listed in Table 3-1 for different bearing types.

The load P_1 governs the radial load-depending frictional moment M_m. It takes into account the fact that M_m changes with the load angle and is listed in Table 3-1 for different bearing types.

3.1.3 Axial load dependent component of the frictional moment

The axial load dependent component of the frictional moment is given by

$$M_a = 6\times10^{-5} f_a F_a d_m \tag{3.6}$$

The index f_a, which depends on the axial load F_a and the lubricating condition, is given by

$$f_a = \begin{cases} 0.15, x_1 < 1 \\ -0.0699 \ln x_1 + 0.15, 1 \le x_1 \le 7 \\ 0.014, x_1 > 7 \end{cases} \tag{3.7}$$

$$x_1 = \frac{f_b d_m \nu n_{ms}}{F_{a2}^2 (D^2 - d^2)} \tag{3.8}$$

F_b = 0.0048 for caged bearings

F_b = 0.0061 for full complement bearings (without a cage)

For a bent axis piston pump linked to a HPA at the discharge port and to a LPA at the suction port, x_1 in Eq. (3.7) will always be less than 1.0. Therefore, Eq. (3.7) reduces to

$$f_a = 0.15, x_1 < 1 \tag{3.9}$$

3.2 Dynamic Analysis of Main Shaft Assembly

The main shaft includes the drive shaft, the input shaft to the constant velocity joint, the cups of the Connecting Rods, and the disk. The drive shaft transmits power from the engine by means of a splined end of the shaft.

Consider the inertial coordinate axis system "$a_1a_2a_3$" as shown in Figure 3-3. Attach a coordinate system "$b_1b_2b_3$" to the main shaft. "$b_1b_2b_3$" is obtained by rotating "$a_1a_2a_3$" about the "a_3" axis with an angle ϕ (3-rotation). Therefore, the transformation matrix can be written as

$$T_1 = \begin{bmatrix} \cos\phi & \sin\phi & 0 \\ -\sin\phi & \cos\phi & 0 \\ 0 & 0 & 1 \end{bmatrix} \tag{3.10}$$

The angular velocity of the rotating frame of reference expressed in "B" frame with respect to "A" frame in a skew symmetric matrix form is given by [46]

$$\overset{A}{}_{B}\tilde{\omega}^{B} = T_1\dot{T}_1^{T} = \begin{bmatrix} 0 & -1 & 0 \\ 1 & 0 & 0 \\ 0 & 0 & 0 \end{bmatrix}\dot{\phi} \tag{3.11}$$

The angular velocity and angular acceleration of the main shaft in a vector form are given by

$$ {}_B\omega_{ms} = \begin{bmatrix} 0 & 0 & \dot{\phi} \end{bmatrix}^T \tag{3.12} $$

$$ {}_B\alpha_{ms} = \begin{bmatrix} 0 & 0 & \ddot{\phi} \end{bmatrix}^T \tag{3.13} $$

The definition of the "$b_1b_2b_3$" frame in terms of "$a_1a_2a_3$" frame can be expressed as

$$ \begin{bmatrix} b_1 \\ b_2 \\ b_3 \end{bmatrix} = T_1 \begin{bmatrix} a_1 \\ a_2 \\ a_3 \end{bmatrix} = \begin{bmatrix} \cos\phi & \sin\phi & 0 \\ -\sin\phi & \cos\phi & 0 \\ 0 & 0 & 1 \end{bmatrix} \begin{bmatrix} a_1 \\ a_2 \\ a_3 \end{bmatrix} = \begin{bmatrix} \cos\phi\vec{a}_1 + \sin\phi\vec{a}_2 \\ -\sin\phi\vec{a}_1 + \cos\phi\vec{a}_2 \\ \vec{a}_3 \end{bmatrix} \tag{3.14} $$

The velocity and acceleration of the center of gravity of the main shaft equals to zero.

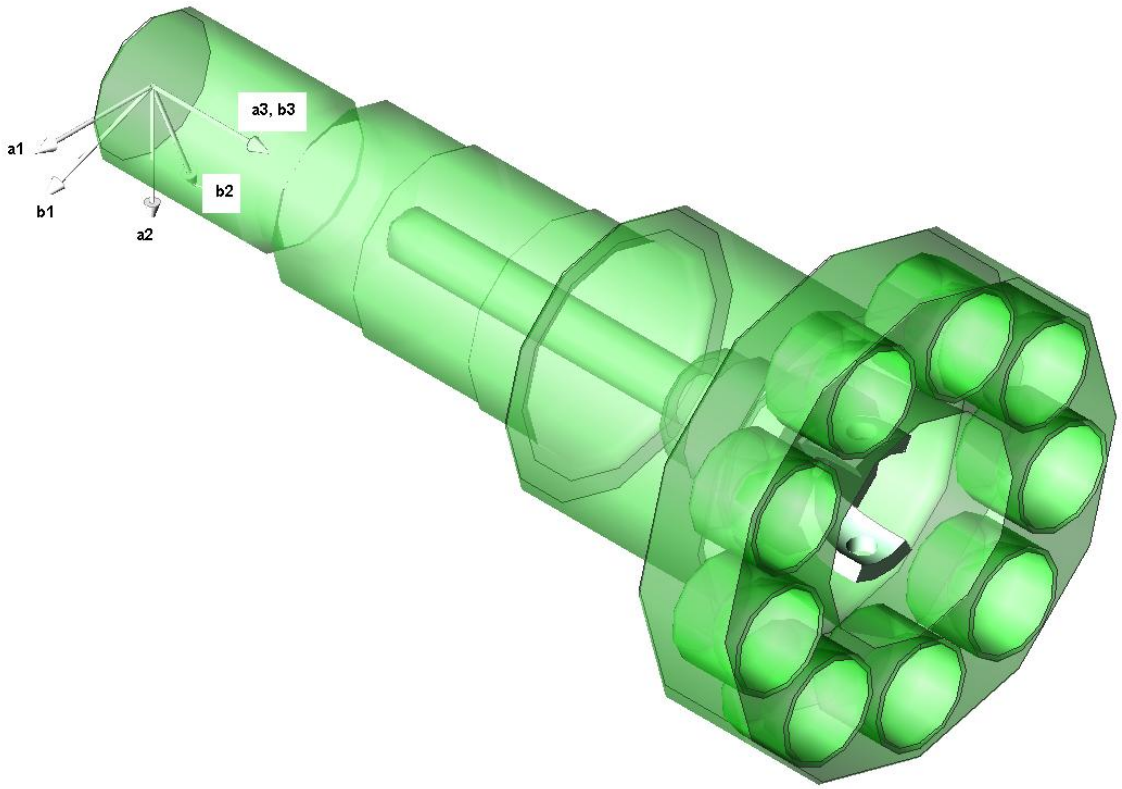

Figure 3-3: Main Shaft

Figure 3-4 shows the Free Body Diagram (FBD) of the main shaft. The forces and moments that act on the FBD of the main shaft include:

1. The torque input, ${}_AT_{in}$, to the main shaft and is expressed as

$$ {}_{A}T_{in} = \begin{bmatrix} 0 & 0 & {}_{A}T_{inz} \end{bmatrix}^{T} \quad \textbf{(3.15)} $$

2. The reaction force from the ball bearing at point (1). It consists of two force components acting perpendicular to the shaft axis and a frictional moment around the shaft axis. The reaction force and the corresponding position vector as measured from the left end of the main shaft can be expressed as

$$ {}_{A}F_{B1toMS} = \begin{bmatrix} {}_{A}F_{B1toMSx} & {}_{A}F_{B1toMSy} & 0 \end{bmatrix}^{T} \quad \textbf{(3.16)} $$

$$ {}_{A}r_{1} = \begin{bmatrix} 0 & 0 & r_{1z} \end{bmatrix}^{T} \quad \textbf{(3.17)} $$

The frictional moment opposes the direction of rotation of the shaft and is expressed as

$$ {}_{A}M_{B1toMS} = -{}_{A}M_{B1toMSz}.sign\left({}_{B}\omega_{ms} \right) \quad \textbf{(3.18)} $$

3. The reaction force from the thrust bearing at point (2). Two force components are perpendicular to the axis of the shaft and the third one is parallel to it. In addition, there is frictional moment acting around the shaft axis. The thrust bearing reaction force and the corresponding position vector as measured from the left end of the main shaft is expressed as

$$ {}_{A}F_{B2toMS} = \begin{bmatrix} {}_{A}F_{B2toMSx} & {}_{A}F_{B2toMSy} & {}_{A}F_{B2toMSz} \end{bmatrix}^{T} \quad \textbf{(3.19)} $$

$$ {}_{A}r_{2} = \begin{bmatrix} 0 & 0 & r_{2z} \end{bmatrix}^{T} \quad \textbf{(3.20)} $$

The frictional moment opposes the direction of rotation of the shaft and is expressed as

$$ {}_{A}M_{B2toMS} = -{}_{A}M_{B2toMSz}.sign\left({}_{B}\omega_{ms} \right) \quad \textbf{(3.21)} $$

4. The reactions from the two side pins of the first cross of the CVJ at points (3) and (4). The reaction force at each pin consists of two perpendicular components

denoted by $-{}_F\mathrm{F}_{\mathrm{MStoC13}}$, $-{}_F\mathrm{F}_{\mathrm{MStoC14}}$. These reaction forces are equal in magnitude and opposite in direction, thus forming a couple. Moreover, there is a frictional moment around the axis of each pin, denoted as $-{}_F\mathrm{M}_{\mathrm{MStoC13}}$ and $-{}_F\mathrm{M}_{\mathrm{MStoC14}}$. The corresponding position vectors of these reaction forces as measured from the left end of the main shaft is given by

$$ {}_B r_3 = \begin{bmatrix} 0 & -r_{C1} & r_{3z} \end{bmatrix}^T \tag{3.22} $$

$$ {}_B r_4 = \begin{bmatrix} 0 & r_{C1} & r_{3z} \end{bmatrix}^T \tag{3.23} $$

5. Reaction forces from the connecting rods at the cups at points (5) through (13). Each connecting rod acts with a reaction force that consists of three force components. Besides, there are three frictional moment components from the spherical end of each connecting rod. The connecting rod reaction forces and the frictional moments at the end of the connecting rod are donated as $-{}_A\mathrm{F}_{\mathrm{MStoCR,i}}$, and $-{}_A\mathrm{M}_{\mathrm{MStoCR,i}}$ respectively, where i = 1, 2, …9. The position vector of this reaction force as measured from the left end of the main shaft is expressed as

$$ {}_A r_{CR}(i) = \left[T_1\left(\phi + \frac{2\pi(i-1)}{9} \right) \right]^T \begin{bmatrix} 0 & -R & r_{5z} \end{bmatrix}^T, \quad i = 1, 2, \ldots 9 \tag{3.24} $$

6. The weight of the main shaft and the corresponding position vector as measured from its left end are expressed as

$$ {}_A W_{MS} = \begin{bmatrix} 0 & gM_{MS} & 0 \end{bmatrix}^T \tag{3.25} $$

$$ {}_A r_{Wms} = \begin{bmatrix} 0 & 0 & r_{Wmsz} \end{bmatrix}^T \tag{3.26} $$

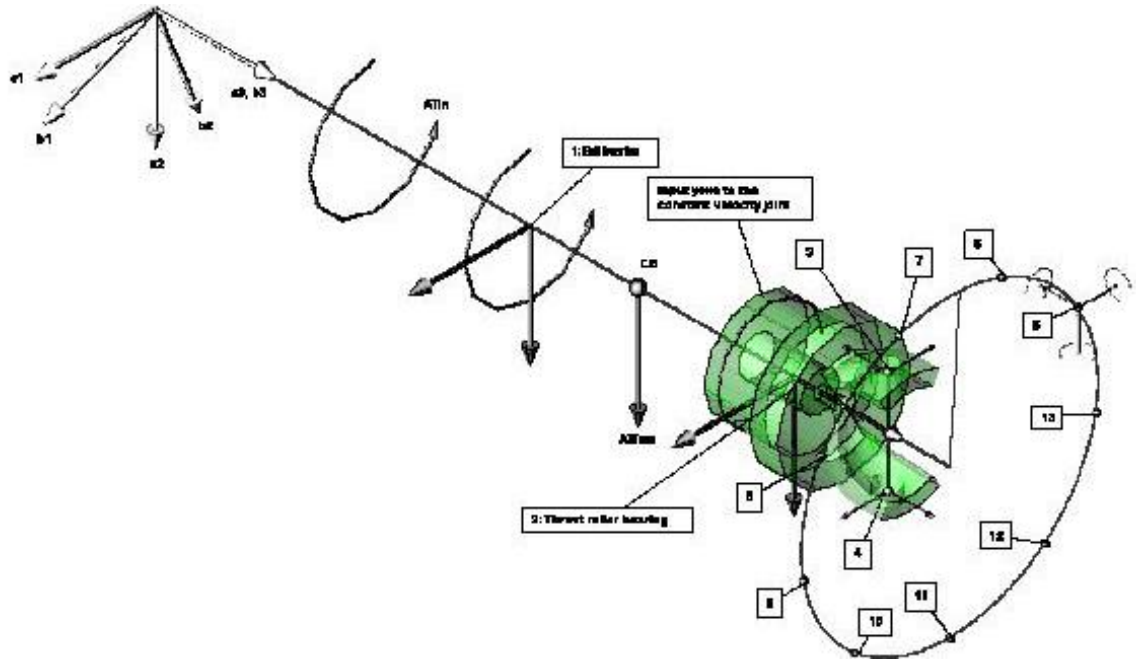

Figure 3-4: Free Body Diagram of the main shaft sub-assembly

3.2.1 The frictional moment at the ball bearing of the main shaft

The frictional moment from the ball bearing opposes the direction of rotation of the main shaft and is expressed as

$$ {}_{A}M_{B1toMS} = \frac{-{}_{B}\omega_{ms}}{\left|{}_{B}\omega_{ms}\right|} M_{B1toMSz} \tag{3.27} $$

A detailed analysis of frictional moment components of roller bearings is presented in section 3.1. The thrust-tapered roller bearing carries out the thrust load from the main shaft. Therefore, the axial load dependent component of the frictional moment from the ball bearing is zero. Hence, the frictional moment on the ball bearing as given by Eq. (3.1) reduces to

$$ M_{B1toMSz} = M_{1m} + M_{1v} \tag{3.28} $$

n_{ms} is the angular velocity of the main shaft in rpm and is given by

$$n_{ms} = \frac{\omega_{ms}[3] \times 60}{2\pi} \tag{3.29}$$

The pitch circle diameter of the bearing, d_{m1} is given by

$$d_{m1} = \frac{D_1 + d_1}{2} \tag{3.30}$$

The index f_{11} which takes into account the magnitude of load is given by [45]

$$f_{11} = 0.005 - 0.009\left(\frac{P_{o1}}{C_{o1}}\right)^{0.5} \tag{3.31}$$

P_{o1} is the equivalent load determined for the operating load and is given by [45]

$$\begin{aligned} P_{o1} &= X_{o1}F_{r1} + Y_{o1}F_{a1} \\ X_{o1} &= 0.6 \text{ and } Y_{o1} = 0.5 \end{aligned} \tag{3.32}$$

C_{o1} is the static load rating of the bearing. The load P_{11} governs the load-depending frictional moment M_{1m}. For deep groove ball bearings with zero thrust loading, it is given by [45]

$$P_{11} = F_{r1} \tag{3.33}$$

F_{r1} is the radial load component of the bearing reaction at point (1) and is given by

$$F_{r1} = \sqrt{F_{B1toMSx}^2 + F_{B1toMSy}^2} \tag{3.34}$$

3.2.2 The frictional moment at the thrust bearing

The frictional moment opposes the direction of rotation of the shaft and is expressed as

$${}_A M_{B2toMS} = \frac{-{}_B\omega_{ms}}{\left|{}_B\omega_{ms}\right|} {}_A M_{B2toMSz} \tag{3.35}$$

Therefore, the frictional moment at the tapered roller bearings is given by

$${}_A M_{B2toMSz} = M_{2m} + M_{2v} + M_{2a} \tag{3.36}$$

The index f_{o2} for bearing and lubrication type = 3 to 6 for tapered roller bearings. The pitch circle diameter of the bearing, d_{m2} is given by

$$d_{m2} = \frac{D_2 + d_2}{2} \tag{3.37}$$

The index f_{12}, which takes into account the magnitude of load, equals to 0.0004. The load P_{12} which governs the load-depending frictional moment M_{2m}, for tapered roller bearings, is given by [45]

$$P_{12} = \max\left(2Y\, F_{a2}, F_{r2}\right) \tag{3.38}$$

Y is a thrust load factor. Brändlein et al. [45] listed equations for the factor Y, where for a tapered roller bearing is given by

$$Y = \begin{cases} 0, \dfrac{F_{a2}}{F_{r2}} \le e \\ 0.4\cot\alpha_o, \dfrac{F_{a2}}{F_{r2}} > e \end{cases} \tag{3.39}$$
$$e = 1.5\tan\alpha_o$$

The axial reaction component at the thrust bearing "F_{a2}" comes from the axial component of the pistons' pressure. Most of the times, the yoke angle (θ) is less than 45°. In addition, "F_{a2}" is proportional to "$P_{OIL}\cos\theta$" while the radial reaction component is proportional P_{OIL} sin θ. Therefore, the ratio of the axial reaction component to the radial reaction component ($\frac{F_{a2}}{F_{r2}}$) will be more than 1.0 as long as θ is less than 45°. Moreover, the nominal contact angle (α_o) usually ranges from 10° to 20°, which leads to the fact that e in Eq. (3.39) will always be less than 1.0. Consequently, the ratio $\frac{F_{a2}}{F_{r2}}$ will be greater than e. As a result, Eq. (3.39) reduces to

$$Y = 0.4 \cot \alpha_o \tag{3.40}$$

The nominal contact angle (α_o) usually ranges from 10° to 20°. Therefore, cot α_o will vary between 5.67 and 2.74. Hence, Y in Eq. (3.40) will range between 1.1 and 2.27. As a result, the term "2Y F_{a2}" will be larger than F_{r2} in Eq. (3.38). Thus, Eq. (3.38) reduces to

$$P_{12} = 2Y\ F_{a2} \tag{3.41}$$

F_{r2} is the radial load component of the bearing reaction and is given by

$$F_{r2} = \sqrt{{}_A F_{B2toMSx}^2 + {}_A F_{B2toMSy}^2} \tag{3.42}$$

3.2.3 Equations of motion

Since the main shaft is in pure rotation, its CG has a zero translational acceleration. Therefore, the sum of all forces is zero in all directions.

$${}_A F_{B1toMS} + {}_A F_{B2toMS} - T_{c1}^T \cdot {}_F F_{MStoC13} - T_{c1}^T \cdot {}_F F_{MStoC14} + {}_A W_{MS} - \sum_{i=1}^{9} {}_A F_{MStoCR,i} = 0 \tag{3.43}$$

The sum of the moments of all forces about the center of the thrust roller bearing equals to the rotational acceleration times the moment of inertia.

$$\begin{aligned} &{}_A T_{in} + \left({}_A r_1 - {}_A r_2\right) \times {}_A F_{B1toMS} + {}_A M_{B1toMS} + {}_A M_{B2toMS} \\ &- \left(T_1^T(\phi) \cdot {}_B r_3 - {}_A r_2\right) \times T_{c1}^T \cdot {}_F F_{MStoC13} - T_{c1}^T \cdot {}_F M_{MStoC13} \\ &- \left(T_1^T(\phi) \cdot {}_B r_4 - {}_A r_2\right) \times T_{c1}^T \cdot {}_F F_{MStoC14} - T_{c1}^T \cdot {}_F M_{MStoC14} \\ &- \sum_{i=1}^{9} \left({}_A r_{CRi} - {}_A r_2\right) \times {}_A F_{MStoCRi} - \sum_{i=1}^{9} {}_A M_{MStoCRi} \\ &+ \left({}_A r_{Wms} - {}_A r_2\right) \times {}_A W_{MS} = T_1^T(\phi) \cdot \left({}_B I_{ms} \cdot {}_B \alpha_{MS}\right) \end{aligned} \tag{3.44}$$

3.3 Dynamic Analysis of the Constant Velocity Joint

The constant velocity joint (CVJ) is a double cardan joint that connects the main shaft and the barrel to assure a positive drive. With reference to Figure 3-5, the CVJ consists of

the input shaft to the joint, the first cross, the intermediate shaft, the second cross, and the output shaft. The input shaft has the same angular velocity as the drive shaft. The analysis of the input shaft was lumped with main shaft in the previous section. The intermediate shaft consists of two parts: the first intermediate shaft that connects to the first cross, and the second intermediate shaft that connects to the second cross. The second intermediate shaft can slide with respect to the first intermediate shaft along its own axis to allow for the variation of the length of the intermediate shaft as the yoke rotates. The output shaft of the joint has the same angular velocity as the barrel. The analysis of the output shaft is lumped to the barrel.

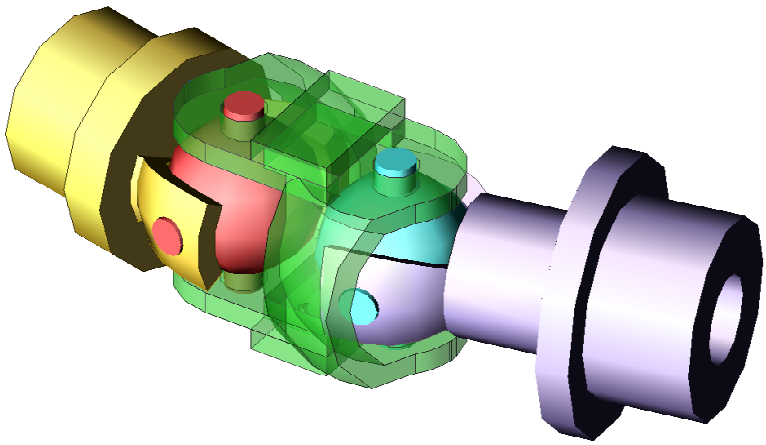

Figure 3-5: Double Cardan constant velocity joint

Johnson et al. [47] presented the conditions for a double cardan joint to be a CVJ. First, the axis of the input yoke that is attached to the input shaft should be parallel to the axis of the output yoke that is attached to the output shaft. In addition, the axes of the two yokes attached to the intermediate shafts should be parallel as can be seen in Figure 3-5 and Figure 3-6. Second, the angle between the input shaft and the intermediate shaft should equal to the angle between the intermediate shaft and the output shaft.

Hence, the swivel angle, θ is related to the angle between the input shaft and the intermediate shaft, β by

$$\beta = \frac{\theta}{2} \tag{3.45}$$

To start analyzing the CVJ, the inertial frame of reference "$a_1a_2a_3$" is defined as shown in Figure 3-6. "a_1" axis is normal to the plane formed by the axes of the input and intermediate shaft and is initially parallel to the input yoke and is always normal to the input axis. "a_3" is aligned with the input axis of the first joint. "a_2" is normal to both "a_1" and "a_3" according to the right hand rule.

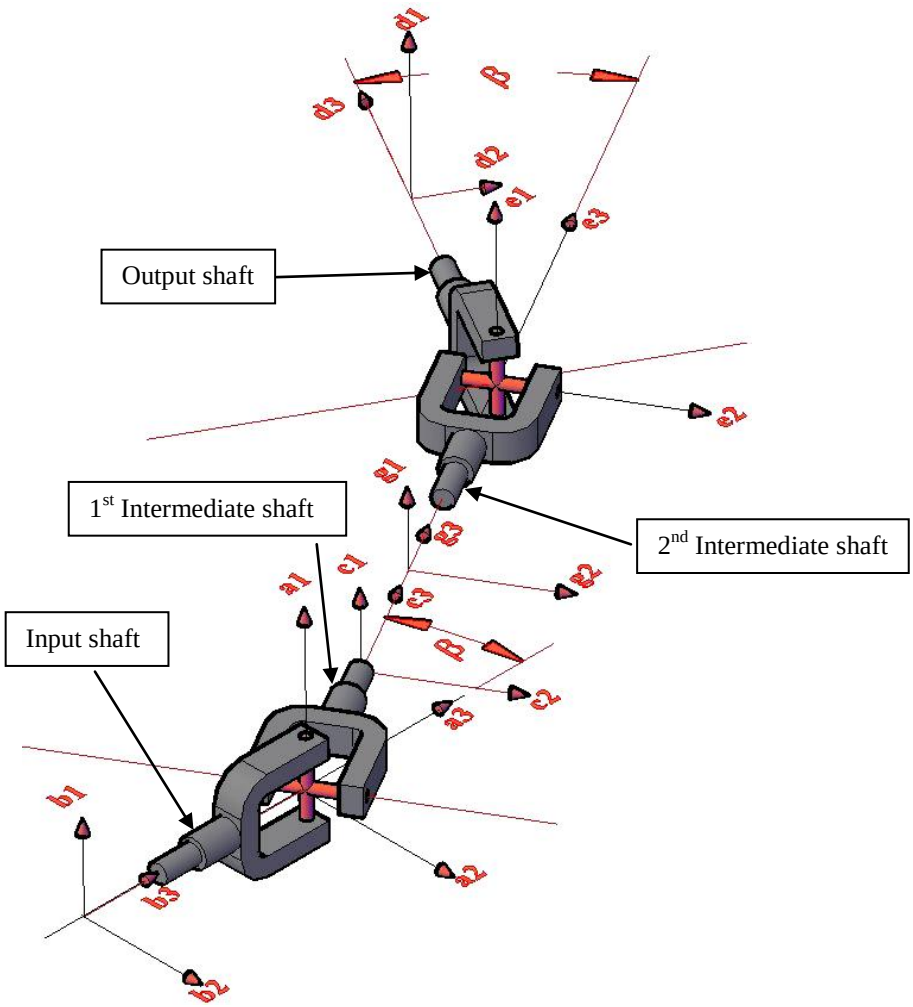

Figure 3-6: Double Cardan Joint Geometric relations

Attach a reference frame "$b_1b_2b_3$" to the input shaft axis such that: "b_1" is parallel to the input yoke axis, "b_3" is aligned along the axis of the input shaft, and "b_2" is normal to both "b_3" and "b_1" according to the right hand rule. The frame of reference "$b_1b_2b_3$" relates to the inertial frame through the relation given by Eq. (3.14).

3.3.1 Analysis of the first intermediate shaft

Attach a coordinate system "$c_1c_2c_3$" to the first intermediate shaft such that: "c_2" is aligned with the axis of the output yoke of the first joint, "c_3" is aligned with the axis of the intermediate shaft (output shaft of first joint), and "c_1" is normal to both "c_2" and "c_3" according to the right hand rule.

One can obtain "$c_1c_2c_3$" in two steps. First, "$a_1a_2a_3$" is rotated about "a_1" (1-rotation) by an angle of $\theta/2$ to get "$a_1'a_2'a_3'$". Then, "$a_1'a_2'a_3'$" is rotated about "a_3'" (3-rotation) an angle of δ to get "$c_1c_2c_3$".

$$T_2(\theta) = \begin{bmatrix} 1 & 0 & 0 \\ 0 & \cos\frac{\theta}{2} & \sin\frac{\theta}{2} \\ 0 & -\sin\frac{\theta}{2} & \cos\frac{\theta}{2} \end{bmatrix} \tag{3.46}$$

$$T_3 = \begin{bmatrix} \cos\delta & \sin\delta & 0 \\ -\sin\delta & \cos\delta & 0 \\ 0 & 0 & 1 \end{bmatrix} \tag{3.47}$$

Therefore, "$c_1c_2c_3$" and "$a_1a_2a_3$" are related by

$$\begin{bmatrix} c_1 \\ c_2 \\ c_3 \end{bmatrix} = T_3 T_2 (\theta) \begin{bmatrix} a_1 \\ a_2 \\ a_2 \end{bmatrix} = \begin{bmatrix} \cos\delta & \sin\delta\cos\frac{\theta}{2} & \sin\delta\sin\frac{\theta}{2} \\ -\sin\delta & \cos\delta\cos\frac{\theta}{2} & \cos\delta\sin\frac{\theta}{2} \\ 0 & -\sin\frac{\theta}{2} & \cos\frac{\theta}{2} \end{bmatrix} \begin{bmatrix} a_1 \\ a_2 \\ a_3 \end{bmatrix} \quad \textbf{(3.48)}$$

The total transformation matrix between the "A" and "C" frames is given by

$$T_{im1} = T_3 T_2 (\theta) = \begin{bmatrix} \cos\delta & \sin\delta\cos\frac{\theta}{2} & \sin\delta\sin\frac{\theta}{2} \\ -\sin\delta & \cos\delta\cos\frac{\theta}{2} & \cos\delta\sin\frac{\theta}{2} \\ 0 & -\sin\frac{\theta}{2} & \cos\frac{\theta}{2} \end{bmatrix} \quad \textbf{(3.49)}$$

The angular velocity and angular acceleration of the first intermediate shaft in vector form are given by

$${}_C\omega_{im1} = \begin{bmatrix} \frac{\dot{\theta}}{2}\cos\delta & -\frac{\dot{\theta}}{2}\sin\delta & \dot{\delta} \end{bmatrix}^T \quad \textbf{(3.50)}$$

$${}_C\alpha_{im1} = \frac{1}{2}\begin{bmatrix} \ddot{\theta}\cos\delta - \dot{\theta}\dot{\delta}\sin\delta \\ -\dot{\theta}\dot{\delta}\cos\delta - \ddot{\theta}\sin\delta \\ 2\ddot{\delta} \end{bmatrix} \quad \textbf{(3.51)}$$

The position vector of the CG of the first intermediate shaft with respect to the origin of the first cross is given by

$${}_C r_{im1} = \begin{bmatrix} 0 & 0 & r_{im1z} \end{bmatrix}^T \quad \textbf{(3.52)}$$

The linear velocity and linear acceleration of the center of gravity of the first intermediate shaft are given by

$${}_C v_{im1} = {}_C\omega_{im1} \times {}_C r_{im1} = -\frac{1}{2} r_{im1z}\dot{\theta}\begin{bmatrix} \sin\delta & \cos\delta & 0 \end{bmatrix}^T \quad \textbf{(3.53)}$$

$$ {}_{C}a_{im1} = -\frac{1}{4} r_{im1z} \begin{bmatrix} 2\ddot{\theta}\sin\delta & 2\ddot{\theta}\cos\delta & \dot{\theta}^2 \end{bmatrix}^T \quad \textbf{(3.54)} $$

Orthogonalty constraint between the yoke axes

The two yokes of the joint are constrained by the inside cross, resulting in the orthogonalty constraint between the yoke axes as follows:

$$ \vec{b}_1 \cdot \vec{c}_2 = 0 \quad \textbf{(3.55)} $$

$$ \vec{b}_1 = \cos\phi\vec{a}_1 + \sin\phi\vec{a}_2 \quad \textbf{(3.56)} $$

$$ \vec{c}_2 = -\sin\delta\vec{a}_1 + \cos\delta\cos\beta\vec{a}_2 + \cos\delta\sin\beta\vec{a}_3 \quad \textbf{(3.57)} $$

Therefore,

$$ \delta = \tan^{-1}\left(\tan\phi\cos\left(\frac{\theta}{2}\right)\right) \quad \textbf{(3.58)} $$

Figure **3-7** shows the forces that act on the FBD of the first intermediate shaft, which include:

1. The reaction forces from the first cross at points (23) and (24) denoted as $-{}_{F}F_{IM1toC123}$ and $-{}_{F}F_{IM1toC124}$. These reaction forces are equal in magnitude and opposite in direction, thus forming a couple.
2. The frictional moments from the first cross at points (23) and (24) denoted as $-{}_{F}M_{IM1toC123}$ and $-{}_{F}M_{IM1toC124}$.
3. The reaction forces from the second intermediate shaft that acts at points (25). It consists of a sliding force component and a couple around the axis of the intermediate shaft. The sliding force component can be expressed as

$$ {}_{C}F_{IM2toIM125} = \begin{bmatrix} 0 & 0 & F_{IM2toIM125z} \end{bmatrix}^T \quad \textbf{(3.59)} $$

The reaction couple from the second intermediate shaft to the first intermediate shaft is expressed as

$$ {}_{C}M_{IM2toIM125} = \begin{bmatrix} 0 & 0 & M_{IM2toIM125z} \end{bmatrix}^{T} \tag{3.60} $$

4. The weight of the first intermediate shaft and is expressed as

$$ {}_{A}W_{im1} = \begin{bmatrix} 0 & gM_{im1} & 0 \end{bmatrix}^{T} \tag{3.61} $$

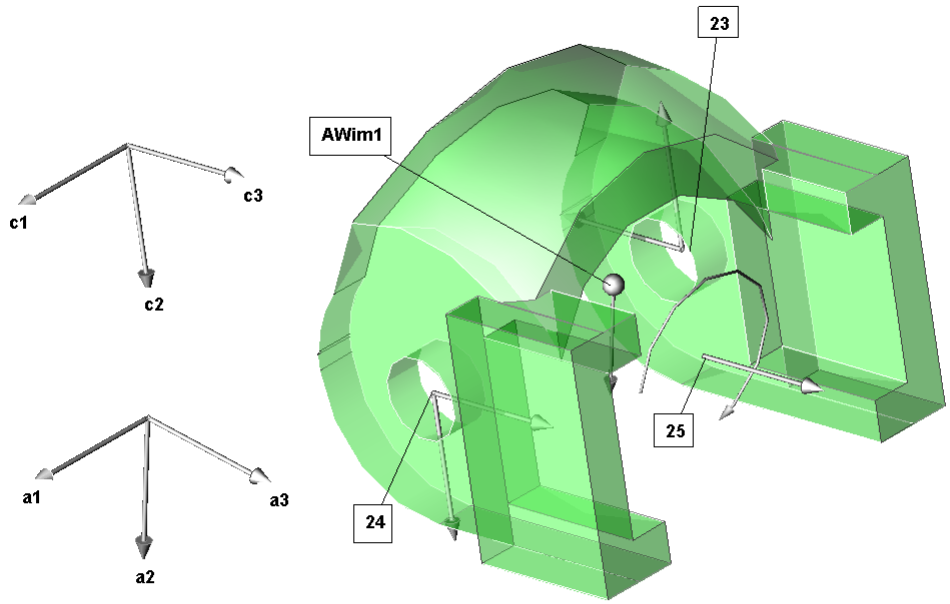

Figure 3-7: FBD of the first intermediate shaft

Equations of motion of the first intermediate shaft

The sum of all forces acting on the first intermediate shaft equals to its mass multiplied by the acceleration.

$$ -T_{c1}^{T}.({}_{F}F_{IM1toC123} + {}_{F}F_{IM1toC124}) + T_{im1}^{T}.{}_{C}F_{IM2toIM125} + {}_{A}W_{im1} = M_{im1}.{}_{A}a_{im1} \tag{3.62} $$

Let the origin of the C frame be at the center of the first cross. Therefore, expressing the position vectors of all forces acting on the FBD of the first intermediate with respect to the center of the first cross:

$$ {}_{C}r_{23} = \begin{bmatrix} -r_{C2} & 0 & 0 \end{bmatrix}^{T} \tag{3.63} $$

$$ {}_{C}r_{24} = -{}_{C}r_{23} \tag{3.64} $$

Sum of moments of all forces about the center of the first cross is given by

$$ \begin{aligned} &-(T^{T}_{im1\cdot C}\, r_{23}) \times T^{T}_{c1\cdot F}\, F_{IM1toC123} - T^{T}_{c1\cdot F}\, M_{IM1toC123} - (T^{T}_{im1\cdot C}\, r_{24}) \times T^{T}_{c1\cdot F}\, F_{IM1toC124} \\ &-T^{T}_{c1\cdot F}\, M_{IM1toC124} + T^{T}_{im1\cdot C}\, M_{IM2toIM125} \\ &+ (T^{T}_{im1\cdot C}\, r_{im1}) \times {}_{A}W_{im1} = T^{T}_{im1}.({}_{C}I_{im1\cdot C}\,\alpha_{im1}) + (T^{T}_{im1\cdot C}\, r_{im1}) \times \left(M_{im1\cdot A}\, a_{im1}\right) \end{aligned} \tag{3.65} $$

3.3.2 Dynamic analysis of the cross of the first joint

With reference to Figure 3-6, the $f_1f_2f_3$ coordinate system is attached to the first cross of the joint such that: "f_1" is parallel to "b_1", "f_2" is parallel to "c_2", and "f_3" is perpendicular to "f_1" and "f_2" according to the right hand rule. Therefore, the expression of the "$f_1f_2f_3$" frame with respect to "A" frame is given by

$$ [f_1] = [b_1] = \begin{bmatrix} \cos\phi & \sin\phi & 0 \end{bmatrix}^{T} \tag{3.66} $$

$$ [f_2] = [c_2] = \begin{bmatrix} -\sin\delta & \cos\delta\cos\dfrac{\theta}{2} & \cos\delta\sin\dfrac{\theta}{2} \end{bmatrix}^{T} \tag{3.67} $$

$$ [f_3] = [f_1 \times f_2] = \begin{bmatrix} \cos\delta\sin\dfrac{\theta}{2}\sin\phi \\ -\cos\delta\cos\phi\sin\dfrac{\theta}{2} \\ \cos\delta\cos\dfrac{\theta}{2}\cos\phi + \sin\delta\sin\phi \end{bmatrix} \tag{3.68} $$

Therefore, the rotation matrix of the first cross is given by

$$T_{c1}=\begin{bmatrix} \cos\phi & \sin\phi & 0 \\ -\sin\delta & \cos\delta\cos\frac{\theta}{2} & \cos\delta\sin\frac{\theta}{2} \\ \cos\delta\sin\frac{\theta}{2}\sin\phi & -\cos\delta\cos\phi\sin\frac{\theta}{2} & \cos\delta\cos\frac{\theta}{2}\cos\phi+\sin\delta\sin\phi \end{bmatrix} \quad \textbf{(3.69)}$$

The angular velocity and angular acceleration of the first cross in vector form are given by

$${}_F\omega_{c1}=\begin{bmatrix} -\dot{\delta}\sin\frac{\theta}{2}\sin\phi+\frac{\dot{\theta}}{4}\left(2\cos^2\delta\cos\phi+\cos\frac{\theta}{2}\sin 2\delta\sin\phi\right) \\ \dot{\phi}\cos\delta\sin\frac{\theta}{2} \\ \dot{\phi}\left(\cos\frac{\theta}{2}\cos\phi\cos\delta+\sin\delta\sin\phi\right) \end{bmatrix} \quad \textbf{(3.70)}$$

$${}_F\alpha_{c1}=\frac{d}{dt}\,{}_F\omega_{c1} \quad \textbf{(3.71)}$$

Figure 3-8 shows the forces that act on the FBD of the first cross which include:

1. The reaction forces from the main shaft which act at points (3) and (4) and are given by

$${}_F F_{MStoC13} = \begin{bmatrix} F_{MStoC13x} & 0 & F_{MStoC13z} \end{bmatrix}^T \quad \textbf{(3.72)}$$

$${}_F\mathrm{F}_{\mathrm{MStoC14}} = -{}_F\mathrm{F}_{\mathrm{MStoC13}} \quad \textbf{(3.73)}$$

2. The frictional moments from the main shaft at the pins of the cross at points (3) and (4) which are expressed as

$${}_F M_{MStoC13} = M_{MStoC13}\begin{bmatrix} 0 & -sign({}_F\omega_{C1}[2]) & 0 \end{bmatrix}^T \quad \textbf{(3.74)}$$

$${}_F M_{MStoC14} = M_{MStoC14}\begin{bmatrix} 0 & -sign({}_F\omega_{C1}[2]) & 0 \end{bmatrix}^T \quad \textbf{(3.75)}$$

3. The reaction forces from the first intermediate shaft which act at points 23 and 24 given by

$$ {}_F F_{IM1toC123} = \begin{bmatrix} 0 & {}_F F_{IM1toC123y} & {}_F F_{IM1toC123z} \end{bmatrix}^T \quad \textbf{(3.76)} $$

$$ {}_F F_{IM1toC124} = -{}_F F_{IM1toC123} \quad \textbf{(3.77)} $$

4. The frictional moments from the first intermediate shaft at points (23) and (24) expressed as

$$ {}_F M_{IM1toC123} = M_{IM1toC123} \begin{bmatrix} -sign({}_F \omega_{C1}[1]) & 0 & 0 \end{bmatrix}^T \quad \textbf{(3.78)} $$

$$ {}_F M_{IM1toC124} = M_{M1toC124} \begin{bmatrix} -sign({}_F \omega_{C1}[1]) & 0 & 0 \end{bmatrix}^T \quad \textbf{(3.79)} $$

5. The weight of the cross and is expressed as

$$ {}_A W_{c1} = [0 \quad g\ M_{c1} \quad 0]^T \quad \textbf{(3.80)} $$

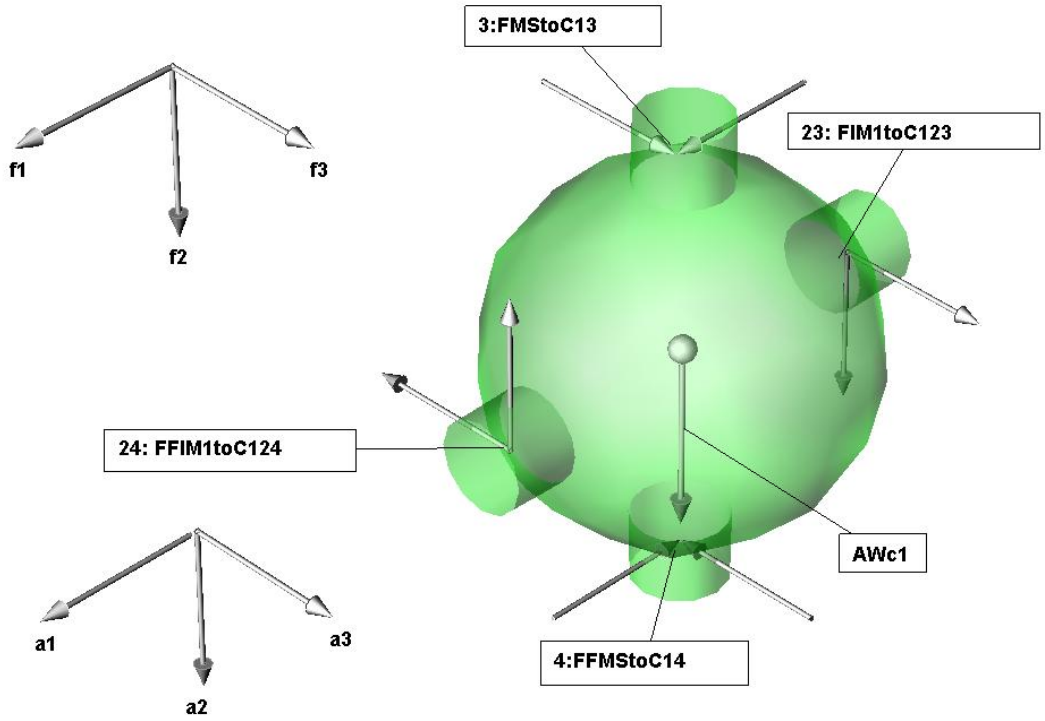

Figure 3-8: FBD of the first cross of the CVJ

The frictional moments of the pins of the first cross are given by

$$ M_{MStoC13} = \mu_{C1} r_{CP1} \sqrt{{}_F F^2_{MStoC13x} + {}_F F^2_{MStoC13z}} \quad \textbf{(3.81)} $$

$$M_{MStoC14} = \mu_{C1} r_{CP1} \sqrt{{}_F F^2_{MStoC14x} + {}_F F^2_{MStoC14z}} \quad \textbf{(3.82)}$$

$$M_{IM1toC123} = \mu_{C1} r_{CP2} \sqrt{F^2_{IM1toC123y} + F^2_{IM1toC123z}} \quad \textbf{(3.83)}$$

$$M_{IM1toC124} = \mu_{C1} r_{CP3} \sqrt{F^2_{IM1toC124y} + F^2_{IM1toC124z}} \quad \textbf{(3.84)}$$

μ_{C1} = the friction coefficient at the pins of the first cross

Equations of motion of the first cross:

Since the acceleration of the CG of the first cross is zero, the sum of all forces acting on the FBD is zero:

$${}_F F_{MStoC13} + {}_F F_{MStoC14} + {}_F F_{IM1toC123} + {}_F F_{IM1toC124} + T_{C1} \cdot {}_A W_{c1} = 0 \quad \textbf{(3.85)}$$

Attach the F frame to the origin of the first cross and express the position vectors of the forces acting on the FBD of the first cross in terms of the F frame:

$${}_F r_3 = \begin{bmatrix} 0 & -r_{C1} & 0 \end{bmatrix}^T \quad \textbf{(3.86)}$$

$${}_F r_4 = -{}_F r_3 \quad \textbf{(3.87)}$$

$${}_F r_{23} = \begin{bmatrix} -r_{C2} & 0 & 0 \end{bmatrix}^T \quad \textbf{(3.88)}$$

$${}_F r_{24} = -{}_F r_{23} \quad \textbf{(3.89)}$$

The sum of moments about the center of the first cross is given by

$${}_F r_3 \times {}_F F_{MStoC13} + {}_F r_4 \times {}_F F_{MStoC14} + {}_F r_{23} \times {}_F F_{IM1toC123} + {}_F M_{IM1toC123} + {}_F r_{24} \times {}_F F_{IM1toC124} + {}_F M_{IM1toC124} = {}_F I_{c1} \cdot {}_F \alpha_{c1} \quad \textbf{(3.90)}$$

3.3.3 Dynamic analysis of the second intermediate shaft

The second intermediate shaft has the same angular velocity as the first intermediate shaft. However, the second intermediate shaft moves along its longitudinal axis with

respect to the first intermediate shaft. Therefore, the velocity of the center of gravity of the second intermediate shaft is given by

$$ {}_C v_{im2} = {}_C v_{im2/im1} + {}_C \omega_{im1} \times {}_C r_{im2} \quad \textbf{(3.91)} $$

Where

${}_C V_{im2/im1}$ = velocity of CG of the second intermediate shaft with respect to the first intermediate shaft.

Figure 3-9 defines the geometric parameters of a typical bent axes pump as follows:

- IH = axis of rotation of the output shaft of CVJ
- AJ = L_{is} = length of the input shaft of the universal joint
- JK = R_y = distance from center of rotation of the yoke to center of first cross
- IK = R_y = distance from center of rotation of the yoke to center of second cross
- JI = L_{im} = length of intermediate shaft of the universal joint, it changes with the angle of rotation of the yoke, θ.
- CD = L_{CR} = connecting rod at the TDC
- φ_o = connecting rod angle at BDC
- θ = yoke angle
- G = center of gravity of the connecting rod

The distance between the centers of the two-cardan joints at any angular rotation (θ) of the yoke is given by

$$ L_{im} = IJ = 2R_y \cos\frac{\theta}{2} \quad \textbf{(3.92)} $$

- The relative velocity of the second intermediate shaft with respect to the first intermediate shaft equals to the rate of change of L_{im} with respect to time

$$ {}_C v_{im2/im1} = \begin{bmatrix} 0 & 0 & -R_y \dot{\theta} \sin\frac{\theta}{2} \end{bmatrix}^T \tag{3.93} $$

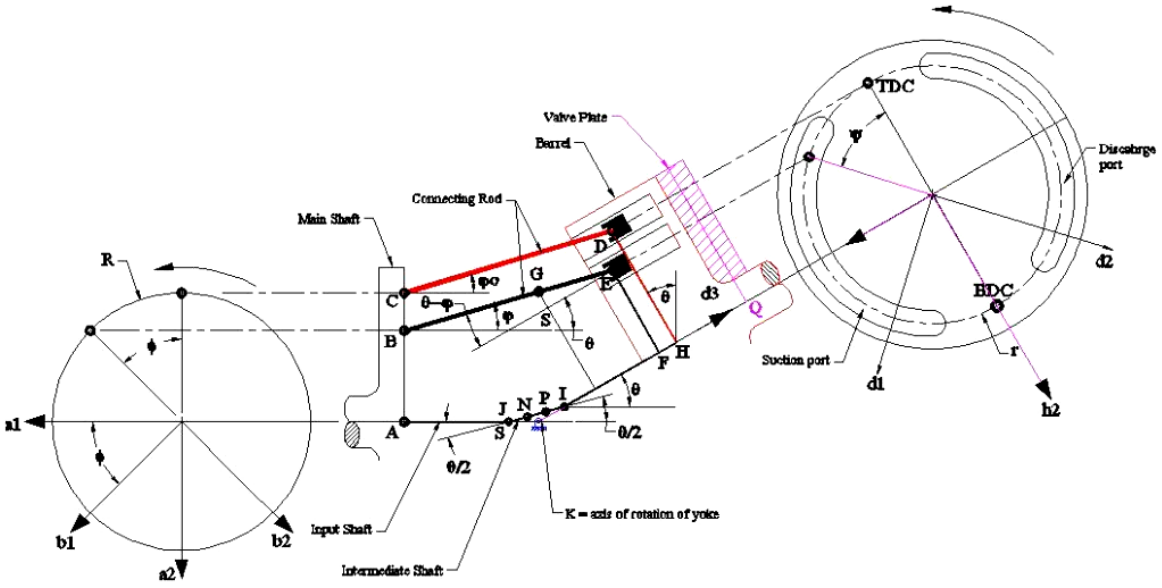

Figure 3-9: Bent axis pump geometric relations

Let ${}_C r_{im2}$ = JP = position vector of CG of the second intermediate shaft with respect to the center of the first cross expressed in C frame.

$$ {}_C r_{im2} = \left(-IP + 2R_y \cos\frac{\theta}{2} \right) \begin{bmatrix} 0 & 0 & 1 \end{bmatrix}^T \tag{3.94} $$

$$ {}_C v_{im2} = \begin{bmatrix} \frac{\dot{\theta} \sin\delta}{2} \left(IP - 2R_y \cos\frac{\theta}{2} \right) \\ \frac{\dot{\theta} \cos\delta}{2} \left(IP - 2R_y \cos\frac{\theta}{2} \right) \\ -\dot{\theta} R_y \sin\frac{\theta}{2} \end{bmatrix} \tag{3.95} $$

The acceleration of the CG of the second intermediate shaft is given by

$$ {}_{C}a_{im2} = \begin{bmatrix} \frac{1}{2}\sin\delta\left(\ddot{\theta}\left(IP - 2R_y\cos\frac{\theta}{2}\right) + 2R_y\dot{\theta}^2\sin\frac{\theta}{2}\right) \\ \frac{1}{2}\cos\delta\left(\ddot{\theta}\left(IP - 2R_y\cos\frac{\theta}{2}\right) + 2R_y\dot{\theta}^2\sin\frac{\theta}{2}\right) \\ \frac{1}{4}\left(IP - 4R_y\cos\frac{\theta}{2}\right)\dot{\theta}^2 - \ddot{\theta}R_y\sin\frac{\theta}{2} \end{bmatrix} \quad \textbf{(3.96)} $$

Figure 3-10 shows the forces that act on the FBD of the second intermediate shaft, which includes:

1. The reaction force and moment from the first intermediate shaft at point (25) are denoted by $-_{C}F_{IM2toIM125}$ and $-_{C}M_{IM2toIM125}$.
2. The reaction forces from the second cross at points (27) and (28) denoted by $-{}_{I}F_{IM2toC227}$ and $-{}_{I}F_{IM2toC228}$.
3. The reaction moments from the second cross at points (27) and (28) and denoted by $-{}_{I}M_{IM2toC227}$ and $-{}_{I}M_{IM2toC228}$.
4. The weight of the second intermediate shaft and is expressed as

$$ {}_{A}W_{im2} = [0,\ g\ M_{im2},\ 0]^T \quad \textbf{(3.97)} $$

Equations of motion of the second intermediate shaft

The sum of forces equals to the mass multiplied by the acceleration as follows:

$$ {}_{A}W_{im2} - T_{im1}^{T}\cdot{}_{C}F_{IM2toIM125} - T_{c2}^{T}.({}_{I}F_{IM2toC227} + {}_{I}F_{IM2toC228}) = T_{im1}^{T}.M_{im2}\cdot{}_{C}a_{im2} \quad \textbf{(3.98)} $$

Let the origin of the C frame be at the center of the first cross. Then, define the position vectors of the forces acting on the second intermediate shaft as follows:

$$ {}_{C}r_{27} = \begin{bmatrix} -r_{C2} & 0 & L_{im} \end{bmatrix}^T \quad \textbf{(3.99)} $$

$$ {}_{C}r_{28} = \begin{bmatrix} r_{C2} & 0 & L_{im} \end{bmatrix}^T \quad \textbf{(3.100)} $$

Summing the moments of the forces acting on the second intermediate shaft about the center of the first cross, yields

$$\begin{aligned} &-(T^T_{im1}\cdot_C r_{27})\times(T^T_{c2}\cdot_I F_{IM\,2toC227})-(T^T_{im1}\cdot_C r_{28})\times(T^T_{c2}\cdot_I F_{IM\,2toC228})+(T^T_{im1}\cdot_C r_{im2})\times {}_AW_{im2} \\ &-T^T_{c2}.\left({}_I M_{IM\,2toC227}+M_{IM\,2toC228}\right)=T^T_{im1}.({}_C I_{im2}\cdot\ {}_C\alpha_{im1})+T^T_{im1}.({}_C r_{im2}\times M_{im2}\cdot_C a_{im2}) \end{aligned} \quad \textbf{(3.101)}$$

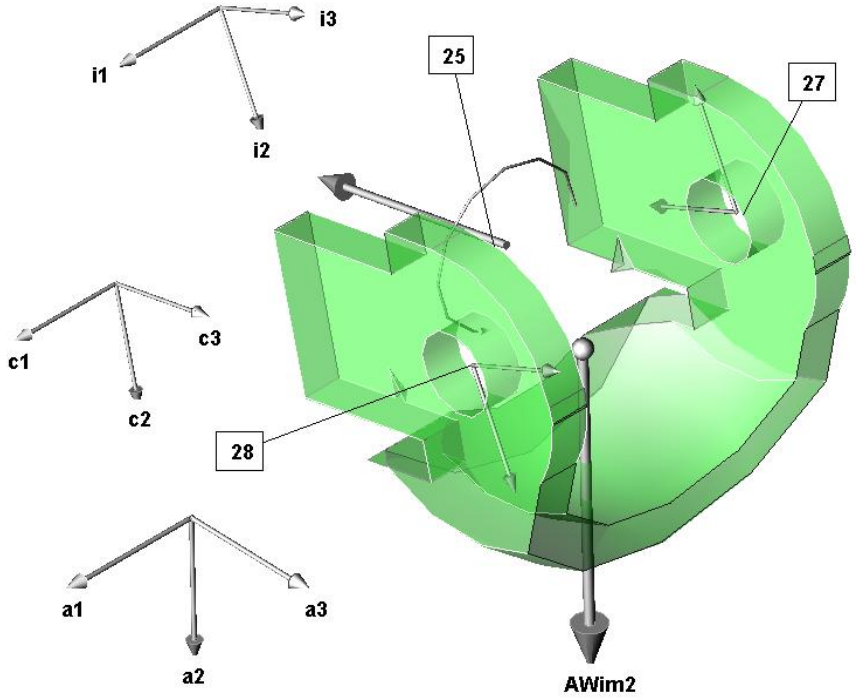

Figure 3-10: FBD of the second intermediate shaft

3.3.4 Dynamic analysis of the second cardan joint

With reference to Figure 3-6, a coordinate frame "$e_1e_2e_3$" is selected. "e_1" axis is normal to the plane formed by the intermediate and output axes of second joint ("e_1" is initially parallel to the output yoke of the second joint as shown and is always normal to the intermediate axis). "e_3" is aligned with the axis of the intermediate shaft. "e_2" is normal to both "e_3" and "e_1" according to the right hand rule. "$e_1e_2e_3$" is obtained by rotating "$a_1a_2a_3$" about "a_1" an angle of $\theta/2$:

$$\begin{bmatrix} e_1 & e_2 & e_3 \end{bmatrix}^T = T_2(\theta)\begin{bmatrix} a_1 & a_2 & a_3 \end{bmatrix}^T \quad \textbf{(3.102)}$$

"$g_1g_2g_3$" is attached to the intermediate axis such that: "g_2" is parallel to the input yoke of the second joint, "g_3" is aligned along the axis of the intermediate shaft, and "g_1" is normal to both "g_2" and "g_3" according to the right hand rule. "$g_1g_2g_3$" is obtained by rotating the "$e_1e_2e_3$" by an angle of δ around the intermediate shaft axis "e_3" yielding the following relationship between "$g_1g_2g_3$" and "$e_1e_2e_3$":

$$\begin{bmatrix} g_1 & g_2 & g_3 \end{bmatrix}^T = [T_3]\begin{bmatrix} e_1 & e_2 & e_3 \end{bmatrix}^T \quad \textbf{(3.103)}$$

A coordinate system "$d_1d_2d_3$" is attached to the output shaft of the second joint such that: "d_1" is aligned with the axis of the output yoke of the second joint, "d_3" is aligned with the axis of the output shaft of the second joint, "d_2" is normal to both "d_3" and "d_1" according to the right hand rule. "$d_1d_2d_3$" is obtained in two steps. First, "$d_1d_2d_3$" is rotated about "e_1" by an angle of $\theta/2$ to get "$e_1'e_2'e_3'$". "$e_1'e_2'e_3'$" relates to "$e_1e_2e_3$" by the transformation matrix $T_2(\theta)$ as given by equation (3.46). Second, "$e_1'e_2'e_3'$" is rotated about "e_3'" an angle of ψ to get "$d_1d_2d_3$".

$$T_4(\psi) = \begin{bmatrix} \cos\psi & \sin\psi & 0 \\ -\sin\psi & \cos\psi & 0 \\ 0 & 0 & 1 \end{bmatrix} \quad \textbf{(3.104)}$$

Therefore, "$d_1d_2d_3$" and "$a_1a_2a_3$" are related by

$$\begin{bmatrix} d_1 \\ d_2 \\ d_3 \end{bmatrix} = T_4(\psi)T_2(\theta)T_2(\theta)\begin{bmatrix} a_1 \\ a_2 \\ a_2 \end{bmatrix} = \begin{bmatrix} \cos\psi & \sin\psi\cos\theta & \sin\psi\sin\theta \\ -\sin\psi & \cos\psi\cos\theta & \cos\psi\sin\theta \\ 0 & -\sin\theta & \cos\theta \end{bmatrix}\begin{bmatrix} a_1 \\ a_2 \\ a_2 \end{bmatrix} \quad \textbf{(3.105)}$$

The rotation matrix of the output shaft with respect to the A frame is given by

$$T_{os}(\theta,\phi)=\begin{bmatrix}\cos\psi & \sin\psi\cos\theta & \sin\psi\sin\theta\\ -\sin\psi & \cos\psi\cos\theta & \cos\psi\sin\theta\\ 0 & -\sin\theta & \cos\theta\end{bmatrix} \quad \textbf{(3.106)}$$

The angular velocity of the output shaft is given by

$${}_D\omega_{os}=\begin{bmatrix}\dot\theta\cos\phi & -\dot\theta\sin\phi & \dot\phi\end{bmatrix}^T \quad \textbf{(3.107)}$$

Orthogonalty constraint between the intermediate shaft and the output shaft of the second joint:

The two yokes of the second joint are also constrained by the inside cross, resulting in the orthogonally constraint between the yoke axes as follows

$$\vec{g}_2\cdot\vec{d}_1=0 \quad \textbf{(3.108)}$$

$$g_2=\begin{bmatrix}-\sin\delta & \cos\delta & 0\end{bmatrix}^T \quad \textbf{(3.109)}$$

$$\vec{d}_1=\begin{bmatrix}\cos\psi & \sin\psi\cos\frac{\theta}{2} & \sin\psi\sin\frac{\theta}{2}\end{bmatrix}^T \quad \textbf{(3.110)}$$

Therefore,

$$\psi=\tan^{-1}\left(\tan\delta\cos\frac{\theta}{2}\right)=\phi \quad \textbf{(3.111)}$$

Attach "$i_1i_2i_3$" coordinate system to the second cross of the joint such that: "i_1" is parallel to "d_1", "i_2" is parallel to "c_2", and "i_3" is perpendicular to "i_1" and "i_2" according to the right hand rule. Therefore, the frame of reference "$i_1i_2i_3$" can be expressed in terms of the A frame as

$$[i_1]=[d_1]=\begin{bmatrix}\cos\phi & \sin\phi\cos\theta & \sin\phi\sin\theta\end{bmatrix}^T \quad \textbf{(3.112)}$$

$$[i_2]=[c_2]=\begin{bmatrix}-\sin\delta & \cos\delta\cos\frac{\theta}{2} & \cos\delta\sin\frac{\theta}{2}\end{bmatrix}^T \quad \textbf{(3.113)}$$

$$\left[i_3\right]=\left[i_1\times i_2\right]=\begin{bmatrix}-\cos\delta\sin\frac{\theta}{2}\sin\phi\\-\cos\phi\cos\delta\sin\frac{\theta}{2}-\sin\delta\sin\theta\sin\phi\\\cos\frac{\theta}{2}\cos\phi\cos\delta+\sin\delta\cos\theta\sin\phi\end{bmatrix} \tag{3.114}$$

Therefore, the rotation matrix of the second cross is given by

$$T_{c2}=\begin{bmatrix}\cos\phi & \sin\phi\cos\theta & \sin\phi\sin\theta\\-\sin\delta & \cos\delta\cos\frac{\theta}{2} & \cos\delta\sin\frac{\theta}{2}\\-\cos\delta\sin\frac{\theta}{2}\sin\phi & -\cos\phi\cos\delta\sin\frac{\theta}{2}-\sin\delta\sin\theta\sin\phi & \cos\frac{\theta}{2}\cos\phi\cos\delta+\sin\delta\cos\theta\sin\phi\end{bmatrix} \tag{3.115}$$

The angular velocity and angular acceleration of the second cross in vector form are given by

$${}_I\omega_{c2}=\begin{bmatrix}\dot{\delta}\sin\frac{\theta}{2}\sin\phi+\frac{\dot{\theta}}{4}\left(2\cos\phi\cos^2\delta+\cos\frac{\theta}{2}\sin 2\delta\sin\phi\right)\\-\dot{\phi}\cos\delta\sin\frac{\theta}{2}-\dot{\theta}\sin\phi\left(\cos\frac{\theta}{2}\cos\phi\cos\delta+\sin\delta\sin\phi\right)\\-\dot{\theta}\sin\phi\sin\frac{\theta}{2}\cos\delta+\dot{\phi}\left(\cos\delta\cos\frac{\theta}{2}\cos\phi+\sin\delta\sin\phi\right)\end{bmatrix} \tag{3.116}$$

$${}_I\alpha_{c2}=\frac{d}{dt}{}_I\omega_{c2} \tag{3.117}$$

The position vectors of points 27 on the pin of the second cross with respect to its CG expressed in the "I" frame is given by

$${}_Ir_{27}=\begin{bmatrix}-r_{C2} & 0 & 0\end{bmatrix}^T \tag{3.118}$$

The center of the second cross does not move with respect to either the second intermediate shaft or the output shaft. Therefore, it is appropriate to assume that the center of the second cross is a common point between the second intermediate shaft and the

output shaft. The velocity of the CG of the second cross (expressed in terms of the C frame) is given by

$$ {}_{C}V_{c2} = {}_{C}V_{im2im1} + {}_{C}\omega_{im1} \times {}_{C}r_{I} = -R_y\dot{\theta}\left[\cos\frac{\theta}{2}\sin\delta \quad \cos\frac{\theta}{2}\cos\delta \quad \sin\frac{\theta}{2}\right]^T \tag{3.119} $$

The position vector of point I (Figure 3-9) with respect to the center of the first cross can be expressed as

$$ {}_{C}r_{I} = \begin{bmatrix} 0 & 0 & L_{im} \end{bmatrix}^T \tag{3.120} $$

The acceleration of the CG of the second cross is given by

$$ {}_{C}a_{c2} = \begin{bmatrix} R_y \sin\delta\left(-\ddot{\theta}\cos\frac{\theta}{2} + \dot{\theta}^2\sin\frac{\theta}{2}\right) \\ R_y \cos\delta\left(-\ddot{\theta}\cos\frac{\theta}{2} + \dot{\theta}^2\sin\frac{\theta}{2}\right) \\ -R_y\left(\dot{\theta}^2\cos\frac{\theta}{2} + \ddot{\theta}\sin\frac{\theta}{2}\right) \end{bmatrix} \tag{3.121} $$

Figure **3-11** shows the FBD of the second cross of the double cardan joint. The reaction forces that act on the second cross include:

1. The reaction forces from the second intermediate shaft at the pins (points 27 and 28) expressed as

$$ {}_{I}F_{IM2toC227} = \begin{bmatrix} 0 & F_{IM2toC227y} & F_{IM2toC227z} \end{bmatrix}^T \tag{3.122} $$

$$ {}_{I}F_{IM2toC228} = -{}_{I}F_{IM2toC227} \tag{3.123} $$

2. The frictional moments from the second intermediate shaft at the pins (points 27 and 28) are expressed as

$$ {}_{I}M_{IM2toC227} = M_{M2toC227}\left[-sign({}_{I}\omega_{C2}[1]) \quad 0 \quad 0\right]^T \tag{3.124} $$

$$ {}_{I}M_{IM2toC228} = M_{M2toC228}\left[-sign({}_{I}\omega_{C2}[1]) \quad 0 \quad 0\right]^T \tag{3.125} $$

3. The reaction forces from the output shaft at the pins (points 29 and 30). They are given by

$$ {}_{I}F_{OStoC229} = \begin{bmatrix} F_{OStoC229x} & 0 & F_{OStoC229z} \end{bmatrix}^{T} \quad \textbf{(3.126)} $$

$$ {}_{I}F_{OStoC230} = -{}_{I}F_{OStoC229} \quad \textbf{(3.127)} $$

4. The frictional moments from the output shaft at the right and left pins of the cross at points (29) and (30) expressed as

$$ {}_{I}M_{OStoC229} = M_{OStoC229} \begin{bmatrix} 0 & -sign({}_{I}\omega_{C2}[2]) & 0 \end{bmatrix}^{T} \quad \textbf{(3.128)} $$

$$ {}_{I}M_{OStoC230} = M_{OStoC230} \begin{bmatrix} 0 & -sign({}_{I}\omega_{C2}[2]) & 0 \end{bmatrix}^{T} \quad \textbf{(3.129)} $$

5. The weight of the second cross (very small compared with other forces) and is expressed as

$$ {}_{A}W_{c2} = [0,\ M_{c2}g\ ,0]^{T} \quad \textbf{(3.130)} $$

The frictional moments of the pins of the second cross are given by

$$ M_{IM2toC227} = \mu_{C1} r_{CP2} \sqrt{F_{IM2toC227y}^{2} + F_{IM2toC227z}^{2}} \quad \textbf{(3.131)} $$

$$ M_{IM2toC228} = \mu_{C1} r_{CP2} \sqrt{F_{IM2toC228y}^{2} + F_{IM2toC228z}^{2}} \quad \textbf{(3.132)} $$

$$ M_{OStoC229} = \mu_{C1} r_{CP1} \sqrt{F_{OStoC229x}^{2} + F_{OStoC229z}^{2}} \quad \textbf{(3.133)} $$

$$ M_{OStoC230} = \mu_{C1} r_{CP1} \sqrt{F_{OStoC230x}^{2} + F_{OStoC230z}^{2}} \quad \textbf{(3.134)} $$

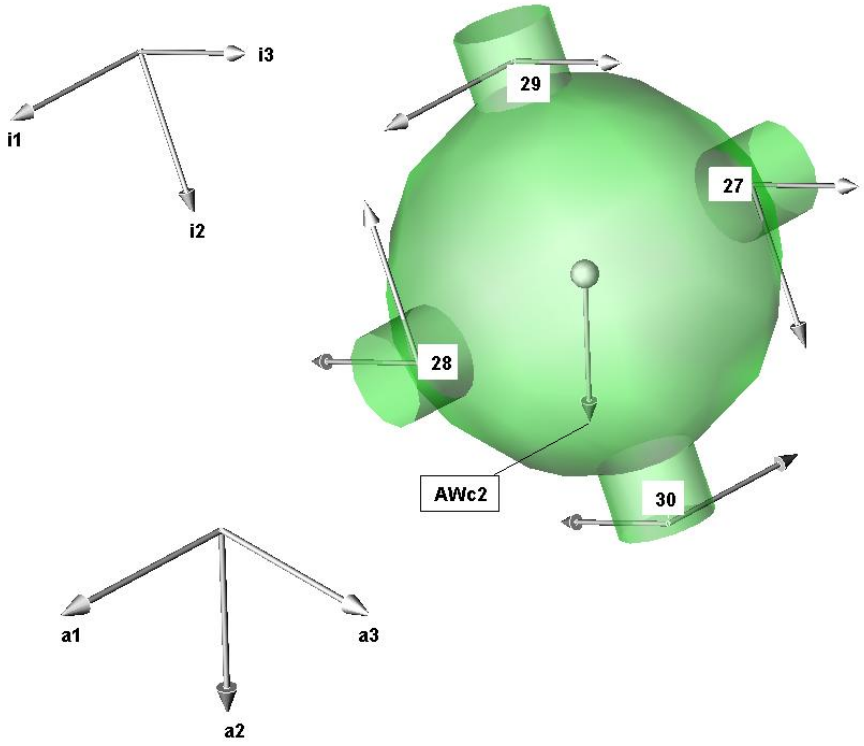

Figure 3-11: FBD of the second cross of the CVJ

Equations of motion of the second cross

The sum of all forces acting on the FBD is given by

$$T_{c2}^{T}.({}_{I}F_{IM\,2toC227} + {}_{I}F_{IM\,2toC228} + {}_{I}F_{OStoC229} + {}_{I}F_{OStoC230}) + {}_{A}W_{C2} = M_{c2}.{}_{A}a_{c2} \quad \textbf{(3.135)}$$

Express the position vectors of the forces acting on the FBD of the second cross in terms of the "I" frame with respect to the center of the second cross:

$${}_{I}r_{28} = -\,{}_{I}r_{27} \quad \textbf{(3.136)}$$

$${}_{I}r_{29} = \begin{bmatrix} 0 & -r_{C1} & 0 \end{bmatrix}^{T} \quad \textbf{(3.137)}$$

$${}_{I}r_{30} = -\,{}_{I}r_{29} \quad \textbf{(3.138)}$$

Find the sum of moments about the center of the second cross:

$$\begin{aligned} &{}_{I}r_{27} \times {}_{I}F_{IM\,2toC227} + {}_{I}M_{IM\,2toC227} + {}_{I}r_{28} \times {}_{I}F_{IM\,2toC228} + {}_{I}M_{IM\,2toC228} \\ &+ {}_{I}r_{29} \times {}_{I}F_{OStoC229} + {}_{I}M_{OStoC229} + {}_{I}r_{30} \times {}_{I}F_{OStoC230} + {}_{I}M_{OStoC230} = {}_{I}I_{c2}.{}_{I}\alpha_{C2} \end{aligned} \quad \textbf{(3.139)}$$

3.4 The Barrel-Output Shaft Assembly

Attach the coordinate frame D to the center of rotation of the yoke (point K in Figure 3-9). The position vector of the CG of the output shaft with respect to point K expressed in the D frame is given by

$$ {}_{D}r_{os} = \begin{bmatrix} 0 & 0 & r_{osz} \end{bmatrix}^{T} \tag{3.140} $$

The position vector of the center of the second cross (point I) with respect to the yoke center of rotation is given by

$$ {}_{D}r_{I} = \begin{bmatrix} 0 & 0 & R_{y} \end{bmatrix}^{T} \tag{3.141} $$

The velocity of the CG of the output shaft is given by

$$ {}_{A}V_{os} = T_{os}^{T}(\theta,\phi).({}_{D}\omega_{os} \times {}_{D}r_{os}) = -r_{osz}\dot{\theta}\begin{bmatrix} 0 & \cos\theta & \sin\theta \end{bmatrix}^{T} \tag{3.142} $$

The acceleration of the output shaft is given by

$$ {}_{A}a_{os} = r_{osz}\begin{bmatrix} 0 \\ -\ddot{\theta}\cos\theta + \dot{\theta}^{2}\sin\theta \\ -\dot{\theta}^{2}\cos\theta - \ddot{\theta}\sin\theta \end{bmatrix} \tag{3.143} $$

Figure 3-12 shows the FBD of the output shaft and barrel assembly. The forces that act on the assembly include:

1. The reactions forces from the second cross at points 29 and 30 denoted by $-{}_{I}F_{OStoC229}$ and $-{}_{I}F_{OStoC230}$. These forces are equal in magnitude and opposite in direction, thus forming a couple. The respective position vectors at points 29 and 30 with respect to the yoke center of rotation are given by:

$$ {}_{A}r_{29} = T_{os}^{T}(\theta,\phi).{}_{D}r_{I} + T_{c2}^{T}.{}_{I}r_{29} \tag{3.144} $$

$$ {}_{A}r_{30} = T_{os}^{T}(\theta,\phi).{}_{D}r_{I} + T_{c2}^{T}.{}_{I}r_{30} \tag{3.145} $$

2. The frictional moment from the second cross at points 29 and 30 and are denoted by $-_{I}M_{OStoC229}$ and $-_{I}M_{OStoC230}$.
3. The reaction forces from the piston and oil film between the barrel and the pistons at points 31 to 39 denoted by $-_{D}F_{BtoP,i}$ where i = 1, 2, …9. The respective position vectors with respect to the yoke axes of rotation are given by:

$$ {}_{D}r_{30+i} = \left[0 \quad -r \quad (R_y + IF\left(\theta, \phi + \frac{2\pi}{9}(i-1)\right) + r_{WP}) \right]^T , \quad i = 1,\ 2,\ ...9 \qquad \textbf{(3.146)} $$

Refer to equation (3.263) for an expression of $\text{IF}\left(\theta, \phi + \frac{2\pi}{9}(i-1)\right)$.

4. The weight of the output shaft and barrel assembly:

$$ {}_{A}W_{os} = \begin{bmatrix} 0 & M_{os}g & 0 \end{bmatrix}^T \qquad \textbf{(3.147)} $$

5. The force from the oil column in the cylinder at points 49 to 57 denoted as $_{D}F_{OILtoB,\ i}$.
6. The hydrodynamic forces $_{D}F_{VPtoBoutD}$, $_{D}F_{VPtoBinD}$, $_{D}F_{VPtoBinS}$, $_{D}F_{VPtoBoutS}$, due to the oil film between the valve plate and the barrel at points 59, 60, 61, and 62 respectively.
7. The frictional moment due to the fluid film between the barrel and the valve plate, $_{D}M_{VPtoB}$.
8. The reaction forces from the needle bearings at the end of the barrel (point 58). The bearings are fixed to the valve plate. These reaction forces with their respective position vectors can be expressed in the D frame as

$$ {}_{D}F_{B3FtoB} = \begin{bmatrix} F_{B3FtoBx} & F_{B3FtoBy} & 0 \end{bmatrix}^T \qquad \textbf{(3.148)} $$

$$ {}_{D}r_{B3FtoB} = \begin{bmatrix} 0 & 0 & r_{B3FtoBz} \end{bmatrix}^{T} \quad \textbf{(3.149)} $$

$$ {}_{D}\mathrm{F}_{\mathrm{B3StoB}} = \begin{bmatrix} \mathrm{F}_{\mathrm{B3StoBx}} & \mathrm{F}_{\mathrm{B3StoBy}} & 0 \end{bmatrix}^{T} \quad \textbf{(3.150)} $$

$$ {}_{D}r_{B3StoB} = \begin{bmatrix} 0 & 0 & r_{B3StoBz} \end{bmatrix}^{T} \quad \textbf{(3.151)} $$

9. The frictional moments form the needle bearings at point 58 are given by

$$ {}_{D}M_{B3FtoB} = M_{B3FtoBz} \begin{bmatrix} 0 & 0 & -sign({}_{D}\omega_{os}[3]) \end{bmatrix}^{T} \quad \textbf{(3.152)} $$

$$ {}_{D}M_{B3StoB} = M_{B3StoBz} \begin{bmatrix} 0 & 0 & -sign({}_{D}\omega_{os}[3]) \end{bmatrix}^{T} \quad \textbf{(3.153)} $$

   The next section presents the derivation of the equations for these moments.

10. The reaction force from the thrust ball bearing at the end of the barrel at point 65, which is denoted by ${}_{\mathrm{D}}\mathrm{F}_{\mathrm{B4toB}}$. The corresponding position vector is given by

$$ {}_{D}r_{B4toB} = \begin{bmatrix} 0 & 0 & r_{B4toBz} \end{bmatrix}^{T} \quad \textbf{(3.154)} $$

11. The frictional moment from the thrust ball bearing at the end of the barrel at point 65 denoted as ${}_{\mathrm{D}}\mathrm{M}_{\mathrm{B4toB}}$

12. The reaction forces between the discharge/suction port of the valve plate and the solid area located between each successive cylinder on the barrel at points 69 to 77, respectively. These forces denoted as $-{}_{\mathrm{D}}\mathrm{F}_{\mathrm{BStoVP,i}}$ where i = 1, 2…9. The corresponding position vectors are expressed as

$$ {}_{D}r_{BStoVP} = \begin{bmatrix} 0 & -r & L_{YtoVP} \end{bmatrix}^{T} \quad \textbf{(3.155)} $$

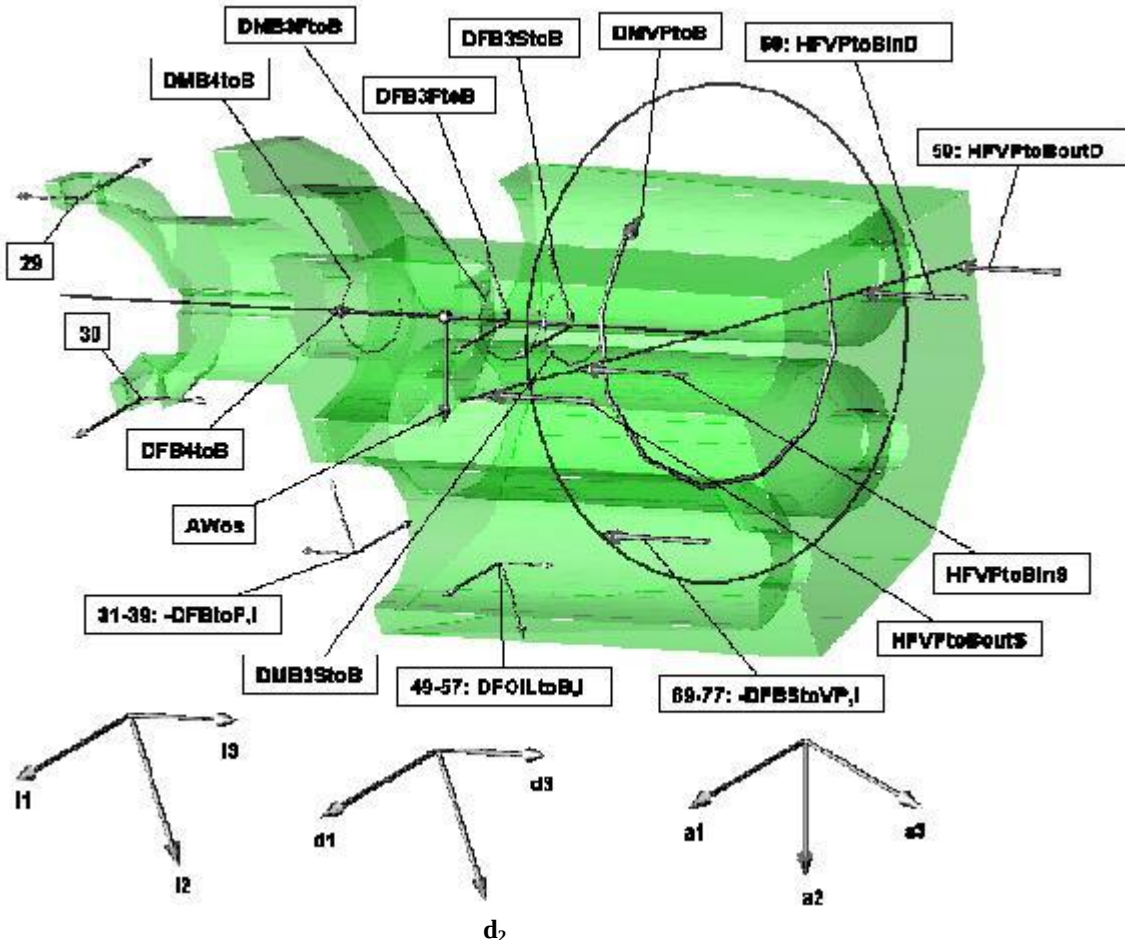

Figure 3-12: FBD of the output shaft and barrel assembly

3.4.1 The frictional moment at the needle bearings at end of the barrel

There are two radial needle bearings at point 58 denoted F (First) and S (Second). Section 3.1 presents a detailed analysis of the frictional moment components of roller bearings. The thrust ball bearing at the upper end of the barrel carries out the thrust load from the barrel. Therefore, the axial load dependent component of the frictional moment from the needle bearings is zero. Hence, the frictional moment on the needle bearings as given by Eq. (3.1) reduces to

$$M_{B3FtoBz} = M_{3Fm} + M_{3Fv} \qquad \textbf{(3.156)}$$

$$M_{B3StoBz} = M_{3Sm} + M_{3Sv} \quad \textbf{(3.157)}$$

Where

M_{3Fv} and M_{3Sv} = the viscous frictional component at the first and second needle bearings and are given by Eq. (3.2)

M_{3Fm} and M_{3Sm} = the radial load dependent component of the frictional moment of the first and second needle bearings and are given by Eq. (3.5)

The index f_{o3} for bearing and lubrication type ranges from 5 to 5.5 for needle roller bearings. The index f_{13F} which takes into account the magnitude of load has a value of 0.0005 [45]. For needle bearings, P_{13F} and P_{13S} are given by [45]

$$P_{13F} = F_{B3FtoBr} \quad \textbf{(3.158)}$$

$$P_{13S} = F_{B3StoBr} \quad \textbf{(3.159)}$$

$F_{B3FtoBr}$ and $F_{B3StoBr}$ are the radial load components of the bearing reactions at the needle bearings point (58) and are given by

$$F_{B3FtoBr} = \sqrt{F_{B3FtoBx}^2 + F_{B3FtoBy}^2} \quad \textbf{(3.160)}$$

$$F_{B3StoBr} = \sqrt{F_{B3StoBx}^2 + F_{B3StoBy}^2} \quad \textbf{(3.161)}$$

3.4.2 The frictional moment at the thrust bearing at the end of the barrel

The frictional moment opposes the direction of the angular velocity component along the "d_3" direction of the barrel

$$_D M_{B4toB} = -sign(_D \omega_{os}[3]) M_{B4toBz} \begin{bmatrix} 0 & 0 & 1 \end{bmatrix}^T \quad \textbf{(3.162)}$$

The frictional moment at the thrust ball bearings carries only the axial load from the barrel:

$$M_{B4toBSz} = M_{4v} + M_{4a} \tag{3.163}$$

The index f_{o4} for bearing and lubrication type has a value of 1.5 for thrust ball bearings. The pitch circle diameter of the bearing, d_{m4} is given by

$$d_{m4} = \frac{D_4 + d_4}{2} \tag{3.164}$$

The index f_{14} which takes into account the magnitude of load and is given by [45]

$$f_{14} = 0.0012\left(\frac{F_{a4}}{C_{o4}}\right)^{0.33} \tag{3.165}$$

The load P_{14} governs the load-depending frictional moment M_{4m}. For thrust ball bearings, P_{14} is given by [45]

$$P_{14} = F_{B4toBz} \tag{3.166}$$

The index f_{a4}, which depends on the axial load F_{B4toBz} and the lubricating condition, equals to 0.15 as given by Eq. (3.9).

3.4.3 Hydrodynamic forces due to the oil film between the valve plate and barrel

The following analysis is based on an analysis done by Franco [8], which is based on the following assumptions:

a. Because the clearance between the barrel and valve plate is small, and because leakage through it has to be a small predetermined quantity, fluid flow can be assumed to be laminar in that clearance.
b. Neglect forces due to pressure drop peripherally between the two orifices (both sides between the suction and discharge ports).
c. Leakage flow is assumed to spread in the radial direction between the lands.

The differential equation relating the velocity distribution with pressure and angular velocity in the outer land is given by

$$\frac{d}{dz}\left(\frac{dv}{dz}\right)=\frac{1}{\mu}\left(\frac{dP}{dR}-\frac{P}{R}+R\omega^2\rho\right) \quad \textbf{(3.167)}$$

R = varies between R_2 and R_1 as shown in Figure 2-5**Error! Reference source not found.**

P = pressure at radius R

ω = angular velocity of barrel around its axis

ρ = fluid density

τ = tangential stress

μ = coefficient of dynamic viscosity

The relative velocity is zero at both the lower and upper surfaces. Therefore, the velocity distribution in the clearance for the outer land can be expressed as

$$v=\frac{1}{2\mu}\left(\frac{dP}{dR}-\frac{P}{R}+R\rho\omega^2\right)\left(z^2-\frac{h^2}{4}\right) \quad \textbf{(3.168)}$$

The leakage flow q can be computed as

$$q=\int_{-h/2}^{h/2} vds=\int_{-h/2}^{h/2} v\zeta Rdz=-\frac{\zeta R}{12\mu}\left(\frac{dP}{dR}-\frac{P}{R}+\rho\omega^2R\right)h^3 \quad \textbf{(3.169)}$$

The negative sign for q denotes that crescent pressure and leakage flow are in opposite directions. Expressing the pressure distribution as a linear differential equation:

$$\frac{dP}{dR}-\frac{1}{R}P=-\frac{12\mu q}{\zeta h^3}\frac{1}{R}-\rho\omega^2R \quad \textbf{(3.170)}$$

Integrating, given that pressure in the outer side of the land is practically zero, P = 0 at $R = R_1$ and $P = P_b$, boundary pressure = discharge P_D, or suction pressure P_S at $R = R_2$ yields

$$P = \rho\omega^2 (R_1 - R)(R - R_2) + P_b \frac{(R_1 - R)}{(R_1 - R_2)} \quad \textbf{(3.171)}$$

Pressure distribution on the inner land

The velocity distribution is related to the pressure and angular velocity of the barrel through the following relation:

$$\frac{dP}{dR} + \frac{P}{R} - R\omega^2 \rho = \mu \frac{d}{dz}\left(\frac{dv}{dz}\right) \quad \textbf{(3.172)}$$

Given that, the relative velocity of the fluid film contacting the barrel or the valve plate is zero (no-slip condition); the velocity distribution of the fluid film for the inner land can be written as

$$v = \frac{1}{2\mu}\left(\frac{dP}{dR} + \frac{P}{R} - \rho\omega^2 R\right)\left(z^2 - \frac{h^2}{4}\right) \quad \textbf{(3.173)}$$

Moreover, the leakage flow is

$$q = -\frac{\zeta R h^3}{12\mu}\left(\frac{dP}{dR} + \frac{P}{R} - \rho\omega^2 R\right) \quad \textbf{(3.174)}$$

The linear differential equation of the pressure variation with the radial distance is given by

$$\frac{dP}{dR} + \frac{1}{R}P = -\frac{12\mu q}{\zeta h^3} \cdot \frac{1}{R} + R\rho\omega^2 \quad \textbf{(3.175)}$$

Solving this linear differential equation knowing that the pressure in the inner side of the land is practically zero, i.e. P = 0 at R = R_4, and P = boundary pressure, P_b = discharge pressure, P_D or suction pressure P_S at R = R_3, therefore pressure distribution can be expressed by

$$P = \frac{P_b R_3}{R}\left(\frac{R_4 - R}{R_4 - R_3}\right) + \rho\omega^2\left(\frac{R_4 - R}{3R}\right)(R_3 - R)(R_3 + R_4 + R) \quad \textbf{(3.176)}$$

Resultant hydraulic force on the port plate:

The hydraulic force in differential form is given by

$$dF = Pds = PRdRd\zeta \quad \textbf{(3.177)}$$

Where

P = pressure acting on surface of the port plate lands and is given by equations (3.171) and (3.176)

For the outside land, R varies from R_2 to R_1, and ζ from - $\zeta/2$ to + $\zeta/2$. For the inside land, R varies from R_4 to R_3, and ζ from - $\zeta/2$ to + $\zeta/2$. Therefore, the hydrodynamic forces normal to the interface between the valve plate and the barrel are given by

Discharge: $${}_H F_{VPtoBoutD} = -\frac{\zeta(R_1 - R_2)}{12}\left[0,0,2P_D(R_1 + 2R_2) + \rho\left(\frac{2\pi}{60}n_{ms}\right)^2(R_1 + R_2)(R_1 - R_2)^2\right] \quad \textbf{(3.178)}$$

Suction: $${}_H F_{VPtoBoutS} = -\frac{\zeta(R_1 - R_2)}{12}\left[0,0,2P_S(R_1 + 2R_2) + \rho\left(\frac{2\pi}{60}n_{ms}\right)^2(R_1 + R_2)(R_1 - R_2)^2\right] \quad \textbf{(3.179)}$$

Discharge: $${}_H F_{VPtoBinD} = -\frac{\zeta(R_3 - R_4)}{12}\left[0,0,6P_D R_3 - \rho\left(\frac{2\pi}{60}n_{ms}\right)^2(R_3 + R_4)(R_3 - R_4)^2\right] \quad \textbf{(3.180)}$$

Suction: $${}_H F_{VPtoBinS} = -\frac{\zeta(R_3 - R_4)}{12}\left[0,0,6P_S R_3 - \rho\left(\frac{2\pi}{60}n_{ms}\right)^2(R_3 + R_4)(R_3 - R_4)^2\right] \quad \textbf{(3.181)}$$

Point of application of the hydraulic forces

The points of application of the forces acting on the outer land are given by

$$\text{Discharge: } R_{outD} = \frac{5P_D\left(R_1^2 + 2R_1R_2 + 3R_2^2\right) + \rho\left(\frac{2\pi}{60}n_{ms}\right)^2 (R_1 - R_2)^2\left(3R_1^2 + 4R_1R_2 + 3R_2^2\right)}{5\left(2P_D\left(R_1 + 2R_2\right) + \rho\left(\frac{2\pi}{60}n_{ms}\right)^2 (R_1 - R_2)^2\left(R_1 + R_2\right)\right)} \quad \textbf{(3.182)}$$

$$\text{Suction: } R_{outS} = \frac{5P_S\left(R_1^2 + 2R_1R_2 + 3R_2^2\right) + \rho\left(\frac{2\pi}{60}n_{ms}\right)^2 (R_1 - R_2)^2\left(3R_1^2 + 4R_1R_2 + 3R_2^2\right)}{5\left(2P_S\left(R_1 + 2R_2\right) + \rho\left(\frac{2\pi}{60}n_{ms}\right)^2 (R_1 - R_2)^2\left(R_1 + R_2\right)\right)} \quad \textbf{(3.183)}$$

The points of application of the forces acting on the inner land are given by

$$\text{Discharge: } R_{inD} = \frac{30P_DR_3\left(2R_3 + R_4\right) - 2\rho\left(\frac{2\pi}{60}n_{ms}\right)^2 (R_3 - R_4)^2\left(4R_3^2 + 7R_3R_4 + 4R_4^2\right)}{90P_DR_3 - 15\rho\left(\frac{2\pi}{60}n_{ms}\right)^2 (R_3 - R_4)^2\left(R_3 + R_4\right)} \quad \textbf{(3.184)}$$

$$\text{Suction: } R_{inS} = \frac{30P_SR_3\left(2R_3 + R_4\right) - 2\rho\left(\frac{2\pi}{60}n_{ms}\right)^2 (R_3 - R_4)^2\left(4R_3^2 + 7R_3R_4 + 4R_4^2\right)}{90P_SR_3 - 15\rho\left(\frac{2\pi}{60}n_{ms}\right)^2 (R_3 - R_4)^2\left(R_3 + R_4\right)} \quad \textbf{(3.185)}$$

The position vectors of the hydrodynamic forces are given by

$${}_H r_{IND} = \begin{bmatrix} -R_{inD} & 0 & L_{YtoVP} \end{bmatrix}^T \quad \textbf{(3.186)}$$

$${}_H r_{INS} = \begin{bmatrix} R_{inS} & 0 & L_{YtoVP} \end{bmatrix}^T \quad \textbf{(3.187)}$$

$${}_H r_{OUTD} = \begin{bmatrix} -R_{outD} & 0 & L_{YtoVP} \end{bmatrix}^T \quad \textbf{(3.188)}$$

$${}_H r_{OUTS} = \begin{bmatrix} R_{outS} & 0 & L_{YtoVP} \end{bmatrix}^T \quad \textbf{(3.189)}$$

Shear moments in the interface between the valve plate and the barrel

The shear moment in the outer land is given by

$$shear = \int_{-\zeta/2}^{\zeta/2} \int_{R_2}^{R_1} \tau R^2 dR d\zeta \tag{3.190}$$

$$\tau = \mu \frac{dv}{dz} \tag{3.191}$$

Therefore, the shear moment at the outer land for both the discharge and suction ports is given by

$$Shear_{out} = \frac{h\zeta R_1}{4}\left(R_1 + R_2\right)\left(-P_D - P_S + 2\left(R_1 - R_2\right)R_2\rho\left(\frac{2\pi}{60}n_{ms}\right)^2\right) \tag{3.192}$$

Similarly, the shear moment at the inner land for both the discharge and suction ports is given by

$$Shear_{in} = \frac{h\zeta}{12}\left(R_3 + R_4\right)\left(3R_3\left(P_D + P_S\right) + 2\left(-R_3^3 + R_4^3\right)\rho\left(\frac{2\pi}{60}n_{ms}\right)^2\right) \tag{3.193}$$

Therefore, the total moment due to the fluid film between the barrel and the valve plate is given by

$${}_D M_{VPtoB} = -\left[0 \quad 0 \quad \left(Shear_{out} + Shear_{in}\right)\right]^T * sign\left({}_D\omega_{os}[3]\right) \tag{3.194}$$

3.4.4 Equations of motion of the barrel-output shaft assembly

The sum of all forces on the output shaft and barrel assembly equals to mass multiplied by acceleration.

$$\begin{aligned} &T_{os}[\theta,\phi].\left(T_{c2}^T.(-{}_I F_{OStoC229} - {}_I F_{OStoC230})\right) + \left({}_D F_{B3FtoB} + {}_D F_{B3StoB} + {}_D F_{B4toB}\right) \\ &+ T_{os}[\theta,\phi].T_{vp}^T\left({}_H F_{VPtoBoutD} + {}_H F_{VPtoBoutS} + {}_H F_{VPtoBinD} + {}_H F_{VPtoBinS}\right) \\ &+ \sum_{i=1}^{9}\left(-{}_D F_{BtoP,i} - {}_D F_{BStoVP,i} + {}_D F_{OILtoB,i}\right) + T_{os}[\theta,\phi].{}_A W_{os} - T_{os}[\theta,\phi].M_{os}\,{}_A a_{os} = 0 \end{aligned} \tag{3.195}$$

Summing moments of all forces about the yoke axis of rotation yields

$$
\begin{aligned}
&-T_{os}[\theta,\phi].\left({}_{A}r_{29}\times\left(T_{c2}^{T}.{}_{I}F_{OStoC229}\right)\right)-T_{os}[\theta,\phi].\left({}_{A}r_{30}\times(T_{c2}^{T}.{}_{I}F_{OStoC230})\right)\\
&-T_{c2}^{T}.({}_{I}M_{OStoC229}+{}_{I}M_{OStoC230})+\sum_{i=1}^{9}\begin{pmatrix}-{}_{D}r_{30+i}\times{}_{D}F_{BtoP,i}+{}_{D}r_{OILtoB,i}\times{}_{D}F_{OILtoB,i}\\ -{}_{D}r_{BStoVP}\times{}_{D}F_{BStoVP,i}\end{pmatrix}\\
&+{}_{D}r_{os}\times\left(T_{os}[\theta,\phi].{}_{A}W_{os}\right)+T_{os}[\theta,\phi].T_{vp}^{T}.({}_{H}r_{OUTD}\times{}_{H}F_{VPtoBoutD})\\
&+T_{os}[\theta,\phi].T_{vp}^{T}.({}_{H}r_{OUTS}\times{}_{H}F_{VPtoBoutS})+T_{os}[\theta,\phi].T_{vp}^{T}.({}_{H}r_{IND}\times{}_{H}F_{VPtoBinD})\\
&+T_{os}[\theta,\phi].T_{vp}^{T}.({}_{H}r_{INS}\times{}_{H}F_{VPtoBinS})+{}_{D}M_{VPtoB}+{}_{D}r_{B3FtoB}\times{}_{D}F_{B3FtoB}\\
&+{}_{D}r_{B3StoB}\times{}_{D}F_{B3StoB}+{}_{D}M_{B3FtoB}+{}_{D}M_{B3StoB}+{}_{D}r_{B4toB}\times{}_{D}F_{B4toB}+{}_{D}M_{B4toB}\\
&-{}_{D}r_{os}\times\left(T_{os}[\theta,\phi].M_{os}.{}_{A}a_{os}\right)-{}_{D}I_{OS}.{}_{D}\alpha_{OS}=0
\end{aligned}
\tag{3.196}
$$

3.5 Control Volume of the Oil in One Cylinder

Figure 3-13 shows the control volume of the fluid inside the vacancy of one cylinder within the barrel. The external forces that act on the control volume include the following:

1. The force from the piston to the control volume at points 40 to 48 denoted as $-{}_{D}F_{OILtoP,i}$. The corresponding position vector with respect to the yoke axis of rotation is given by

$$
{}_{D}r_{OILtoP,i}={}_{D}r_{P}\left(\theta,\phi+\frac{2\pi(i-1)}{9}\right)+\begin{Bmatrix}0\\0\\L_{P1}\end{Bmatrix},\quad i=1,2,...9 \tag{3.197}
$$

   Where ${}_{D}r_{P}\left(\theta,\phi+\frac{2\pi(i-1)}{9}\right)$ is given by Eq. (3.267)

2. The weight of the oil column which varies with the barrel angle of rotation and yoke angular position and is given by

$$
{}_{A}W_{OIL,i}=\begin{bmatrix}0 & \rho g V_{OIL}\left(\theta,\phi+\frac{2\pi(i-1)}{9}\right) & 0\end{bmatrix}^{T},\quad i=1,2,...9 \tag{3.198}
$$

   The volume of the control volume is given by Eq. (3.214).

3. The reaction forces from the barrel to the control volumes at points 49 to 57 denoted as $-_{D}F_{OILtoB,i}$. Eq. (3.206) provides the expression for the corresponding position vectors.
4. The force due to the pressure on the discharge or suction orifice at points 80 to 88 denoted as $-_{D}F_{OILtoVP,i}$. The corresponding position vector is given by Eq. (3.319).

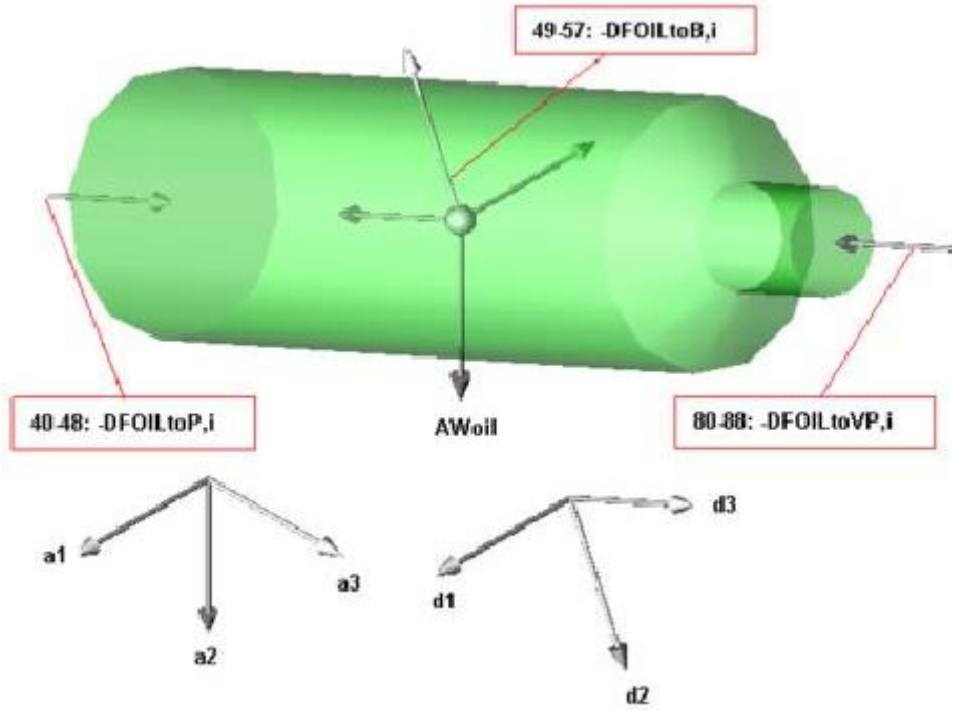

Figure 3-13: Control Volume of the Oil in the cylinder cavity

3.5.1 Linear momentum equation of the oil control volume

The principle of linear momentum can be stated as follows:

$$\sum F_{ext,i} = LM_{cv,i} + LM_{cs,i} \qquad \textbf{(3.199)}$$

$\sum F_{ext,i} =$ sum of external forces acting on the i^{th} control volume

$LM_{cv,i} = \dfrac{\partial}{\partial t}\int_{cv} v\rho dV = \begin{pmatrix} \text{time rate of change of the linear momentum} \\ \text{of the contents of the control volume} \end{pmatrix}$

$LM_{cs,i} = \int_{cs} v\rho v.ndA =$ net rate of the linear momentum through the control surface

The time rate of change of the linear momentum of the contents of the control volume can be changed into derivative format by multiplying the integrand dV by dt/dt and then simplifying to get:

$$ {}_{D}LM_{cv,i} = \frac{\partial}{\partial t}\int_{cv} \rho\, {}_{D}V_{pb}\, dV_{OIL} = \frac{\partial}{\partial t}\int_{cv} \rho\, {}_{D}V_{pb}\, \frac{dV_{OIL}}{dt}\, dt = \rho\, {}_{D}V_{pb}\, \frac{dV_{OIL}}{dt} \qquad \textbf{(3.200)} $$

The term of the time rate of change of the linear momentum of the contents of the control volume for the conical part of the cylindrical cavity is zero because its volume is fixed and the flow in and out of this part is steady. Therefore, the linear momentum of the contents of the control volume is the one due to the volume whose length is L_{c1} + Z and is given by

$$ {}_{D}LM_{cv,i} = \rho\, {}_{D}V_{pb}\left(\theta, \phi + \frac{2\pi(i-1)}{9}\right)\frac{d}{dt}V_{OIL}\left(\theta, \phi + \frac{2\pi(i-1)}{9}\right), \quad i = 1, 2, \ldots 9 \qquad \textbf{(3.201)} $$

Where

${}_{D}V_{pb}$ = velocity of fluid at the section adjacent to the piston and is given by Eq. (3.265).

The net rate of the linear momentum through the control surface is given by

$$ {}_{D}LM_{cs,i} = \rho A_c\, {}_{D}V_{pb}\left[{}_{D}V_{pb} \cdot \begin{Bmatrix} 0 \\ 0 \\ -1 \end{Bmatrix} + \frac{A_c}{A_r}\, {}_{D}V_{pb} \cdot \begin{Bmatrix} 0 \\ 0 \\ 1 \end{Bmatrix} \right], \quad i = 1, 2, \ldots 9 \qquad \textbf{(3.202)} $$

Combining equations (3.198) and (3.200) to (3.202) yields the linear momentum equations of the pistons' control volumes

$$ {}_{D}\mathrm{LM}_{\mathrm{CVi}} + {}_{D}\mathrm{LM}_{\mathrm{CSi}} = T_{os}\left(\theta, \phi + \frac{2\pi(i-1)}{9}\right) \cdot {}_{A}\mathrm{W}_{\mathrm{OILi}} - {}_{D}\mathrm{F}_{\mathrm{OILtoPi}} - {}_{D}\mathrm{F}_{\mathrm{OILtoBi}} - {}_{D}\mathrm{F}_{\mathrm{OILtoVPi}} \qquad \textbf{(3.203)} $$

3.5.2 The position vector of the reaction forces from the barrel to the control volumes at points 49 to 57

The position vector of the force from the oil control volume in the cylinder at points 49 to 57 is determined by the aid of Figure 3-14.

$$\mathrm{L_v}\left(\theta,\phi\right) = \frac{\mathrm{V_{min}} l_{\min} + A_c Z\left(\theta,\phi\right)\left(\frac{Z\left(\theta,\phi\right)}{2} + L_{C1} + L_{C2}\right)}{\mathrm{V_{min}} + A_c Z\left(\theta,\phi\right)} \tag{3.204}$$

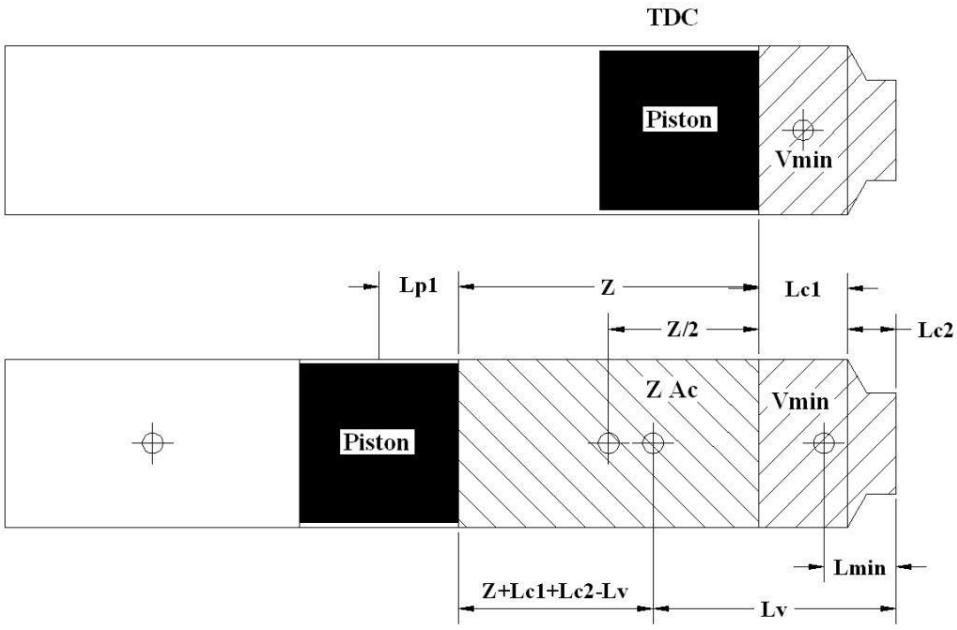

Figure 3-14: Center of gravity of the oil control volume at any angle of rotation of the main shaft, ϕ

Therefore, the position vectors of the reaction forces from the oil control volume to the barrel at points 49 to 57 as measured from the yoke axis of rotation are given by

$${}_D r_{OILtoB}\left(\theta,\phi\right) = \begin{bmatrix} 0 \\ 0 \\ Z\left(\theta,\phi\right) + L_{C1} + L_{C2} - L_V\left(\theta,\phi\right) + L_{p1} \end{bmatrix} \tag{3.205}$$

$${}_D\mathrm{r_{OILtoBi}} = {}_D\mathrm{r_{30+i}} + {}_D\mathrm{r_{OILtoB}}\left(\theta,\phi + \frac{2\pi(i-1)}{9}\right) - {}_D\mathrm{r_{WP}} \tag{3.206}$$

Equation (3.146) gives an expression for $_{D}r_{30+i}$.

3.5.3 Minimum volume of oil column in the i^{th} cylinder at the TDC

The minimum volume of the oil column (V_{min}) in the cylinder at the TDC for any angular rotation of the yoke, θ is determined based on Figure 3-15 as follows:

$$\gamma_1 = \tan^{-1}\frac{r}{EH} \tag{3.207}$$

$$\mathrm{EF} = \sqrt{r^2 + (EH)^2} \tag{3.208}$$

$$\mathrm{GF} = 2EF.\sin\left(\frac{\theta}{2}\right) \tag{3.209}$$

$$\begin{aligned} CG \;=\; & \left(DF - L_{CR}\cos\varphi_o + L_{CR}\cos\gamma_o\right)\cos\theta \\ & -\left(-r + R + L_{CR}\sin\varphi_o\right)\sin\theta - GF\sin\left(\gamma_1 - \frac{\theta}{2}\right) \end{aligned} \tag{3.210}$$

$$L_{C1} = CG - L_{C2} - L_{P1} \tag{3.211}$$

$$V_{min} = L_{C1}A_c + V_{fixed} \tag{3.212}$$

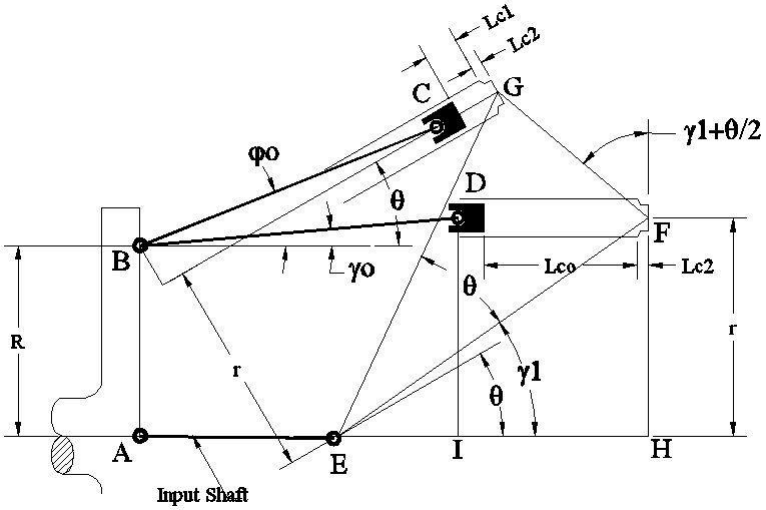

Figure 3-15: Determination of V_{min} as a function of yoke angular rotation, θ

3.5.4 Differential equation of the piston pressure

The mass of oil in the i[th] cylindrical cavity of the barrel is given by

$$M_{OIL,i} = \rho V_{OIL,i} \tag{3.213}$$

The instantaneous oil volume of the i[th] cylindrical cavity of the barrel is given by

$$V_{OIL,i} = V_{min} + A_c Z\left(\theta, \phi + \frac{2\pi(i-1)}{9}\right) \tag{3.214}$$

Differentiating equation (3.213) with respect to time yields

$$\frac{dM_{OIL,i}}{dt} = \rho \frac{dV_{OIL,i}}{dt} + V_{OIL,i} \frac{d\rho}{dt} \tag{3.215}$$

The oil density is related to its bulk modulus, B, through the relation [48]:

$$\frac{d\rho}{dt} = \frac{\rho}{B} \frac{d}{dt} P_{OIL,i}(t) \tag{3.216}$$

In addition, the mass flow rate is related to volume flow rate, Q_i:

$$\frac{dM_{OIL,i}}{dt} = \rho Q_i(t) \tag{3.217}$$

Substituting equations (3.216) and (3.217) in equation (3.215) yields

$$\frac{d}{dt} P_{OIL,i}(t) = \frac{B}{V_{OIL,i}}\left(Q_i(t) - \frac{dV_{OIL,i}}{dt}\right) \tag{3.218}$$

The initial conditions necessary to solve the above differential equations are

1. $P_{OIL,i}(0) = P_{\max L}$ for $i = 1, 2, ...5$
2. $P_{OIL,i}(0) = P_{\min H}$ for $i = 6, 7, ...9$

Figure 3-16 shows a schematic of the hydraulic system under consideration, which consists of the LPA, the pump, and the HPA. The oil leaves the LPA at a rate, Q_{DS}. The leaking oil from the pump is sent back to the accumulator.

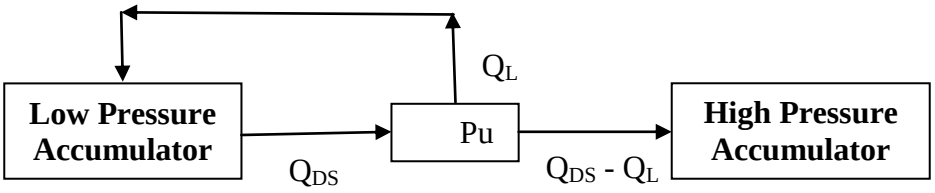

Figure 3-16: System consisting of pump connected to low and high-pressure accumulators

The flow rate at the i[th] cylindrical cavity can be expressed as

$$Q_i(t) = \left|Q_{DSi}\ (t)\right| - Q_{Li}(t) \tag{3.219}$$

$Q_{Dsi}(t)$ is the discharge/suction flow rate at the overlap area. $Q_{Li}(t)$ is the leakage flow rate. It includes leakage in the annular clearance between the cylinder and piston, leakage flow rate in the hole in the middle of the piston head that is used to pass lubrication oil to the ball and socket joints of the connecting rod, and leakage at the barrel and valve plate interface. Therefore, the net flow rate at the exit of the i[th] cylindrical cavity is related to the discharge/suction flow rare via the volumetric efficiency:

$$\mathrm{Q_i}(t) = \eta_{v,i}\mathrm{Q_{DSi}}(t) \tag{3.220}$$

The discharge/suction flow rate at the overlap area is calculated using the orifice formula [49]:

$$Q_{DS,i}(t) = sign(P_{OIL,i}(t) - P_b(\phi))C_d A_r(\phi)\sqrt{\frac{2\left|P_{OIL,i}(t) - P_b(\phi)\right|}{\rho}} \tag{3.221}$$

Where

P_b = the boundary pressure outside the control volume (either P_D or P_S)

C_d = the orifice discharge coefficient which is assumed to be constant in this analysis

A_r = the overlap area of the i^{th} region

P_D = discharge pressure which varies with the SOC of the HPA

P_S = suction pressure which varies with the SOC of the LPA

$\eta_{v,i}$ is the pump volumetric efficiency, which can be read from the efficiency map of the pump. The pump volumetric efficiency is assumed to vary in a parabolic fashion with pump rotational speed and exponentially with the oil pressure according to the following relation:

$$\eta_{v,i} = \left(a_o + a_1 \left(\frac{n_{ms}}{n_{rated}} \right) + a_2 \left(\frac{n_{ms}}{n_{rated}} \right)^2 \right) \exp\left(b_o \left| P_{OIL,i} - P_b(\phi) \right| \right) \quad \textbf{(3.222)}$$

a_o, a_1, a_2, and b_o are experimentally determined constants.

Discharge/Suction pressure variations

The discharge port of the valve plate is connected to the high-pressure accumulator (HPA) while the suction port is connected to the LPA. Therefore, the pressure at the exit of the cylinder is related to the gas pressure in the HPA or LPA depending on the piston angular position:

$$P_b(\phi) = \begin{cases} P_S; & 0 \le \phi \le \phi_9 \\ P_S + \dfrac{(\phi - \phi_9)(P_D - P_S)}{(\pi + \phi_2 - \phi_9)}; & \phi_9 \le \phi \le \phi_2 + \pi \\ P_D; \quad \pi \le \phi \le 2\pi; & \phi_2 + \pi \le \phi \le \phi_1 + 2\pi \\ P_D + \dfrac{(\phi - \phi_1 - 2\pi)(P_S - P_D)}{(\phi_2 - \phi_1)}; & \phi_1 + 2\pi \le \phi \le \phi_2 + 2\pi \\ P_S; & \phi_2 + 2\pi \le \phi \le 2\pi \end{cases} \quad \textbf{(3.223)}$$

$$P_D = P_H(t) + P_{lossH} \quad \textbf{(3.224)}$$

$$P_S = P_L(t) - P_{lossL} \quad \textbf{(3.225)}$$

$P_H(t)$ = gas pressure in the HPA

$P_L(t)$ = gas pressure in the LPA

The pressure losses (friction and minor) between the discharge/suction port and the HPA/LPA are assumed negligible in this analysis.

3.5.5 Analysis of the high pressure and low-pressure accumulators

The gas volume at pre-charge condition is found using the ideal gas low for both the HPA and LPA as follows:

$$V_{PH} = \frac{M_H R_N T_g}{p_{PH}} \quad \textbf{(3.226)}$$

$$V_{PL} = \frac{M_L R_N T_g}{p_{PL}} \quad \textbf{(3.227)}$$

The gas pre-charge pressure is to be slightly lower than the minimum hydraulic pressure so that the bladder does not continually contact the oil valve (wear). In order to reduce bladder wear on the inlet valve, the gas pre-charge pressure at room temperature with-no fluid is related to the minimum operating pressure by [50]:

$$p_{PH} \approx 0.9 P_{\min H} \quad \textbf{(3.228)}$$

$$p_{PL} \approx 0.9 P_{\min L} \quad \textbf{(3.229)}$$

Assuming that a polytrophic relation relates the pressure and volume of the gas in the HPA/LPA, therefore the gas pressures in the HPA and LPA are given by

$$P_H(t) = P_{\min H}\left(\frac{V_{\max H}}{V_H(t)}\right)^{1.4} \tag{3.230}$$

$$P_L(t) = P_{\min L}\left(\frac{V_{\max L}}{V_L(t)}\right)^{1.4} \tag{3.231}$$

The sum of the gas in the LPA and HPA is constant at any instant of time leading to

$$V_L + V_H = V_{\max H} + V_{\min L} \tag{3.232}$$

The gas volume at the minimum operating pressure for both the HPA and the LPA are given by

$$V_{\max H} = \left(\frac{p_{PH}}{p_{\min H}} V_{PH}^{1.4}\right)^{1/1.4} \tag{3.233}$$

$$V_{\max L} = \left(\frac{p_{PL}}{p_{\min L}} V_{PL}^{1.4}\right)^{1/1.4} \tag{3.234}$$

The maximum hydraulic pressure is not to exceed 4 times the pre-charge pressure; otherwise, the elasticity of the bladder will be adversely affected. In addition, excessive changes in pressure result in considerable heating of the gas. Reducing the pressure differential between the HPA and LPA increases the bladder service life. On the other hand, it must be taken into account that a lower pressure differential also reduces the utilization of available storage capacity [50].

$$p_{\max H} \le 4P_{PH} \tag{3.235}$$

$$p_{\max L} \le 4P_{PL} \tag{3.236}$$

The actual flow rate through the pump is related to the gas volume through the continuity equation. The actual total flow rate of the hydraulic fluid entering the HPA equals to the rate of contraction of the gas in the HPA:

$$\frac{dV_H}{dt} = -Q_{TTD} \tag{3.237}$$

The total actual flow rate equals to the rate of change of the total oil volumes within the barrel at the discharge port side

$$Q_{TTD} = \sum_{i=1}^{9} \frac{|Q_i|}{2} \tag{3.238}$$

Initially, the gas volume in the high-pressure accumulator equals to the maximum gas volume in the HPA. Therefore, the initial condition necessary to solve equation (3.237) can be expressed as

$$V_H\left(t=0\right) = V_{\max H} \tag{3.239}$$

3.5.6 Orifice area

In finding the pressure force effects, Schoenau et al. had considered the pressure variations through one complete revolution of the swash plate. The valve ports have relief notches to avoid step changes in pressure in the transition regions. The resulting overlap produces six distinct pressure regions for each revolution of the piston barrel [17]. Each region gives rise to a different expression for pressure and flow.

The value of the cylinder pressure, $P_{OIL1,i}$, depends on the angular position of the piston with respect to the TDC. In fact, the resulting overlap produces 16 distinct pressure regions for each revolution of the piston barrel as shown in Figure 3-17. These regions are:

1. Regions 1 and 9: the cylinder is completely closed by the land between the suction and discharge ports.
2. Regions 2 to 8: the cylinder is open to the suction port.

3. Regions 10 to 16: the cylinder is open to the discharge port.

The above regions have different exit areas and they are grouped as shown in Table 3-2.

Table 3-2: Orifice area classification

Region	Area	Angular range	Region	Area	Angular range
1	$A_{r1} = 0$	$\phi_1 < \phi < \phi_2$	9	$A_{r1} = 0$	$\phi_9 < \phi < \phi_{10}$
2	A_{r2}	$\phi_2 < \phi < \phi_3$	10	A_{r2}	$\phi_{10} < \phi < \phi_{11}$
3	A_{r3}	$\phi_3 < \phi < \phi_4$	11	A_{r3}	$\phi_{11} < \phi < \phi_{12}$
4	A_{r4}	$\phi_4 < \phi < \phi_5$	12	A_{r4}	$\phi_{12} < \phi < \phi_{13}$
5	A_{r5}	$\phi_5 < \phi < \phi_6$	13	A_{r5}	$\phi_{13} < \phi < \phi_{14}$
6	A_{r6}	$\phi_6 < \phi < \phi_7$	14	A_{r6}	$\phi_{14} < \phi < \phi_{15}$
7	A_{r7}	$\phi_7 < \phi < \phi_{88}$	15	A_{r7}	$\phi_{15} < \phi < \phi_{16}$
8	A_{r8}	$\phi_8 < \phi < \phi_9$	16	A_{r8}	$\phi_{16} < \phi < \phi_1$

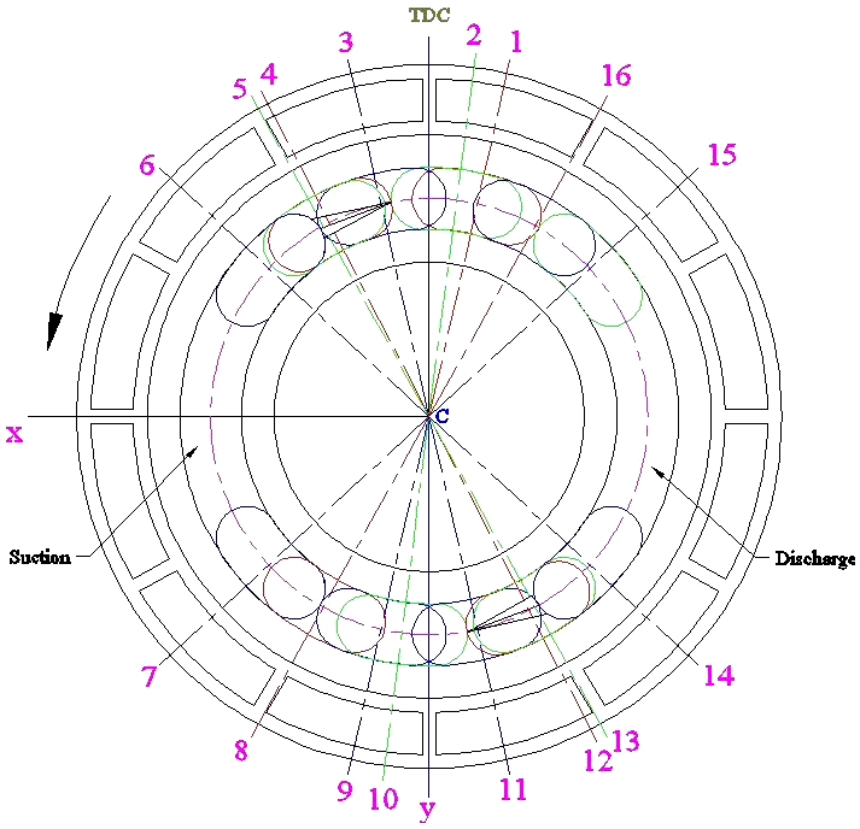

Figure 3-17: Pressure regions as seen by cylinders

The overlap area varies with the angular position of the barrel as shown in Figure 3-18:

$$A_r(\phi) = \sum_{i=1}^{16} \left(H(\phi - \phi_i) - H(\phi - \phi_{i+1}) \right) A_{r,i} \qquad \textbf{(3.240)}$$

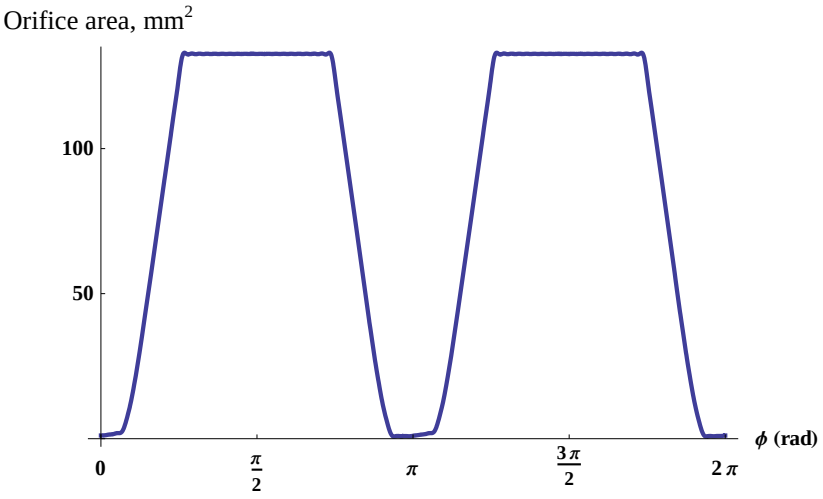

Figure 3-18: Orifice area variation with main shaft angular rotation

The area profile shown in Figure 3-18 repeats in the same manner every revolution of the barrel. Therefore, a Fourier series can represent the expression of area given by Eq. (3.240):

$$\begin{aligned} A_r(\phi) &= \sum_{i=1}^{16} \left(H(\phi - \phi_i) - H(\phi - \phi_{i+1}) \right) A_{r,i}(\phi) \\ &= \frac{a_o}{2} + \sum_{n=1}^{\infty} a_n \cos n\phi + \sum_{n=1}^{\infty} b_n \sin n\phi \end{aligned} \quad \textbf{(3.241)}$$

$$a_o = \frac{1}{\pi} \int_0^{2\pi} A_r(\phi).d\phi \quad \textbf{(3.242)}$$

$$a_n = \frac{1}{\pi} \int_0^{2\pi} A_r(\phi) \cos n\phi.d\phi \quad \textbf{(3.243)}$$

$$b_n = \frac{1}{\pi} \int_0^{2\pi} A_r(\phi) \sin n\phi.d\phi \quad \textbf{(3.244)}$$

3.5.6 Expressions of the overlap areas

Regions 1 and 9: When the cylinder is at either region 1 or region 9, it is totally closed by the land between the discharge and suction ports. However, in reality there is some leakage at these regions because of the clearance between the barrel and the valve. Thus, the overlap area at regions 1 and 9 is assumed around 1% of the overlap area where the cylinder is completely open to either the discharge or suction port. Therefore, the net overlap area for either region (1) or (9) is given by

$$A_{r9} = A_{r1} = 0.01 A_{r6}(\phi) \quad \textbf{(3.245)}$$

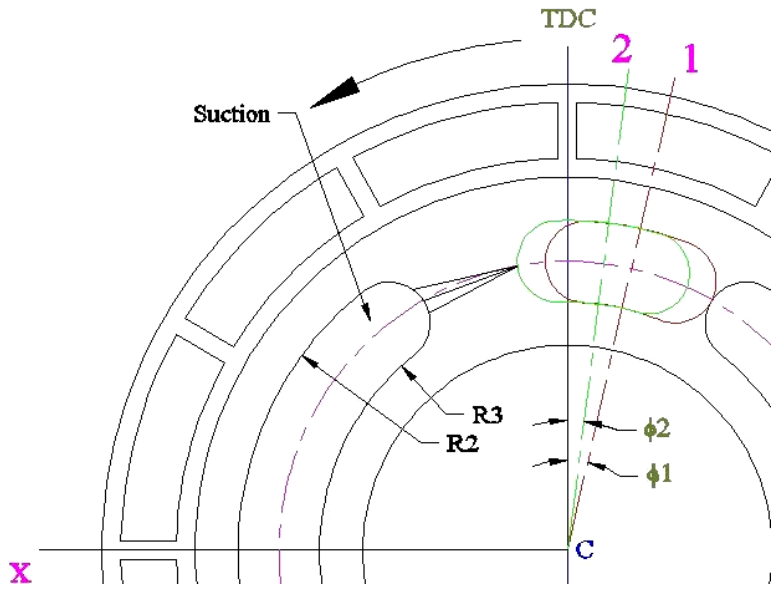

Figure 3-19: Geometric parameters of pressure region 1

Regions 2 and 10: The net suction area or discharge area is given by

$$A_{r2}(\phi)=\left(L_{45}\frac{L_{16}}{2L_{17}}\right)^2+A_{r1} \tag{3.246}$$

$$L_{16}=\sqrt{\frac{\sin^2\left(\frac{\phi-\phi_2}{2}\right)}{8\left(R_2+R_3\right)^2}\begin{pmatrix}2C_1^2+C_2^2\left(R_2-R_3\right)^2\\+C_2\left(R_2-R_3\right)\begin{pmatrix}C_2\left(R_2-R_3\right)\cos\left(\phi+\phi_2+\zeta_c\right)\\+2C_1\sin\left(\phi+\phi_2+\zeta_c\right)\end{pmatrix}\end{pmatrix}} \tag{3.247}$$

$$L_{17}=\sqrt{\frac{1}{16\left(R_2+R_3\right)^2}\begin{pmatrix}\left(\begin{pmatrix}C_1\left(\cos\zeta_1-\cos\left(\phi_2+\frac{\zeta_c}{2}\right)\right)\\+C_2\left(R_2-R_3\right)\left(\sin\zeta_1+\sin\left(\phi_2+\frac{\zeta_c}{2}\right)\right)\end{pmatrix}^2\\\left(C_1\left(-\sin\zeta_1+\sin\left(\phi_2+\frac{\zeta_c}{2}\right)\right)+2C_2\left(R_2-R_3\right)\right)^2\end{pmatrix}} \tag{3.248}$$

$$C_1=R_2^2+6R_2R_3+R_3^2 \tag{3.249}$$

$$C_2=\sqrt{\left(3R_2+R_3\right)\left(R_2+3R_3\right)} \tag{3.250}$$

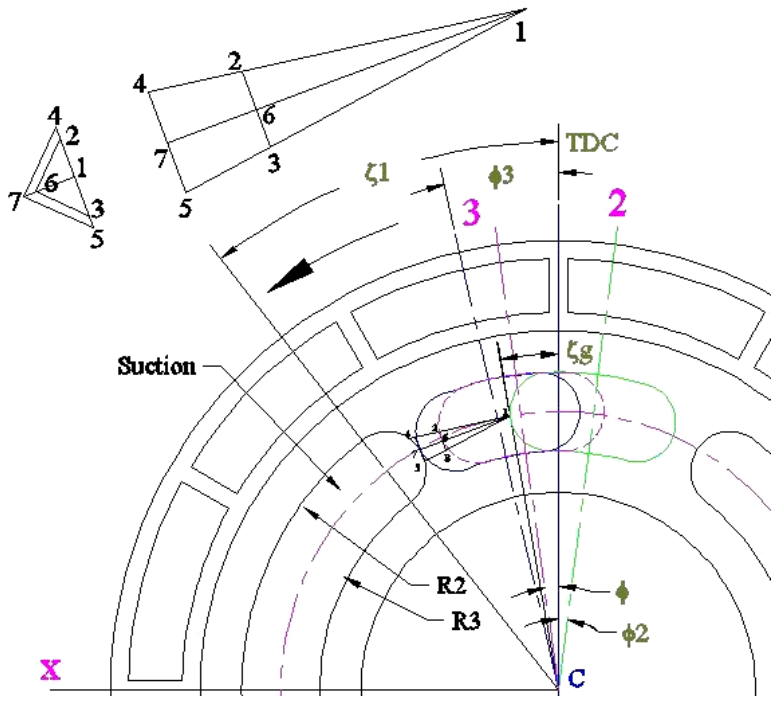

Figure 3-20: Geometric parameters of pressure region 2

Regions 3 and 11: The expression for the net suction or discharge area of is given by

$$A_{r3}(\phi) = \delta_1\left(R_2^2 - R_3^2\right) + A_{r3}(\phi_3) \tag{3.251}$$

The angle between lines AC and BC is given by:

$$\delta_1 = 2\sin^{-1}\frac{L_{AB}}{2R_k} \tag{3.252}$$

The length of line AB is given by

$$L_{AB} = \sqrt{0.5\left(R_2^2 - 6R_2R_3 + R_3^2 + \left(R_2 + R_3\right)^2 \cos\left(\phi - \zeta_1 + \frac{\zeta_c}{2}\right)\right)} \tag{3.253}$$

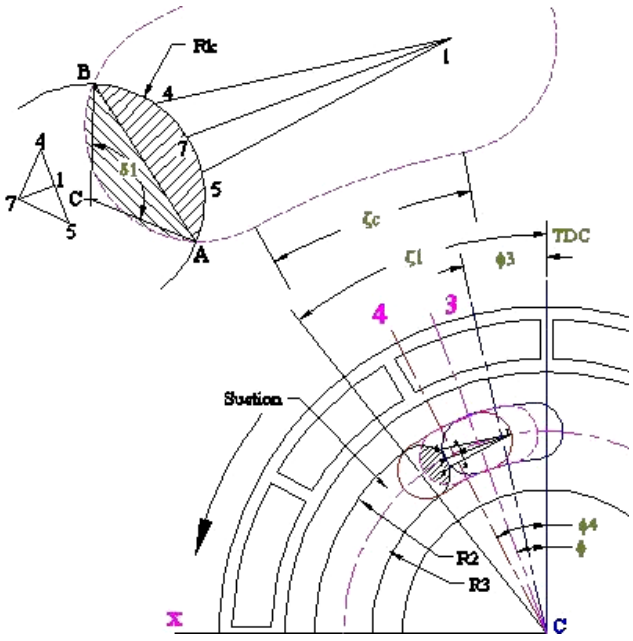

Figure 3-21: Geometric parameters of pressure region 3

Region 5 and 13: The net suction or discharge area is given by

$$A_{r5}(\phi) = \pi R_k^2 + 0.5\delta_2\left(R_2^2 - R_3^2\right) + \frac{L_{45}^2}{4} + A_{r1} \tag{3.254}$$

$$\delta_2 = \phi + \frac{\zeta_c}{2} - \zeta_1 \tag{3.255}$$

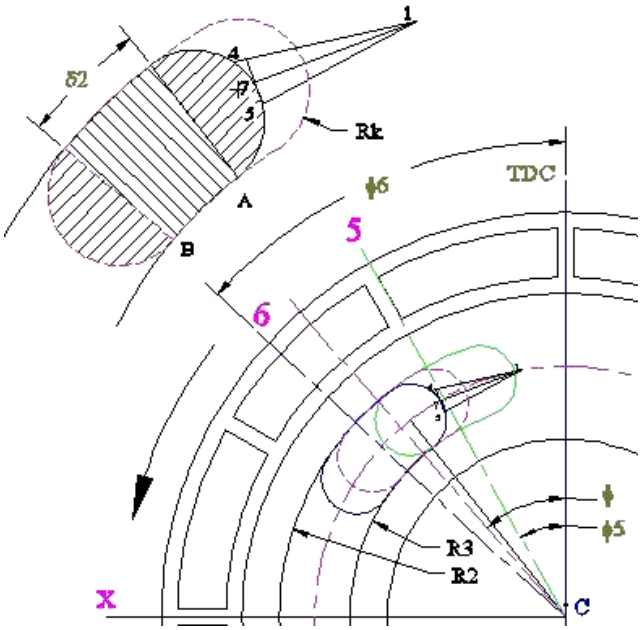

Figure 3-22: Geometric parameters of pressure region 5

Regions 6 and 14: The net suction area or discharge area is given by

$$A_{r6} = \pi R_k^2 + 0.5\left(R_2^2 - R_3^2\right)\left(\phi_6 + \frac{\zeta_c}{2} - \zeta_1\right) + \frac{L_{45}^2}{4} + A_{r1} \tag{3.256}$$

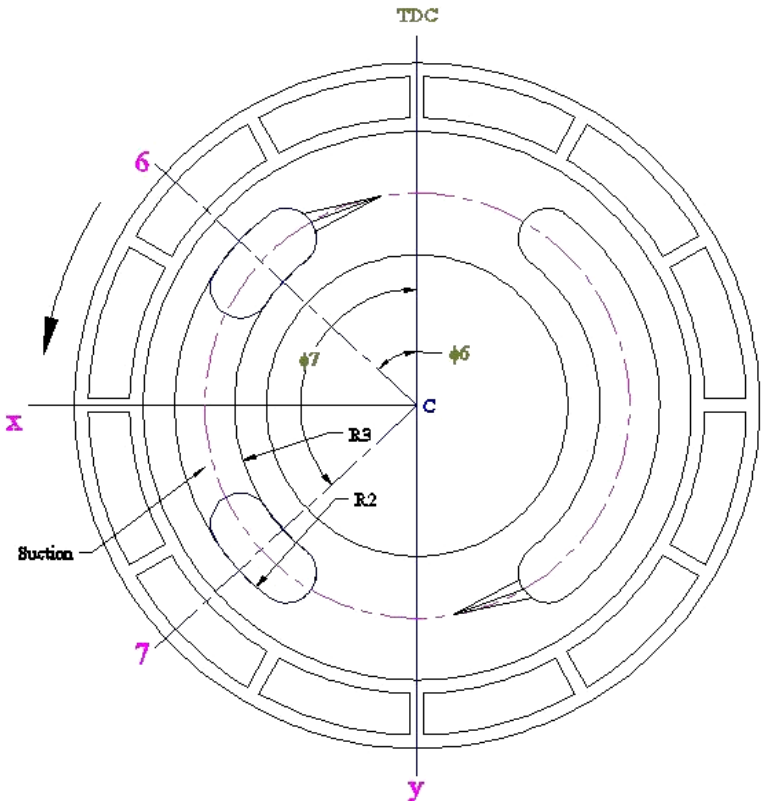

Figure 3-23: Geometric parameters of pressure region 6

Regions 7 and 15: The net suction area or discharge area is given by

$$A_{r7}\left(\phi\right) = \pi R_k^2 + 0.5\left(R_2^2 - R_3^2\right)\left(\pi - \phi + \frac{\zeta_c}{2} - \zeta_1\right) + \frac{L_{45}^2}{4} + A_{r1} \tag{3.257}$$

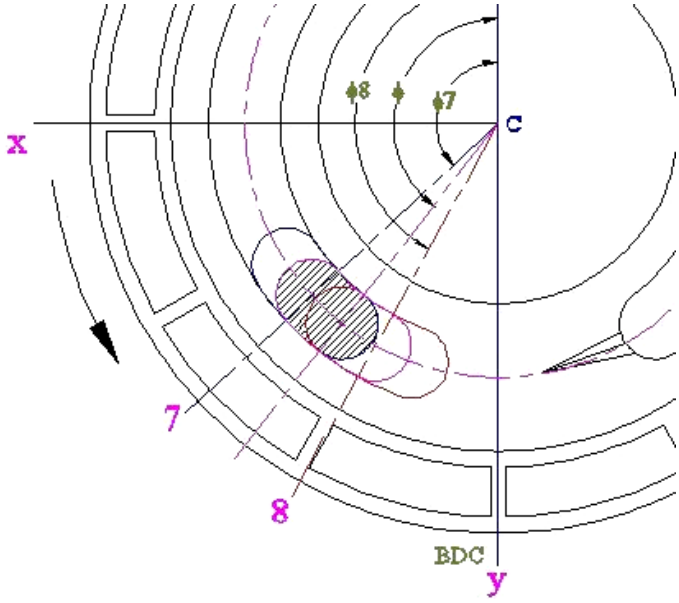

Figure 3-24: Geometric parameters of pressure region 7

Regions 8 and 16: The net suction area or discharge area is given by

$$A_{r8}(\phi) = R_k^2(\delta_1 - \sin\delta_1) \tag{3.258}$$

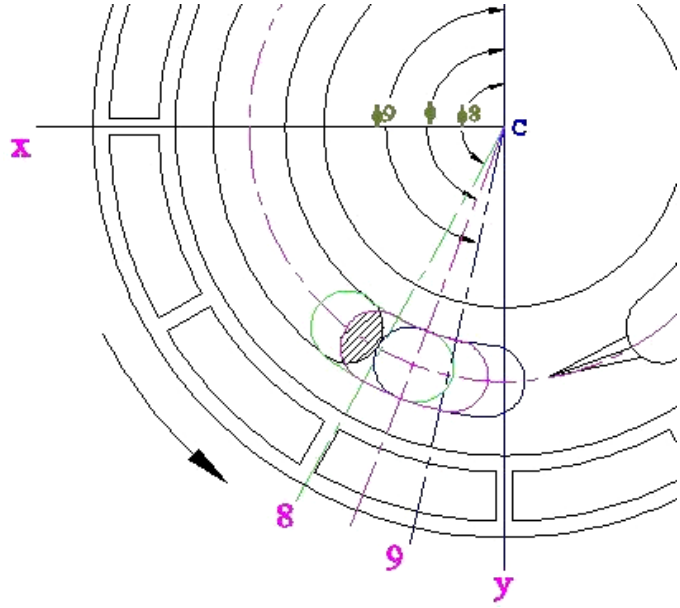

Figure 3-25: Geometric parameters of pressure region 8

3.6 Dynamic Analysis of the Piston

3.6.1 Displacement and velocity of the piston with respect to barrel

With reference to Figure 3-9, equate the vertical distance at the main shaft side to the vertical distance at the barrel side when the connecting rod is at the TDC yields

$$R + \mathrm{L_{CR}} \sin\varphi_{\mathrm{o}} = r\cos\theta + IJ\sin\frac{\theta}{2} + IH\sin\theta \tag{3.259}$$

Equate the horizontal distances when the connecting rod is at the TDC yields

$$\mathrm{L_{CR}} \cos\varphi_{\mathrm{o}} + r\sin\theta = L_{is} + IJ\cos\frac{\theta}{2} + IH\cos\theta \tag{3.260}$$

Solving equations: (3.259) and (3.260) yields:

$$\varphi_o = \theta + \sin^{-1}\left(\frac{r - R\cos\theta - \left(R_y + L_{is}\right)\sin\theta}{L_{CR}}\right) \tag{3.261}$$

$$IH = -R_y + L_{CR}\cos(\varphi_o - \theta) - (L_{is} + R_y)\cos\theta + R\sin\theta \tag{3.262}$$

Knowing that the value of the vector $_{\mathrm{A}}\mathrm{r}_{\mathrm{EB}}$ given by equation (3.281) is equal to the length of the connecting rod $\mathrm{L_{CR}}$, therefore, the distance IF is given by

$$\begin{aligned} IF(\theta,\phi) = {} & -R_y - \left(L_{is} + R_y\right)\cos\theta + R\sin\theta\cos\phi \\ & + \sqrt{\begin{array}{l} L_{CR}^2 - \left(L_{is} + R_y\right)^2\sin^2\theta - r^2 + 2rR\left(1 - 2\cos^2\phi\sin^2\frac{\theta}{2}\right) \\ + R^2\left(\sin^2\theta\cos^2\phi - 1\right) + 2\cos\phi\sin\theta\left(L_{is} + R_y\right)\left(r - R\cos\theta\right) \end{array}} \end{aligned} \tag{3.263}$$

The piston is assumed to have a value of zero displacement at the TDC. The displacement of the piston with respect to the barrel at any angle of rotation of main shaft is denoted by the letter z and is given by

$$\mathrm{Z}\ (\theta,\phi) = IH\text{-}\mathrm{IF}(\theta,\phi) \tag{3.264}$$

The velocity of the piston with respect to the barrel is given by

$$ {}_{\mathrm{D}}\mathrm{v}_{\mathrm{p/b,i}} = -\frac{\mathrm{d}}{\mathrm{dt}}\mathrm{Z}\left(\theta,\phi+\frac{2\pi(i-1)}{9}\right)\begin{bmatrix}0 & 0 & 1\end{bmatrix}^{T} \quad \textbf{(3.265)} $$

The angular velocity of the piston is the same as the angular velocity of the barrel and is given by

$$ {}_{\mathrm{D}}\omega_{\mathrm{p}} = {}_{\mathrm{D}}\omega_{\mathrm{os}} \quad \textbf{(3.266)} $$

The position vector of the geometric center of the ball joint between the piston and the connecting rod with respect to the center of the yoke axis of rotation is given by

$$ {}_{D}r_{p}\left(\theta,\phi\right) = \begin{bmatrix}0 & -r & IF\left(\theta,\phi\right)+R_{y}\end{bmatrix}^{T} \quad \textbf{(3.267)} $$

The position vector of the CG of the piston with respect to the center of the ball joint between the piston and the connecting rod is given by

$$ {}_{D}r_{WP} = [0,\ 0,\ r_{WP}]^{T} \quad \textbf{(3.268)} $$

The velocity of the CG of the piston is given by

$$ {}_{D}V_{\mathrm{p}} = {}_{D}V_{\mathrm{Pb}} + {}_{\mathrm{D}}\omega_{\mathrm{p}} \times \left({}_{\mathrm{D}}r_{\mathrm{p}} + {}_{\mathrm{D}}r_{\mathrm{WP}}\right) \quad \textbf{(3.269)} $$

The angular acceleration of the piston is given by

$$ {}_{D}\alpha_{\mathrm{p}}\left(\theta,\phi\right) = \begin{bmatrix}\ddot{\theta}\cos\phi - \dot{\theta}\dot{\phi}\sin\phi \\ -\dot{\theta}\dot{\phi}\cos\phi - \ddot{\theta}\sin\phi \\ \ddot{\phi}\end{bmatrix} \quad \textbf{(3.270)} $$

The absolute acceleration of the CG of the piston is given by

$$ {}_{D}a_{\mathrm{p}}\left(\theta,\phi\right) = {}_{D}a_{\mathrm{Pb}} + {}_{\mathrm{D}}\omega_{\mathrm{p}} \times {}_{\mathrm{D}}\omega_{\mathrm{p}} \times \left({}_{\mathrm{D}}r_{\mathrm{p}} + {}_{\mathrm{D}}r_{\mathrm{WP}}\right) + {}_{\mathrm{D}}\alpha_{\mathrm{p}} \times \left({}_{\mathrm{D}}r_{\mathrm{p}} + {}_{\mathrm{D}}r_{\mathrm{WP}}\right) \quad \textbf{(3.271)} $$

3.6.2 Force analysis of the piston

Figure 3-26 shows the FBD of the i^{th} piston. The forces that act on the piston include:

1. The reaction forces from the connecting rod to the piston denoted by - ${}_{\mathrm{A}}\mathrm{F}_{\mathrm{PtoCR,i}}$ at points (14) to (22), where i = 1, 2, …9

2. The frictional moment from the connecting rod to the piston denoted by - ${}_{A}M_{PtoCR,i}$ at points (14) to (22), where i = 1, 2, …9

3. The pressure force from the hydraulic oil given by

$$ {}_{D}F_{OILtoP,i} = [0 \quad 0 \quad -P_{OIL,i}A_p]^T, \quad i = 1, 2, ...9 \tag{3.272}$$

4. The reaction force from the barrel to the piston at points 31 to 39 given by

$$ {}_{D}F_{BtoP,i} = \begin{bmatrix} F_{BtoPx,i} & F_{BtoPy,i} & F_{BtoPz,i} \end{bmatrix}^T, \quad i = 1, 2, ...9 \tag{3.273}$$

5. The weight of the piston given by

$$ {}_{A}W_p = \begin{bmatrix} 0 & M_p g & 0 \end{bmatrix}^T \tag{3.274}$$

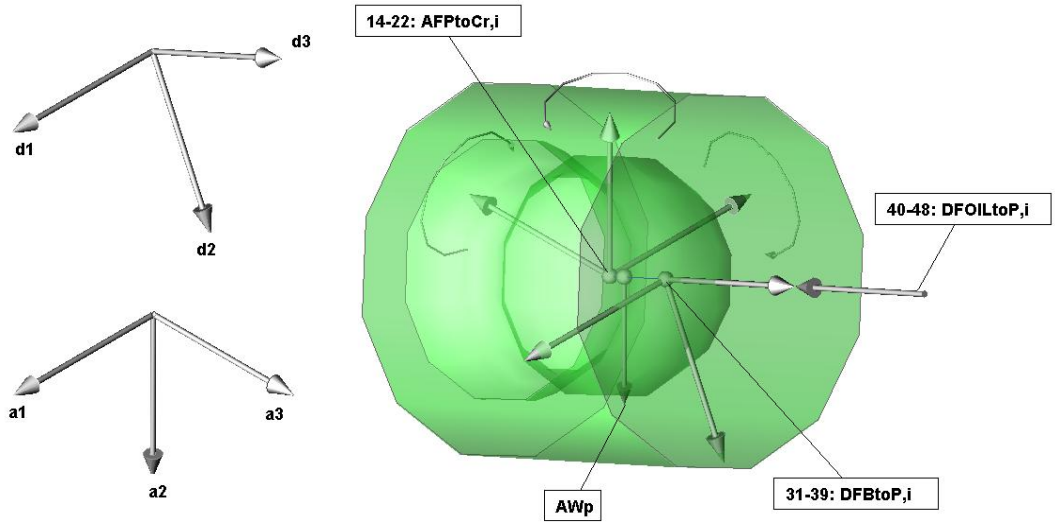

Figure 3-26: FBD of the piston

3.6.3 The frictional force between the barrel and the piston

Based on laminar incompressible flow, the viscous force on one piston can be expressed as [51]

$$ \mathrm{F}_{\mathrm{BtoPz,i}} = -\frac{\pi \nu r_{p\ D} v_{pb,i} L_p}{C_p}, \quad \mathrm{i} = 1, 2, ...9 \ \textbf{[17]} \tag{3.275}$$

L_p is the length of the piston that is inserted in the cylinder when the axial displacement is zero. It is assumed equal to the total length of the piston for all yoke angular positions.

r_p = the piston radius

${}_DV_{pb,i}$ = the axial velocity of the i^{th} piston with respect to the barrel

C_p = one half the radial clearance between the piston and the cylinder

ν = oil viscosity, Ns/m^2

3.6.4 Equations of motion of the pistons

Attach the origin of the D coordinate system to point (14 to 22) (center point of contact between the connecting rod and the piston). Assuming that the reaction force from the barrel to the piston acts at the CG of the piston length, therefore, its position vector is given by

$$ {}_Dr_{BtoP} = \begin{bmatrix} 0 & 0 & r_{WP} \end{bmatrix}^T \tag{3.276} $$

Summing forces along the three inertial directions yields

$$ \begin{aligned} & -{}_AF_{PtoCR,i} + T_{os}^T\left(\theta,\phi+\frac{2\pi(i-1)}{9}\right).\left({}_DF_{OILtoP,i} + {}_DF_{BtoP,i}\right) \\ & +{}_AW_p - M_p\,{}_Aa_p\left(\theta,\phi+\frac{2\pi(i-1)}{9}\right)=0, \quad i = 1, 2, \ldots 9 \end{aligned} \tag{3.277} $$

Summing moments about the common point between the connecting rod and the piston (points 14 to 22) yields

$$ \begin{aligned} & -T_{os}\left(\theta,\phi+\frac{2\pi(i-1)}{9}\right).{}_AM_{PtoCR,i} + {}_Dr_{BtoP}\times{}_DF_{BtoP,i} + {}_Dr_{WP}\times\left(T_{os}\left(\theta,\phi+\frac{2\pi(i-1)}{9}\right).{}_AW_p\right) \\ & -{}_DI_p.{}_D\alpha_p\left(\theta,\phi+\frac{2\pi(i-1)}{9}\right) - {}_Dr_{WP}\times M_p\,{}_Aa_p\left(\theta,\phi+\frac{2\pi(i-1)}{9}\right)=0, \ i = 1, 2, \ldots 9 \end{aligned} \tag{3.278} $$

3.7 Dynamic Analysis of the Connecting Rod

With reference to Figure 3-9, the position vector of point B with respect to point A is given by

$$ {}_{B}r_{B} = \begin{bmatrix} 0 & -R & 0 \end{bmatrix}^{T} \tag{3.279} $$

The position vector of point E with respect to point A is given by

$$ {}_{A}r_{E}\left(\theta,\phi\right) = \begin{pmatrix} 0 \\ 0 \\ L_{is} \end{pmatrix} + T_{im1}^{T}.\begin{pmatrix} 0 \\ 0 \\ L_{im} \end{pmatrix} + T_{os}^{T}\left(\theta,\phi\right).\begin{pmatrix} 0 \\ -r \\ IF\left(\theta,\phi\right) \end{pmatrix} \tag{3.280} $$

The position vector of point E with respect to point B is given by

$$ {}_{A}r_{EB}\left(\theta,\phi\right) = {}_{A}r_{E} - T_{1}^{T}\left(\phi\right).{}_{B}r_{B} \tag{3.281} $$

The velocity of point B is related to the rotation of the main shaft and is given by

$$ {}_{A}V_{B} = T_{1}^{T}.\left({}_{B}\omega_{MS} \times {}_{B}r_{B}\right) = R\dot{\phi}\begin{pmatrix} \cos\phi \\ \sin\phi \\ 0 \end{pmatrix} \tag{3.282} $$

The position vector of the CG of the ith Connecting rod with respect to point A (Figure 3-9) is given by

$$ {}_{A}r_{CRG}\left(\theta,\phi\right) = T_{1}^{T}\left(\phi\right).{}_{B}r_{B} + \frac{r_{CR}}{L_{CR}}\,{}_{A}r_{EB}\left(\theta,\phi\right) \tag{3.283} $$

The velocity of the CG of the connecting rod is given by

$$ {}_{A}V_{CR,i} = \frac{d}{dt}\,{}_{A}r_{CRG}\left(\theta,\phi + \frac{2\pi(i-1)}{9}\right) \tag{3.284} $$

The linear acceleration of the connecting rod can be expressed in terms of the inertial coordinate frame as

$$ {}_A a_{CR,i} = \frac{d^2}{dt^2}\, {}_A r_{CRG}\left(\theta, \phi + \frac{2\pi(i-1)}{9}\right) \tag{3.285} $$

Figure 3-27 shows the forces that act on the FBD of the connecting rod that include:

1. The weight of the connecting rod expressed as

$$ {}_A W_{CR} = \begin{bmatrix} 0 & M_{CR} g & 0 \end{bmatrix} \tag{3.286} $$

2. The reaction force from the cup at the main shaft side at points (5) to (13) and is expressed in terms of the A frame as

$$ {}_A F_{MStoCR,i} = \begin{bmatrix} F_{MStoCR,ix} & F_{MStoCR,iy} & F_{MStoCR,iz} \end{bmatrix}, \quad i = 1, 2, \ldots 9 \tag{3.287} $$

3. The frictional moment from the cup at the main shaft-side at points (5) to (13) that will be explained in detail in the next section.

4. The reaction force from the piston to the connecting rod at points (14) to (22) and is expressed as

$$ {}_A F_{PtoCR,i} = \begin{bmatrix} F_{PtoCR,ix} & F_{PtoCR,iy} & F_{PtoCR,iz} \end{bmatrix}^T, \quad i = 1, 2, \ldots 9 \tag{3.288} $$

5. The frictional moment from the piston to the connecting rod at points (14) to (22) and will be explained in detail below.

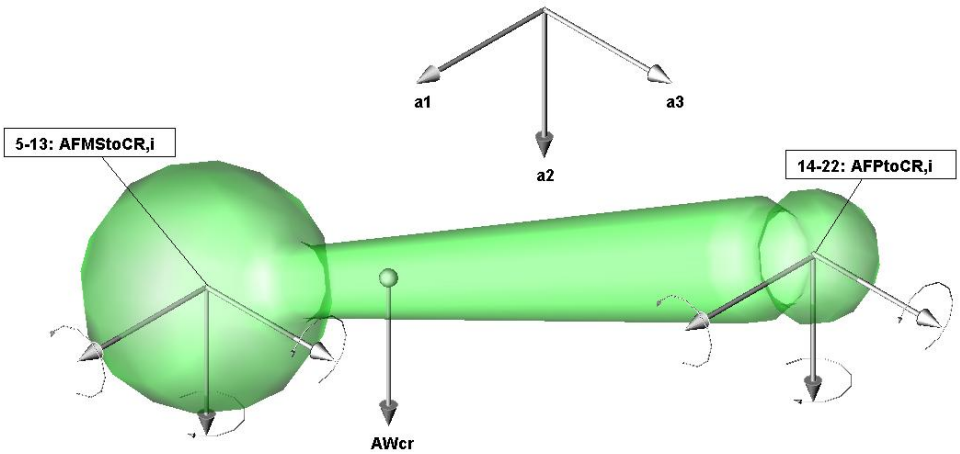

Figure 3-27: FBD of the connecting rod

3.7.1 The frictional moment from the cup at the main shaft

The friction moments, ${}_AM_{MStoCR,i}$, generated on the spherical joint at points (5) to (13) are determined by the reaction force "${}_AF_{MStoCR,i}$", friction coefficient "$\mu_{CRL,i}$", and radius "R_{CRL}". Its direction is opposite to the angular velocity of the connecting rod. The friction moments, ${}_AM_{MStoCR,i}$ are expressed by [25]

$$ {}_AM_{MStoCR,i} = \frac{-T_{CR}^{T}\left(\theta,\phi+\frac{2\pi(i-1)}{9}\right)\cdot {}_J\omega_{CR}\left(\theta,\phi+\frac{2\pi(i-1)}{9}\right)}{\left|{}_J\omega_{CR}\left(\theta,\phi+\frac{2\pi(i-1)}{9}\right)\right|} $$
$$ R_{CRL}\mu_{CRL,i}\sqrt{F_{MStoCR,ix}^2+F_{MStoCR,iy}^2+F_{MStoCR,iz}^2}, \mathrm{i}=1,2,\ldots 9 \quad \textbf{(3.289)} $$

Experimental tangential speeds below 0.7m/s was not possible because of the stick-slip phenomena [25]. However, the friction coefficient in the low speed range can be assumed by linear interpolation between 0.04 and 0.09, the static friction coefficient [25]. The spherical joint makes slide motion on its surface with the velocity lower than 0.3m/s even at the max input shaft speed of 10, 000 rpm and its friction coefficient changes between 0.07 and 0.09 within this speed range [25]. The coefficient of friction is almost of constant value (0.04) for sliding speeds above 0.7m/s [25]. Therefore, using the three points of coefficient of friction variation with slide speed as shown in Table **3-3**, a linear fit can be obtained as follows:

$$ \mu_{CRL,i} = \begin{cases} -0.0716V_{CRL,i}+0.0905 & 0 \le V_{CRL,i} < 0.7 \\ 0.04038 & V_{CRL,i} \ge 0.7 \end{cases} \quad \textbf{(3.290)} $$

Where i = 1, 2, …, 9 and H denotes the Heaviside function and V_{CRLi} is the absolute value of the sliding velocity at the surface of contact with the cup at the main shaft side.

$$ V_{CRLi} = R_{CRL}\left|{}_J\omega_{CR}\left(\theta,\phi+\frac{2\pi(i-1)}{9}\right)\right|, \quad \mathrm{i}=1,2,\ldots 9 \quad \textbf{(3.291)} $$

Table 3-3: Coefficient of friction variation with Spherical joint sliding speed [25]

Spherical joint sliding speed (m/s)	Coefficient of friction
0	0.09
0.3	0.07
0.7	0.04

3.7.2 The frictional moment from the spherical joint at the piston side

The friction moments, ${}_AM_{PtoCR,i}$, generated on the spherical joint at points (14) to (22) are determined by the reaction force, ${}_AF_{PtoCR,i}$, friction coefficient, $\mu_{CRR,i}$, and radius, R_{CRR}, while its direction is opposite to the angular velocity of the connecting rod ${}_JW_{CR}$. The friction moments, ${}_AM_{PtoCR,i}$ are expressed by [25]

$$
{}_AM_{PtoCR,i} = \frac{-T_{CR}^{T}\left(\theta,\phi+\frac{2\pi(i-1)}{9}\right)\cdot {}_J\omega_{CR}\left(\theta,\phi+\frac{2\pi(i-1)}{9}\right)}{\left|{}_J\omega_{CR}\left(\theta,\phi+\frac{2\pi(i-1)}{9}\right)\right|} \qquad \textbf{(3.292)}
$$

$$
R_{CRR}\mu_{CRR,i}\sqrt{F_{PtoCR,ix}^2+F_{PtoCR,iy}^2+F_{PtoCR,iz}^2}, \quad \text{i = 1, 2, ..., 9}
$$

Where i = 1, 2… 9 and j = 0, 1… 8

As before, the friction coefficients are expressed as

$$
\mu_{CRR,i} = \begin{cases} -0.0716V_{CRR,i}+0.0905 & 0 \le V_{CRR,i} < 0.7 \\ 0.04038 & V_{CRR,i} \ge 0.7 \end{cases} \qquad \textbf{(3.293)}
$$

Where

$$
V_{CRR,i} = R_{CRR}\left|{}_J\omega_{CR}\left(\theta,\phi+\frac{2\pi(i-1)}{9}\right)\right|, \text{i} = 1, 2, \ldots 9 \qquad \textbf{(3.294)}
$$

$V_{CRR,i}$ is the absolute value of the sliding velocity at the surface of contact between the piston and the right end of connecting rod.

3.7.3 Equations of motion of the connecting rods

Applying Newton's second law along the three inertial coordinates, yields

$$ {}_{A}W_{CR} + {}_{A}F_{MStoCR,i} + {}_{A}F_{PtoCR,i} - M_{CR}\,{}_{A}a_{CR}\left(\theta,\phi+\frac{2\pi(i-1)}{9}\right) = 0,\quad i = 1,\ 2,\ \ldots 9 \qquad \textbf{(3.295)} $$

3.8 Dynamic Analysis of the Valve Plate-Yoke Assembly

Attach a coordinate system $h_1h_2h_3$ to the valve plate at the axis of rotation of the yoke. "$h_1h_2h_3$" is obtained by rotating "$a_1a_2a_3$" about "a_1" by an angle of θ:

$$ T_{vp} = \begin{bmatrix} 1 & 0 & 0 \\ 0 & \cos\theta & \sin\theta \\ 0 & -\sin\theta & \cos\theta \end{bmatrix} \qquad \textbf{(3.296)} $$

The angular velocity and angular acceleration of the valve plate is given by

$$ {}_{H}\omega_{vp} = \begin{bmatrix} \dot{\theta} & 0 & 0 \end{bmatrix}^{T} \qquad \textbf{(3.297)} $$

$$ {}_{H}\alpha_{vp} = \begin{bmatrix} \ddot{\theta} & 0 & 0 \end{bmatrix}^{T} \qquad \textbf{(3.298)} $$

The origin of the "H" frame is located at the center of rotation of the yoke. Therefore, with reference to Figure 3-9 the position vector of the CG of the valve plate-yoke assembly is given by

$$ {}_{H}r_{vp} = \begin{bmatrix} r_{vpx} & 0 & r_{vpz} \end{bmatrix}^{T} \qquad \textbf{(3.299)} $$

The velocity and acceleration of the valve plate CG are given by

$$ {}_{H}V_{vp} = {}_{H}\omega_{vp} \times {}_{H}r_{vp} = \dot{\theta}\begin{bmatrix} 0 & -r_{vpz} & 0 \end{bmatrix}^{T} \qquad \textbf{(3.300)} $$

$$ {}_{H}a_{vp} = -r_{vpz}\begin{bmatrix} 0 & \ddot{\theta} & \dot{\theta}^2 \end{bmatrix}^{T} \qquad \textbf{(3.301)} $$

Figure 3-28 shows the forces acting on the FBD of the valve plate-yoke assembly that include:

1. The reaction forces at the axis of rotation of the yoke at points 67 and 68 and their respective position vectors given by

$$ {}_{A}F_{CtoY67} = \begin{bmatrix} F_{CtoY67x} & F_{CtoY67y} & F_{CtoY67z} \end{bmatrix}^{T} \quad \textbf{(3.302)} $$

$$ {}_{A}r_{CtoY67} = \begin{bmatrix} -r_{CtoY67x} & 0 & 0 \end{bmatrix}^{T} \quad \textbf{(3.303)} $$

$$ {}_{A}F_{CtoY68} = \begin{bmatrix} 0 & F_{CtoY68y} & F_{CtoY68z} \end{bmatrix}^{T} \quad \textbf{(3.304)} $$

$$ {}_{A}\mathrm{r}_{CtoY68} = -{}_{A}\mathrm{r}_{CtoY67} \quad \textbf{(3.305)} $$

2. The friction moments at the axis of the yoke at points 67 and 68 given by

$$ {}_{A}M_{CtoY67} = M_{CtoY67x} \begin{bmatrix} -sign({}_{H}\omega_{vp}[1]) & 0 & 0 \end{bmatrix}^{T} \quad \textbf{(3.306)} $$

$$ {}_{A}M_{CtoY68} = M_{CtoY68x} \begin{bmatrix} -sign({}_{H}\omega_{vp}[1]) & 0 & 0 \end{bmatrix}^{T} \quad \textbf{(3.307)} $$

The derivation of equations for these moments is shown in the next section.

3. The reaction force from the actuating link at point 66 and its respective position vector as measured from the yoke axis of rotation. This force has two components: one is parallel to the actuating link and the other is normal to it.

$$ {}_{A}F_{ACtoY66} = \begin{bmatrix} 0 \\ F_{ACtoY66P}\sin(\varepsilon-\gamma_8) + F_{ACtoY66N}\cos(\varepsilon-\gamma_8) \\ F_{ACtoY66P}\cos(\varepsilon-\gamma_8) - F_{ACtoY66N}\sin(\varepsilon-\gamma_8) \end{bmatrix} \quad \textbf{(3.308)} $$

$$ {}_{H}r_{ACtoY66} = \begin{bmatrix} r_{ACtoY66x} & r_{ACtoY66y} & r_{ACtoY66z} \end{bmatrix}^{T} \quad \textbf{(3.309)} $$

4. The frictional moment from the actuating link at point 66:

$$ {}_{A}M_{ACtoY66} = M_{ACtoY66x} \begin{bmatrix} -sign({}_{A}\omega_{AC}[1]) & 0 & 0 \end{bmatrix}^{T} \quad \textbf{(3.310)} $$

The derivation of equations for these moments is shown in the next section.

5. The reaction forces from the needle bearings at the end of the barrel at point 58, which are denoted as $-{}_{D}\mathrm{F}_{B3FtoB}$ and $-{}_{D}\mathrm{F}_{B3StoB}$. The bearings are fixed to the valve

plate. The corresponding position vector as observed from the yoke axis of rotation denoted as ${}_{D}r_{B3FtoB}$ and ${}_{D}r_{B3StoB}$.

6. The frictional moment form the needle bearings at point 58 denoted as $-{}_{D}M_{B3FtoB}$ and $-{}_{D}M_{B3StoB}$.
7. The weight of the valve plate - yoke assembly given by

$$ {}_{A}W_{vp} = \begin{bmatrix} 0 & M_{vp}\, g & 0 \end{bmatrix}^{T} \tag{3.311} $$

8. The reaction force from the thrust ball bearing at the end of the barrel at point 65, denoted by $-{}_{D}F_{B4toB}$:

$$ {}_{D}F_{B4toB} = \begin{bmatrix} 0 & 0 & F_{B4toBz} \end{bmatrix}^{T} \tag{3.312} $$

9. The frictional moment at the thrust ball bearing (point 65) denoted by $-{}_{D}M_{B4toB}$.
10. The hydrodynamic forces: $-{}_{H}F_{VPtoBoutD}$, $-{}_{H}F_{VPtoBinD}$, $-{}_{H}F_{VPtoBinS}$, and $-{}_{H}F_{VPtoBoutS}$ due to the oil film between the valve plate and the barrel at points 59, 60, 61, and 62 respectively.
11. The frictional moment due to the fluid film between the barrel and the valve plate denoted as $-{}_{D}M_{VPtoB}$
12. The reaction forces between the discharge/suction port of the valve plate and the solid area located between each successive cylinder at points 69 to 77 respectively.

$$ {}_{D}F_{BStoVP,i} = \left[0 \quad 0 \quad P_b\left(\phi + \frac{2\pi(i\text{-}1)}{9}\right) A_s\left(\phi + \frac{2\pi(i\text{-}1)}{9}\right) \right]^{T}, \quad i = 1,2,\ldots 9 \tag{3.313} $$

Where $P_b = P_D$ or P_S depending on the angular position (ϕ)

Section 3.7.1 presents the derivations of the equations of $A_{s,i}$, which depends on the main shaft angular position (ϕ).

13. The reaction force from the fluid inside the hose between the LPA and the suction exit at the yoke axis of rotation at point 78. This force as well as its position vector can be expressed as

$$ {}_{A}F_{LPAtoY78} = P_S A_{78} \begin{bmatrix} 0 & -\sin\theta_L & \cos\theta_L \end{bmatrix}^T \quad \textbf{(3.314)} $$

$$ {}_{A}r_{LPAtoY78} = \begin{bmatrix} -r_{LPAtoY78x} & 0 & 0 \end{bmatrix}^T \quad \textbf{(3.315)} $$

14. The reaction force from the fluid inside the hose between the HPA and the discharge exit at the yoke axis of rotation at point 79. This force as well as its position vector can be expressed as

$$ {}_{A}FL_{HPAtoY79} = P_D A_{78} \begin{bmatrix} 0 & -\sin\theta_L & \cos\theta_L \end{bmatrix}^T \quad \textbf{(3.316)} $$

$$ {}_{A}\mathrm{r}_{HPAtoY79} = - {}_{A}\mathrm{r}_{LPAtoY78} \quad \textbf{(3.317)} $$

15. The force due to the pressure on the discharge or suction orifice at points 80 to 88 as well as its position vector can be expressed as

$$ {}_{D}\mathrm{F}_{OILtoVP,i} = \left[0 \quad 0 \quad \mathrm{P_b}\left(\phi + \frac{2\pi(\mathrm{i}-1)}{9} \right) \mathrm{A_r}\left(\phi + \frac{2\pi(\mathrm{i}-1)}{9} \right) \right]^T, \quad i = 1, 2, \ldots 9 \quad \textbf{(3.318)} $$

$$ {}_{D}r_{OILtoVP} = \begin{bmatrix} 0 & -r & L_{YtoVP} \end{bmatrix}^T \quad \textbf{(3.319)} $$

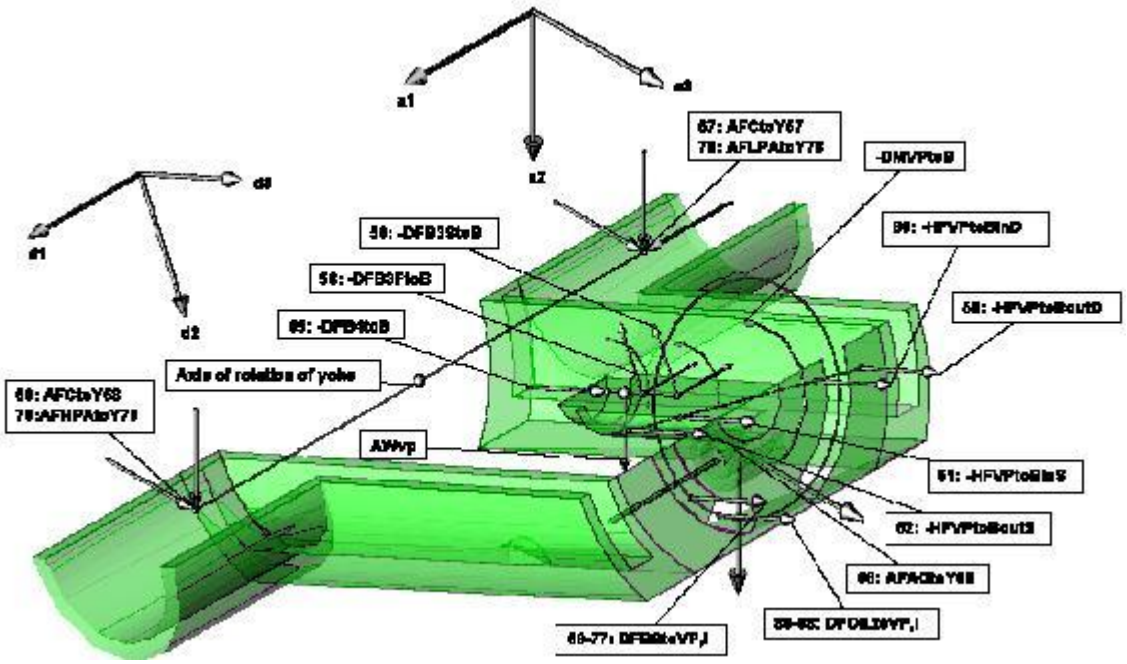

Figure 3-28: FBD of the valve plate-yoke assembly

3.8.1 The frictional moments at the axis of the yoke

The value of the frictional moments components at the axis of the yoke at points 67 and 68 are expressed as

$$M_{CtoY67x} = \mu_Y r_Y \sqrt{F_{CtoY67y}^2 + F_{CtoY67z}^2} \tag{3.320}$$

$$M_{CtoY68x} = \mu_Y r_Y \sqrt{F_{CtoY68y}^2 + F_{CtoY68z}^2} \tag{3.321}$$

μ_Y = the friction coefficient at the right/left pins of the yoke

r_Y = radius of pin of the yoke

3.8.2 The frictional moments at the common axis between the yoke and actuating link

The value of the frictional moment component at the common axis of the yoke and actuating link at points 66 is expressed as

$$M_{ACtoY66x} = \mu_{ACtoY} r_{AC} \sqrt{F_{ACtoY66y}^2 + F_{ACtoY66z}^2} \quad \textbf{(3.322)}$$

μ_{ACtoY} = the friction coefficient at the pin between the yoke and the actuating link

r_{AC} = radius of pin between the yoke and the actuating link

3.8.3 Solid area between two successive cylinders

Figure 3-29 shows the regions of solid area between successive cylinders. There are 12 regions. In regions one and seven, the solid area between successive cylinders coincides with the land between the suction and discharge ports. In regions 2 to 6, the solid area between successive cylinders is under suction pressure. In regions 8 to 12, the solid areas between successive cylinders are under discharge pressure. The solid areas between successive cylinders at any angular rotation of the main shaft is shown in and given by

$$\mathrm{A_s} = \sum_{i=1}^{12} \mathrm{A_{s,i}} \left[H\left(\phi - \lambda_i\right) - H\left(\phi - \lambda_{i+1}\right) \right] \quad \textbf{(3.323)}$$

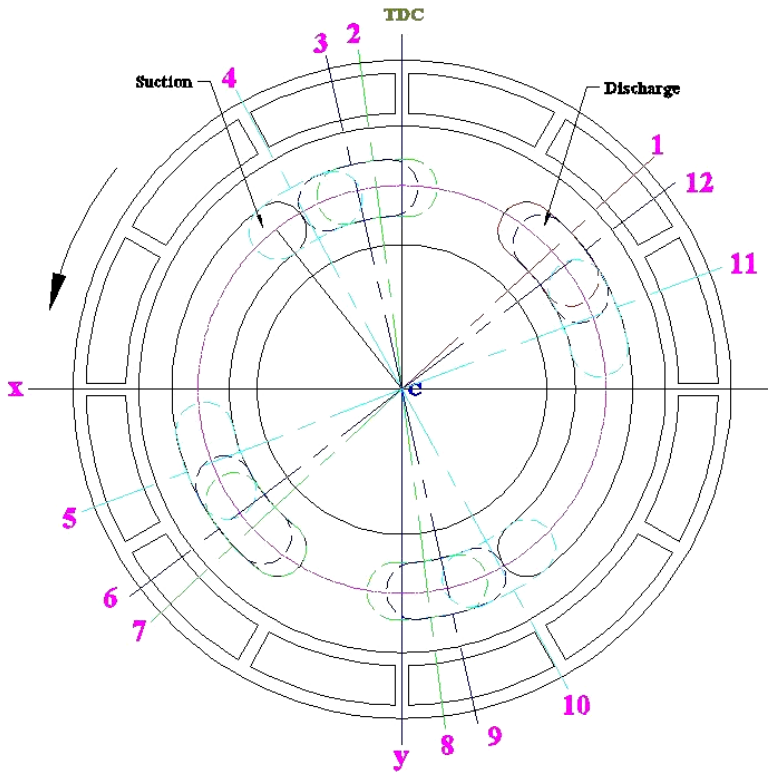

Figure 3-29: Regions of the solid area between successive cylinders

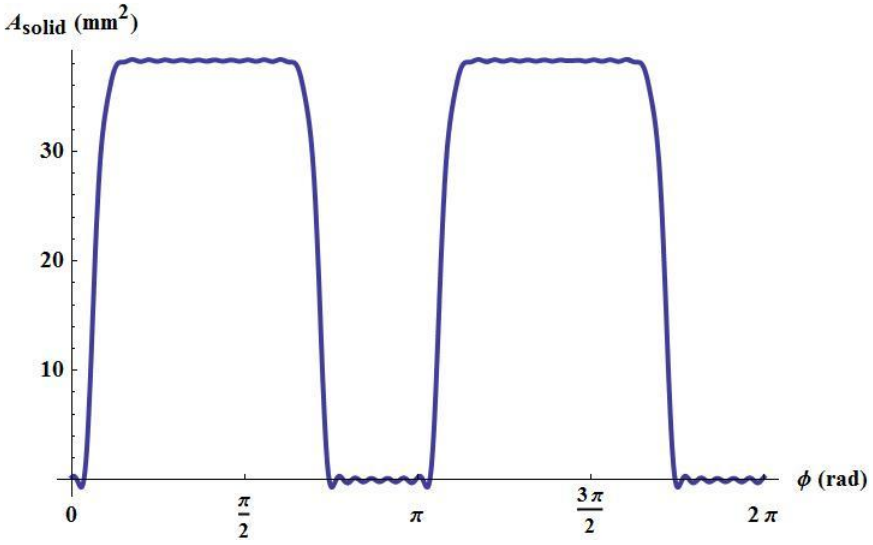

Figure 3-30: Solid area between successive cylinders

Solid area between two successive cylinders for region (1)

Figure 3-31 shows schematic of region 1. Region 1 extends over the angular rotation $\lambda_1 < \phi \leq \lambda_2$. The solid area between the first and second cylinders that is under the suction pressure for region 1 or region 7 is given by

$$A_{s1} = 0 \tag{3.324}$$

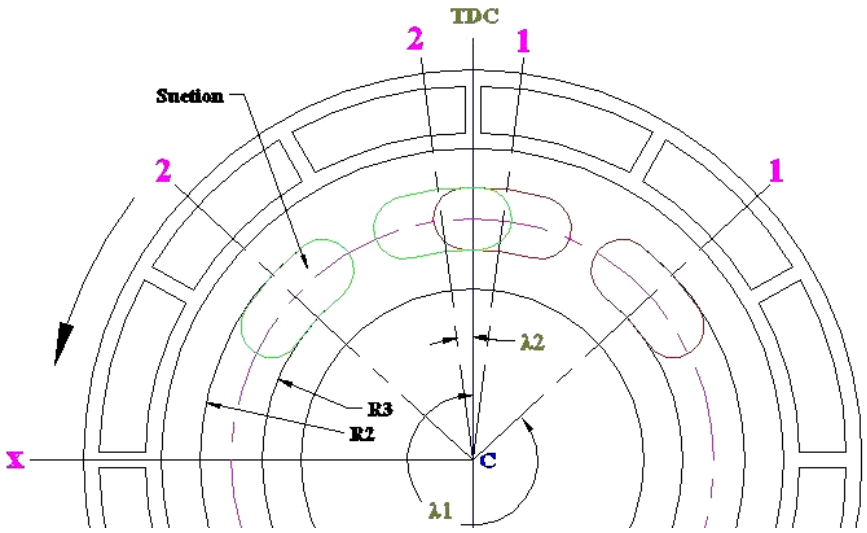

Figure 3-31: Solid area between two successive cylinders for region (1)

Solid area between two successive cylinders for regions (2), (6), (8), and (12)

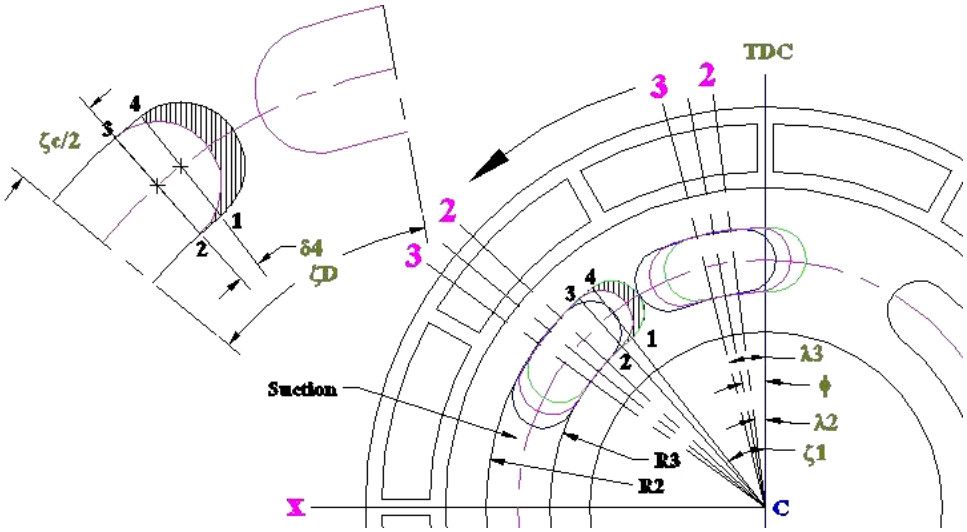

Figure **3-32** shows schematic of region 2. Region 2 extends over the angular range $\lambda_2 < \phi \leq \lambda_3$. The solid area between the first and second cylinders that is under the suction pressure is given by:

$$A_{s2} = \frac{1}{2}\delta_4\left(R_2^2 - R_3^2\right) \tag{3.325}$$

Equation (3.325) applies also to regions (6), (8), and (12) except that δ_4 is different for each region. δ_4 is the angle between lines 1 - 4 and 2 - 3 and is given by

$$\delta_4 = \begin{cases} \phi - \zeta_1 - \frac{\zeta_C}{2} + \zeta_D; & \text{for region (2 \& 3)} \\ \pi - \phi - \zeta_1 - \frac{\zeta_C}{2}; & \text{for region (5 \& 6)} \\ -\phi + \zeta_1 + \frac{\zeta_C}{2} - \zeta_D; & \text{for region (8 \& 9)} \\ \phi + \zeta_1 + \frac{\zeta_C}{2}; & \text{for region (11 \& 12)} \end{cases} \tag{3.326}$$

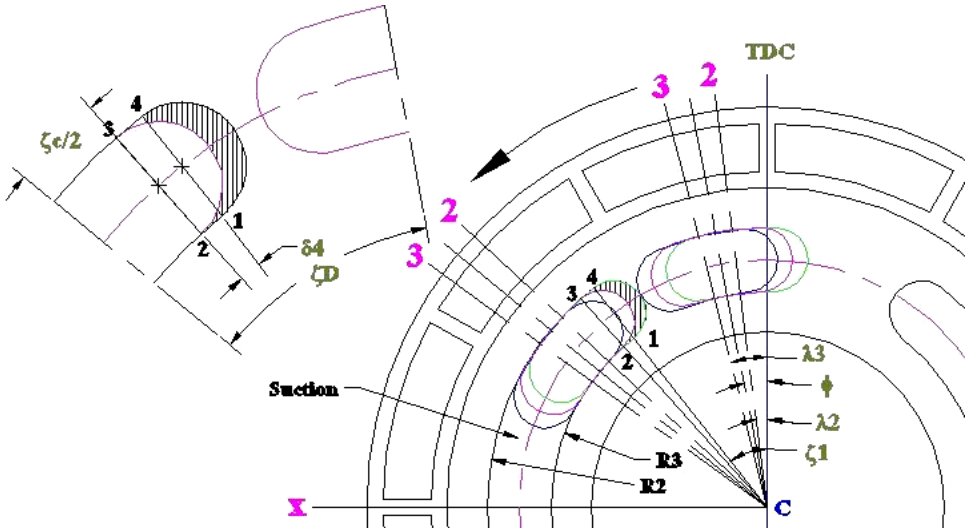

Figure 3-32: Solid area between two successive cylinders for region (2)

Solid area between two successive cylinders for regions (3), (5), (9), and (11)

Figure 3-33 shows schematic of region 3. Region 3 extends over the angular range: $\lambda_3 < \phi \leq \lambda_4$. The solid area between the first and second cylinders that is under the suction pressure is given by

$$A_{s3} = \frac{1}{2}\delta_4\left(R_2^2 - R_3^2\right) - \frac{1}{4}\left(R_2 - R_3\right)^2\left(\delta_1 - \sin\delta_1\right) \tag{3.327}$$

This equation also applies to regions (5), (9), and (11) except that δ_1 and δ_4 are different for each region. δ_4 is given by equation (3.326), while δ_1 is given by

$$\delta_1 = \begin{cases} \sqrt{k_1 + k_2\cos\left(\zeta_1 - \frac{\zeta_c}{2} - \phi\right)}; & \text{for region (3)} \\ \sqrt{k_1 - k_2\cos\left(\zeta_1 - \frac{\zeta_c}{2} + \zeta_D + \phi\right)}; & \text{for region (5)} \\ \sqrt{k_1 - k_2\cos\left(\zeta_1 - \frac{\zeta_c}{2} - \phi\right)}; & \text{for region (9)} \\ \sqrt{k_1 + k_2\cos\left(\zeta_1 - \frac{\zeta_c}{2} + \zeta_D + \phi\right)}; & \text{for region (11)} \end{cases} \tag{3.328}$$

$$k_1 = \frac{R_2^2 - 6R_2R_3 + R_3^2}{2\left(R_2 - R_3\right)^2} \text{ and } k_2 = \frac{\left(R_2 + R_3\right)^2}{2\left(R_2 - R_3\right)^2} \tag{3.329}$$

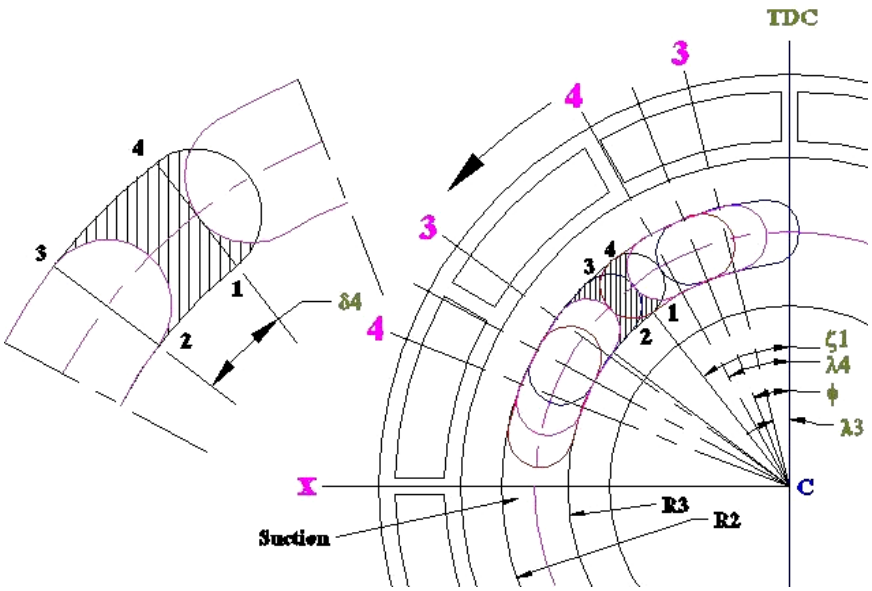

Figure 3-33: Solid area between two successive cylinders for region (3)

Solid area between two successive cylinders for region (4)

Figure 3-34 shows schematic of region 4. Region 4 extends over the angular range $\lambda_4 < \phi \leq \lambda_5$. The solid area between the first and second cylinders that is under the suction pressure for region 4 or region 10 is given by

$$A_{s4} = \frac{1}{2}\left(\zeta_D - \zeta_C\right)\left(R_2^2 - R_3^2\right) - \pi R_k^2 \qquad \textbf{(3.330)}$$

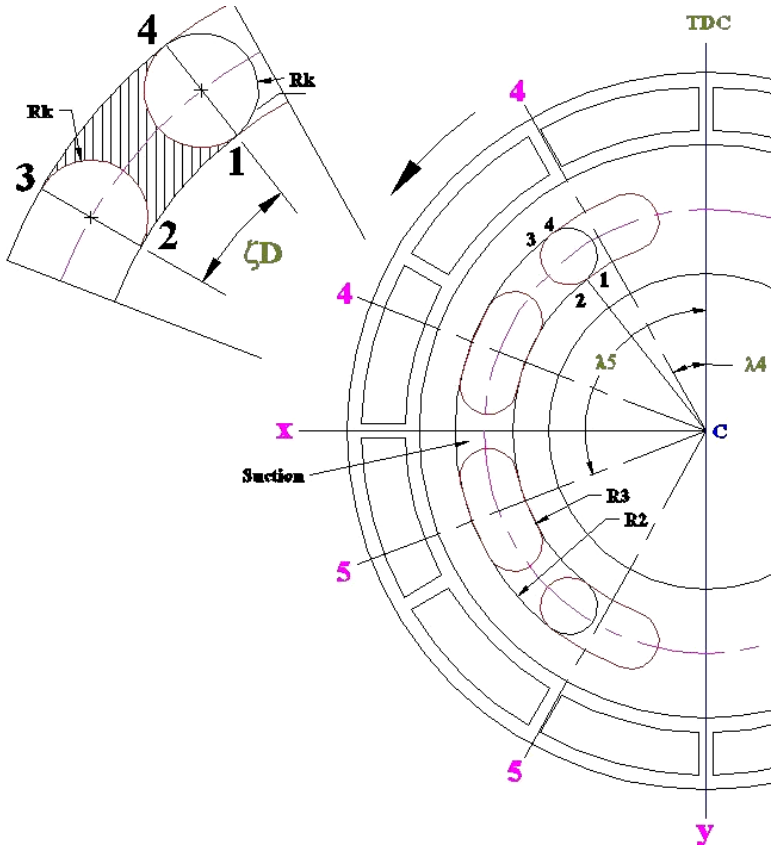

Figure 3-34: Solid area between two successive cylinders for region (4)

3.8.4 Equations of motion of the valve plate-yoke assembly

The sum of all forces on the valve plate-yoke assembly should equal to mass multiplied by acceleration:

$$
\begin{aligned}
&{}_{A}F_{CtoY67} + {}_{A}F_{CtoY68} + {}_{A}F_{ACtoY66} + {}_{A}W_{vp} - T_{vp}^{T}.\left(\begin{array}{l} {}_{H}F_{VPtoBoutD} + {}_{H}F_{VPtoBoutS} \\ + {}_{H}F_{VPtoBinD} + {}_{H}F_{VPtoBinS} \end{array} \right) \\
&-T_{os}^{T}\left(\theta,\phi\right).\left({}_{D}F_{B3FtoB} + {}_{D}F_{B3StoB} + {}_{D}F_{B4toB} \right) + T_{os}^{T}\left(\theta,\phi + \frac{2\pi(i-1)}{9} \right).{}_{D}F_{BStoVP,i} \\
&+ {}_{A}F_{HPAtoY79} + {}_{A}F_{LPAtoY78} + T_{os}^{T}\left(\theta,\phi + \frac{2\pi(i-1)}{9} \right).{}_{D}F_{OILtoVPD,i} - T_{vp}^{T}.(M_{vp}.{}_{H}a_{vp}) = 0 \\
&i=1,\ 2,\ \ldots 9
\end{aligned}
\qquad \textbf{(3.331)}
$$

Summing moments of all forces about point k (axis of rotation of the yoke):

$$
\begin{aligned}
&{}_A r_{CtoY67} \times {}_A F_{CtoY67} + {}_A r_{CtoY68} \times {}_A F_{CtoY68} + {}_A M_{CtoY67} + {}_A M_{CtoY68} \\
&+\left(T_{vp}^T \cdot {}_H r_{ACtoY66}\right) \times {}_A F_{ACtoY66} + {}_A M_{ACtoY66} - T_{os}^T(\theta,\phi).({}_D r_{B3FtoB} \times {}_D F_{B3FtoB}) \\
&- T_{os}^T(\theta,\phi).({}_D r_{B3StoB} \times {}_D F_{B3StoB}) - {}_D M_{B3FtoB} - {}_D M_{B3StoB} \\
&+ (T_{vp}^T \cdot {}_H r_{vp}) \times {}_A W_{vp} - T_{os}^T(\theta,\phi).({}_D r_{B4toB} \times {}_D F_{B4toB}) - {}_D M_{B4toB} \\
&- T_{vp}^T \cdot \begin{pmatrix} {}_H r_{OUTD} \times {}_H F_{VPtoBoutD} + {}_H r_{OUTS} \times {}_H F_{VPtoBoutS} \\ + {}_H r_{IND} \times {}_H F_{VPtoBinD} + {}_H r_{INS} \times {}_H F_{VPtoBinS} \end{pmatrix} + T_{os}^T(\theta,\phi).{}_D M_{VPtoB} \\
&+ T_{os}^T\left(\theta,\phi + \frac{2\pi(i-1)}{9}\right).({}_D r_{BStoVP} \times {}_D F_{BStoVP,i}) + {}_A r_{HPAtoY79} \times {}_A F_{HPAtoY79} \\
&+ {}_A r_{LPAtoY78} \times {}_A F_{LPAtoY78} + T_{os}^T\left(\theta,\phi + \frac{2\pi(i-1)}{9}\right).({}_D r_{OILtoVP,i} \times {}_D F_{OILtoVP,i}) \\
&- T_{vp}^T.({}_H r_{vp} \times (M_{vp} \cdot {}_H a_{vp})) - T_{vp}^T.({}_H I_{vp} \cdot {}_H \alpha_{vp}) = 0
\end{aligned}
\tag{3.332}
$$

3.9 Dynamic Analysis of the Yoke-Displacement Mechanism

The yoke rotates through an angle of θ by the aid of a slider crank mechanism as shown in Figure 3-35. The ram moves with a translational motion, with position given by

$$
\begin{aligned}
x = {} & L_3\left(\cos(\varepsilon+\gamma_5) - \cos(\varepsilon+\gamma_5+\theta)\right) \\
& + \sqrt{L_{ac}^2 - \left(L_4 - L_3\sin(\varepsilon+\gamma_5+\theta)\right)^2} - \sqrt{L_{ac}^2 - \left(L_4 - L_3\sin(\varepsilon+\gamma_5)\right)^2}
\end{aligned}
\tag{3.333}
$$

L_3 = the radius of rotation of the yoke

L_{ac} = length of the actuating link

The velocity and acceleration of the ram in vector form is given by

$$
{}_A V_{RAM} = -\dot{x}\begin{bmatrix} 0 & \sin\varepsilon & \cos\varepsilon \end{bmatrix}^T \tag{3.334}
$$

$$
{}_A a_{RAM} = \frac{d}{dt}\,{}_A V_{RAM} = {}_A a_{RAM} = -\ddot{x}\begin{bmatrix} 0 & \sin\varepsilon & \cos\varepsilon \end{bmatrix}^T \tag{3.335}
$$

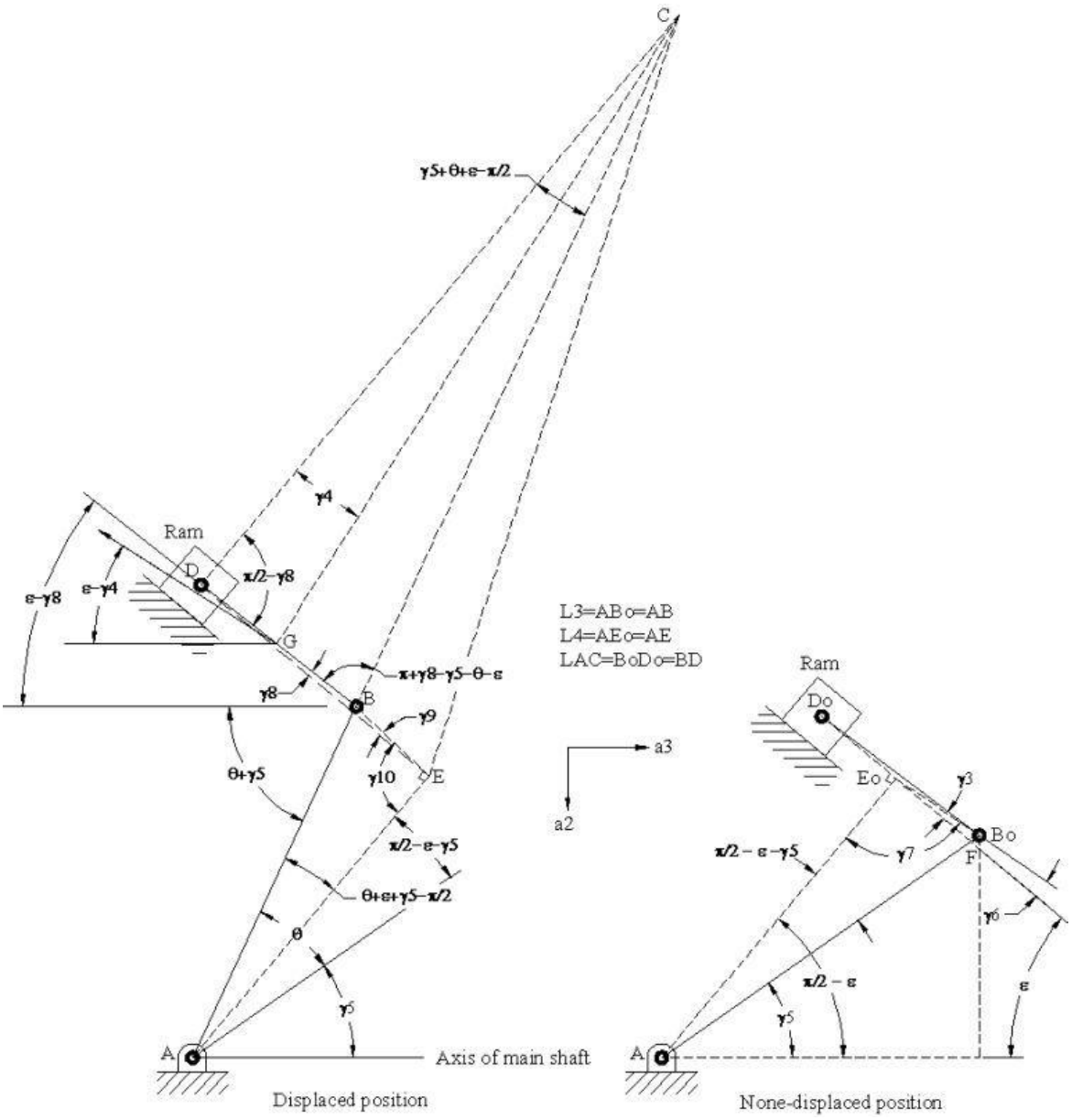

Figure 3-35: Geometric parameters of the displacement mechanism

The angular velocity of the actuating link is determined using the instant center method as shown in Figure 3-35:

$$ {}_A\omega_{AC} = \frac{\dot{x}}{CD}\begin{bmatrix} -1 & 0 & 0 \end{bmatrix}^T \tag{3.336} $$

$$CD = -\sqrt{L_{ac}^2 - \left(L_4 - L_3 \sin\left(\gamma_5 + \varepsilon + \theta\right)\right)^2}\tan\left(\gamma_5 + \varepsilon + \theta\right) - \left(L_4 - L_3 \sin\left(\gamma_5 + \varepsilon + \theta\right)\right) \quad \textbf{(3.337)}$$

The angular acceleration of the actuating link is given by

$$_A\alpha_{AC} = \frac{d}{dt}\,{}_A\omega_{AC} \quad \textbf{(3.338)}$$

The distance from the center of gravity of the actuating link to the instant center is given by

$$CG = \sqrt{DG^2 + CD^2 - 2DG.CD.\cos\left(\frac{\pi}{2} - \gamma_8\right)} \quad \textbf{(3.339)}$$

$$\gamma_8 = -\sin^{-1}\frac{L_4 - L_3\sin(\varepsilon + \gamma_5 + \theta)}{L_{ac}} \quad \textbf{(3.340)}$$

The velocity of the center of gravity of the actuating link is given by

$$\gamma_4 = \sin^{-1}\left\{\frac{DG}{CG}\cos\left(\gamma_8\right)\right\} \quad \textbf{(3.341)}$$

$$_AV_{AC} = {}_A\omega_{AC}.CG\begin{bmatrix}0 & -\sin(\varepsilon - \gamma_4) & -\cos(\varepsilon - \gamma_4)\end{bmatrix}^T \quad \textbf{(3.342)}$$

The acceleration of the center of gravity of the actuating link is given by

$$_Aa_{AC} = \frac{d}{dt}\,{}_AV_{AC} \quad \textbf{(3.343)}$$

Figure 3-36 shows the forces acting on FBD of the actuating link that include:

1. The reaction force from the pin of the ram at point 90. This forces as well as its respective position vector as measured from the axis of rotation of the yoke are given by

$$_AF_{RAMtoAC90} = \begin{bmatrix} 0 \\ F_{RAMtoAC90z}\sin(\varepsilon - \gamma_8) + F_{RAMtoAC90y}\cos(\varepsilon - \gamma_8) \\ F_{RAMtoAC90z}\cos(\varepsilon - \gamma_8) - F_{RAMtoAC90y}\sin(\varepsilon - \gamma_8) \end{bmatrix} \quad \textbf{(3.344)}$$

$$ {}_{A}r_{RAMtoAC90} = \begin{bmatrix} 0 \\ -L_3 \sin(\theta+\gamma_5) - L_{ac} \sin(\varepsilon-\gamma_8) \\ L_3 \cos(\theta+\gamma_5) - L_{ac} \cos(\varepsilon-\gamma_8) \end{bmatrix} \quad \textbf{(3.345)} $$

2. The reaction from the yoke at point 66 denoted as - ${}_{A}F_{ACtoY66}$. The respective position vector is given by

$$ {}_{A}r_{ACtoY66} = T^{T}_{vp} \cdot_{H} r_{ACtoY66} \quad \textbf{(3.346)} $$

3. The frictional moment from the yoke at point 66 denoted as - ${}_{A}M_{ACtoY66}$

4. The weight of the actuating link and its corresponding position vector as measured from the yoke axis of rotation are given by

$$ {}_{A}W_{AC} = \begin{bmatrix} 0 & M_{AC}\, g & 0 \end{bmatrix}^{T} \quad \textbf{(3.347)} $$

$$ {}_{A}r_{WAC} = \begin{bmatrix} 0 \\ -L_3 \sin\left(\theta+\gamma_5\right) - \left(L_{ac} - DG\right) \sin\left(\varepsilon-\gamma_8\right) \\ L_3 \cos\left(\theta+\gamma_5\right) - \left(L_{ac} - DG\right) \cos\left(\varepsilon-\gamma_8\right) \end{bmatrix} \quad \textbf{(3.348)} $$

Force balance of the actuating link

$$ {}_{A}F_{RAMtoAC90} - {}_{A}F_{ACtoY66} + {}_{A}W_{AC} - M_{AC}.a_{AC} = 0 \quad \textbf{(3.349)} $$

Sum of moments about center of rotation of the yoke (point A) is given by

$$ \begin{aligned} &{}_{A}r_{RAMtoAC90} \times {}_{A}F_{RAMtoAC90} - {}_{A}r_{ACtoY66} \times_{A} F_{ACtoY66} + {}_{A}r_{WAC} \times_{A} W_{AC} \\ &- {}_{A}M_{ACtoY66} - {}_{A}r_{WAC} \times M_{AC} \cdot {}_{A}a_{AC} - {}_{A}I_{AC} \cdot {}_{A}\alpha_{AC} = 0 \end{aligned} \quad \textbf{(3.350)} $$

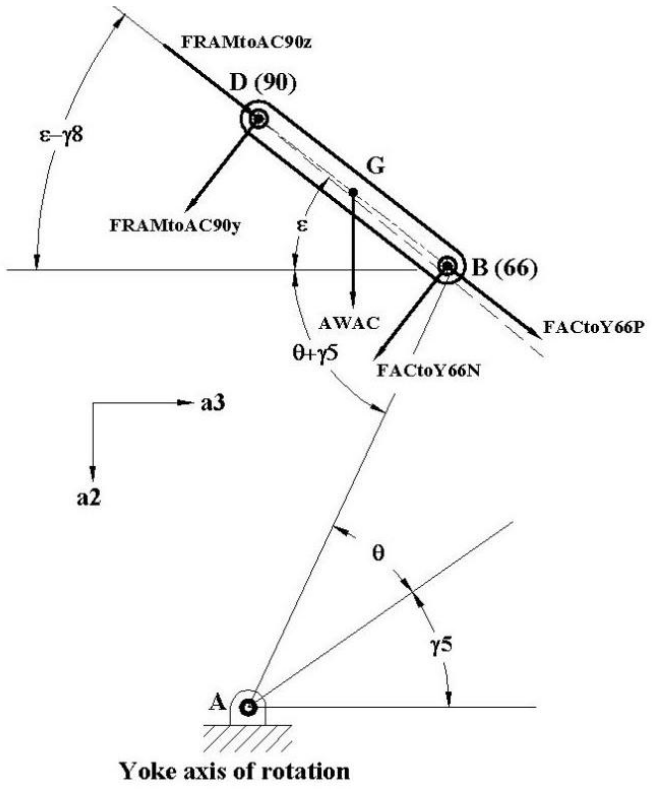

Figure 3-36: FBD of the actuating link

Figure 3-37 shows the forces acting on the FBD of the ram that include:

1. The reaction force from the pin between the ram and the actuating link at point 90 denoted as - ${}_{A}F_{RAMtoAC90}$.
2. The reaction force from the ram cylinder interface at point 90 and is expressed as

$$ {}_{A}F_{CtoRAM\,90} = \begin{bmatrix} 0 \\ \mu_{CtoRAM\,90} N_{CtoRAM\,90} \sin\varepsilon - N_{CtoRAM\,90} \cos\varepsilon \\ \mu_{CtoRAM\,90} N_{CtoRAM\,90} \cos\varepsilon + N_{CtoRAM\,90} \sin\varepsilon \end{bmatrix} \quad \textbf{(3.351)} $$

3. The weight of the ram is given by

$$ {}_{A}W_{RAM} = \begin{bmatrix} 0 & M_{RAM}\ g & 0 \end{bmatrix}^{T} \quad \textbf{(3.352)} $$

4. The cylinder pressure force on the ram and is given by

$$ {}_{A}F_{PtoRAM} = P_{RAM} A_{RAM} \begin{bmatrix} 0 & \sin\varepsilon & \cos\varepsilon \end{bmatrix}^{T} \quad \textbf{(3.353)} $$

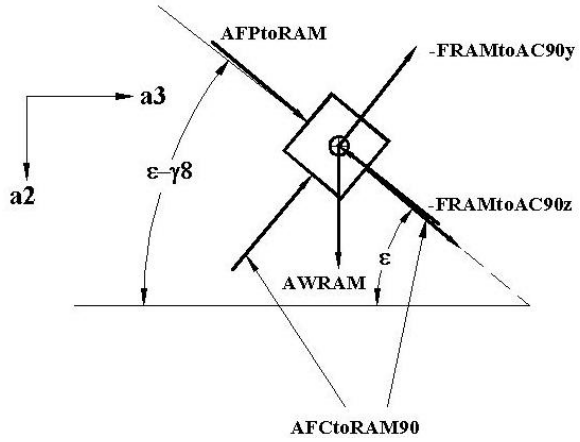

Figure 3-37: FBD of the ram

Force balance of the ram

$$-_A F_{RAMtoAC90} +_A F_{CtoRAM90} +_A W_{RAM} +_A F_{PtoRAM} - M_{RAM} \cdot_A a_{RAM} = 0 \quad \textbf{(3.354)}$$

3.10 Summary of the Theoretical Analysis

This chapter presented the mathematical derivations of the equations of motion of the parts of the pump. In the process of developing these equations, hydrodynamic analysis was introduced at the pistons. The hydrodynamic analysis at the pistons of the pump resulted in differential equations that relate cylinder pressures and flow rates to the geometric parameters of the pump, the physical properties of the hydraulic oil, and the thermodynamic states of the nitrogen gas in the HPA and LPA. In addition, the hydrodynamic forces acting at the interface between the barrel and the valve plate were determined by defining and deriving the differential equations governing the oil film at the interface.

In the next chapter, the equations of motion of the parts, the differential equations of the piston pressure, and the hydrodynamic force will be solved numerically using Mathematica^{TM} software.

CHAPTER 4: NUMERICAL SOLUTION AND SIMULATION OF THE MATHEMATICAL MODEL

The theoretical model is created using Mathematica^{TM} and is examined against well know conditions of the rotation of the main shaft and the yoke. It is also compared against experimental data that is created by the Environmental Protection Agency. The geometric data of an actual variable displacement pump was used. The technical data of the actual pump under consideration and the results of the experimental testing are not shown here because it is propriety of the Environmental Protection Agency and we do not get permission to release such data.

4.1 Kinematics of the Pump Components

The kinematic model is compared against a CAD model created using ADAMS/View software. This study considers two cases. In the first case, the yoke has no angular rotation while the main shaft angular motion is a function of time. In the second case, the yoke has a fixed angular position while the main shaft rotates at a constant angular velocity.

Case 1: Yoke angle of zero degrees

Because the yoke is not displaced, all the parts except the pistons and the connecting rods are in pure rotation with velocities and accelerations as given in Table 4-1. The yoke and the displacement mechanism are stationary. If the pitch radius R at the main shaft side

and the pitch radius r at the barrel side are the same, then the velocities and accelerations of the pistons and the connecting rods are the same. The main shaft, the first and second intermediate shafts, the first and second crosses, the barrel, the pistons, and the connecting rods have the same angular velocity and angular acceleration as given by Eq. (3.12) and Eq. (3.13). In addition, the pistons do not move with respect to the barrel.

Table 4-1: Parameters of the pump for a yoke angle of zero degrees

${}_A a_{CR}(\theta, \phi)$	$\left(R+\frac{(r-R)r_{CR}}{L_{CR}}\right)\begin{bmatrix}\ddot{\phi}\cos\phi-\dot{\phi}^2\sin\phi\\ \ddot{\phi}\sin\phi+\dot{\phi}^2\cos\phi\\ 0\end{bmatrix}$
${}_A a_p$	$r\begin{bmatrix}\ddot{\phi}\cos\phi-\dot{\phi}^2\sin\phi\\ \ddot{\phi}\sin\phi+\dot{\phi}^2\cos\phi\\ 0\end{bmatrix}$
${}_A V_p$	$\dot{\phi}r\begin{bmatrix}\cos\phi & \sin\phi & 0\end{bmatrix}^T$
${}_A V_{CR}(\theta, \phi)$	$\dot{\phi}\left(R+\frac{(r-R)r_{CR}}{L_{CR}}\right)\begin{bmatrix}\cos\phi & \sin\phi & 0\end{bmatrix}^T$

Case 2: Fixed yoke angle and constant angular velocity of the main shaft

In this case, the main shaft rotates at a constant angular velocity of 1500 rpm while the yoke is kept at 30°. Therefore, one complete revolution of the main shaft is equivalent to 0.04 seconds of time.

The intermediate shaft has one angular velocity component along its longitudinal axes "c_3". As can be seen from Figure 4-1, the angular velocity of the intermediate shaft oscillates between 1449 rpm and 1553 rpm with an average value of around 1500 rpm every half a revolution of the main shaft.

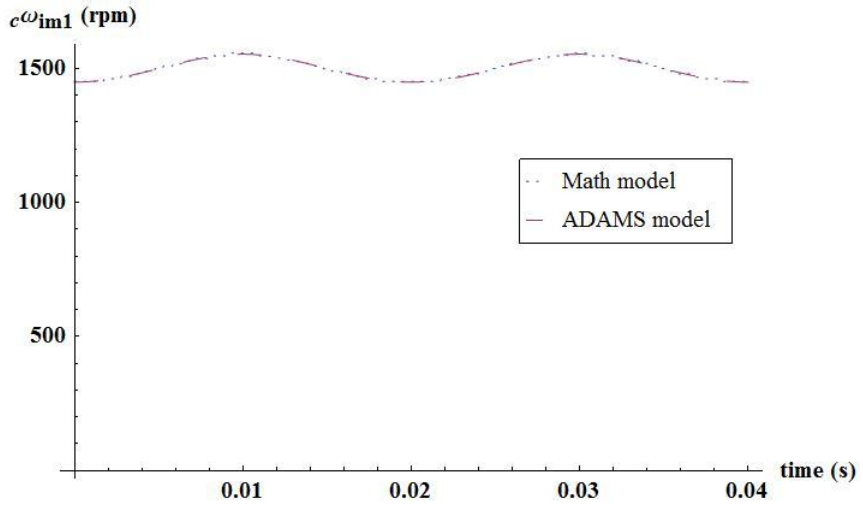

Figure 4-1: Angular velocity of the intermediate shaft (Case 2)

Observing the intermediate shaft from the inertial coordinate system, the intermediate shaft has two components of angular acceleration. One component is along the "a_2" direction as can be seen from Figure 4-2, and oscillates between - 442 and 442 rad/s^2 every half revolution of the main shaft.

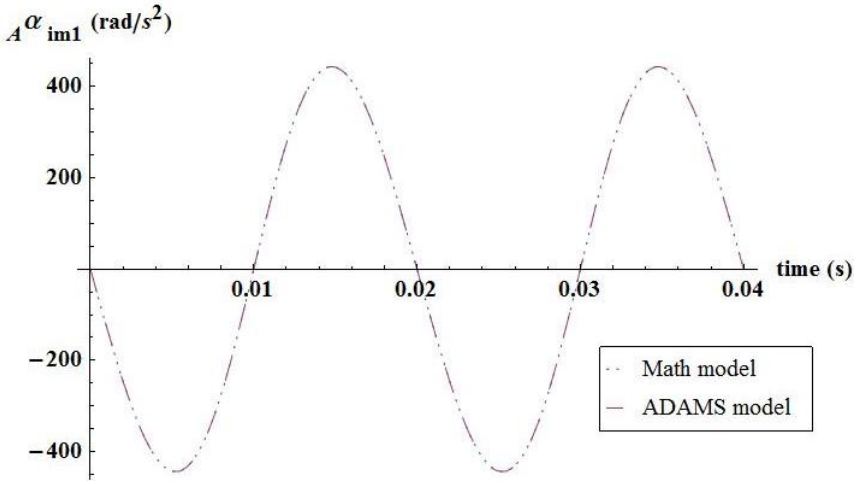

Figure 4-2: Angular acceleration of the intermediate shaft along the "a_2" direction (case-2)

The component of the angular acceleration of the intermediate shaft along the "a_3" direction is shown in Figure 4-3. This component fluctuates between - 1650 rad/s^2 and 1650 rad/s^2 for each revolution of the main shaft.

Both the translational velocity and acceleration of the intermediate shaft are zero since it undergoes pure rotation.

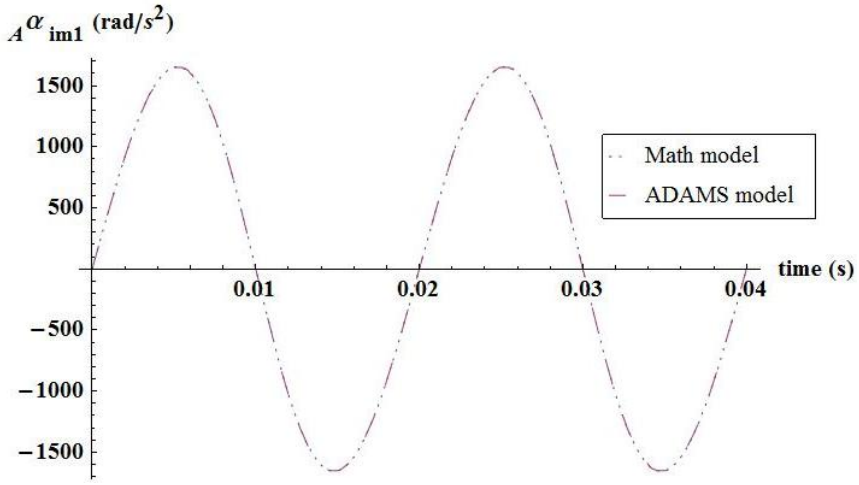

Figure 4-3: Angular acceleration of the intermediate shaft along the "a_3" direction (case-2)

Figure 4-4 shows that the variation of the angular velocity component along the "a_1" direction of the first cross for a complete revolution of the main shaft. The "a_1" component varies smoothly from zero at $\phi = 0$ to - 194 rpm at $\phi = \pi/4$ to 0 at $\phi = \pi/2$ to 194 rpm at $\phi = 3\pi/4$ and back to zero at $\phi = \pi$ in half a revolution.

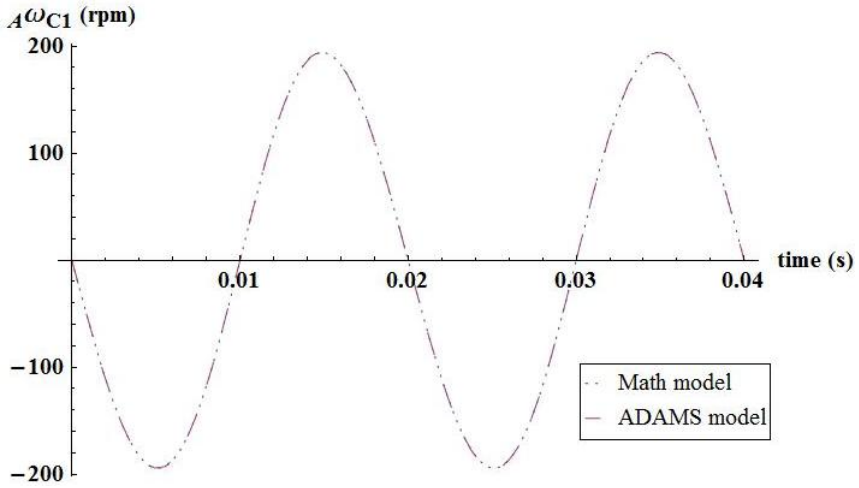

Figure 4-4: Angular velocity component of the first cross along the "a_1" direction of the CVJ (case 2)

The "a_2" component shown in Figure 4-5 varies between 0 and - 402 rpm. In addition, the "a_3" has a constant value of 1500 rpm as shown in Figure 4-6.

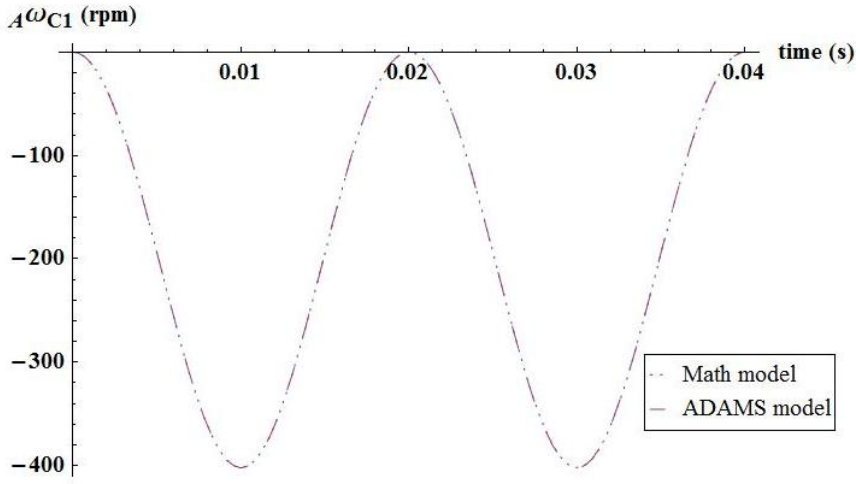

Figure 4-5: Angular velocity component of the first cross along the "a_2" direction of the CVJ (case 2)

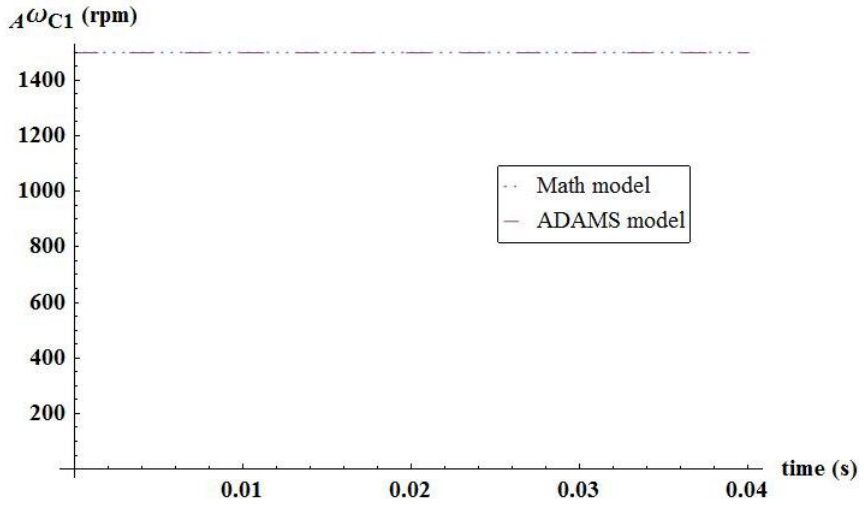

Figure 4-6: Angular velocity component of the first cross along the "a_3" direction of the CVJ (case 2)

With reference to Figure 4-7 the angular acceleration component of the first cross along the "a_1" direction changes sinusoidally between - 6170 to 6170 rad/s^2 in half a revolution of the main shaft. The "a_2" component varies between - 6600 and 6600 every half revolution. There is no acceleration component along the "a_3" direction.

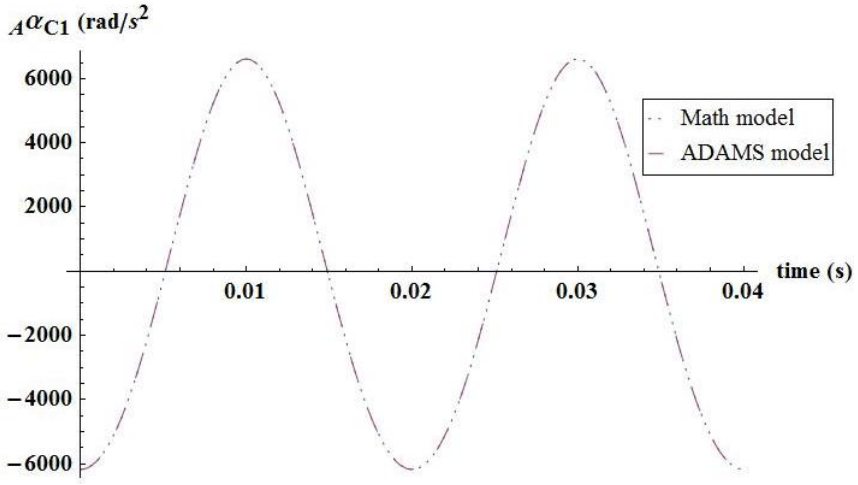

Figure 4-7: Angular acceleration component along the "a_1" direction of the first cross of CVJ (case 2)

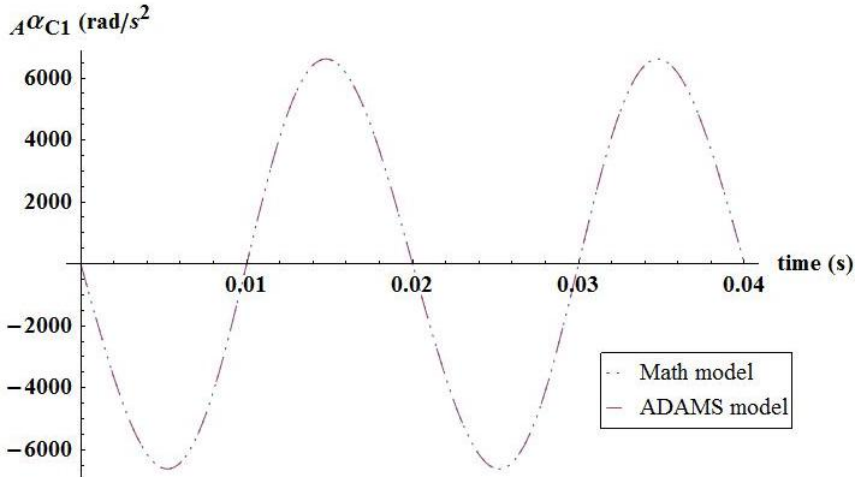

Figure 4-8: Angular acceleration component along the "a_2" direction of the first cross of CVJ (case 2)

The angular rotation of the barrel around its axis of rotation is the same as the angular rotation of the main shaft.

Figure 4-9 to Figure 4-11 show the angular velocity components of the second cross. Comparing Figure 4-4 with Figure 4-9, one can notice that the angular velocity component along the "a_1" direction of the first cross is canceled out by that of the second cross. The component along the "a_2" direction varies between - 750 and - 402 rpm in a sinusoidal manner. In addition, the "a_3" component fluctuates between 1299 and 1499 rpm.

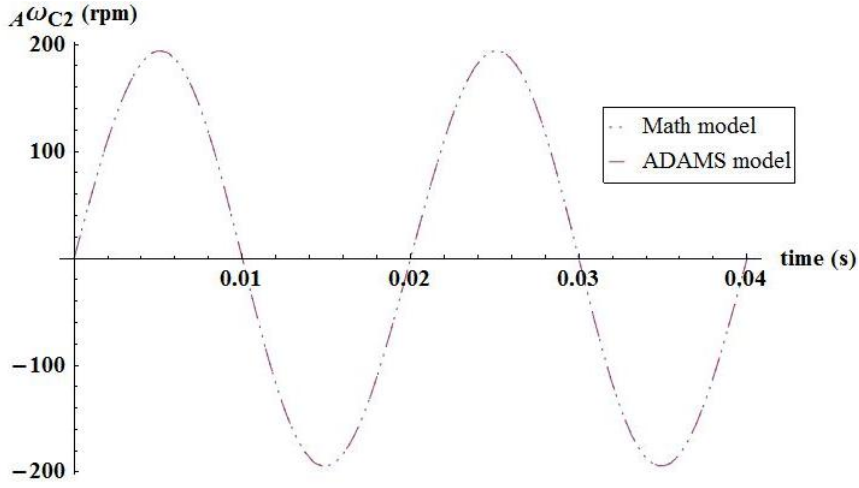

Figure 4-9: Angular velocity component along the "a_1" direction of the second cross of CVJ (case 2)

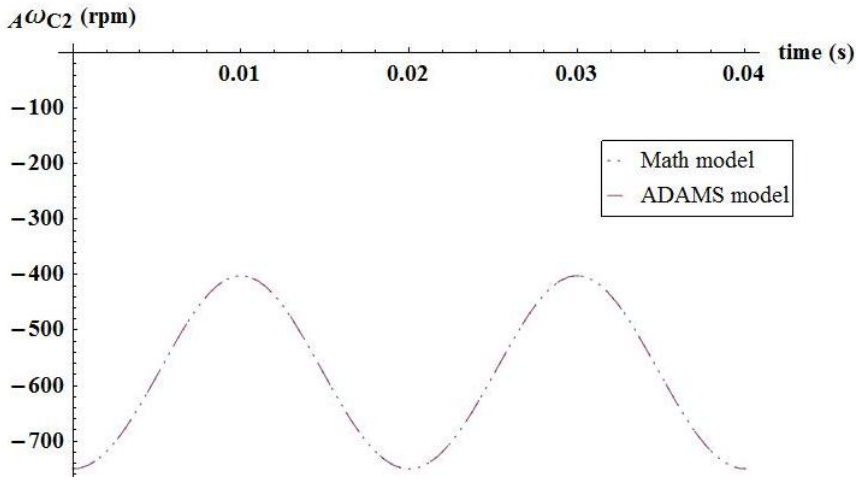

Figure 4-10: Angular velocity component along the "a_2" direction of the second cross of CVJ (case 2)

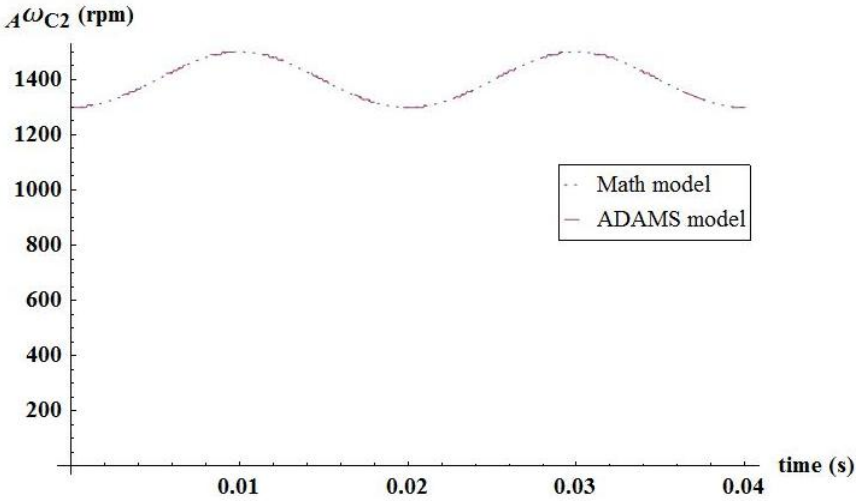

Figure 4-11: Angular velocity component along the "a_3" direction of the second cross of CVJ (case 2)

Figure 4-12 to Figure 4-14 show the components of the angular acceleration of the second crossed expressed with respect to the inertial frame of reference. The component along the "a_1" direction of the second cross cancels out the "a_1" component of the first cross. The components along the "a_2" and "a_3" directions are in phase and change in a sinusoidal mannar.

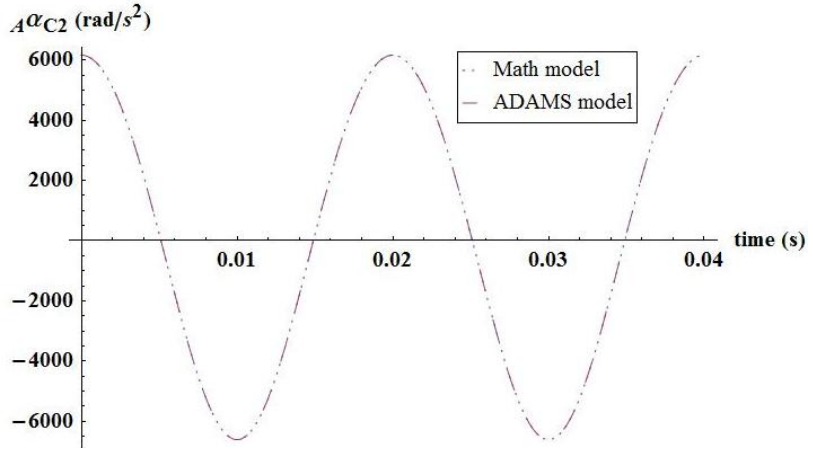

Figure 4-12: Angular acceleration ("a_1" component) of the second cross of CVJ (case 2)

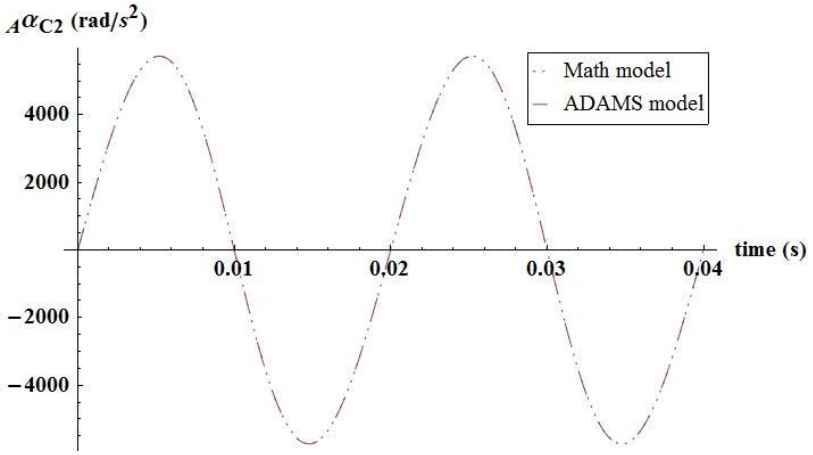

Figure 4-13: Angular acceleration ("a_2" component) of the second cross of CVJ (case 2)

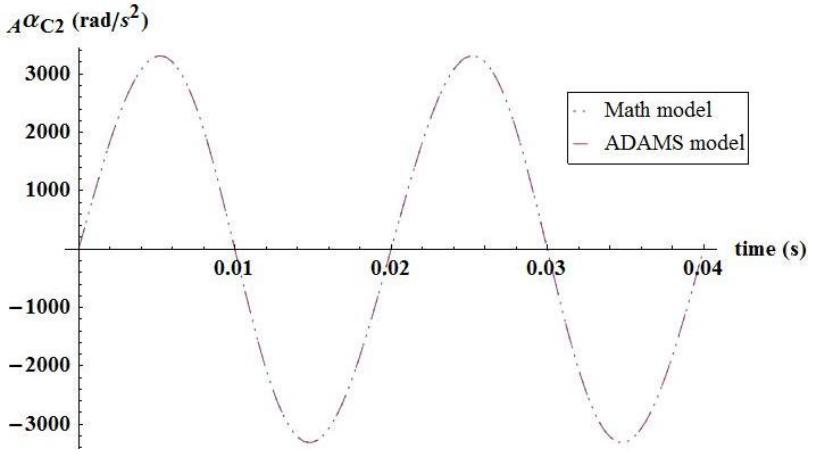

Figure 4-14: Angular acceleration ("a_3" component) of the second cross of CVJ (case 2)

The velocity and acceleration of the second cross are zero. The velocity and acceleration of the CG of the barrel are also zero.

Figure 4-15 shows the piston displacement as a function of the main shaft and yoke rotations. The piston is not displaced relative to the barrel if the yoke angle is zero regardless of the angular rotation of the main shaft. In addition, for a given yoke angle the piston displacement with respect to the barrel varies sinusoidally with the main shaft rotation.

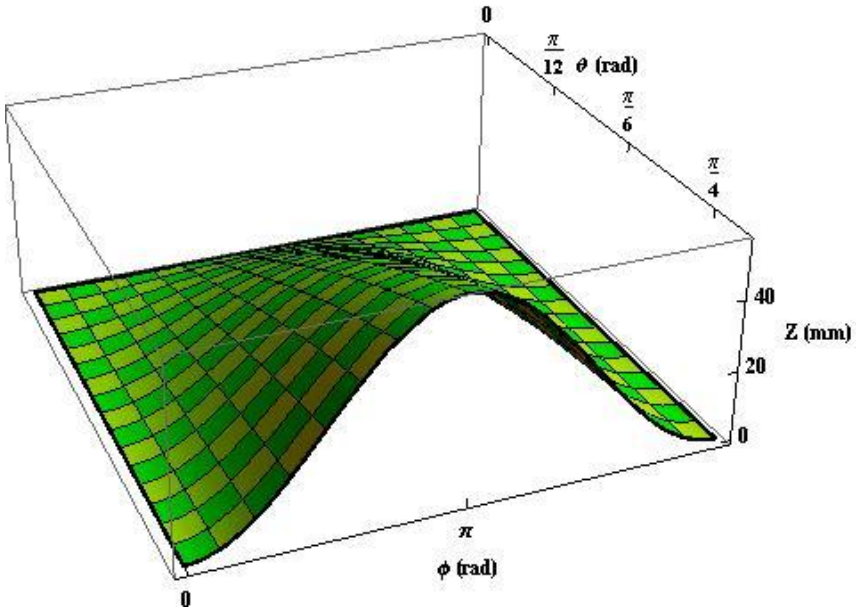

Figure 4-15: Piston displacement as a function of main shaft and yoke rotations

The velocity components of the first piston are shown in Figure 4-16 to Figure 4-18. Notice that the mathematical model matches that of ADAMS/View model along the "a_1" and "a_2" directions. Although there is a phase shift of around 40° between the mathematical model and the ADAMS model along the "a_3" direction, both models indicate the same trend and the same maximum and minimum values. In addition, the "a_3" component is insignificant because it is only around 3% of the value of either the "a_1" or

the "a_2" component. The solution of the Mathematica^{TM} model is exact. On the other hand, the numerical solution obtained from ADAMS/View is approximate and involves some simplifications. Therefore, the difference between the Mathematica^{TM} model and ADAMS/View model could be attributed to numerical approximations involved in the ADAMS model.

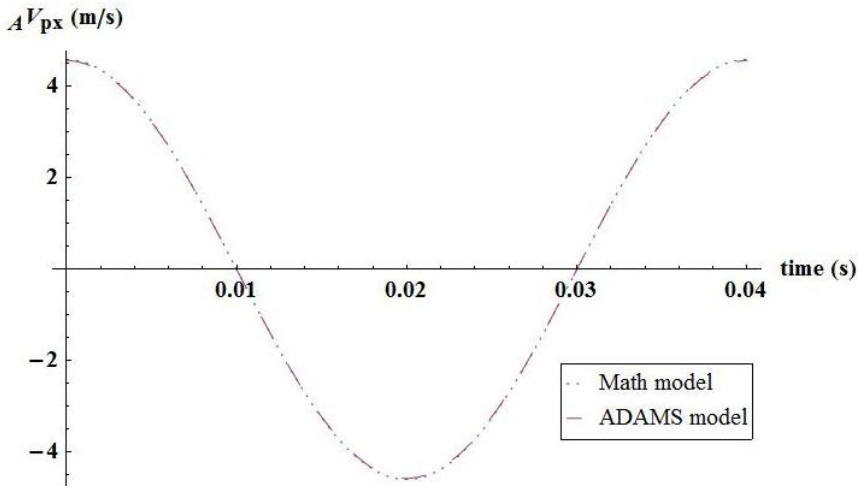

Figure 4-16: The velocity of the piston along the "a_1" direction (Case 2)

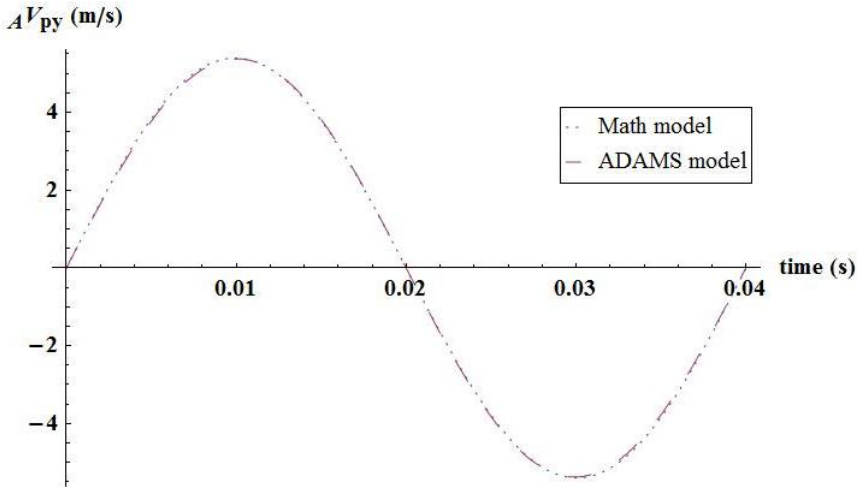

Figure 4-17: The velocity of the piston along the "a_2" direction (Case 2)

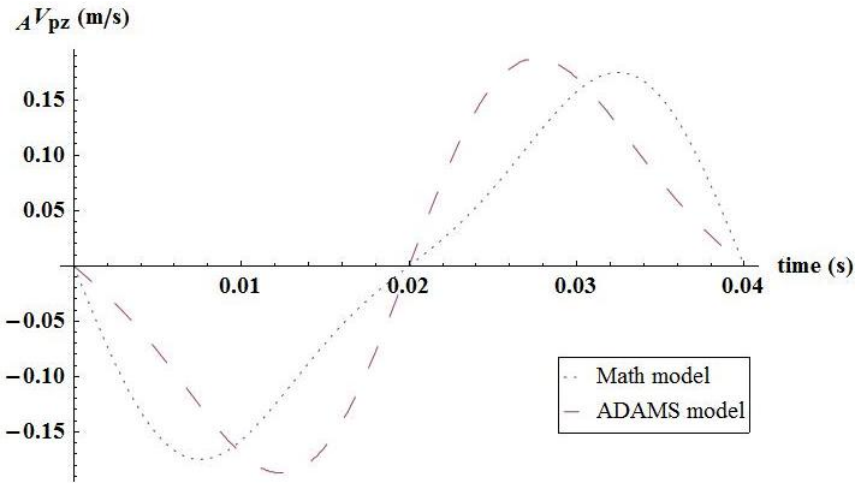

Figure 4-18: The velocity of the piston along the "a_3" direction (Case 2)

The acceleration components of the piston are shown in Figure 4-19 to Figure 4-21. Both the mathematical and ADAMS model match accurately along the "a_1" and "a_2" directions. There is a small difference (less than 2%) between the two models in the "a_3" direction.

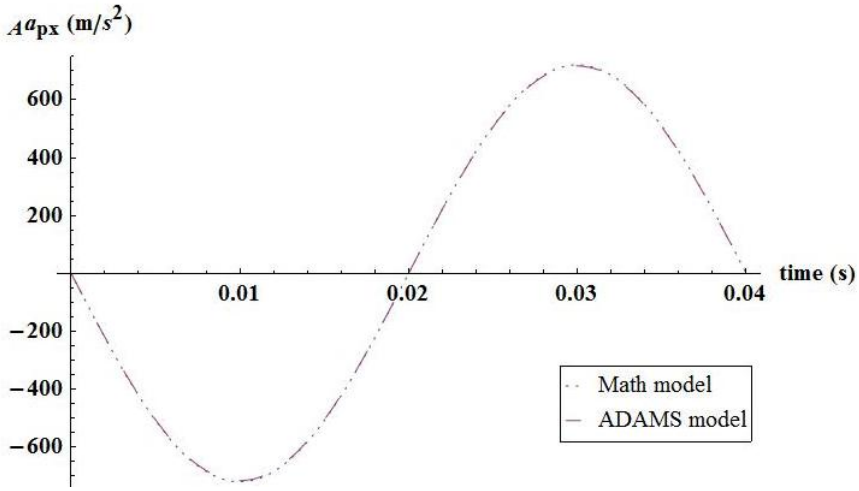

Figure 4-19: The acceleration of the first piston along the "a_1" direction (case 2)

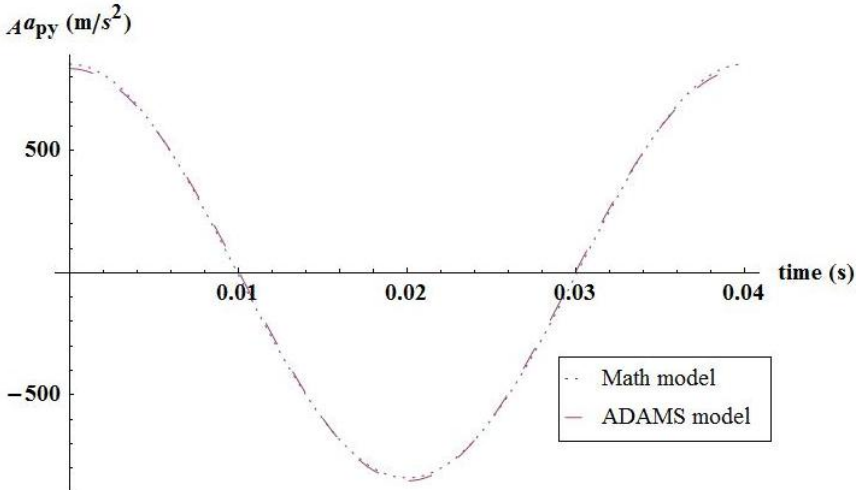

Figure 4-20: The acceleration of the first piston along the "a_2" direction (case 2)

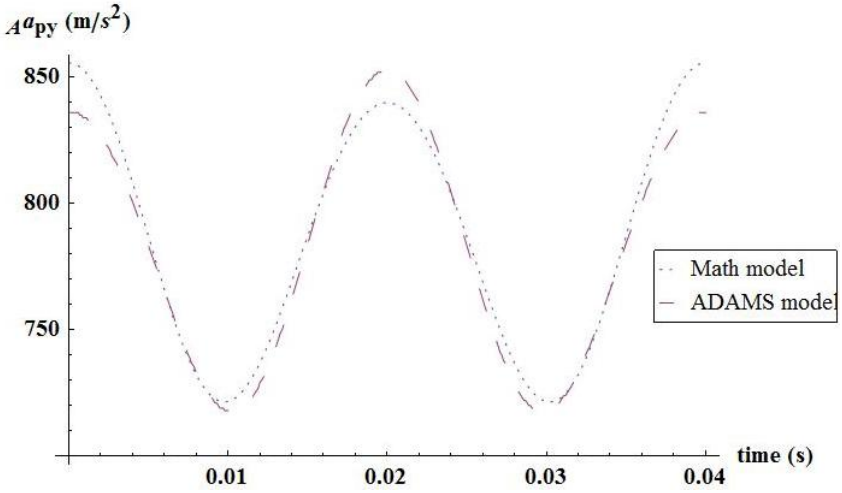

Figure 4-21: The acceleration magnitude of the first piston (case 2)

Figure 4-22 to Figure 4-24 show the variation of the velocity components of the connecting rod along the three inertial directions. There is a matching between the mathematical model and the ADAMS model along the "a_1" and "a_2" directions. Although there is a small phase shift between the mathematical and ADAMS model along the "a_3" direction, the trend is the same and the maximum and minimum of both models have the same values.

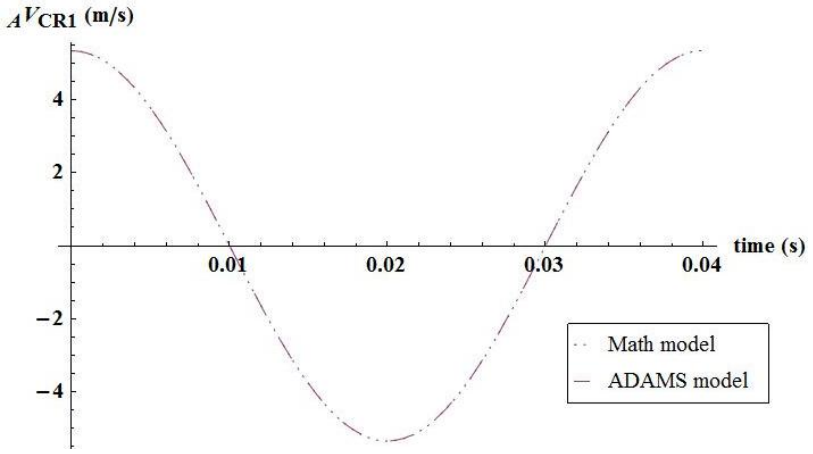

Figure 4-22: The velocity component of the connecting rod along the "a_1" directions (case 2)

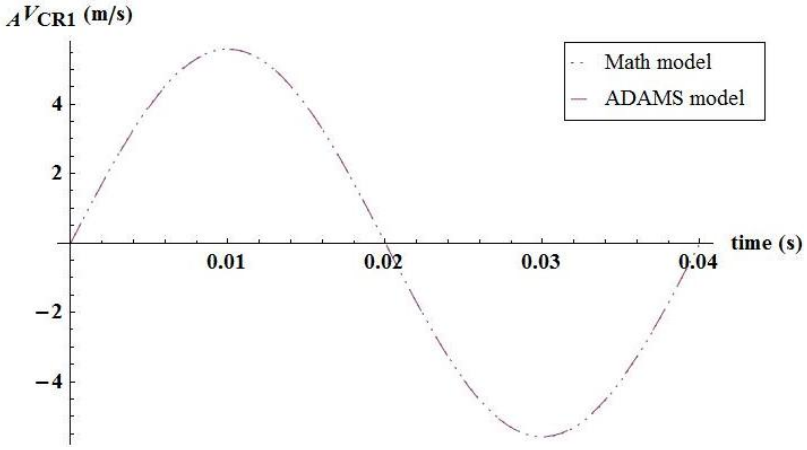

Figure 4-23: The velocity component of the connecting rod along the "a_2" direction (case 2)

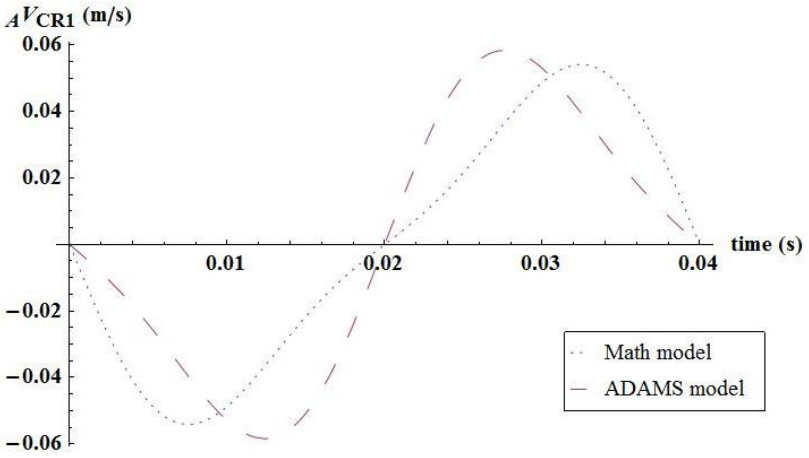

Figure 4-24: The velocity component of the connecting rod along the "a_3" direction (case 2)

As can be seen from Figure 4-25, the acceleration components along the "a_1" and "a_2" directions vary in a sinusoidal manner and they match the plots from ADAMS model. The velocities and accelerations of all pistons and connecting rods are shown in Appendix A.

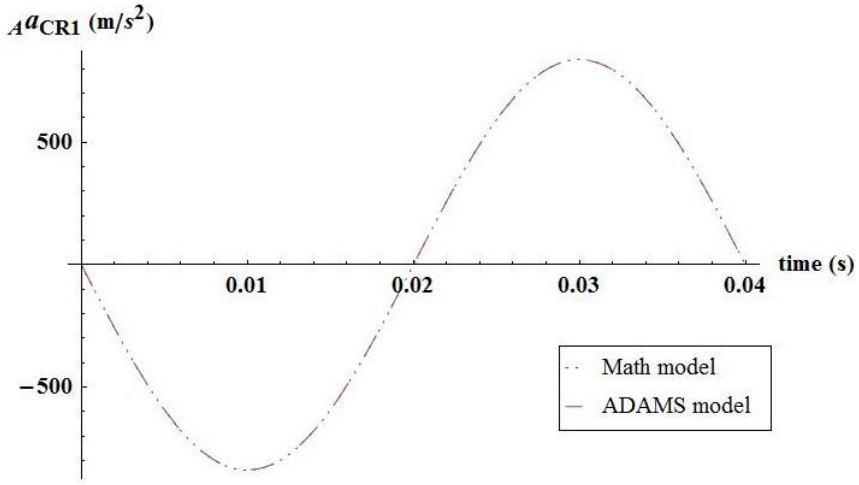

Figure 4-25: The acceleration component of the connecting rod along the "a_1" direction (case 2)

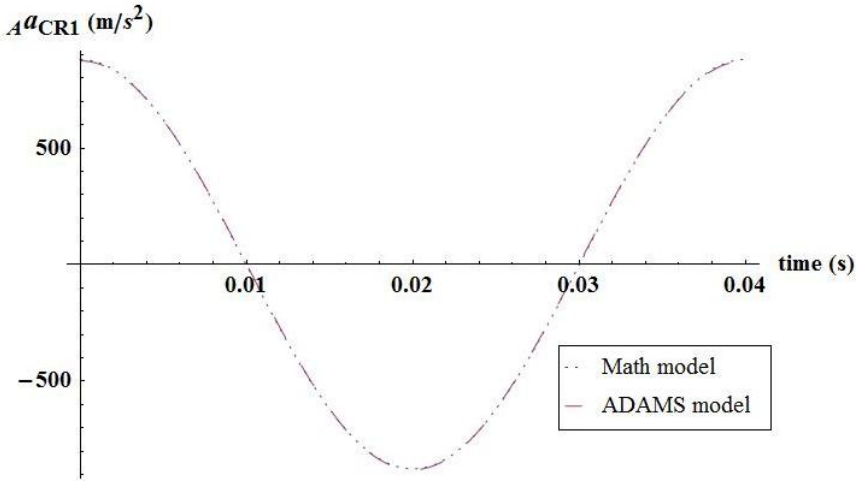

Figure 4-26: The acceleration component along the "a_2" direction of the connecting rod (case 2)

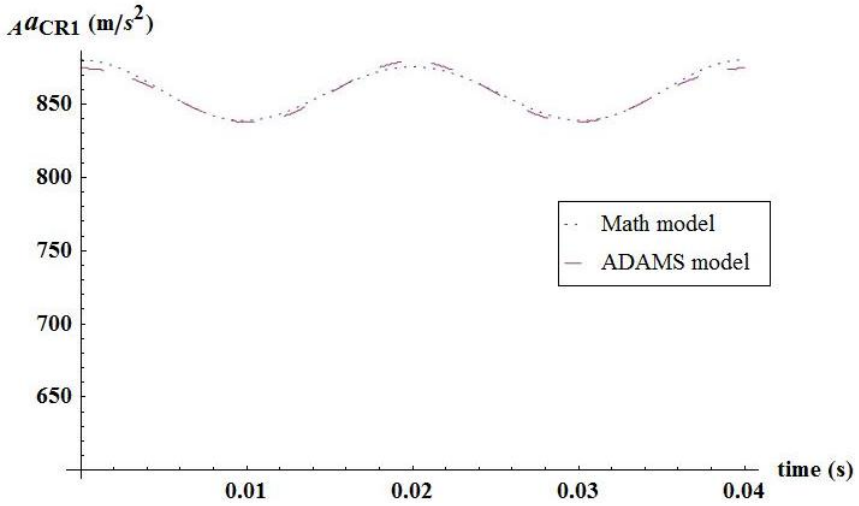

Figure 4-27: The magnitude of the acceleration of the connecting rod (case 2)

The yoke-valve plate assembly, the ram, and the actuating link of the yoke displacement mechanism are stationary because the yoke angle is fixed.

4.2 Numerical Solution of the Piston Flow Rate and Pressure

The theoretical model of the piston pressure as given by equations (3.213) to (3.264) is examined numerically against well know conditions of the rotation of the main shaft and the yoke. The geometric data of an actual variable displacement pump was used. The main shaft rotates at a constant angular velocity of 1500 rpm while the yoke is kept at 5°, 10°, 20°, 30°, and 40° respectively.

4.2.1 The piston displacement

The piston's displacement and velocity is covered in a previous section from a kinematic context and it is revisited here as it is directly related to piston's pressure and pump's flow rate. Figure 4-15 shows a 3-dimensional plot of the piston's displacement as a function of the main shaft and yoke rotations. The piston is not displaced relative to the

barrel if the yoke angle is zero regardless of the angular rotation of the main shaft. In addition, for a given yoke angle the piston's displacement varies periodically with the main shaft rotation.

The velocity of the first piston (Figure 4-28), assuming that it starts from the top dead center, with respect to the barrel varies in a sinusoidal manner with the main shaft angular rotation. It has maximum values at the middle of the discharge/suction ports ($\phi = \pi/2$ and $\phi = 3\pi/2$).

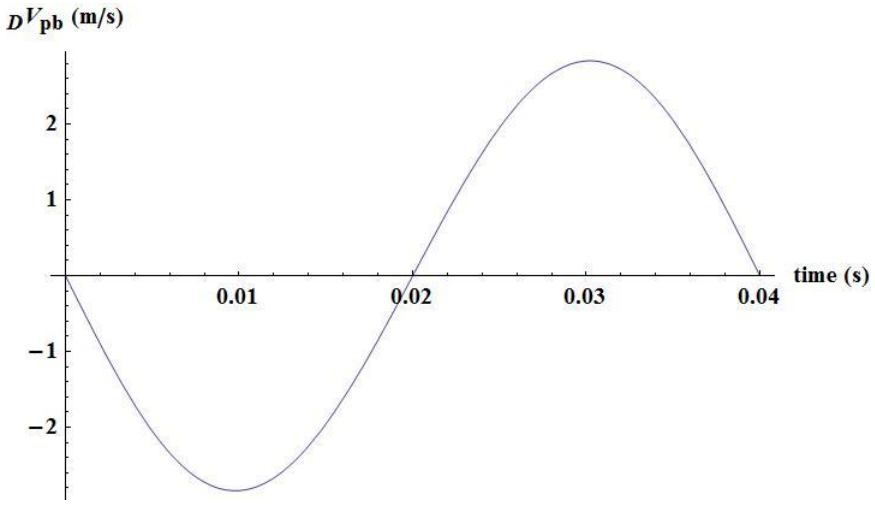

Figure 4-28: The velocity of the first piston with respect to the barrel

4.2.2 Cylinder flow rate (time domain)

Figure 4-29 shows the cylinder flow rate as a function of time at a constant main shaft speed of 1500 rpm for yoke angles of 5°, 10°, 20°, 30°, and 40° respectively.

The numerical solution at a yoke angle of 0° did not converge, however the trend at this angle can be anticipated by extrapolating the results at the other angles (0° to 40°). At 0° yoke angle, the piston displacement is always zero regardless of barrel rotation. Therefore, there will be no flow rate due to the piston kinematics except for the flow in or out of the pistons due to leakage through the clearances between the mating parts. Upon

transition at the BDC from the suction port to the discharge port (at t = 0.02 seconds), there will be a sharp pulse of oil flow in the cylinder coming from the high-pressure accumulator. Similarly, there will be also a pulse as the oil flows from the cylinder to the low-pressure accumulator as the cylinder switches from the discharge to the suction port at the TDC.

As the yoke angle increases from 5° to 40°, the cylinder flow rate increases accordingly because the piston displacement increases.

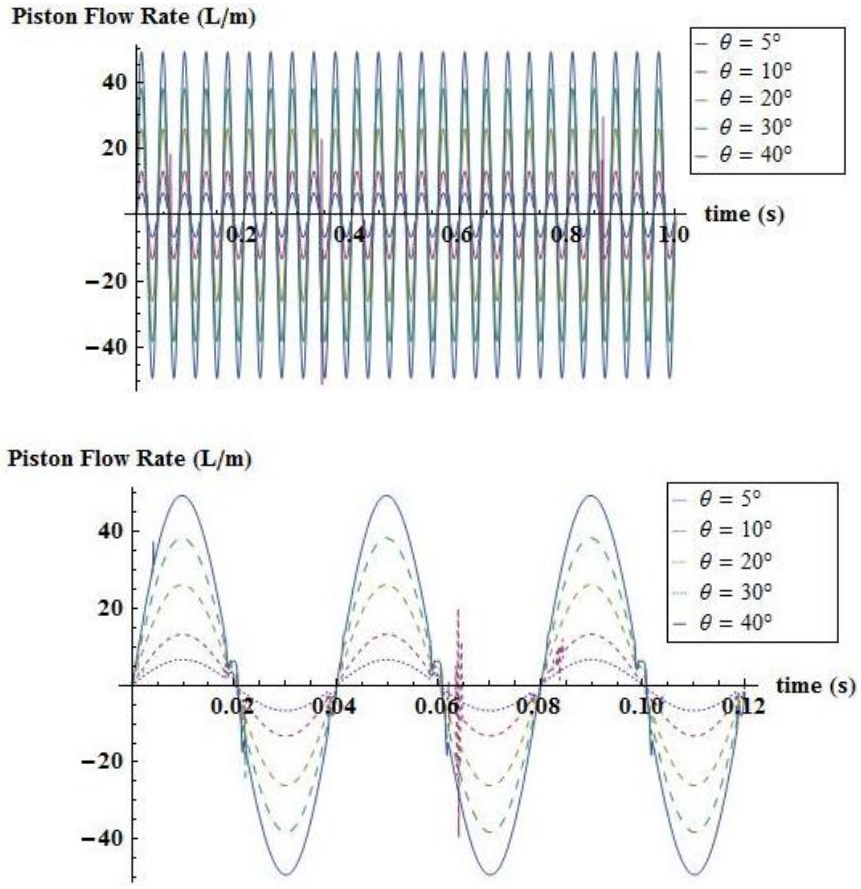

Figure 4-29: Cylinder flow rate profile for yoke angles of 5°, 10°, 20°, 30°, and 40°

Zooming on the period just before 0.02 sec to just above 0.04 sec for yoke angle of 10° will clarify why the sudden jump occurs as shown in Figure 4-30. As the cylinder moves

from the TDC (ϕ = 0) ccw, the piston's displacement increases. In the meantime, the cylinder inflow to the cylinder increases and reaches a maximum at ϕ = 90° (t = 0.01 sec). After this maximum, the oil inflow to the cylinder starts to decrease until the cylinder exit is totally closed by the land between the suction and discharge ports. While the cylinder is closed, except for some leakage through clearances between mating parts, its volume increases leading to a negative pressure buildup until the cylinder starts to open to the notch groove before the start of the discharge port. Because of this negative pressure build up inside the cylinder while in the closed state, a reverse flow from the discharge port enters the cylinder causing the inflow to increase abruptly. Then after the reverse flow balances the negative pressure build up, the inflow again decreases until reaching the BDC.

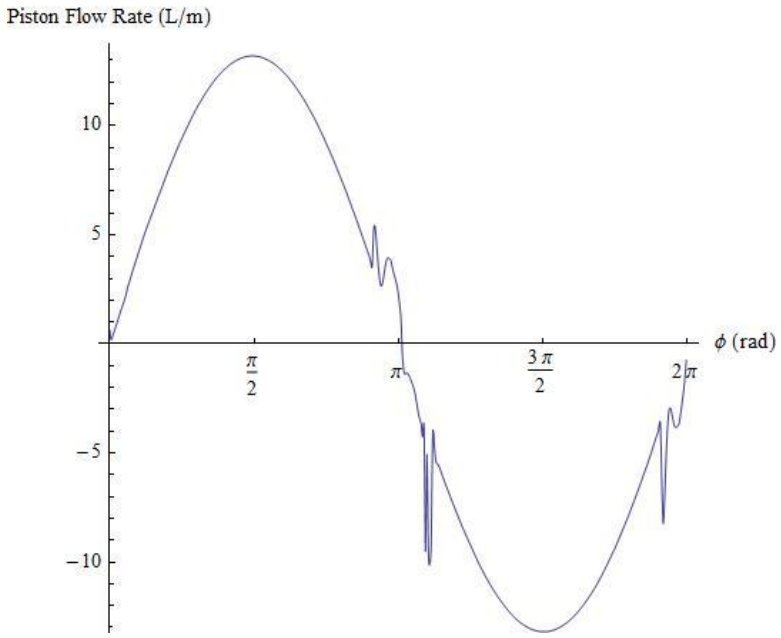

Figure 4-30: Enlarged view of the Cylinder flow rate profile, θ = 10° (time domain)

As the cylinder pass the BDC, the volume of the cylinder starts to decrease while the outflow increases until reaching a maximum at ϕ = 270°. After that, the outflow starts to

decrease again until the cylinder is completely closed by the land between discharge and suction ports. During the closure region, the cylinder volume continues to decrease causing a positive pressure buildup. As soon as the cylinder is open to the notch groove (before the start of the suction port), the oil moves out rapidly from the cylinder in order to balance the effect of pressure buildup during the closer period. This causes the outflow to increase abruptly. After which the outflow decreases back again until reaching zero at the TDC.

4.2.3 Cylinder flow rate (frequency domain)

Figure 4-31 shows the amplitude spectrum for the cylinder flow rate at a yoke angle of 30°. The plots of the cylinder flow rate at yoke angles of 5°, 10°, 20°, and 40° are similar to those at 30° except for the magnitudes of the respective harmonics. As can be seen from the figure, there is a major harmonic that occurs at a frequency of 25 Hz. The other harmonics are very small and die very quickly at higher frequencies.

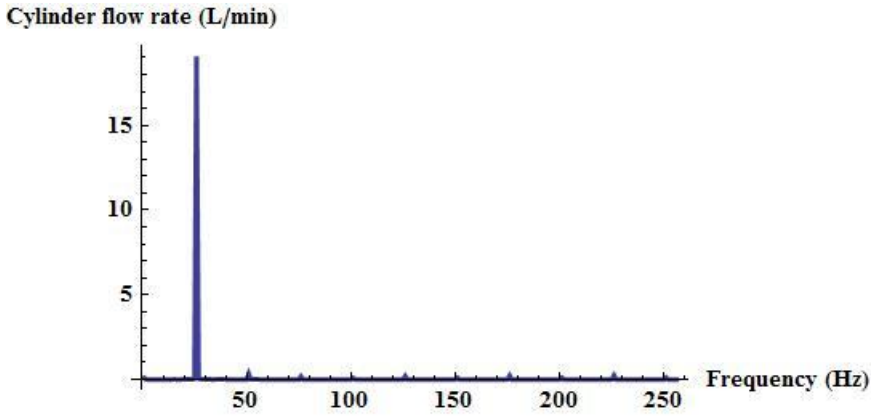

Figure 4-31: Cylinder flow harmonics (frequency domain), θ = 30°

The fundamental cylinder flow harmonic occurs at a frequency of 25 Hz for all angular yoke rotations under investigation as can be seen in Figure 4-32. The cylinder flow

amplitude of the fundamental harmonic increases linearly with the yoke angle because of the higher piston displacement as the yoke angle increases.

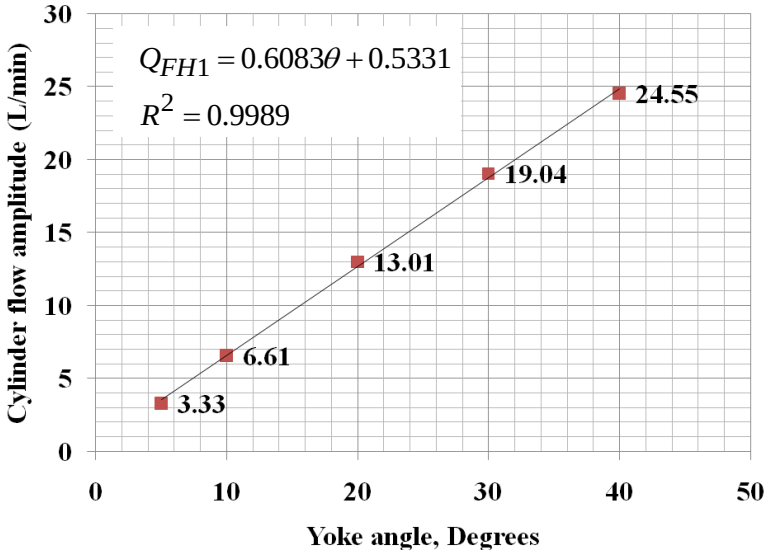

Figure 4-32: Fundamental harmonic amplitude of cylinder flow vs. yoke angle

4.2.4 Pump flow rate (time domain)

The pump flow rate is the sum of the cylinder flow rates at the discharge or suction port from all individual cylinders less the leakage. The pump flow rate for yoke angles of 5°, 10°, 20°, 30°, and 40° is shown in Figure 4-33. The mean flow rate increases as the yoke angle increases due to increased piston displacement. The pump flow rate has a repeating flow ripple about the mean flow rate with a frequency of 225 Hz.

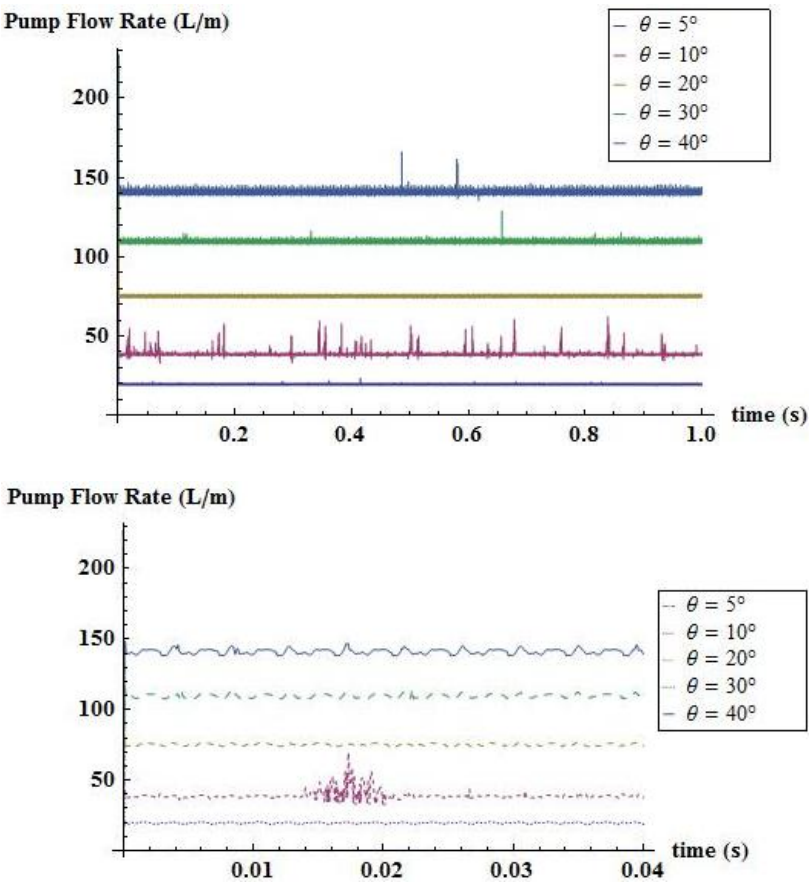

Figure 4-33: Pump flow rate profile for yoke angles of 5°, 10°, 20°, 30°, and 40°

4.2.5 Pump flow rate (Frequency domain)

Figure 4-34 shows the amplitude spectrum of the pump flow as a function of yoke angle. All harmonics are very small and die very quickly for all yoke angles. What is shown at 0 Hz actually represents the steady state pump flow rate which is constant for a given yoke angle. The steady state pump flow rate increases linearly with the yoke angle as can be seen in Figure 4-35 due to the increased piston displacement with increased yoke angle.

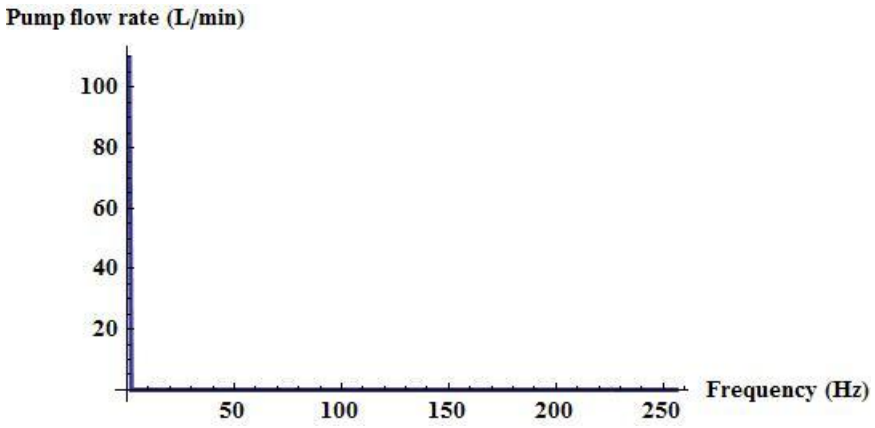

Figure 4-34: Pump flow harmonics (frequency domain), θ = 30°

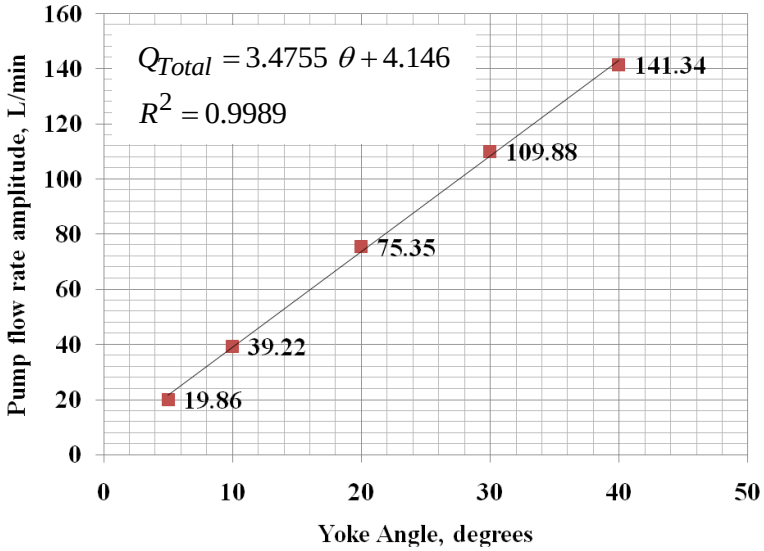

Figure 4-35: Steady state pump flow vs. yoke angle

4.2.6 Piston pressure (time domain):

The cylinder pressure profiles for yoke angles of 5°, 10°, 20°, 30°, and 40° are shown in Figure 4-36. As the yoke angle decreases, the jumps beyond the low pressure or high - pressure accumulators at the points of transitions between the ports decrease accordingly because compression or expansion of the oil near the TDC and BDC gets smaller.

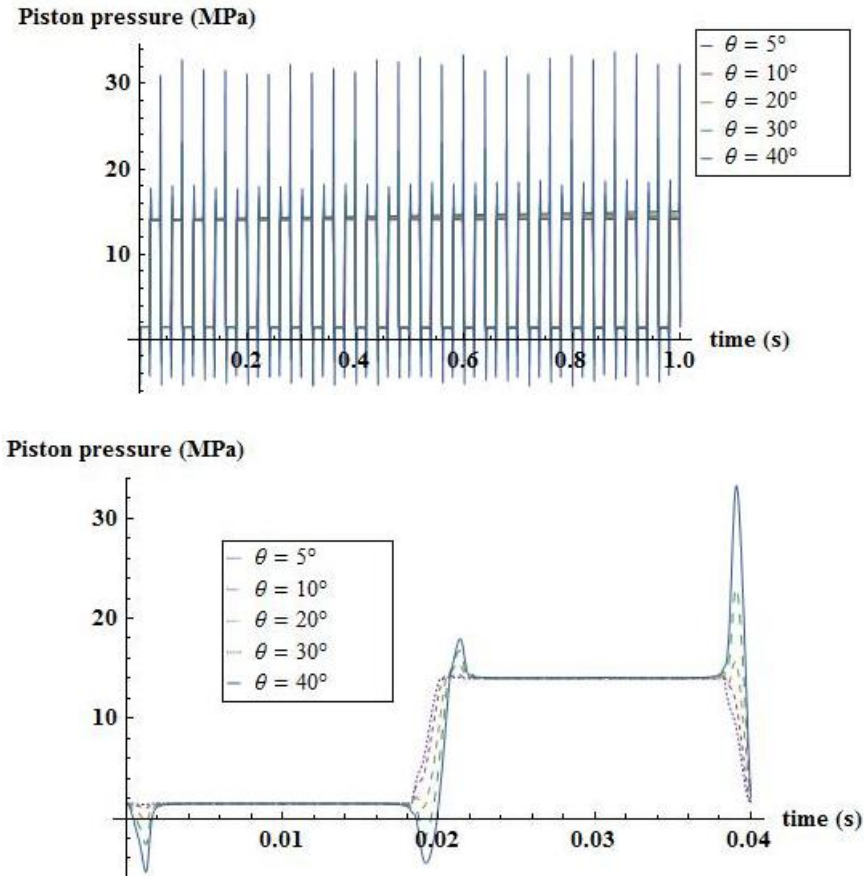

Figure 4-36: Cylinder pressure profile for yoke angles of 5°, 10°, 20°, 30°, and 40°

As the yoke angle starts to increase, a sharp overshoot or undershoot is being noticed and increased while the yoke angle increases. Before reaching the BDC, the orifice exit area of the cylinder is totally closed by the land between the suction and discharge ports. Consequently, as the barrel rotates in this period up to the BDC the volume of the oil inside the cylinder increases causing a negative pressure in the suction port. This leads to pressure undershoot. At angles of 30°, and 40° the pressure undershoot is below zero gage pressure, which might cause cavitation of the pump as the barrel rotates from suction to discharge port. The same explanation applies upon the transition from the discharge to the suction port at the TDC except that the oil is compressed at the TDC while the cylinder is

closed by the land between the discharge and suction ports. Thus, an overshoot in pressure occurs beyond the pressure of the HPA.

4.2.7 Piston pressure (frequency domain)

The cylinder pressure harmonics are shown in Figure 4-37 for a yoke angle of 30°. The trend is similar at other angles.

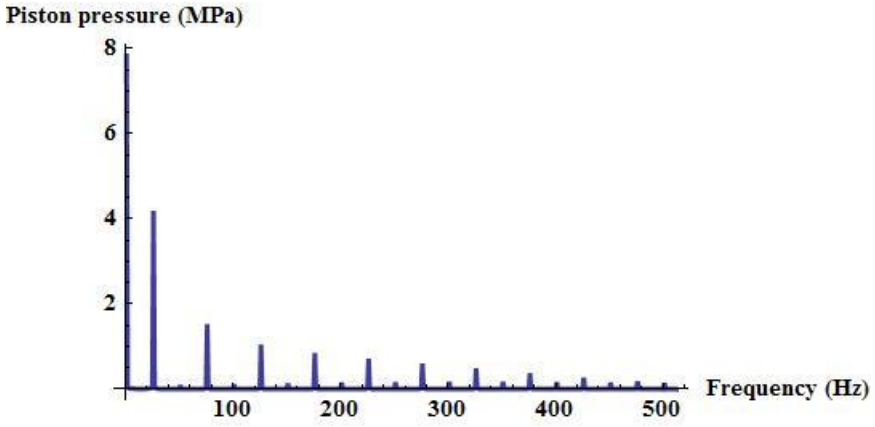

Figure 4-37: Cylinder pressure harmonics (frequency domain), θ = 30°

The piston pressure harmonics vary parabolically and slowly with the yoke angle as can be depicted in Figure 4-38. What looks like a harmonic at 0 Hz is actually the steady state value of the piston pressure.

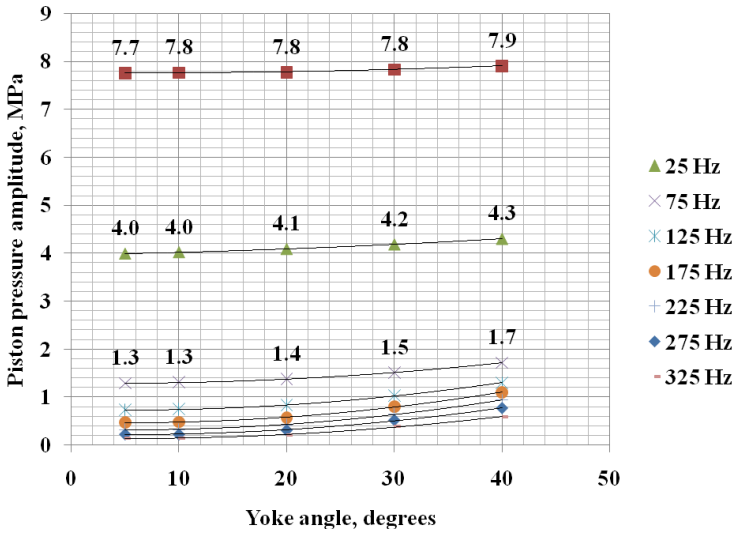

Figure 4-38: Cylinder pressure harmonics vs. yoke angle

4.3 Numerical Solution of the Forces Acting on the Pump Case

To simplify the solution of the mathematical model numerically, the frictional moment is neglected (it is very small) at the ball bearing and the thrust bearing of the main shaft, spherical joints between the main shaft and the connecting rods and between the connecting rods and the pistons, and at all pin joints.

The weights of the very small parts of the CVJ are neglected in this analysis including the weight of the first and second cross, and the weight of the first and second intermediate shafts.

Based on the numerical solution of the equations of motion of the parts of the pumps mentioned in chapter 3, plots of the reactions forces acting on the pump case were obtained. The analysis of these plots will be conducted in both the time and frequency domains.

4.3.1 Reaction forces on the case from the main shaft at the ball bearing

Figure 4-39 to Figure 4-41 shows the reaction force from the main shaft at the radial roller bearing for yoke angles of 5°, 10°, 20°, 30°, and 40° and shaft speed of 1500 rpm. This force has two components that are normal to the axis of the main shaft. All components alternate about the mean value with a frequency that is nine times the frequency of rotation of the main shaft. The component along the "a_1" direction arises from the fact that the pitch circles at the main shaft side and the barrel side are not the same. In addition, the connecting rod is inclined at an angle with the horizontal even when the yoke angle is zero. This means that the connecting rod has three-dimensional inclinations in the sense that if you take a front view or a top view of the connecting rod, you still have the connecting rod inclined in both views. Therefore, the piston forces transmitted through the connecting rod to the main shaft will have components along the three directions. Some of the two components that are normal to the main shaft axes are shared between the ball and thrust bearings, while the component along the shaft axes is carried only by the thrust bearing at the main shaft and at the revolute joints of the yoke axis of rotation.

The pump is connected to the LPA at the inlet port and to the HPA at the discharge port. As the pump delivers the hydraulic oil from the LPA to the HPA, the pressure differential across the pump increases accordingly. For that reason, the mean value of the reaction force along all directions increases very slowly with time. This result applies to other reaction forces.

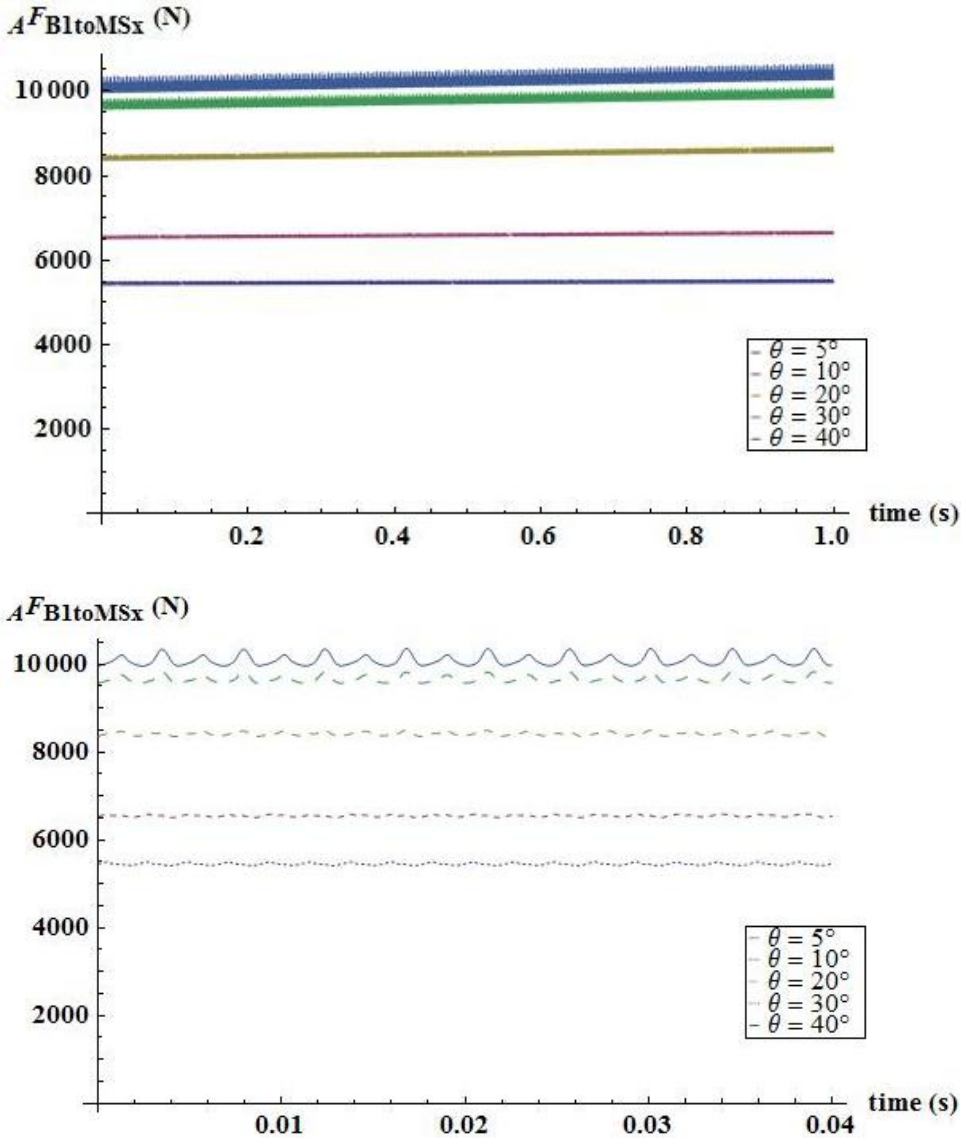

Figure 4-39: Reaction force component along the "a_1" direction on the case of the pump at the Ball bearing (main shaft)

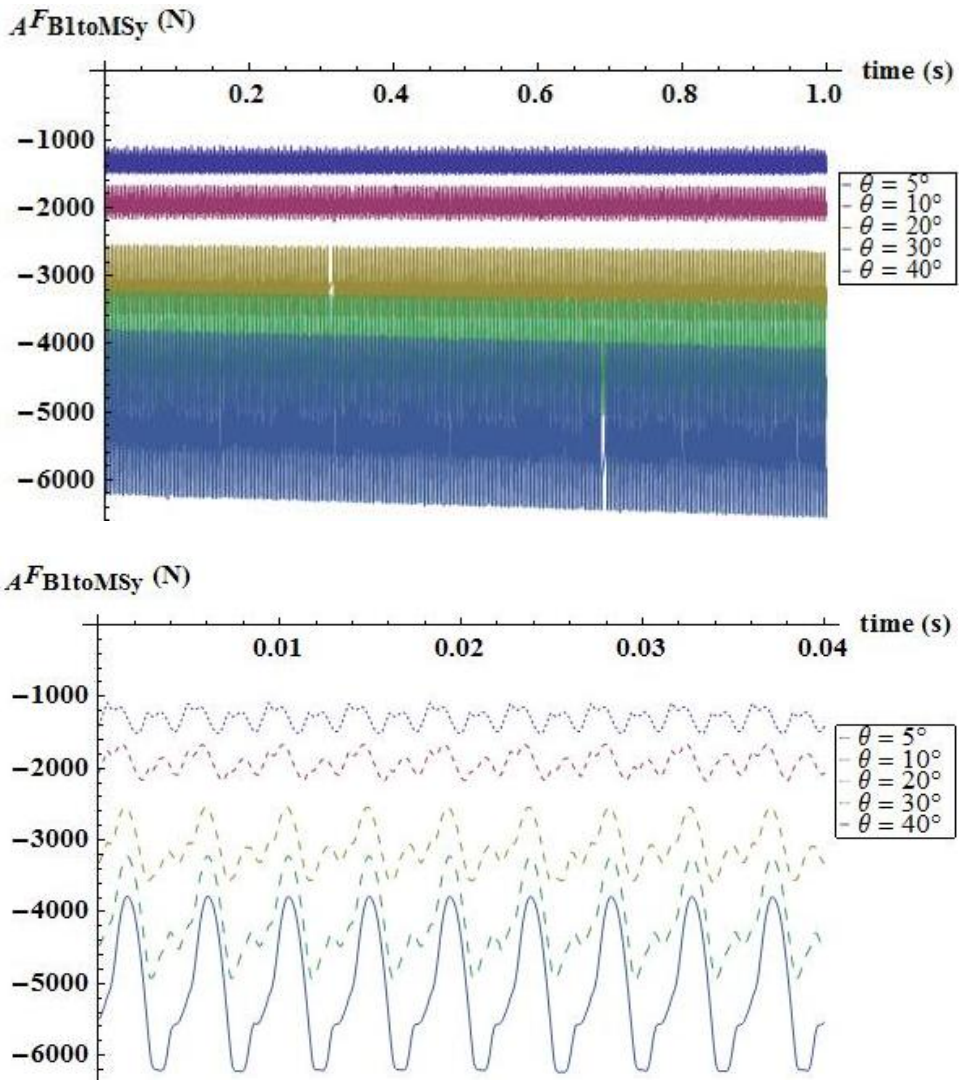

Figure 4-40: Reaction force component along the "a_2" direction on the case of the pump at the Ball bearing (main shaft)

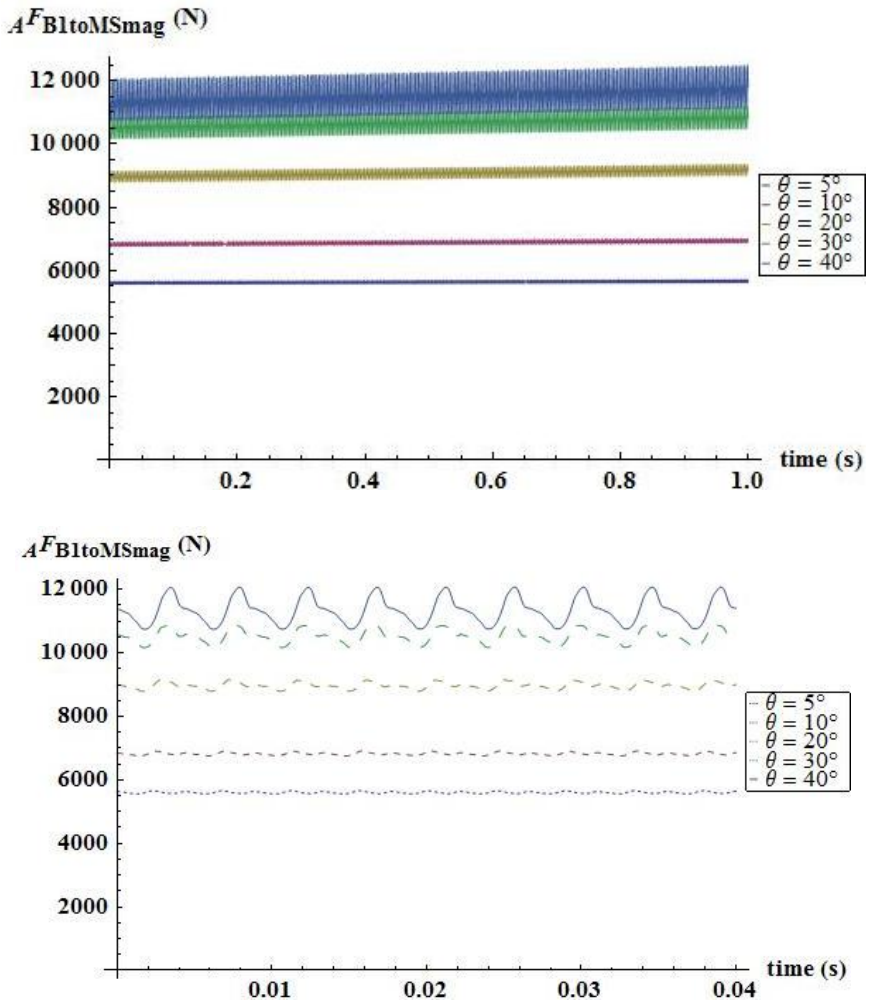

Figure 4-41: Magnitude of the reaction force on the case of the pump at the Ball bearing (main shaft)

The average values of the force components are calculated over a period of 1.0 second. Figure 4-42 shows a plot of these averages as a function of the yoke angle. Both components have some pulsation due to the mechanism of the pistons' movement, the limited number of pistons (9 in this case), and the pressure pulsations in the cylinders within the barrel. The mean value along the "a_1" direction varies parabolically with the yoke angle. The mean value along the "a_2" direction increases linearly with the yoke angle.

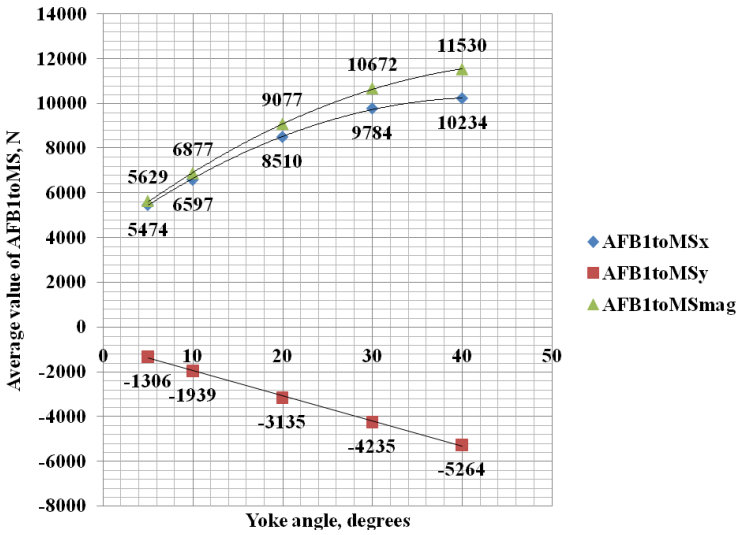

Figure 4-42: Average value of the reaction force at the ball bearing (main shaft) vs. yoke angle

In order to identify the harmonics of the reaction forces acting on the case of the pump, these forces are converted into the frequency domain using Discrete Fourier Transform analysis.

Figure 4-43 shows the amplitude spectrum of the force components from the main shaft to the pump case at the ball bearing at a yoke angle of 30° and shaft speed of 1500 rpm. The harmonics of the component along the "a_1" direction are very small and negligible. What looks like as a harmonic at 0 Hz, really represents the steady state value of the a_1 component. The steady state value of the a_1 component increases parabolically with the yoke angle as can be noticed from Figure 4-44.

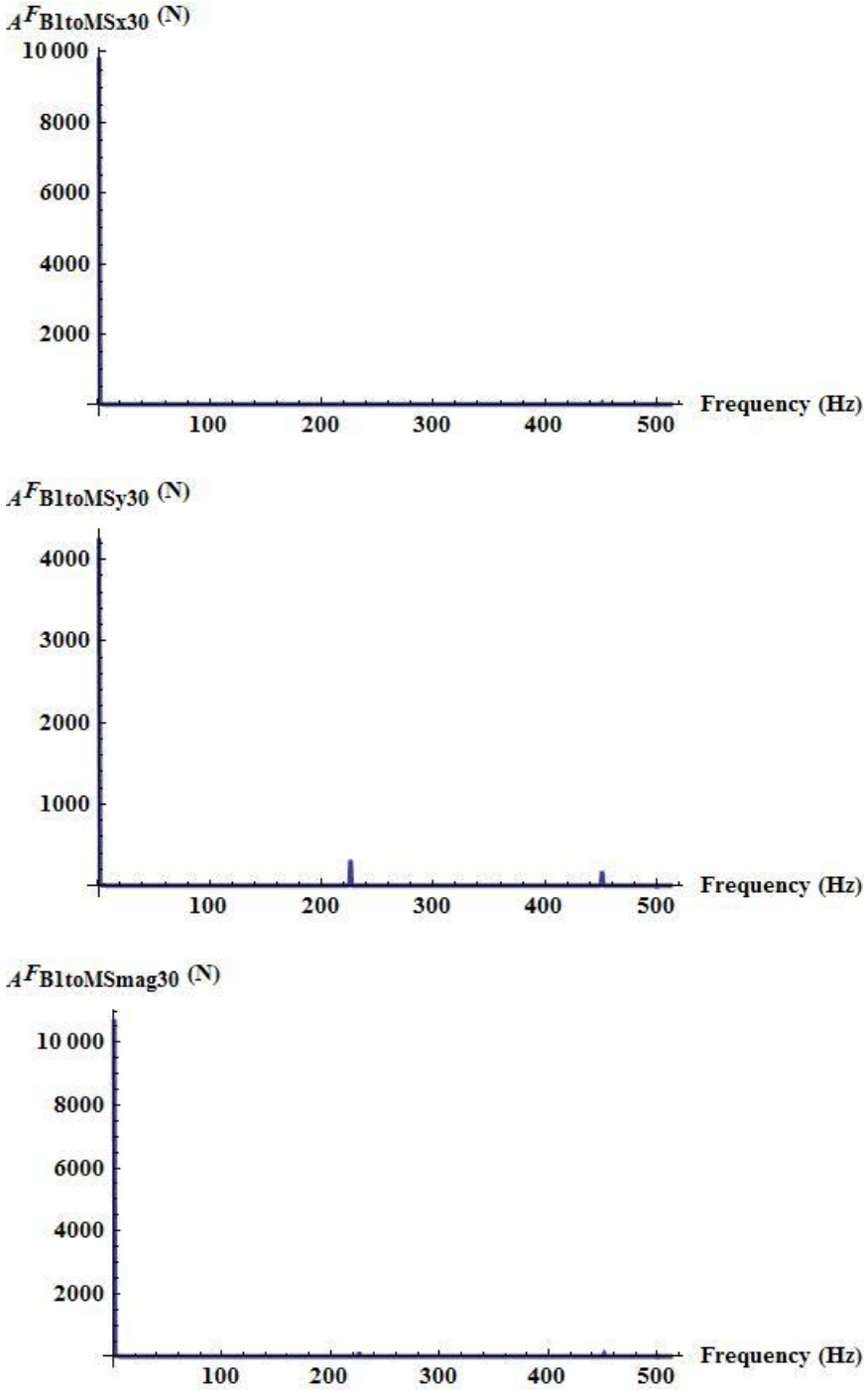

Figure 4-43: Amplitude spectrum of the magnitude of the reaction force from the main shaft at the ball bearing to the pump case ($\theta = 30°$)

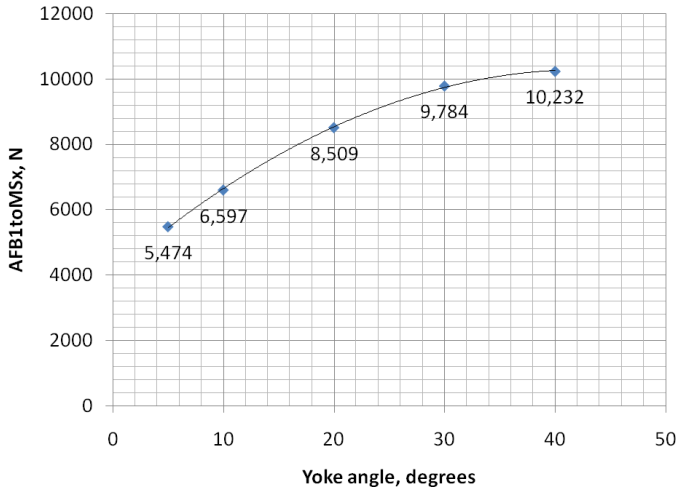

Figure 4-44: Steady state value of the "a_1" component of the reaction force from the main shaft at the ball bearing to the pump case as a function of the yoke angle

The component along the "a_2" direction has two major harmonics at 225 Hz and 450 Hz. What looks like a harmonic at zero Hz actually represents the steady state value of the a_2 component. The steady state value of the a_2 component increases linearly with the yoke angle. The amplitude of the harmonics at 225 Hz and 450 Hz increases parabolically with the yoke angle.

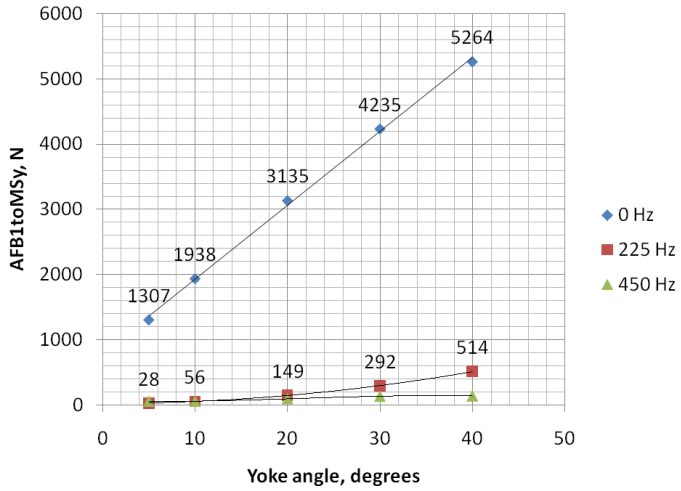

Figure 4-45: Amplitude spectrum of the "a_2" component of the reaction force from the main shaft at the ball bearing to the pump case as a function of the yoke angle

4.3.2 Reaction forces on the case from the main shaft at the thrust rolling bearing

Figure 4-46 to Figure 4-49 show the reaction force components on the case of the pump at the thrust roller bearing at yoke angles of 5°, 10°, 20°, 30°, and 40° and shaft speed of 1500 rpm. Although both components along the "a_1" and "a_2" directions behave in a similar fashion as the components at the radial ball bearing, they are out of phase by 180°. Although the magnitudes of the components increase with the yoke angle, the trend of variation stays the same. In addition, the fluctuation from the mean value increases as the yoke angle increases.

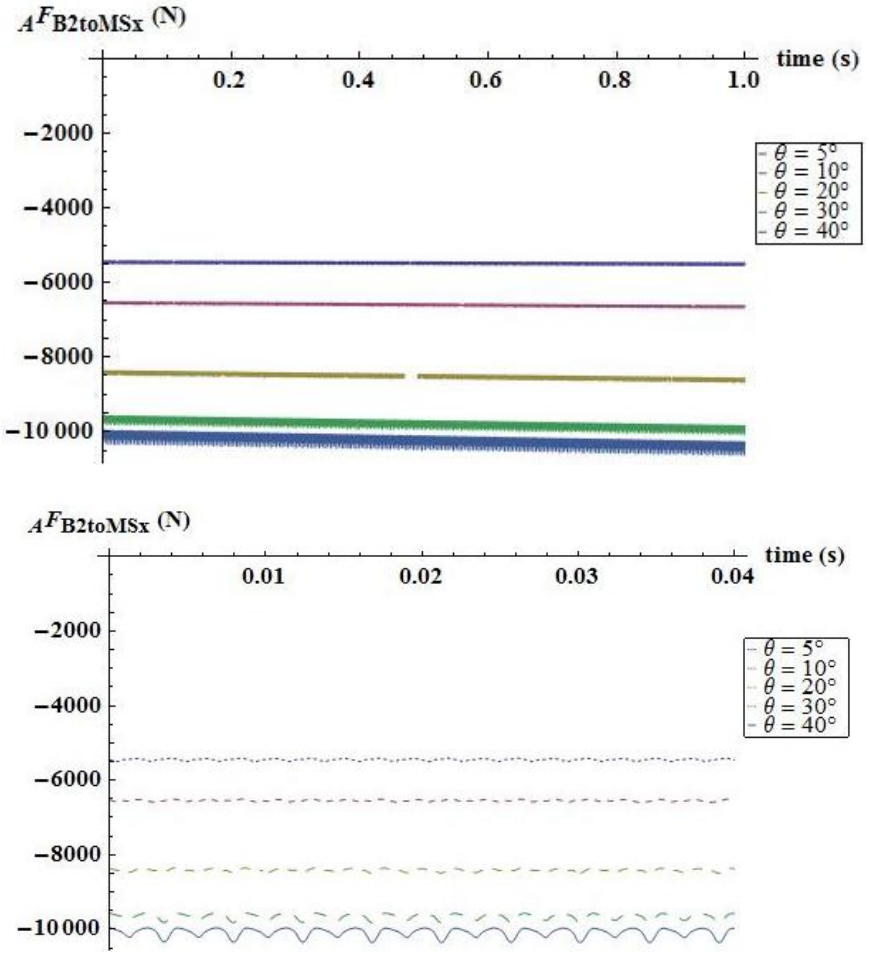

Figure 4-46: Reaction force component along the "a_1" direction on the case of the pump at the thrust roller bearing (main shaft) vs. yoke angle

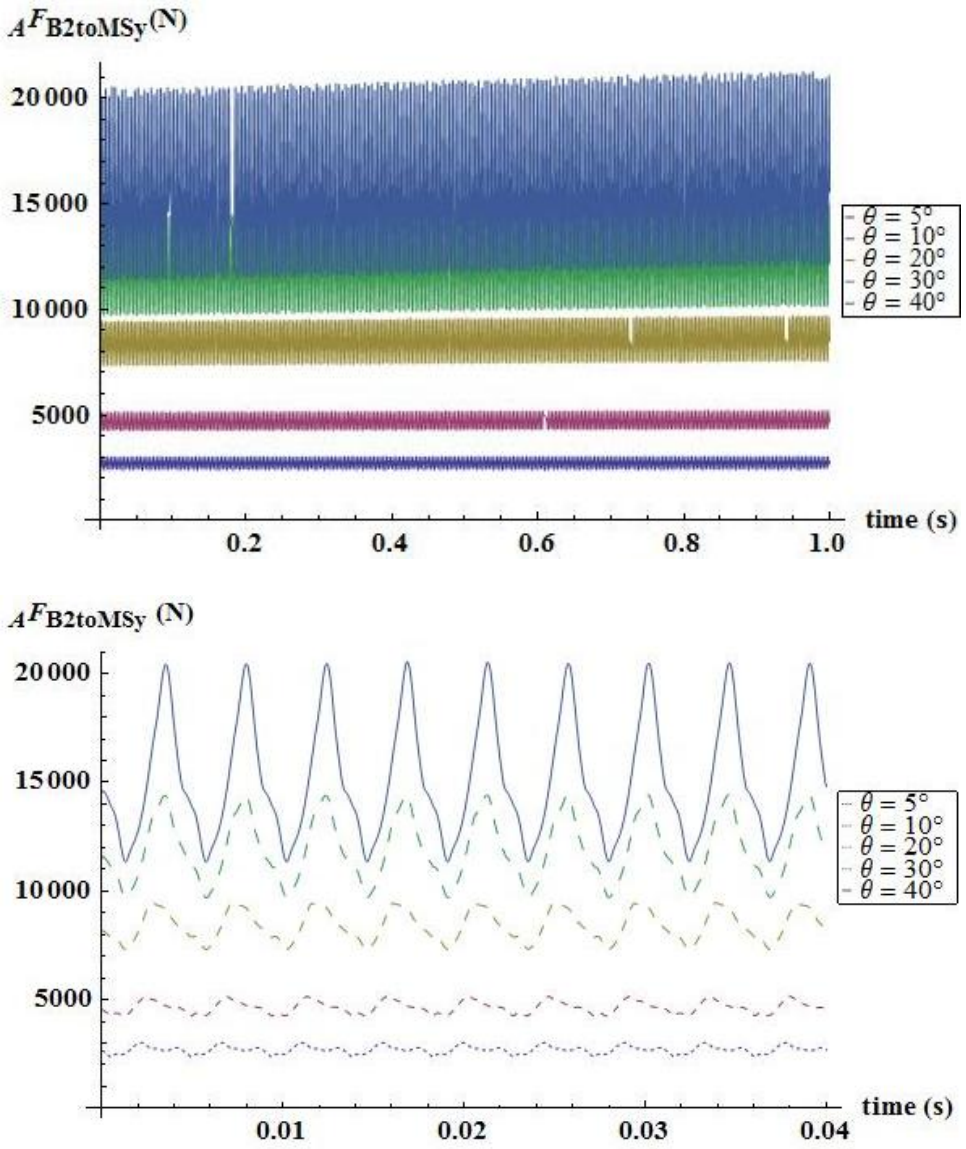

Figure 4-47: Reaction force component along the "a_2" direction on the case of the pump at the thrust roller bearing (main shaft) vs. yoke angle

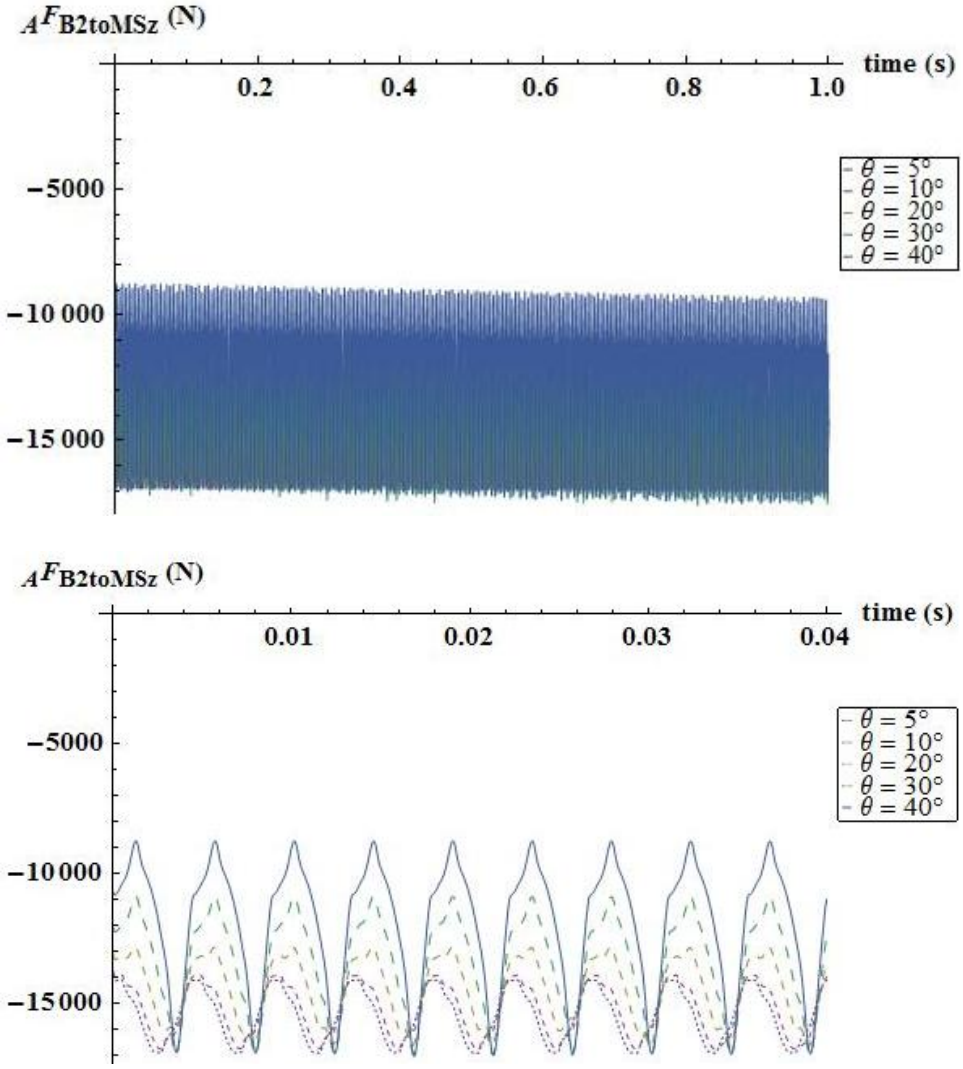

Figure 4-48: Reaction force component along the "a_3" direction on the case of the pump at the thrust roller bearing (main shaft) vs. yoke angle

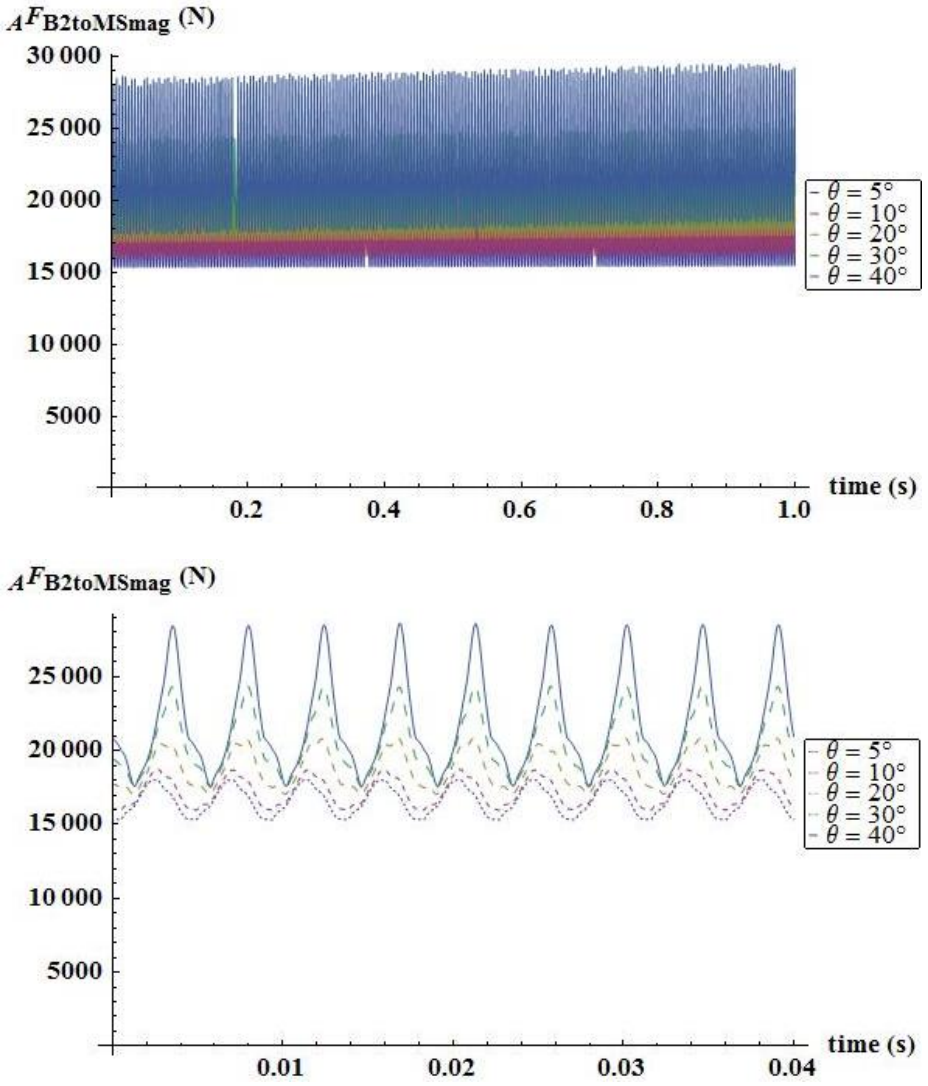

Figure 4-49: The magnitude of the reaction force on the case of the pump at the thrust roller bearing (main shaft) vs. yoke angle

Figure 4-50 shows the average values of the components of the reaction force at the thrust roller bearing calculated over a period of one second. The component along the "a_1" direction increases parabolically with the yoke angle. The component along the "a_2" direction increases linearly steeply with the yoke angle, while the "a_3" component decreases parabolically with the yoke angle. Overall, the magnitude of the force increases linearly with the yoke angle.

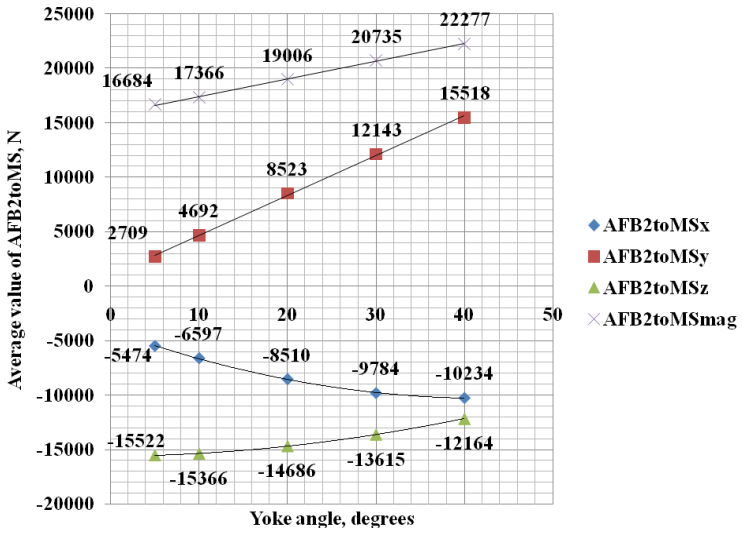

Figure 4-50: The average values of the components of the reaction force on the case of the pump at the thrust roller bearing (main shaft) vs. yoke angle

Figure 4-51 shows the harmonics of the reaction force component along the "a_1" direction from the main shaft to the pump case at the thrust roller bearing at a yoke angle of 30° and shaft speed of 1500 rpm. This component has very small and negligible harmonics. What looks like a harmonic at zero Hz is in fact the steady state value of the component at a given yoke angle. This steady state value increases parabolically with the yoke angle.

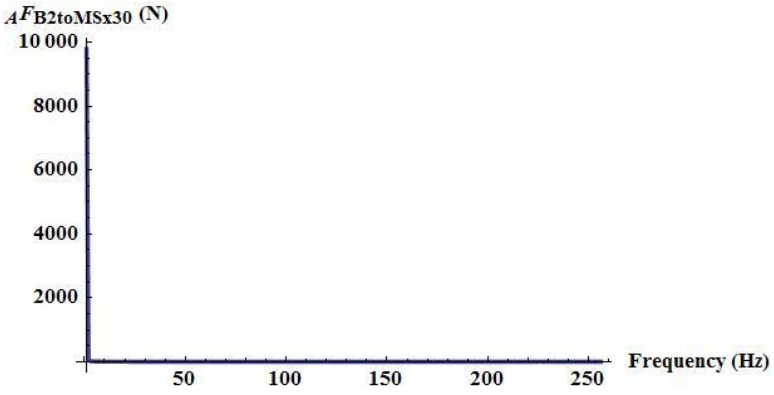

Figure 4-51: Amplitude spectrum of the reaction force component along the "a_1" direction from the main shaft at the thrust roller bearing to the pump case (θ = 30°)

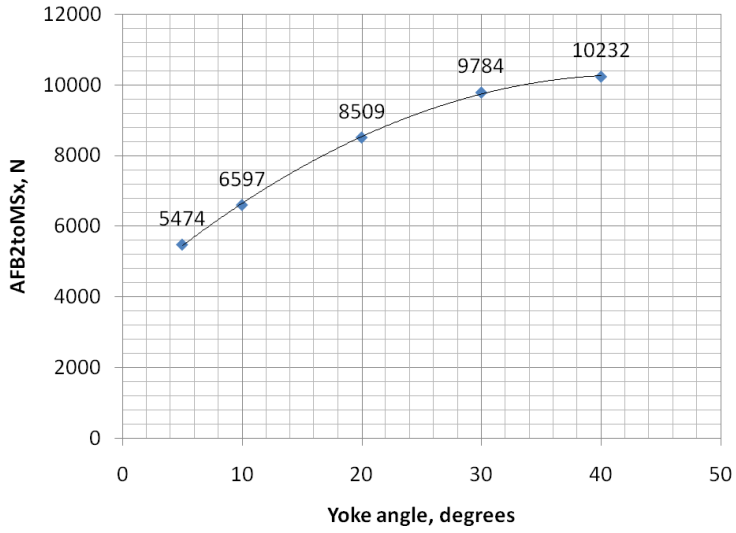

Figure 4-52: Steady state value of the "a_1" component of the reaction force from the main shaft at the thrust roller bearing to the pump case as a function of the yoke angle

The amplitude spectrum of the reaction force from the main shaft to the pump case at the thrust roller bearing along the "a_2" direction is shown in Figure 4-53 for a yoke angle of 30° and shaft speed of 1500 rpm. There are two harmonics, which occur at frequencies of 225 Hz and 450 Hz. What looks like a harmonic at zero Hz is indeed the steady state value of the a_2 component at a given yoke angle. The steady state value increases linearly with the yoke angle.

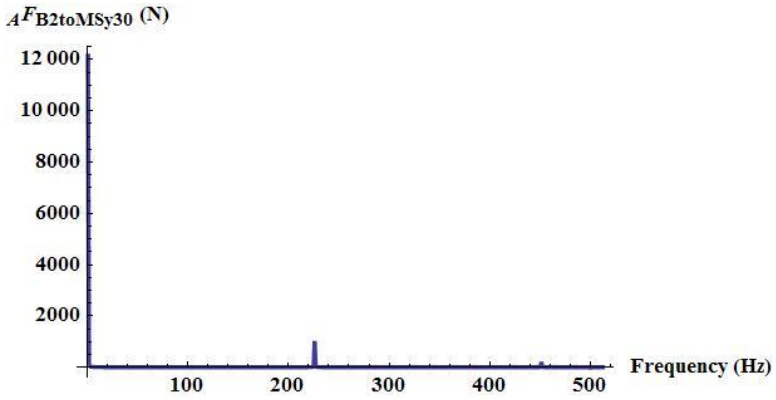

Figure 4-53: Amplitude spectrum of the reaction force component along the "a_2" direction from the main shaft at the thrust roller bearing to the pump case (θ = 30°)

The harmonics at 225 Hz and 450 Hz increase parabolically with the yoke angle as can be illustrated in Figure 4-54.

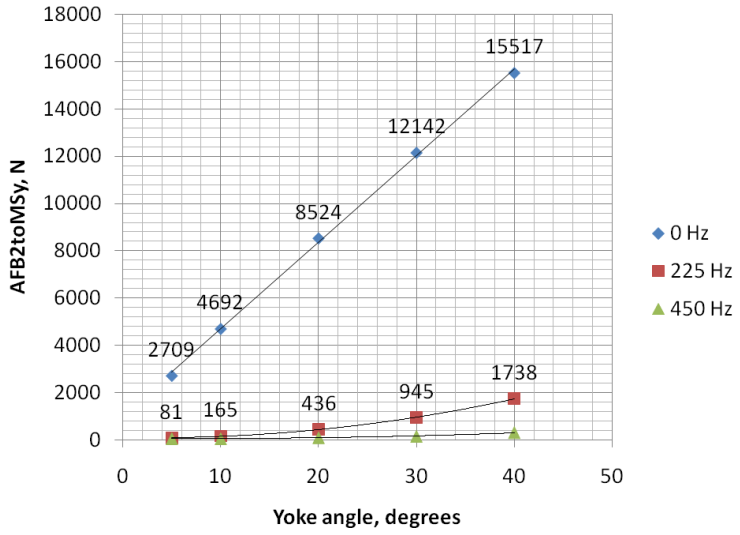

Figure 4-54: Amplitude spectrum of the "a_2" component of the reaction force from the main shaft at the thrust roller bearing to the pump case as a function of the yoke angle

Figure 4-55 shows the amplitude spectrum of the "a_3" component of the reaction force at the thrust roller bearing at a yoke angle of 30° and shaft speed of 1500 rpm. This component has three major harmonics at 225, 350, and 450 Hz respectively. What it looks like as a harmonic at zero Hz is in reality the steady state value of the a_3 component at a given yoke angle. The steady state value of the a_3 component decreases parabolically with the yoke angle as can be seen in Figure 4-56 and that may explain in part the noise heard when testing the pump at zero degrees yoke angle.

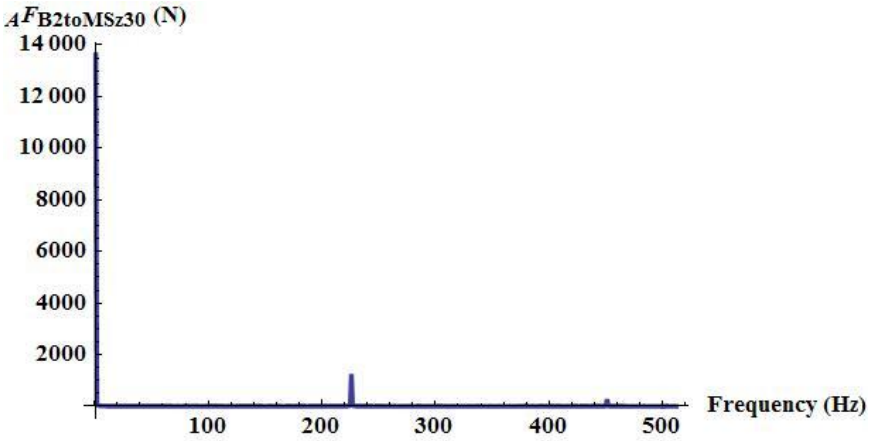

Figure 4-55: Amplitude spectrum of the reaction force component along the "a_3" direction from the main shaft at the thrust roller bearing to the pump case ($\theta = 30°$)

The amplitude of the harmonics at 225, 350, and 450 Hz increases parabolically with the yoke angle.

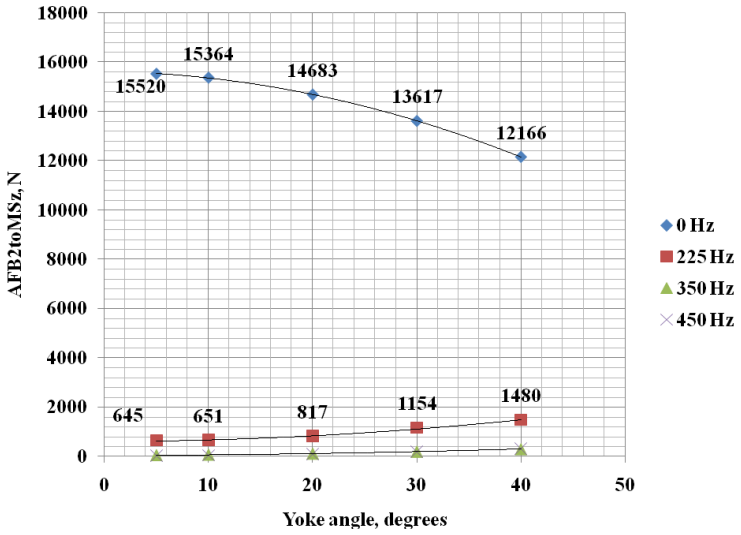

Figure 4-56: Amplitude spectrum of the "a_3" component of the reaction force from the main shaft at the thrust roller bearing to the pump case as a function of the yoke angle

4.3.3 Reaction forces on the case from yoke axis of rotation at the suction port

Figure 4-57 shows the "a_1" component of the reaction force at the yoke axis of rotation (suction port side) for yoke angles of 5°, 10°, 20°, 30°, 40° and shaft speed of 1500 rpm. This force component fluctuates in a sinusoidal fashion and is independent of the yoke angle.

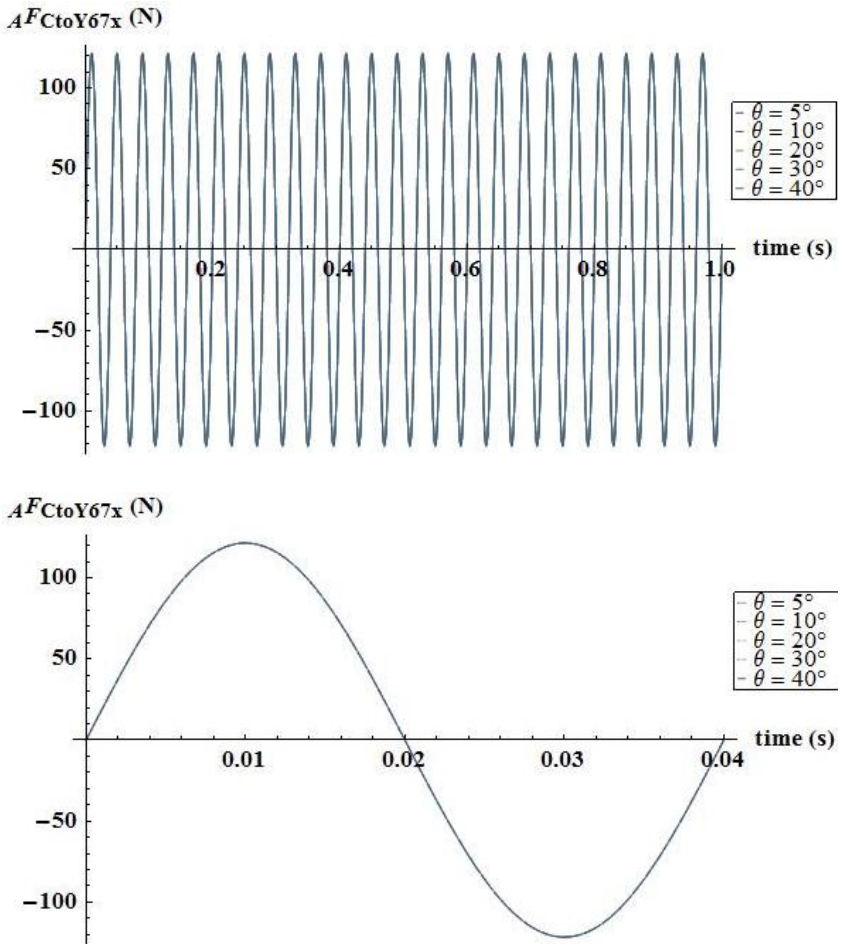

Figure 4-57: Reaction force component along the "a_1" direction from the yoke to the case of the pump at the suction port

Figure 4-58 shows the amplitude spectrum of the "a_1" component of the reaction force from the yoke axis of rotation at the suction port to the pump. This component has one

harmonic that occurs at a frequency of 25 Hz. The amplitude of this fundamental harmonic is independent of the yoke angle as can be depicted in Figure 4-59. Therefore, since this component is independent of the yoke angle, it can be said that this component contribute to the noise heard at zero yoke angle.

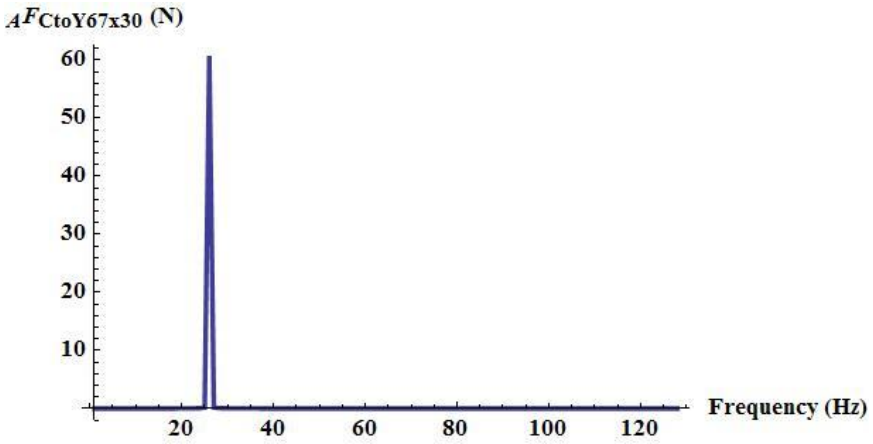

Figure 4-58: Amplitude spectrum of the reaction force component along the "a_1" direction from the yoke axis of rotation to the pump case at the suction port (θ = 30°)

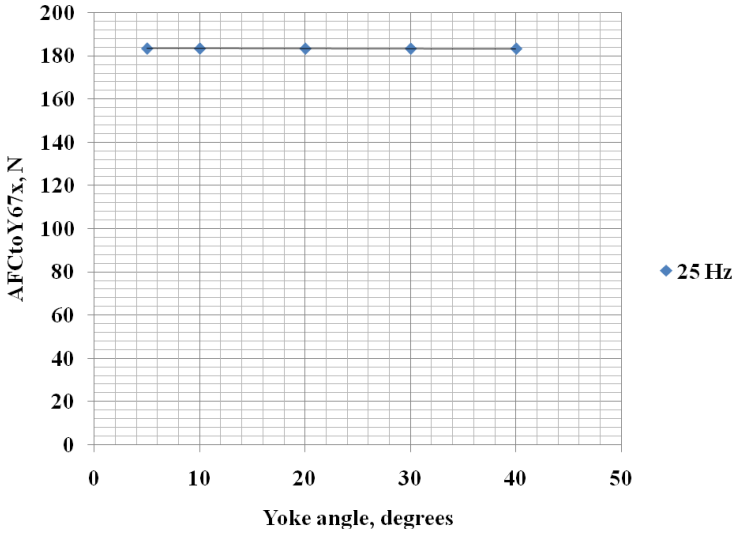

Figure 4-59: Amplitude spectrum of the "a_1" component of the reaction force from the yoke to the pump case (suction portside) as a function of the yoke angle

The variation of the "a_2" component of the force from the yoke to the pump case at the suction port is shown in Figure 4-60. The mean magnitude of this component increases with time because of the increased pressure differential that has to be carried out by the pump to deliver oil from the LPA to the HPA. This component fluctuates about the mean value with nine major pulsations for each revolution of the main shaft.

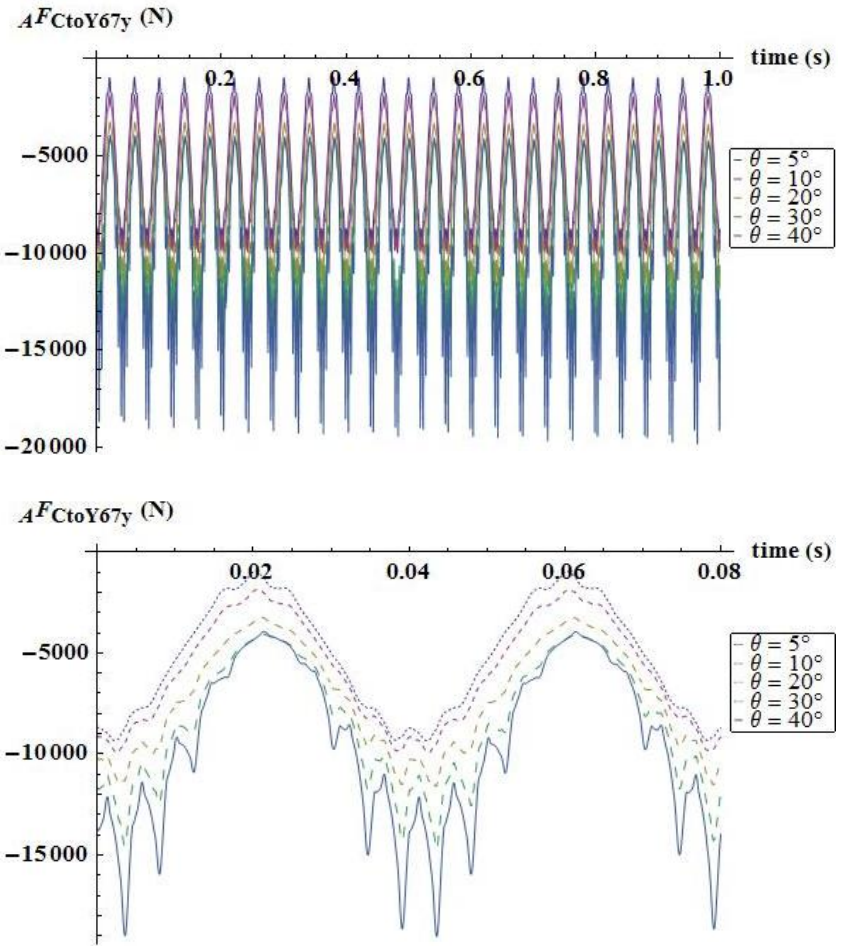

Figure 4-60: Reaction force component along the "a_2" direction from the yoke to the case of the pump at the suction port

Figure 4-61 shows the variation of the mean value of the reaction force at the suction port calculated over a period of one second. The mean value of the "a_2" component increases

linearly with the yoke angle. On the other hand, the value of the component along the "a_3" direction decreases as the yoke angle increases. Overall, the average value of the magnitude of this reaction increases proportionally with the yoke angle.

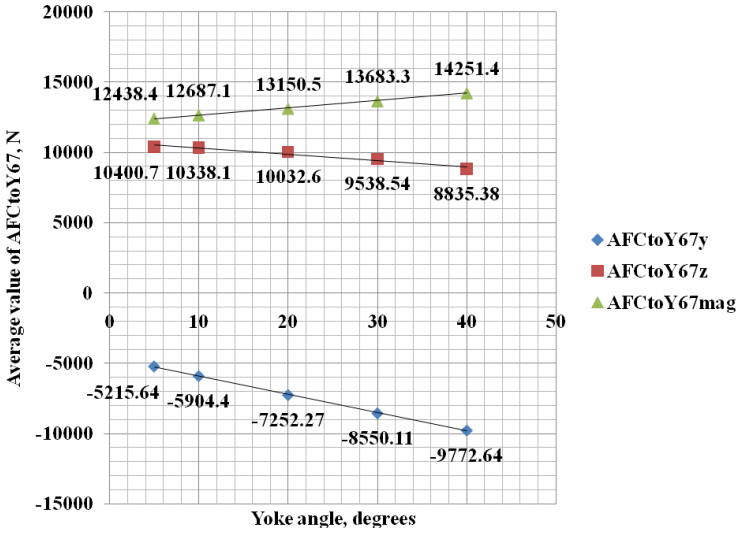

Figure 4-61: Average value of the components of the reaction force from the yoke to the case of the pump at the suction port

The "a_2" component of the force from the yoke to the pump case has four major harmonics at 25, 225, 200, and 250 Hz respectively as can be seen in Figure 4-63. What seems like a harmonic at 0 Hz is indeed the steady state value of the "a_2" component. This steady value increases linearly with the yoke. Initially, the fundamental harmonic at 25 Hz decreases with the yoke angle until reaching a minimum at 20°. After that, it increases again as the yoke angle increases. The remaining harmonics at 225, 200, and 250 Hz increase parabolically and slowly with the yoke angle.

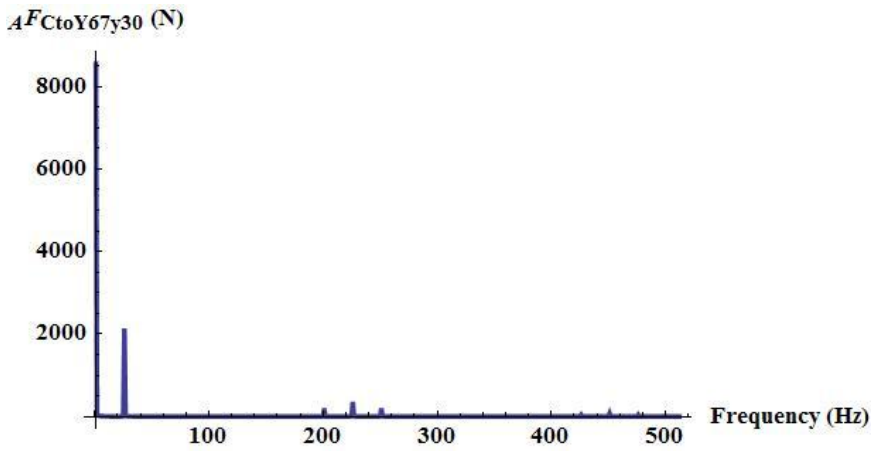

Figure 4-62: Amplitude spectrum of the reaction force component along the "a_2" direction from the yoke axis of rotation to the pump case at the suction port (θ = 30°)

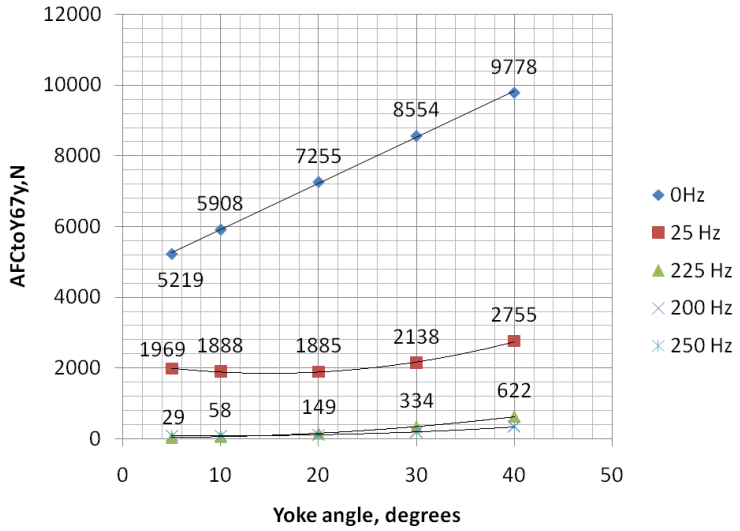

Figure 4-63: Amplitude spectrum of the "a_2" component of the reaction force from the yoke to the pump case (suction portside) as a function of the yoke angle

Figure 4-64 shows the variation of the "a_3" component of the force from the yoke to the pump case with time. This component fluctuates about the mean value with nine major pulsations due to the limited number of pistons.

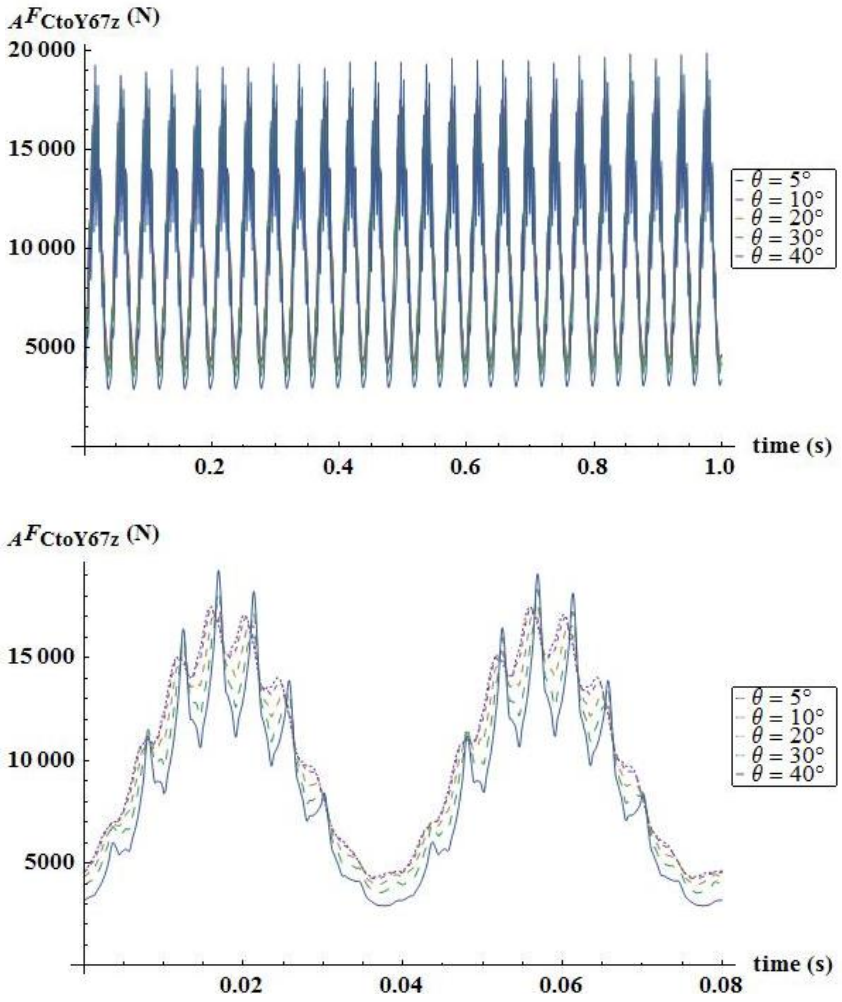

Figure 4-64: Reaction force component along the "a_3" direction from the yoke to the case of the pump at the suction port

The amplitude spectrum of the force component from the yoke to the case at the suction port along the "a_3" direction is shown in Figure 4-65 for a yoke angle of 30° and shaft speed of 1500 rpm.

The "a_3" component has four major harmonics at frequencies of 25, 225, 200, and 250 Hz respectively as can be seen in Figure 4-65 and Figure 4-66. What appears as a harmonic at zero Hz is actually the steady state value of the "a_3" component. This steady state value decreases slowly as the yoke angle increases from 5° to 40. This explains in

part the reason of the noise heard at zero degrees yoke angle. The fundamental harmonic, which occurs at a frequency of 25 Hz, remains unchanged as the yoke angle changes. The harmonics at frequencies of 225, 200, and 250 Hz increase parabolically and slowly with the yoke angle.

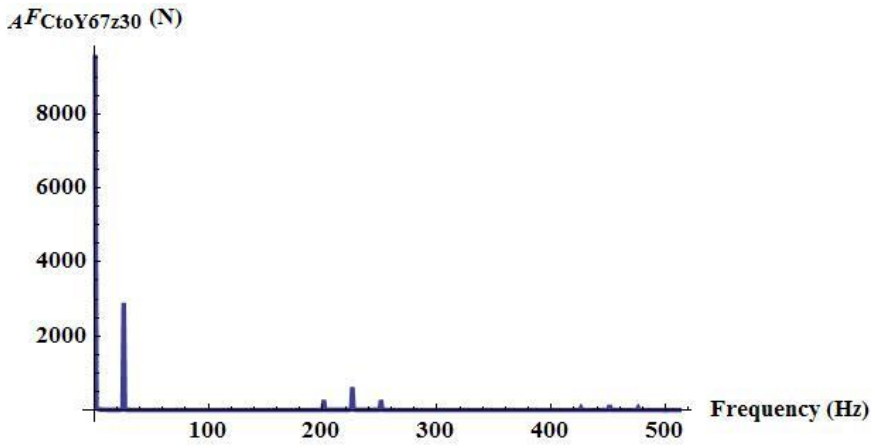

Figure 4-65: Amplitude spectrum of the reaction force component along the "a_3" direction from the yoke axis of rotation to the pump case at the suction port (θ = 30°)

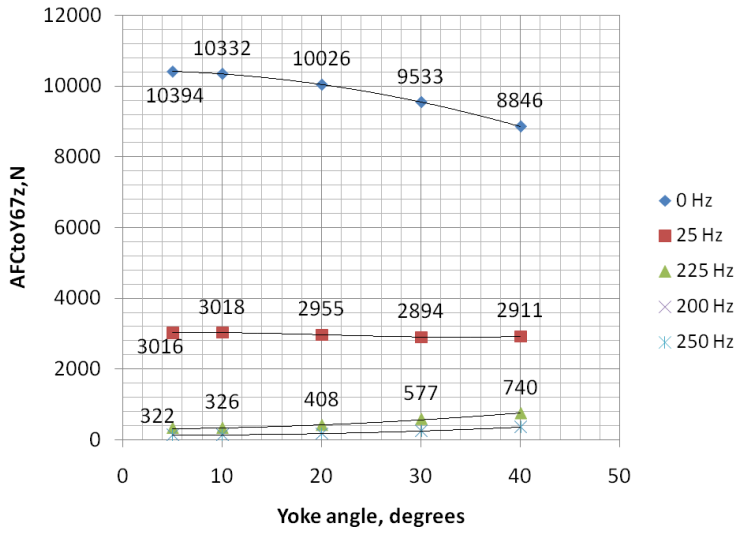

Figure 4-66: Amplitude spectrum of the "a_3" component of the reaction force from the yoke to the pump case (suction portside) as a function of the yoke angle

Figure 4-67 shows the magnitude of the reaction force from the yoke to the pump case at the suction port.

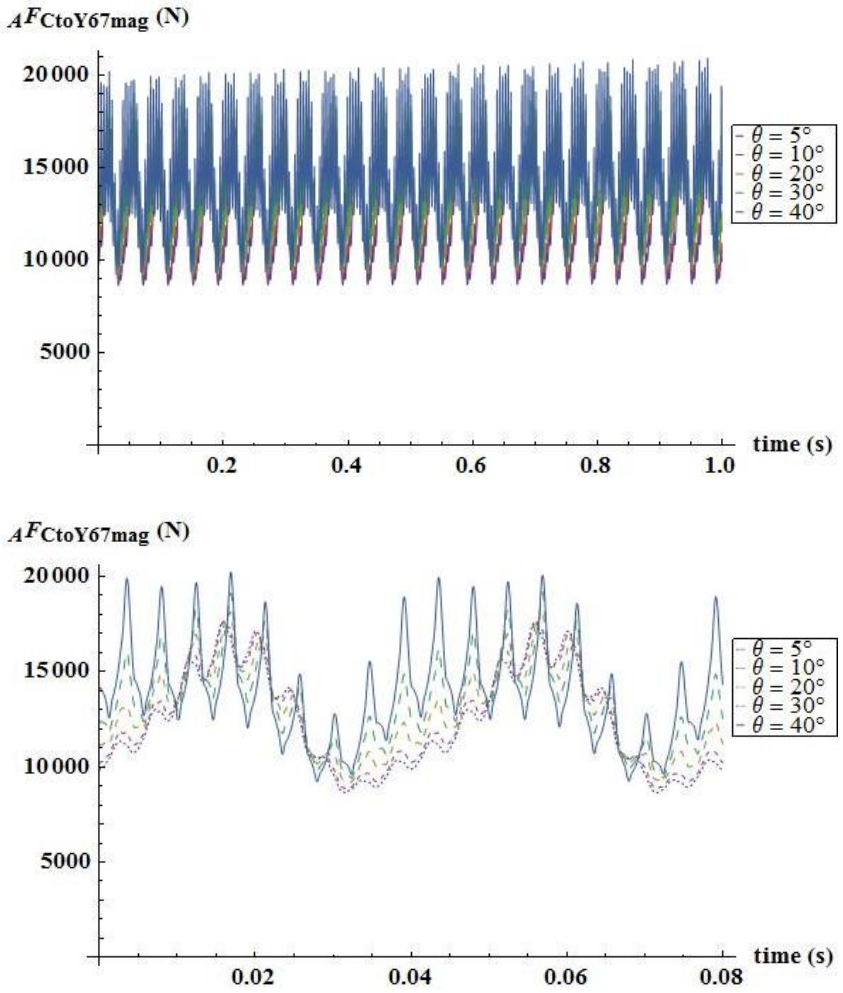

Figure 4-67: magnitude of the reaction force from the yoke to the case of the pump at the suction port

Figure 4-68 shows the amplitude spectrum of the magnitude of the reaction force from the yoke at the suction side. The first highest harmonics occur at frequencies of 25, 225, 50, 450, and 350 Hz respectively. What it looks like a harmonic at zero Hz is in fact the steady state value of the magnitude of the reaction force at the suction port. This steady state value increases linearly with the yoke angle. The fundamental harmonic at 25 Hz

decreases linearly with the yoke angle as illustrated in Figure 4-69. The second harmonic at 225 Hz increases parabolically and slowly with the yoke angle. The remaining harmonics are independent of the yoke angle.

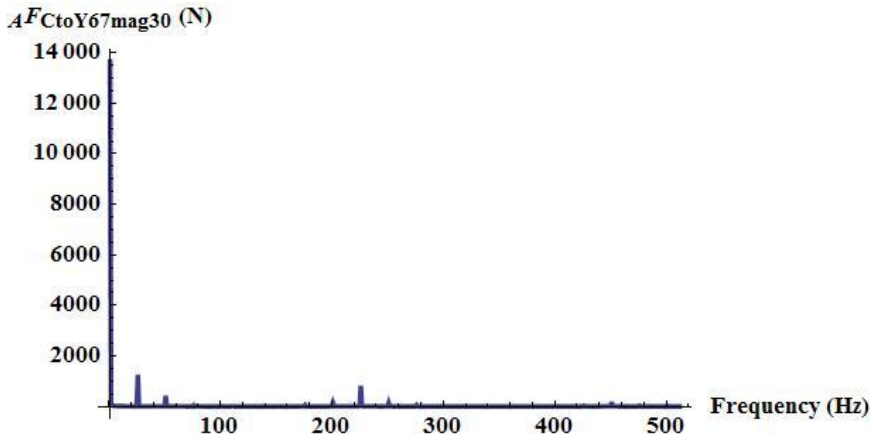

Figure 4-68: Amplitude spectrum of the magnitude of the reaction force from the yoke axis of rotation to the pump case at the suction port (θ = 30°)

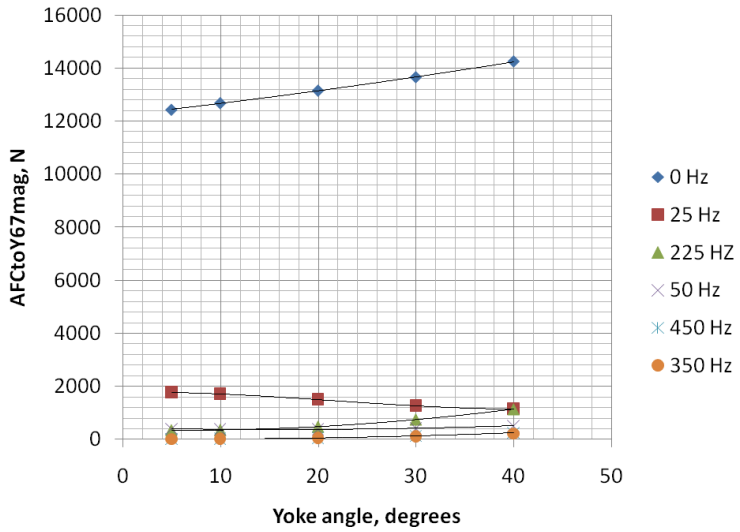

Figure 4-69: Amplitude spectrum of magnitude of the reaction force from the yoke to the pump case (suction portside) as a function of the yoke angle

4.3.4 Reaction forces on the case from yoke axis of rotation at the discharge port

Figure 4-70 to Figure 4-72 show the variation of the reaction force from the yoke to the pump case at the yoke axis of rotation (Discharge side) at a shaft speed of 1500 rpm. The force components at the discharge side behave in a similar fashion as those at the suction side. In addition, these components have a pulse every 40° of the main shaft rotation.

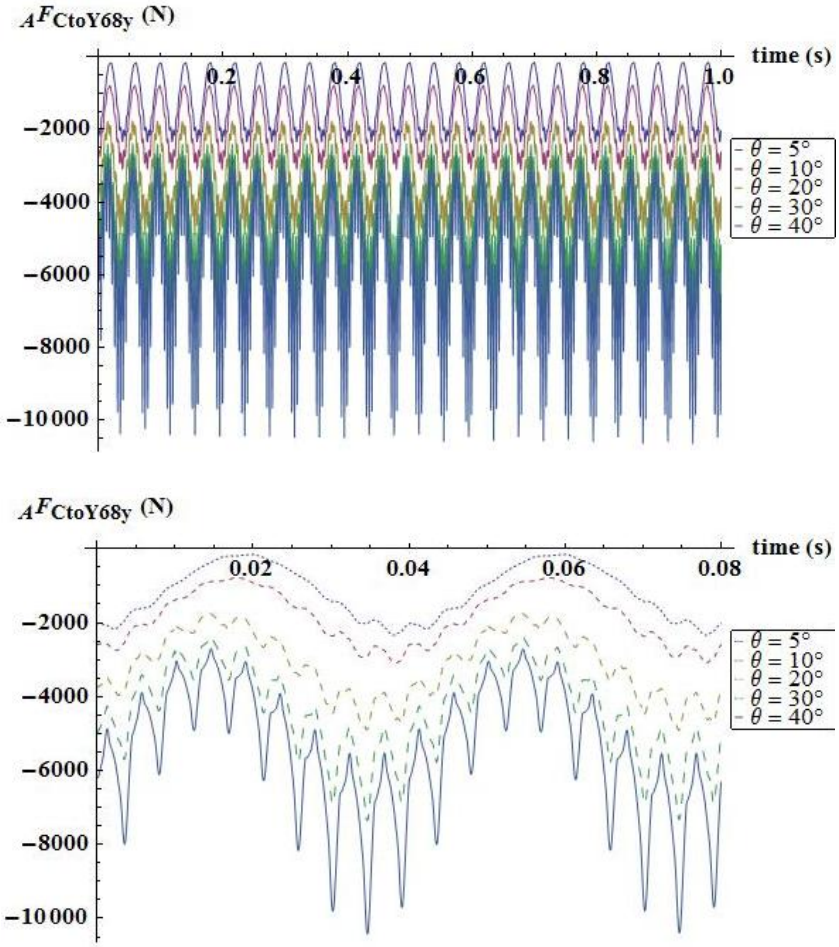

Figure 4-70: Reaction force component along the "a_2" direction from the yoke to the case of the pump at the discharge port

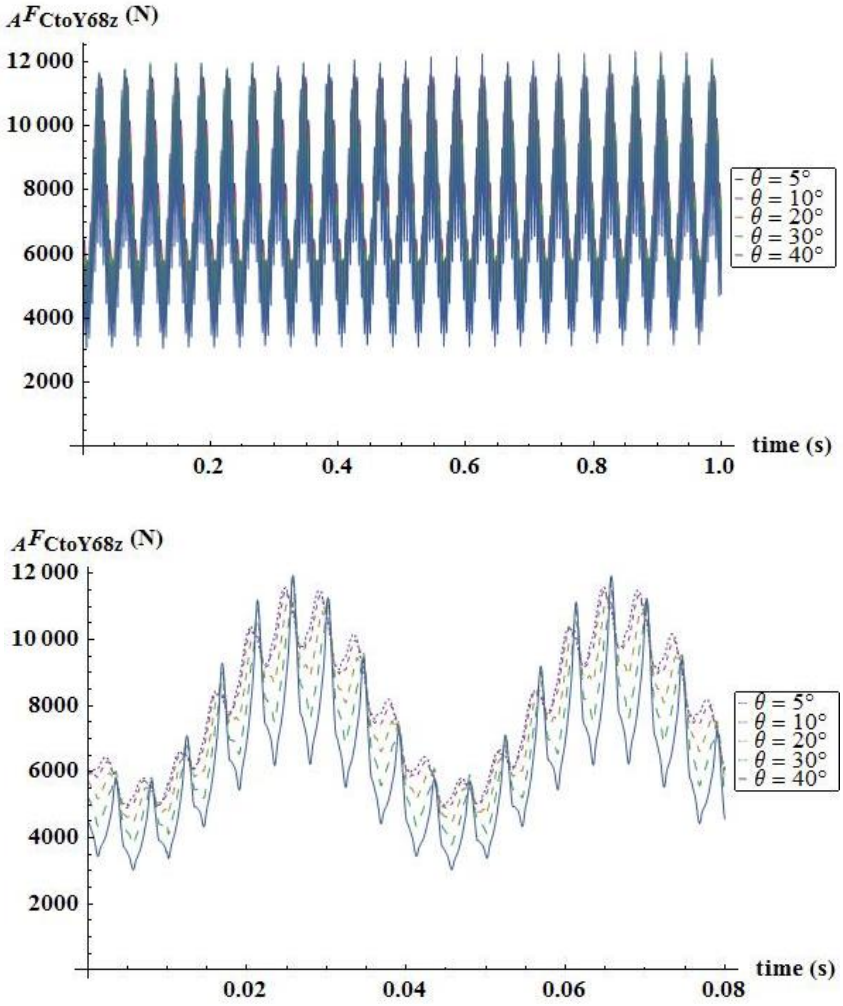

Figure 4-71: Reaction force component along the "a_3" direction from the yoke to the case of the pump at the discharge port

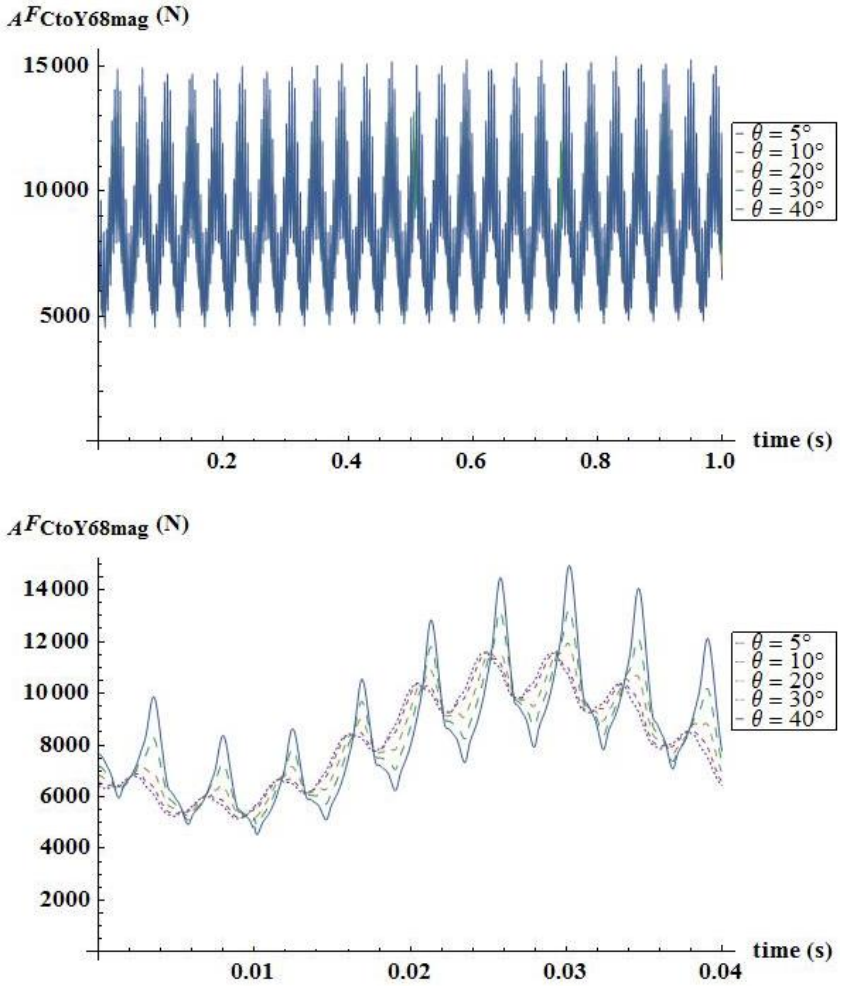

Figure 4-72: Magnitude of the reaction force from the yoke to the case of the pump at the discharge port

Figure 4-73 shows the variation of the average value (calculated over a period of one second) of the components of the reaction force from the yoke to the pump case with the yoke angle. The value of the average of the component along the "a_2" direction increases linearly with the yoke angle at a relatively rapid rate. On the other hand, the value along the "a_3" direction decreases slowly with the yoke angle. Overall, the average value of the magnitude of this force increases very slowly with the yoke angle.

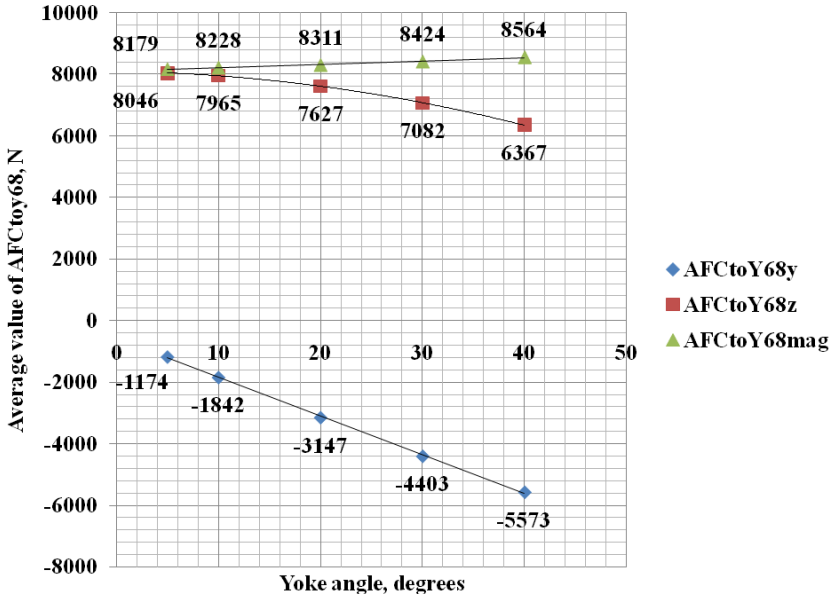

Figure 4-73: Average values of the components of the reaction force from the yoke to the pump case at the discharge port vs. yoke angle

Generally, the amplitude of the harmonics of the force from the yoke to the pump case at the discharge port increases with the yoke angle as can be noticed from Figure 4-74 and Figure 4-75. What appears as a harmonic at zero Hz is indeed the steady state value of "a_2" component. This steady state value increases linearly with the yoke angle. The fundamental harmonic at 25 Hz and the second harmonic at 225 Hz increase parabolically

with the yoke angle. The remaining smaller harmonics at 200, 250, and 350 Hz are nearly independent of the yoke angle.

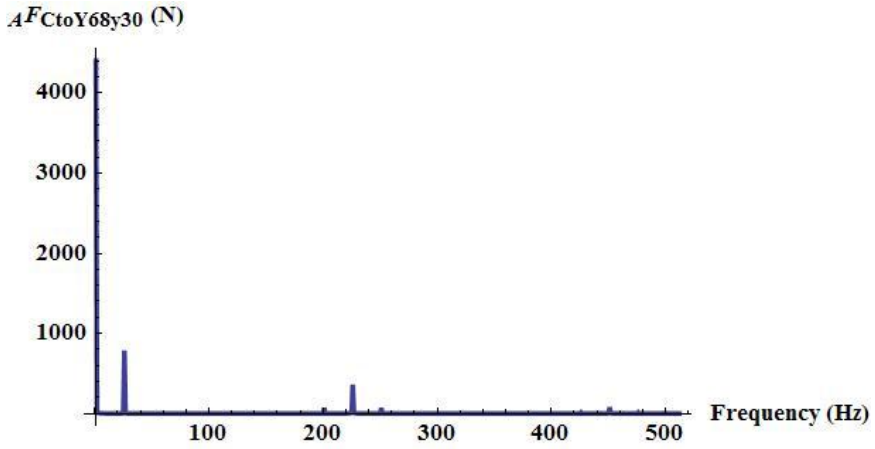

Figure 4-74: Amplitude spectrum of the "a_2" component of the reaction force from the yoke axis of rotation to the pump case at the discharge port (θ = 30°)

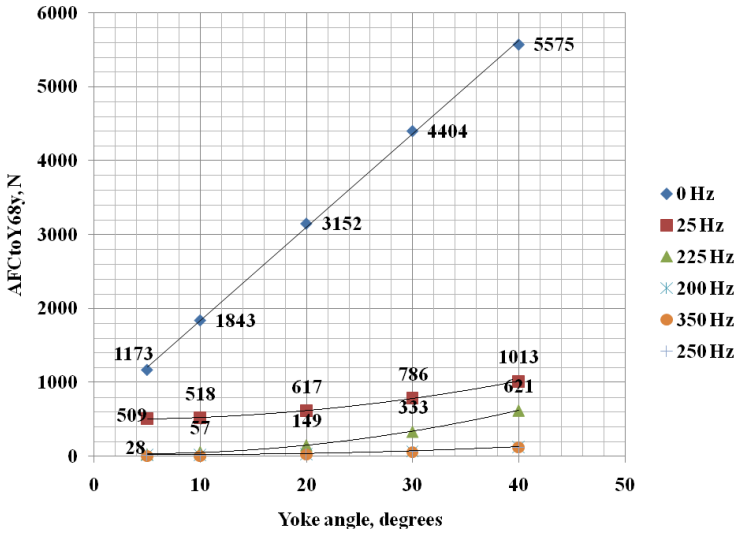

Figure 4-75: Amplitude spectrum of the "a_2" component of the reaction force from the yoke to the pump case (discharge portside) as a function of the yoke angle

The amplitude spectrum of the "a_3" component of the force from the yoke to the pump case at the discharge port side is shown in Figure 4-76. It has two major harmonics at 25

Hz, and 225 Hz. What it looks like, as a harmonic at zero Hz is actually the steady state value of the "a3 component. The steady state value decreases parabolically and slowly with the yoke angle.

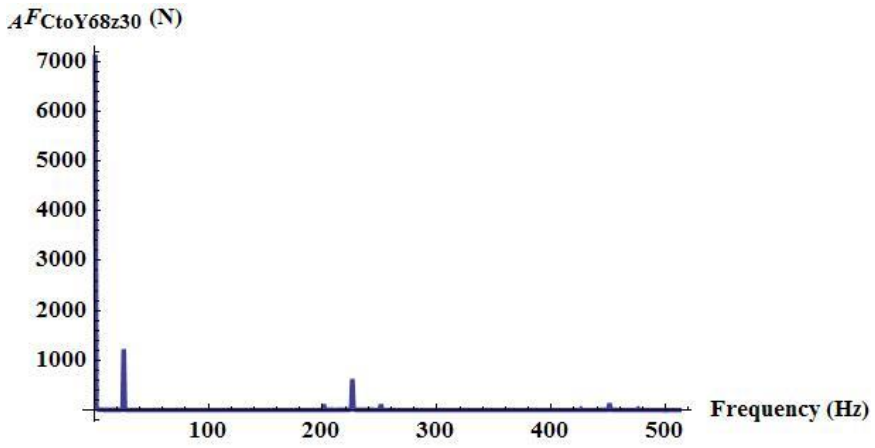

Figure 4-76: Amplitude spectrum of the "a_3" component of the reaction force from the yoke axis of rotation to the pump case at the discharge port ($\theta = 30°$)

The fundamental harmonic at 25 Hz decreases very slowly with the yoke angle as can be seen in Figure 4-77. The second harmonic at 225 Hz increases parabolically with the yoke angle. The remaining higher frequency harmonics are nearly independent of the yoke angle.

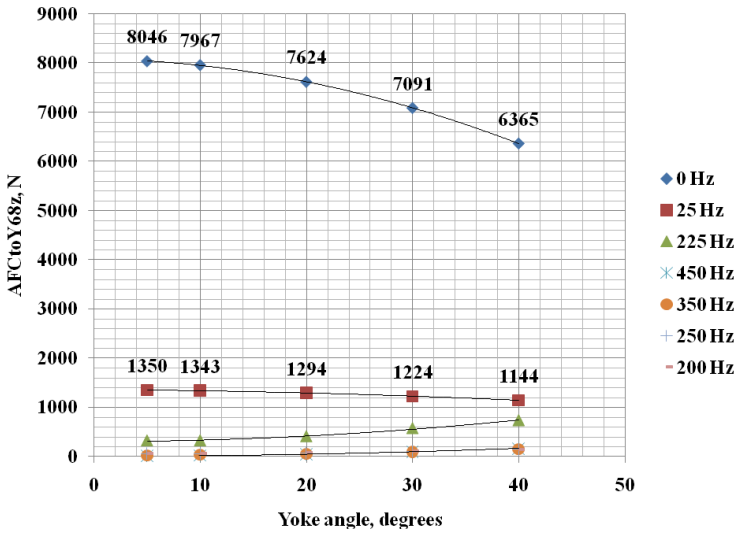

Figure 4-77: Amplitude spectrum of the "a_3" component of the reaction force from the yoke to the pump case (discharge portside) as a function of the yoke angle

4.3.5 Reaction force on the case from the ram

Figure 4-78 to Figure 4-80 shows the variation of the reaction force from ram to the pump case as a function of yoke angle at a shaft speed of 1500 rpm. The average value of the magnitude of the force at the ram is computed over a period of 1 second. The average value increases as the yoke angle increases until reaching a maximum at 15° as can be seen in Figure 4-81. Then it decreases until reaching a minimum at 35°. Beyond a yoke angle of 35°, the average value increases again.

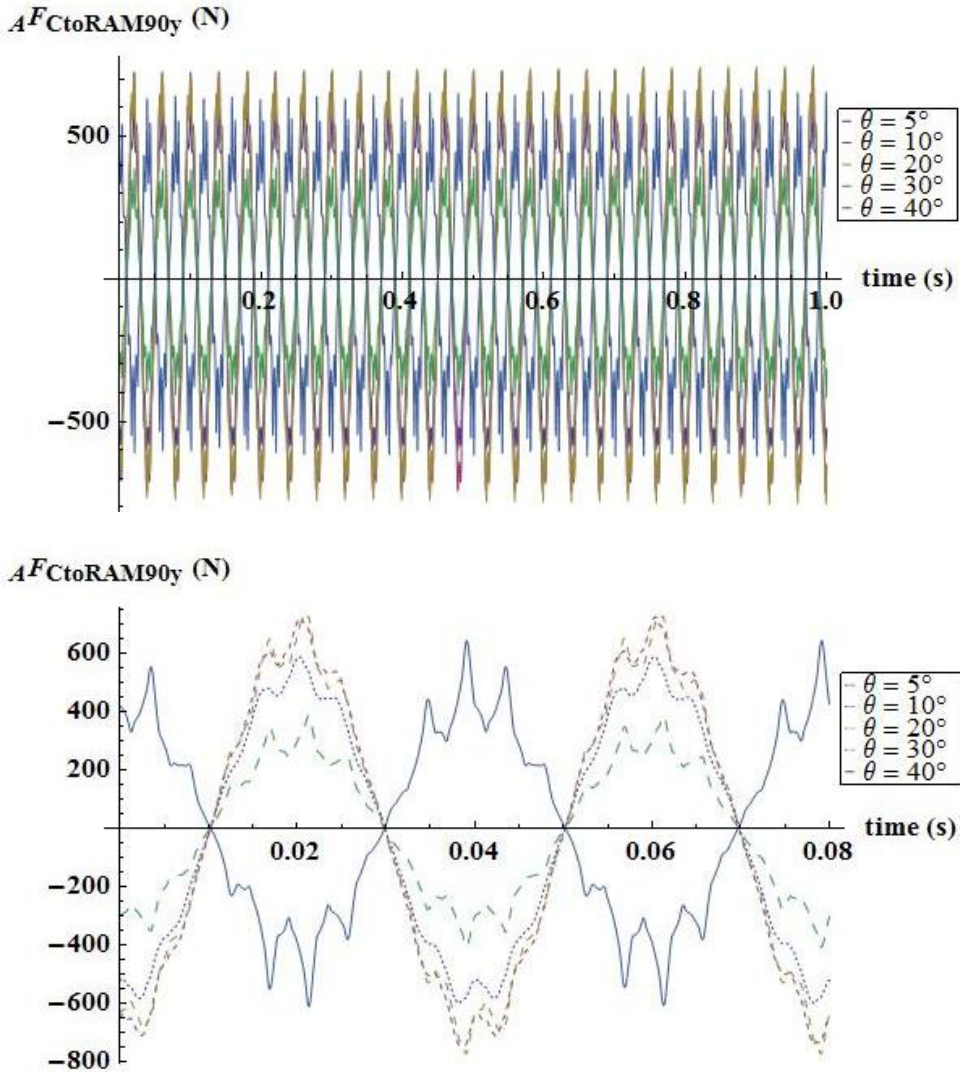

Figure 4-78: Reaction force from the ram along the "a_2" direction

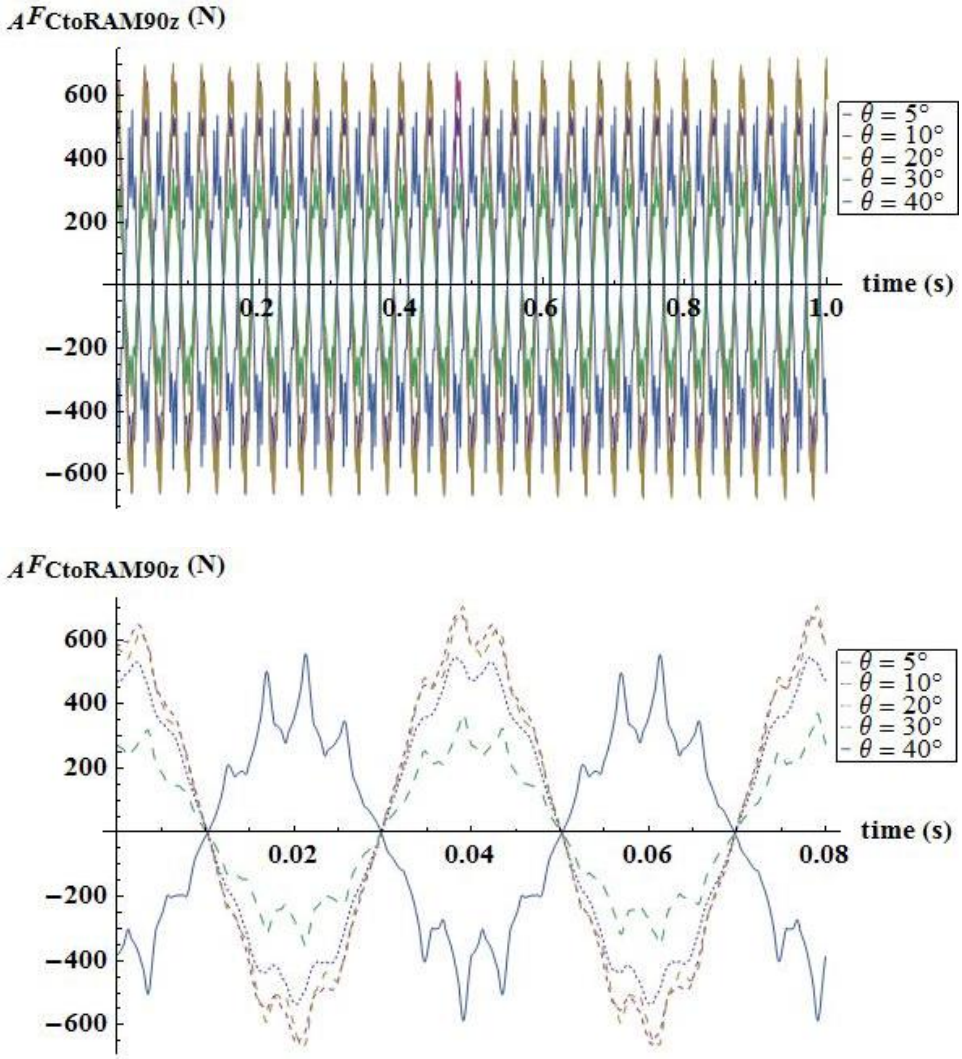

Figure 4-79: Reaction force from the ram along the "a_3" direction

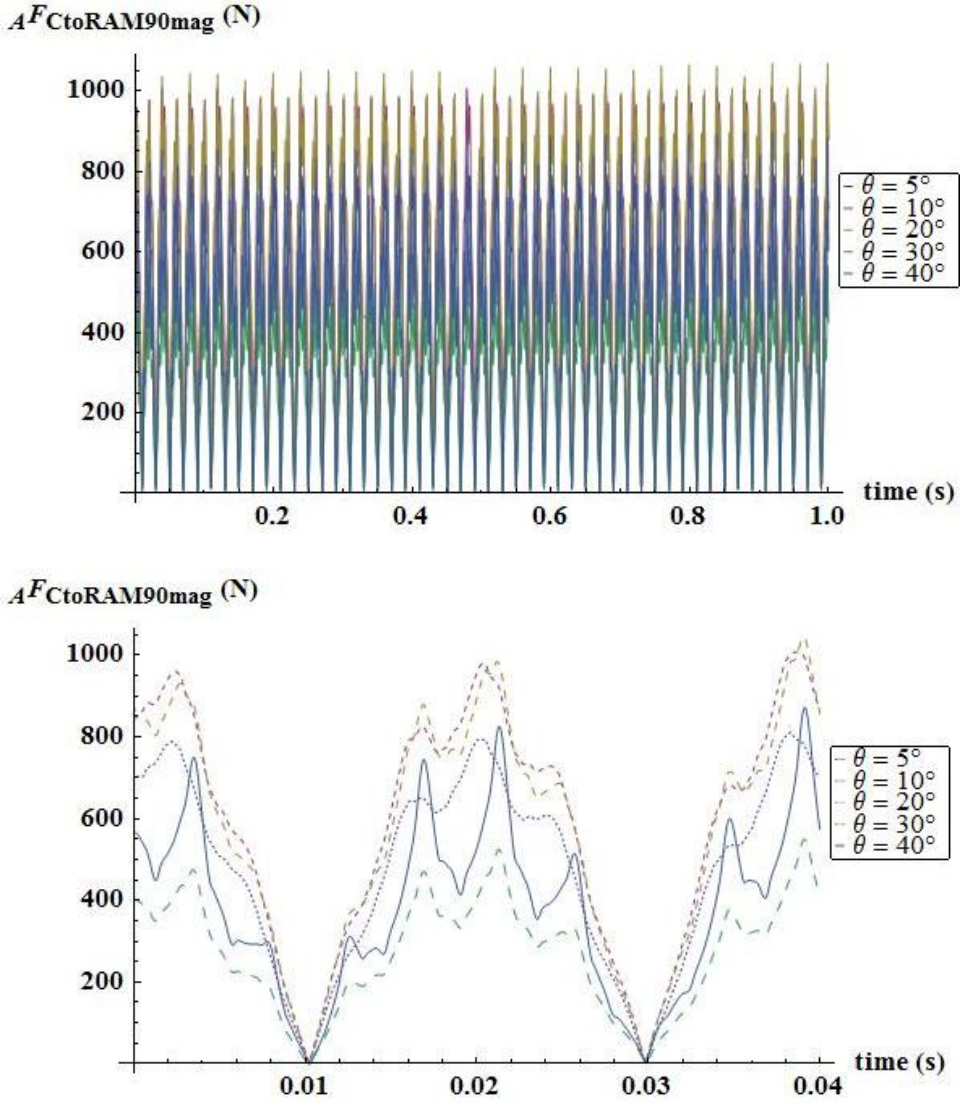

Figure 4-80: Magnitude of the reaction force from the ram

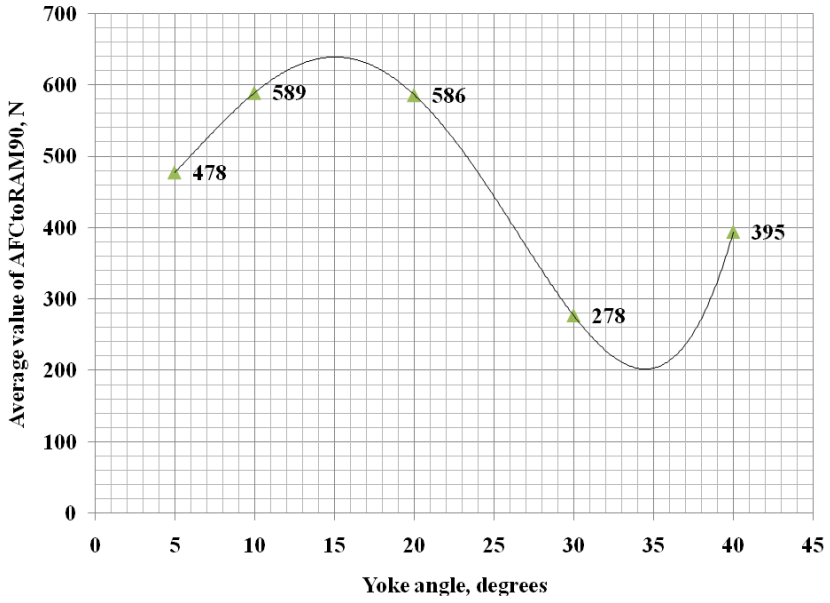

Figure 4-81: Average value of the magnitude of the force at the ram

Figure 4-82 shows the amplitude spectrum of the reaction force at the ram as a function of the yoke angle. There are three major harmonics at 25, 200, and 250 Hz respectively. The amplitude of the fundamental harmonic at 25 Hz increases with the yoke angle until reaching a maximum at 15°. After that, it decreases until reaching a minimum at 35°. Beyond 35°, the amplitude resumes to increase as the yoke angle increases. The amplitude of the harmonics at 200 Hz and 250 Hz increases with the yoke angle until reaching a maximum at 20°. After that, it decreases until reaching a minimum at 30°. Beyond 30°, the amplitude resumes to increase as the yoke angle increases.

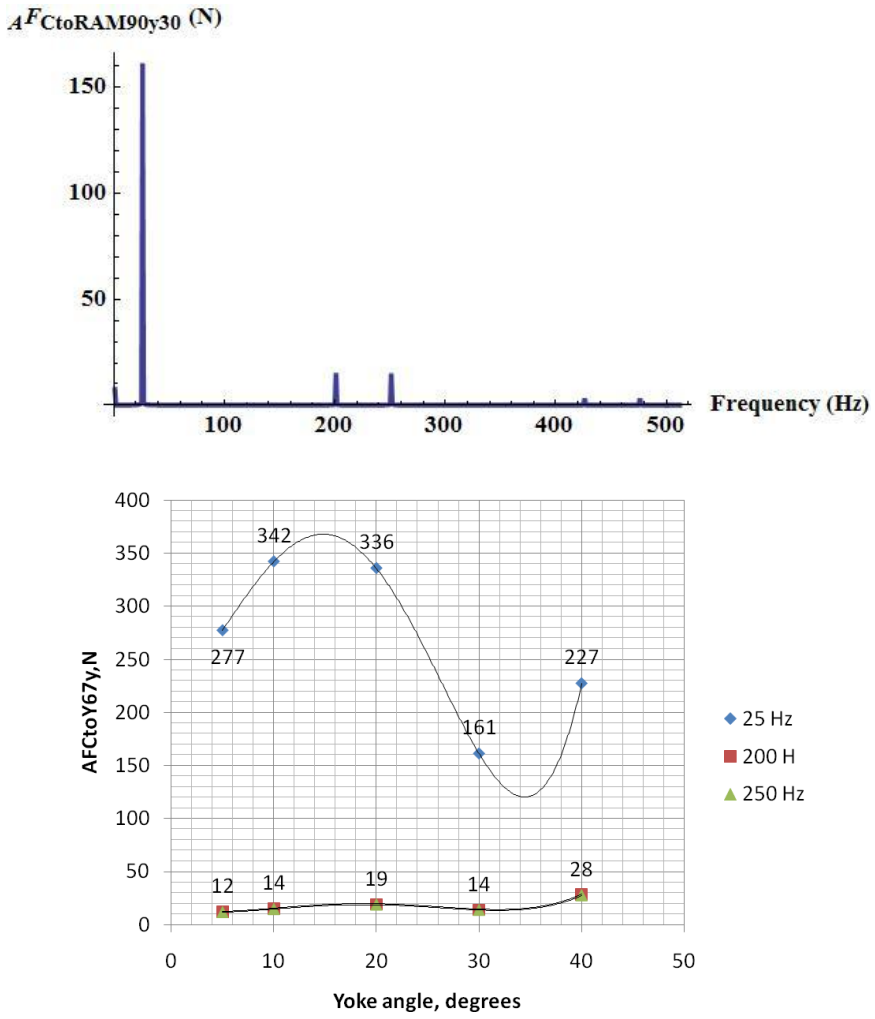

Figure 4-82: Amplitude spectrum of the reaction force component along the "a_2" direction at the ram (upper graph for θ = 30°)

Figure 4-83 shows the amplitude spectrum of the reaction force at the ram along the "a_3" direction. This component has three major harmonics at 25, 200, and 250 Hz respectively. These harmonics vary with the yoke angle in the same way as the component along the "a_2" direction varies.

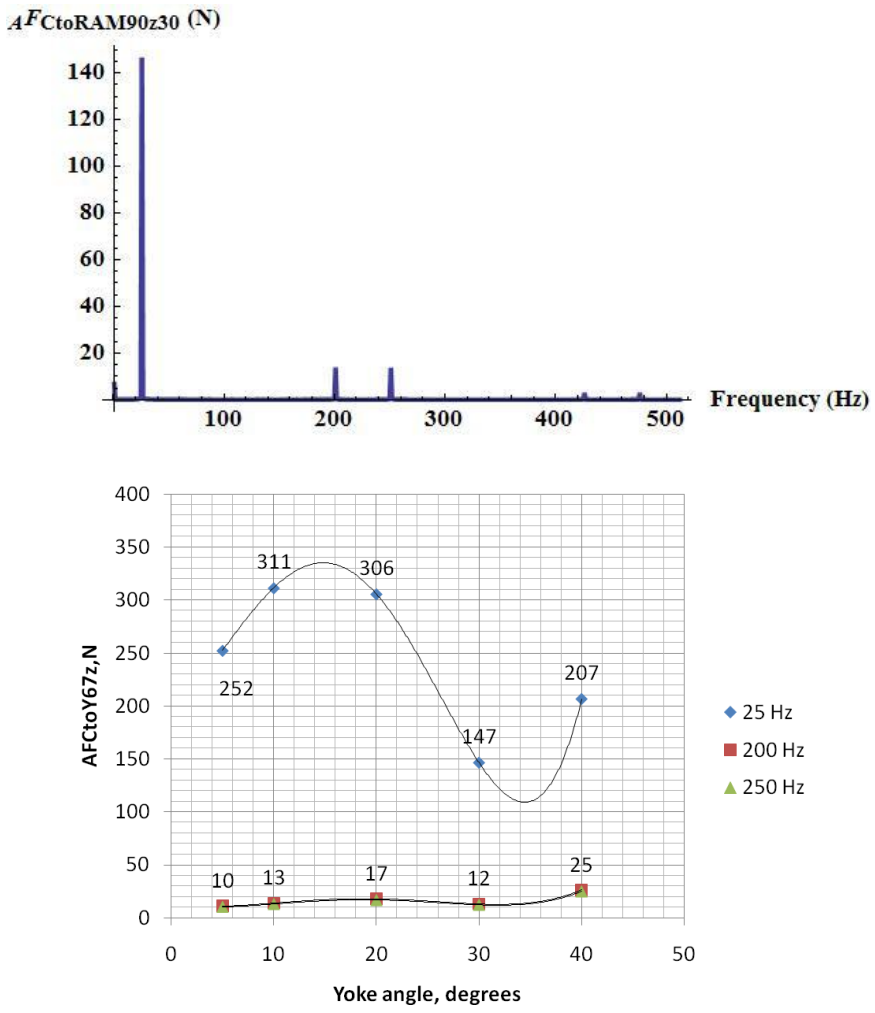

Figure 4-83: Amplitude spectrum of the reaction force component along the "a_3" direction at the ram (upper graph for θ = 30°)

Figure 4-84 shows the amplitude spectrum of the magnitude of the reaction force at the ram. There are three major harmonics at 50, 100, and 225 Hz. What it looks like a harmonic at zero Hz is indeed the steady state value of the reaction force. The harmonics of the magnitude of the reaction force at the ram vary with the yoke angle as the component along the "a_2" direction does.

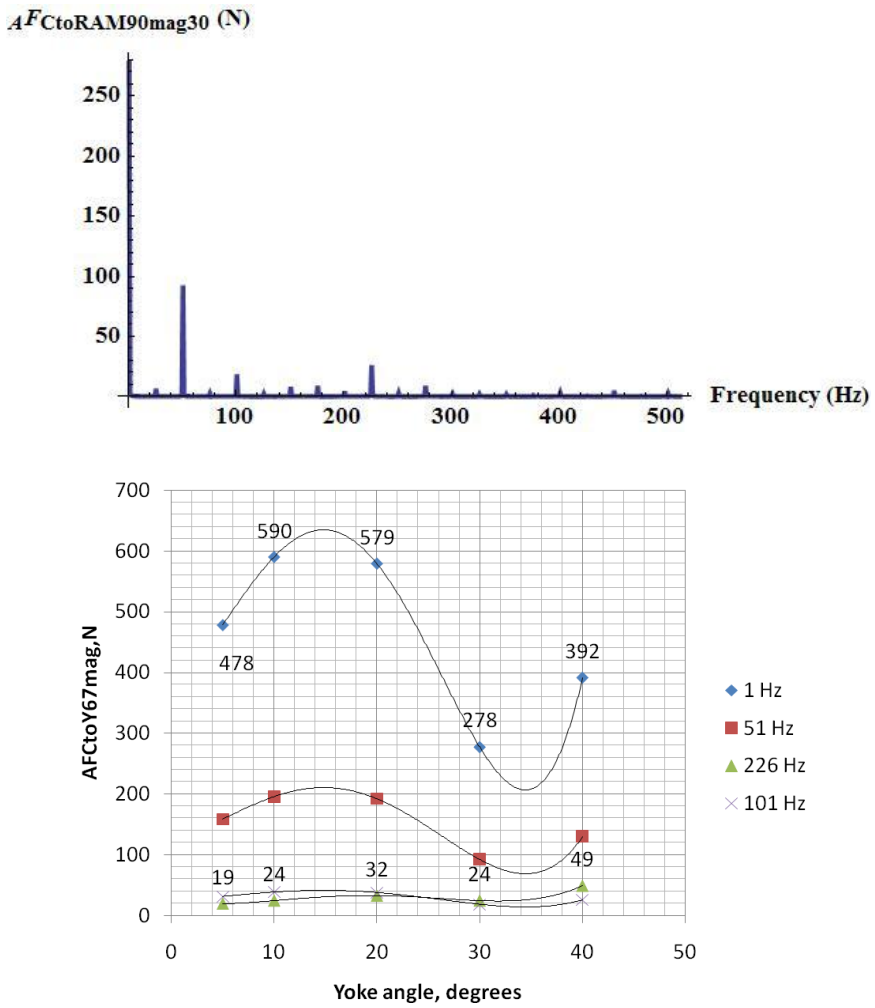

Figure 4-84: Amplitude spectrum of the magnitude of the reaction force at the ram

CHAPTER 5:SUMMARY AND CONCLUSIONS

This chapter summarizes the presented analytical work and dynamic modeling of the bent axes pump, which is connected to LPA at the suction port and HPA at the discharge port. In addition, it presents the conclusions and recommendations for future research.

5.1 Summary

The objective of this research is to find the dominating harmonics that create the noise in the bent axis pump. The pump will be working within the circuit of a hydraulic hybrid vehicle. Knowing the sources of noise enables taking the appropriate decisions in terms of design, control strategy, and the implementation of anti-noise techniques and procedures either to the pump or to the hydraulic system to reduce the noise level to acceptable levels.

This study derived a dynamic mathematical model of a bent axis pump with the purpose of finding the variation of pressure head, flow rate, and dynamic forces acting on the pump's case as a function of the angular rotations of both the main shaft and the yoke. The forces acting on the pump's case due to the interaction with the moving internal parts of the pump were determined both in the time and frequency domains.

A kinematic analysis was implemented to find velocities, accelerations, angular velocities, and angular accelerations for each part of the pump. Then, the equation of motion for each part as well as the whole system has been determined using Newtonian

mechanics. Consequently, the forces acting on the pump case are determined numerically using Mathematica^{TM} in the time and frequency domains.

The theoretical model was created using Mathematica^{TM} and is examined against well know conditions of the rotation of the main shaft and the yoke and compared against a CAD model created using ADAMS/View software.

The theoretical model of the piston pressure and flow rate was also solved numerically against well know conditions of the rotation of the main shaft and the yoke. The geometric data of an actual variable displacement pump was used in getting the numerical solutions.

Although the numerical solution of the mathematical model is implemented at main shaft speed of 1500 rpm for yoke angles of 5°, 10°, 20°, 30°, and 40° respectively, one has to keep in mind that this model can solve for any conditions of main shaft rotation and yoke angular positions no matter how they vary with time.

5.2 Conclusions

The following conclusions are based on the analytical and modeling work presented in this study:

Kinematics of the pump components

- The kinem**a**tic model was able to predict the variations of the angular velocities and accelerations and the velocities and the accelerations of the center of gravity of the entire pump's parts starting from the main shaft up to the yoke.

- For the case when the main shaft rotates at a constant angular velocity at a fixed angular position of the yoke, the angular rotation of the barrel is the same as the angular rotation of the main shaft.
- For a given yoke angle the piston displacement with respect to the barrel varies sinusoidally with the main shaft rotation.
- For the piston and the connecting rod, there is a matching between the mathematical model and the ADAMS model along the "a_1" and "a_2" directions for both velocity and acceleration. Although there is some phase shift between the mathematical model and ADAMS model along the "a_3" direction, the trend is the same and the maximum and minimum of both models have the same values. In addition, the "a_3" component is about 3% of either the "a_1" or the "a_2" component.

Piston Hydrodynamics

- All equations necessary to solve for the piston pressure and pump flow rate as a function of main shaft and yoke rotations have been derived, tested, and verified at a constant angular speed (1500 rpm) of the main shaft and yoke angles ranging from 5° to 40°. The model was able to predict the variations of pressure profile and flow rate.
- At zero degrees yoke angle, the piston displacement is always zero regardless of barrel rotation. Therefore, there will be no flow rate due to piston kinematics, except for the leakage flow through the clearances between the mating parts. Upon transition from the BDC at the suction port to the discharge port, there is a sharp pulse of oil flow in the cylinder coming from the HPA. Similarly, there is also a

pulse as the oil flows from the cylinder to the LPA as the cylinder switches from the discharge to the suction port at the TDC.

- The cylinder flow rate increases as the yoke angle increases due to increased piston displacement.
- The fundamental cylinder flow harmonic occurs at a frequency of 25 Hz at 1500 rpm of the main shaft and for all angular yoke rotations under investigation and increases linearly with the yoke angle because of the higher piston displacement with increased yoke angle.
- The mean pump flow rate increases as the yoke angle increases due to increased piston displacement. The pump flow rate has a repeating flow ripple about the mean flow rate with a frequency equals to nine times the frequency of rotation of the main shaft. The harmonics of the pump flow rate are very small and negligible for all yoke angles.
- As the yoke angle decreases, the jumps in pressure beyond the LPA or HPA pressures at the points of transitions between the ports decrease accordingly because compression or expansion of the oil near the TDC and BDC is getting smaller.
- The overshoot at the TDC or undershoot at the BDC in piston pressure increases with the yoke angle. At angles of 30° and 40°, the pressure undershoot is below zero gage pressure which might cause cavitation of the pump as the barrel rotates from suction to discharge port.
- The piston pressure harmonics vary very slowly and parabolically with the yoke angle.

Reaction forces on the case from the main shaft at the ball bearing

This force has two components that are normal to the axis of the main shaft. All components alternate about the mean value with a frequency that is nine times the frequency of rotation of the main shaft. The mean value along the "a_1" direction increases parabolically with the yoke angle. The component along the "a_2" direction increases linearly with the yoke angle. The component along the "a_1" direction has very small and negligible harmonics.

The component along the "a_2" direction has two major harmonics at 225 Hz and 450 Hz. The amplitude of these harmonics increases parabolically with the yoke angle.

Reaction forces on the case from the main shaft at the thrust rolling bearing

Both components along the "a_1" and "a_2" directions behave in a similar fashion as the components at the radial ball bearing, but they are out of phase by 180°. The component along the "a_1" direction increases parabolically with the yoke angle. The component along the "a_2" direction increases linearly and steeply with the yoke angle, while the "a_3" component decreases parabolically with the yoke angle. Overall, the magnitude of the force increases linearly with the yoke angle.

The reaction force component along the "a_1" direction has very small and negligible harmonics for all yoke angles. The "a_2" component has two major harmonics at frequencies of 225 Hz, and 450 Hz. The amplitude of these harmonics increase parabolically with the yoke angle.

The "a_3" component of the reaction force at the thrust roller bearing has three major harmonics at 225, 350, and 450 Hz respectively. The amplitude of these harmonics increases parabolically with the yoke angle.

Reaction forces on the case from yoke axis of rotation at the suction port

The "a_1" component of the reaction force at the yoke axis of rotation (suction port side) fluctuates in a sinusoidal fashion and is independent of the yoke angle. This component has one harmonic that occurs at a frequency of 25 Hz. The amplitude (60 N) of this fundamental harmonic is independent of the yoke angle. Therefore, it can be concluded that this component contribute in part to the noise heard at zero yoke angle.

The mean value of the "a_2" component increases linearly with the yoke angle. This component fluctuates about the mean value with nine major pulsations for each revolution of the main shaft. The value of the component along the "a_3" direction decreases as the yoke angle increases. Overall, the average value of the magnitude of this reaction increases proportionally with the yoke angle.

The first four major harmonics of the "a_2" component occur at 25, 225, 200, and 250 Hz respectively. The amplitude of the fundamental harmonic at 25 Hz decreases with the yoke angle up to a yoke angle of 20°. After that, it increases again as the yoke angle increases. The remaining harmonics at 225, 200, and 250 Hz increase parabolically and slowly with the yoke angle.

The first four harmonics of "a_3" component occurs at 25, 225, 200, and 250 Hz. The fundamental harmonic, which occurs at a frequency of 25 Hz, remains nearly constant as

the yoke angle changes. The harmonics at frequencies of 225, 200, and 250 Hz increase parabolically and slowly with the yoke angle.

Reaction forces on the case from yoke axis of rotation at the discharge port

The force components at the discharge side behave in a similar fashion as those at the suction side. The value of the average of the component along the "a_2" direction increases linearly with the yoke angle at a relatively rapid rate. On the other hand, the value along the a_3 direction decreases slowly with the yoke angle. Overall, the average value of the magnitude of this force increases very slowly with the yoke angle. The fundamental harmonic at 25 Hz and the second harmonic at 225 Hz increase parabolically with the yoke angle. The remaining smaller amplitude harmonics are nearly independent of the yoke angle.

The fundamental harmonic of the "a_3" component occurs at a frequency of 25 Hz and decreases very slowly with the yoke angle. The second harmonic at 225 Hz increases parabolically with the yoke angle. The remaining high frequency harmonics are nearly independent of the yoke angle.

Reaction force on the case from the ram

The average value of the magnitude of this force increases as the yoke angle increases until reaching a maximum at 15°. Then it decreases until reaching a minimum at 35°. Beyond a yoke angle of 35°, the average value increases again.

The "a_2" component has three major harmonics at 25, 200, and 250 Hz respectively. The amplitude of the fundamental harmonic at 25 Hz increases with the yoke angle until

reaching a maximum at 15°. After that, it decreases until reaching a minimum at 35°. Beyond 35°, the amplitude resumes to increase as the yoke angle increases. The amplitude of the harmonics at 200 Hz and 250 Hz increases with the yoke angle until reaching a maximum at 20°. After that, it decreases until reaching a minimum at 30°. Beyond 30°, the amplitude resumes to increase as the yoke angle increases.

The "a_3" component has three major harmonics at 25, 200, and 250 Hz respectively. These harmonics vary with the yoke angle in the same way as the component along the "a_2" direction varies.

5.3 Recommendations and Future Work

The study presented in this dissertation represents the infrastructure for further work that is related to bent axis pump design, analysis, performance, and application to hydraulic hybrid vehicles. The application and extension of concepts presented in this study would significantly benefit the analysis of the structures that would be connected to the pump within a hydraulic system. Some of the recommendations for future work include:

- Knowing the constraints at all joints in the pump structure and the forces in the time domain as obtained from the current study, a transient finite element model could be implemented for both the pump's case and the pump's internal parts.
- With all forces at the joints within the structure of the pump being determined, a vibration analysis could be conducted to the structure to which the pump is mounted. Therefore, the mounts to which the pump is tied can be designed effectively.

- Given the forces on the pump case as obtained from the mathematical model, a vibration and acoustic finite element analysis of the pump may be performed to find the effect of the different forces that act on the pump case on noise level variations created by the pump.

REFERENCES

1. Alson, J., et al., *Progress Report on Clean and Efficient Automotive Technologies under Development at EPA*, O.o.T.a.A.Q. Advanced Technology Division, U.S. Environmental Protection Agency, Editor. 2004.
2. Kutz, M., ed. *Environmentally Conscious Transportation*. Wiley Series in Environmentally Conscious Engineering. Vol. 5. 2008, John Wiley & Sons, Inc.: New Jersey.
3. Mohaghegh Motlagh, A., et al. *"Application of Smart Materials for Noise and Vibration of Hydraulic Systems"*. in *DETC/CIE*. 2007. Las Vegas, NV, USA.
4. Mohaghegh Motlagh, S.A., *Modeling a Bent-Axis Pump/Motor in Hydraulic Hybrid Vehicles to Determine Reaction Force Components Leading to Vibration*, in *"Mechanical, Industrial, and Manufacturing Engineering Department"*. 2008, The University of Toledo: Toledo. p. 90.
5. Esposito, A., *Fluid Power with Applications*. 6th ed. 2003, New Jersey: Prentice Hall.
6. Skaistis, S., *Noise Control of Hydraulic Machinery*. 1988, New York: M. Dekker. 324.
7. Kim, J.-K., et al., *Measurement of Fluid Film Thickness on the Valve Plate in Oil Hydraulic Axial Piston Pumps (Part II: Spherical Design Effects).* Journal of Mechanical Science and Technology, 2005. **19**(2): p. 655-663.
8. Franco, N., *Pump Design by Force Balance.* Hydraulics & Pneumatics, 1961. **14**(11): p. 101-107.

9. Manring, N.D., *The Control and Containment Forces on the Swash Plate of an Axial-Piston Pump.* Journal of Dynamic Systems Measurement & Control, 1999. **121**(4): p. 599-605.

10. Manring, N.D., *The Impact of Using a Secondary Swash-Plate Angle Within an Axial Piston Pump.* Journal of Dynamic Systems, Measurement, and Control, 2004. **126**(1): p. 65-74.

11. Manring, N.D., *"Tipping the Cylinder Block of an Axial-Piston Swash-Plate Type Hydrostatic Machine".* Journal of Dynamic Systems Measurement and Control-Transactions of the ASME, 2000. **122**(1): p. 216-221.

12. Bergada, J.M., J. Watton, and S. Kumar, *Pressure, Flow, Force, and Torque Between the Barrel and Port Plate in an Axial Piston Pump.* Journal of Dynamic Systems Measurement & Control, 2008. **130**(1): p. 110-125.

13. McKeown, J., et al., *Hydrodynamic Factors Affecting the Design of Valve Plates and Thrust Bearings.* Proc Instn Mech Engrs, 1966. **181**(Pt. 1 No. 24): p. 653-665.

14. Casoli, P., et al., *Modeling of Fluid Properties in Hydraulic Positive Displacement Machines.* Simulation Modeling Practice & Theory, 2006. **14**(8): p. 1059-1072.

15. Manring, N.D., *The Improved Volumetric-Efficiency of an Axial-Piston Pump Utilizing a Trapped-Volume Design.* Journal of Dynamic Systems, Measurement, and Control, 2001. **123**(3): p. 479-487.

16. Zloto, T. and A. Nagorka, *An Efficient FEM for Pressure Analysis of Oil Film in a Piston Pump.* Applied Mathematics & Mechanics, 2009. **30**(1): p. 49-61.

17. Schoenau, G.J., R.T. Burton, and G.P. Kavanagh, *Dynamic Analysis of a Variable Displacement Pump.* Transactions of the ASME, 1990. **112**: p. 122-132.

18. Bartos, R.D., *Mathematical Modeling of Bent-Axis Hydraulic Piston Motors*, in *TDA Progress Report 42-111*, J.P. Laboratory, Editor. 1992, Jet Propulsion Laboratory: Pasadena, California. p. 224-235.

19. Karkoub, M.A., O.E. Gad, and M.G. Rabie, *Predicting Axial Piston Pump Performance Using Neural Networks.* Mechanism and Machine Theory, 1999. **34**(8): p. 1211-1226.

20. Canbulut, F., et al., *Design of Neural Network Model for Analyzing Hydrostatic Circular Recessed Bearings with Axial Piston Pump Slipper.* Industrial Lubrication and Tribology, 2004. **56**(5): p. 288-299.

21. Gad, O., M.G. Rabie, and R.M. El-Taher, *Prediction and Improvement of Steady-State Performance of a Power Controlled Axial Piston Pump.* Journal of Dynamic Systems Measurement & Control, 2002. **124**(3): p. 443-451.

22. Zhang, X., et al., *New Swash Plate Damping Model for Hydraulic Axial-Piston Pump.* Journal of Dynamic Systems Measurement & Control, 2001. **123**(3): p. 463-470.

23. Kim, J.-K. and J.-Y. Jung, *Driving Mechanism of Tapered Pistons in Bent-Axis Design Axial Piston Pumps.* KSME International Journal, 2003. **17**(2): p. 181-186.

24. Baek, I.-H., et al., *Analysis of Piston Behavior According to Eccentricity Ratio of Disk in Bent-Axis Type Piston Pump.* Journal of Mechanical Science and Technology, 2008. **22**(9): p. 1726-1733.

25. Hong, Y.-S. and Y.-H. Doh, *Analysis on the Friction Losses of a Bent-Axis Type Hydraulic Piston Pump.* KSME International Journal, 2004. **18**(9): p. 1668-1679.

26. Nie, S.L., G.H. Huang, and Y.P. Li, *"Tribological Study on Hydrostatic Slipper Bearing with Annular Orifice Damper for Water Hydraulic Axial Piston Motor"*. Tribology International, 2006. **39**(11): p. 1342-1354.

27. Watton, J., *An Explicit Design Approach to Determine the Optimum Steady State Performance of Axial Piston Motor Drives.* Proceedings of the Institution of Mechanical Engineers -- Part I -- Journal of Systems & Control Engineering, 2005. **220**(2): p. 131-143.

28. Johansson, A., J. Andersson, and J.-O. Palmberg. *Effect of Cross-Angle on Flow Pulsations and Internal Force Dynamics in Axial Piston Pumps*. in *Triennial International Symposium*. 2003. Sorrento, Italy.

29. Johansson, A., J.Ö. johan, and J.-O. Palmberg, *Experimental Verification of Cross-Angle for Noise Reduction in Hydraulic Piston Pumps.* Proceedings of the Institution of Mechanical Engineers -- Part I -- Journal of Systems & Control Engineering, 2007. **221**(3): p. 321-330.

30. Manring, N.D., *The Discharge Flow Ripple of an Axial-Piston Swash-Plate Type Hydrostatic Pump.* Journal of Dynamic Systems Measurement & Control, 2000. **122**(2): p. 263-268.

31. Helgestad, B.O., K. Foster, and F.K. Bannister, *Pressure Transients in an Axial-Piston Hydraulic Pump.* Proc Instn Mech Engrs, 1974. **188**(17/74): p. 189-199.

32. Rebel, J., *Active Liquid Noise-Suppressions in Oil Hydraulics.* VDI-Z, 1977. **119**: p. 937-943.

33. Currie, J. and J. Kane. *The Design of Low Noise Hydraulic Equipment*. in *First European Fluid Power Conference*. 1973. NEL, East Kilbride.

34. Edge, K.A. and Y. Lui. *Reduction of Piston Pump Pressure Ripple*. in *Second International Conference on Fluid Power Transmission and Control*. 1989. People's Republic of China: Zhejiang University.

35. Martin, M.J. and R. Taylor. *Optimized Port-Plate Timing for an Axial Piston Pump*. in *Fifth International Fluid Power Symposium*. 1978. Durham.

36. Boltyanski, A.D. and A.L. Levontin, *Axial Piston Pump Distributer System Spool Valve Chambers Connected to Delivery Port and Valves with Varying Area Slots to Reduce Noise and Vibration*. 1986: Soviet Union.

37. Boyer, J.J., *Noise Reducing Device for Swash-Plate Pump has Pressure Responsive Piston to Control Trapped Volume in Delivery Ports*. 1980: France.

38. Pettersson, M., *Design of Fluid Power Piston Pump: With Special Reference to Noise Reduction*, in *Department of Mechanical Engineering*. 1995, Linkoping University: Linkoping, Sweden.

39. Bartos, R.D., *Reducing the Net Torque and Flow Ripple Effects of Multiple Hydraulic Piston Motor Drives*, in *TDA Progress Report 42-111*. 1992, Jet Propulsion Laboratory: Pasadena, California. p. 236-245.

40. Harrison, A.M. and K.A. Edge, *Reduction of Axial Piston Pump Pressure Ripple.* Proceedings of the Institution of Mechanical Engineers -- Part I -- Journal of Systems & Control Engineering, 2000. **214**(1): p. 53-63.

41. Kim, J.-K., et al., *Relation Between Pressure Variations and Noise in Axial Type Oil Piston Pumps.* KSME International Journal, 2004. **18**(6): p. 1019-1025.

42. Mandal, N.P., R. Saha, and D. Sanyal, *Theoretical Simulation of Ripples for Different Leading-Side Groove Volumes on Manifolds in Fixed-Displacement Axial-*

Piston Pump. Proceedings of the Institution of Mechanical Engineers - Part I - Journal of Systems & Control Engineering, 2008. **222**(6): p. 557-570.

43. Kumar, S., J.M. Bergada, and J. Watton, *Axial Piston Pump Grooved Slipper Analysis by CFD Simulation of Three-Dimensional NVS Equation in Cylindrical Coordinates.* Computers & Fluids, 2009. **38**(3): p. 648-663.
44. Kim, K.-H., et al., *Reduction of Pressure Ripples Using a Parallel Line in Hydraulic Pipeline.* International Journal of Automotive Technology, 2005. **6**(1): p. 65-70.
45. Brändlein, J., et al., *Ball and Roller Bearings: Theory, Design, and Application*. 3rd ed. 1999, New York: Chichester: John Wiley.
46. Baruh, H., *Analytical Dynamics*. 1999, Boston: WCB/McGraw-Hill.
47. Johnson, D.A. and P.Y. Willems, *On the Necessary and Sufficient Conditions for Homokinetic Transmission in Chains of Cardan Joints.* Journal of Mechanical Design, 1993. **115**: p. 255-261.
48. Cho, J., *Dynamic Modeling and Analysis for Swash-Plate Type Axial Pump Control Utilizing Indexing Valve Plate*, in *Mechanical and Aerospace Engineering*. 2000, University of Missouri: Columbia. p. 193.
49. Munson, B.R., D.F. Young, and T.H. Okiishi, *Fundamentals of Fluid Mechanics*. 1990, Ney York: John Wiley & Sons.
50. Wesley, B., *Spread Sheet Accumulator Sizing for Hybrid Hydraulic Applications Using the Benedict-Webb-Rubin Equation of State*. 2003, U.S. Army Tank-Automotive and Armaments Research Development and Engineering Center: Warren. p. 12.

51. Zeiger, G. and A. Akers, *Torque on the Swash-Plate of an Axial Piston Pump.* Journal of Dynamic Systems Measurement and Control-Transactions of the ASME, 1985. **107**(3): p. 220-226.

APPENDIX A: VELOCITY AND ACCELERATION OF PISTONS AND CONNCETING RODS

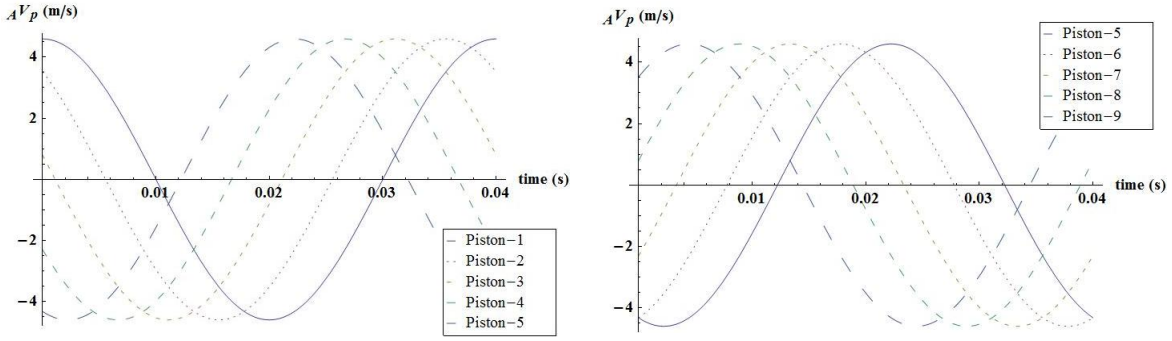

A- 1: The velocity of all pistons along the "a_1" direction (Case 2)

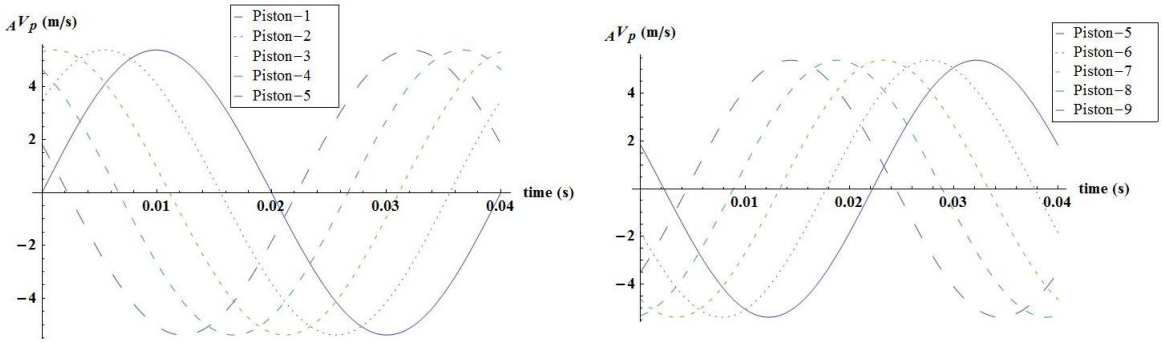

A- 2: The velocity of all pistons along the "a_2" direction (Case 2)

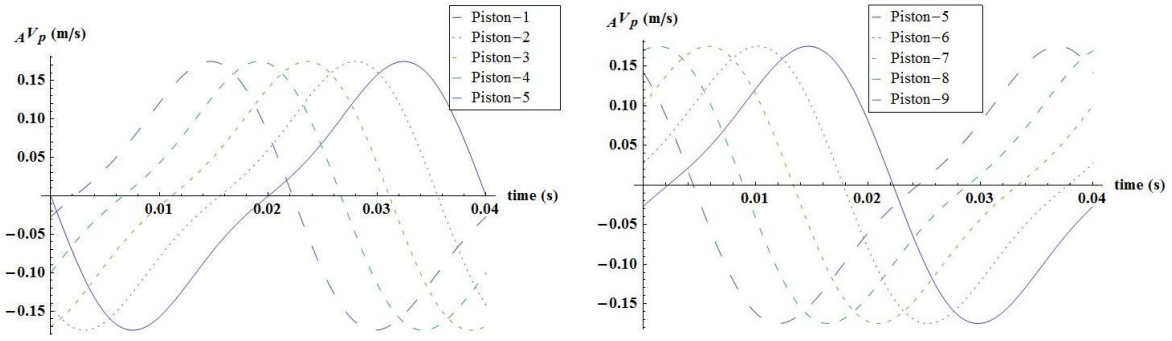

A- 3: The velocity of all pistons along the "a_3" direction (Case 2)

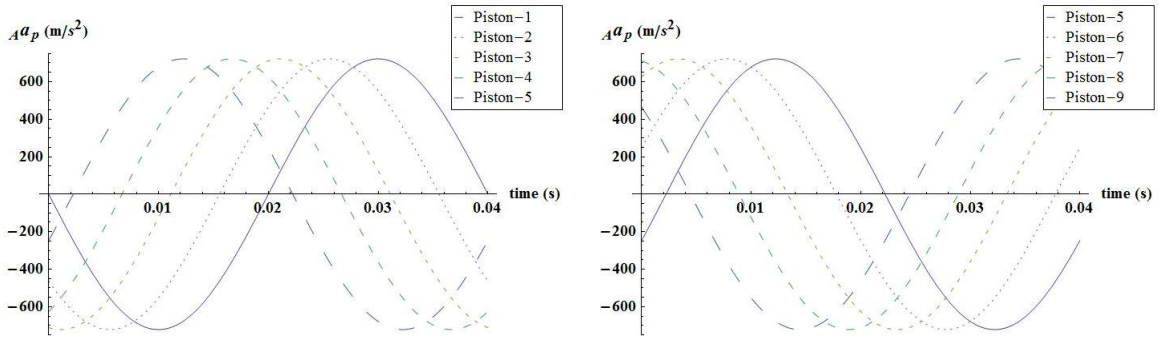

A- 4: Acceleration of all pistons along the "a_1" direction (Case 2)

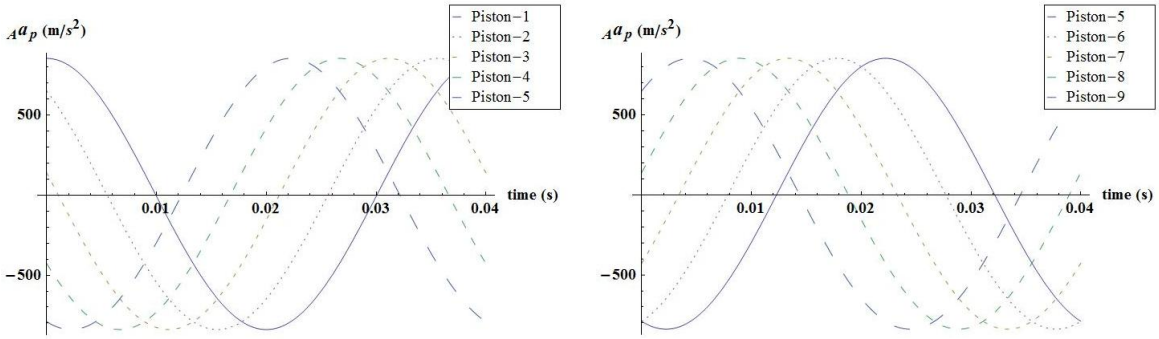

A- 5: Acceleration of all pistons along the "a_2" direction (Case 2)

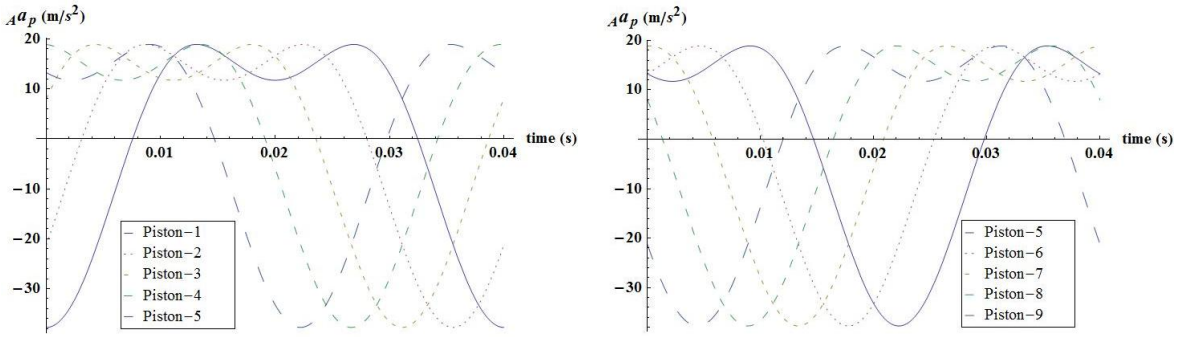

A- 6: Acceleration of all pistons along the "a_3" direction (Case 2)

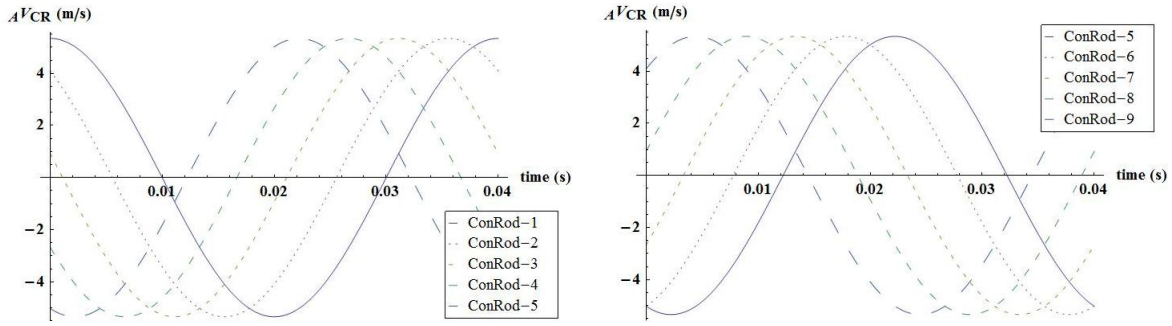

A- 7: Velocity of all connecting rods along the "a_1" direction (Case 2)

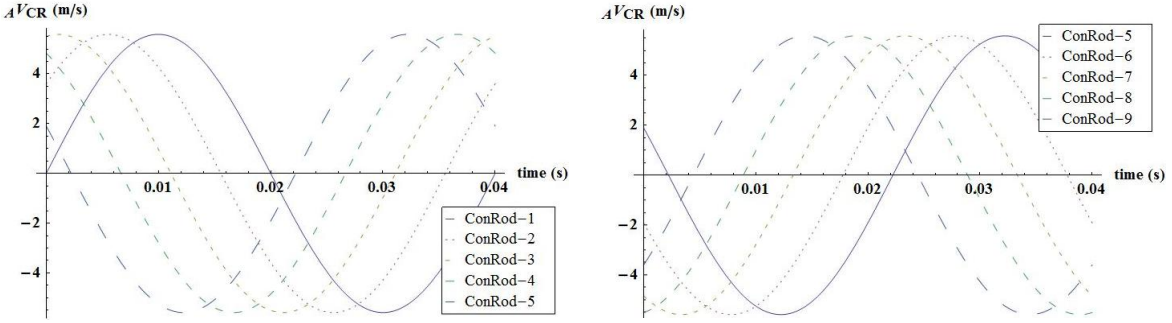

A- 8: Velocity of all connecting rods along the "a_2" direction (Case 2)

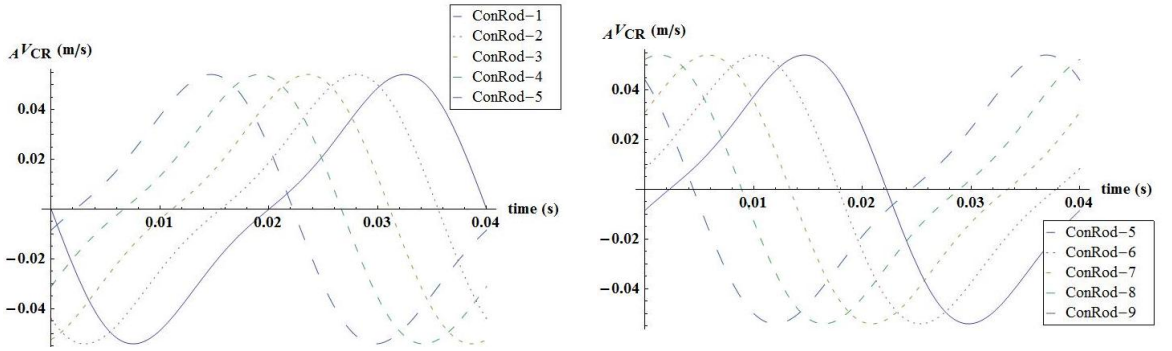

A- 9: Velocity of all connecting rods along the "a_3" direction (Case 2)

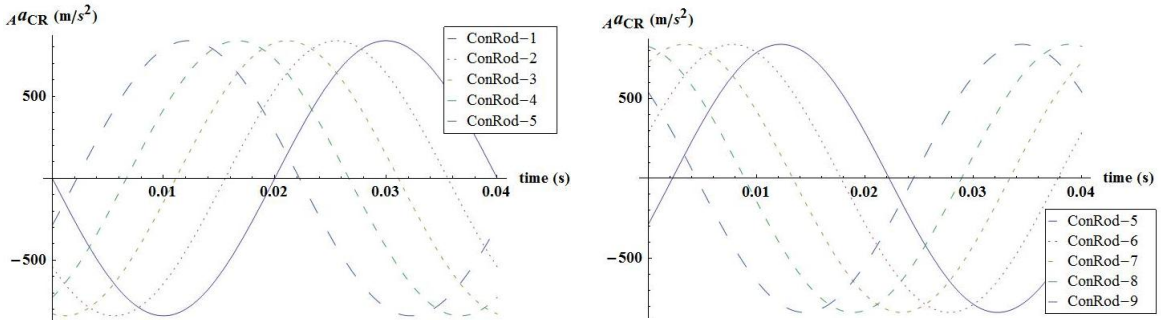

A- 10: Acceleration of all connecting rods along the "a_1" direction (Case 2)

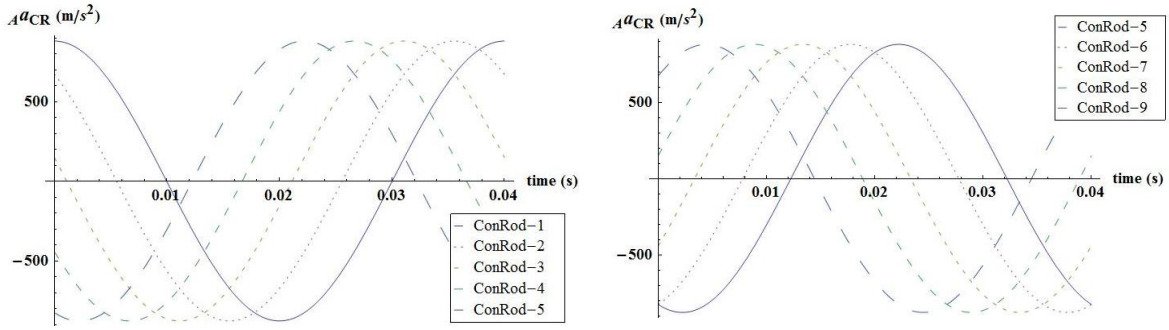

A- 11: Acceleration of all connecting rods along the "a_2" direction (Case 2)

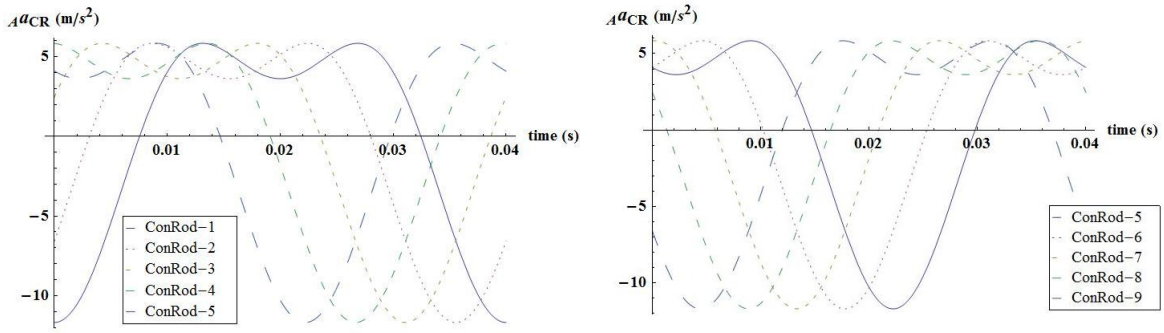

A- 12: Acceleration of all connecting rods along the "a_3" direction (Case 2)

APPENDIX B: MATHEMATICA NOTEBOOK TO SOLVE THE EQUATIONS OF MOTION OF THE PUMP

```
(*Equations of Motion of parts of bent axis piston pump*)
(*Rotation matrix functions*)
MatrixForm[Tx[Ω_] : = RotationMatrix[Ω, {1, 0, 0}]^T];

MatrixForm[Ty[Ω_] : = RotationMatrix[Ω, {0, 1, 0}]^T];

MatrixForm[Tz[Ω_] : = RotationMatrix[Ω, {0, 0, 1}]^T];

(*Derivative wrt time of the rotation matrix functions*)
dTx[Ω_, t_] : = Dt[Tx[Ω], t];
dTy[Ω_, t_] : = Dt[Ty[Ω], t];
MatrixForm[dTz[Ω_, t_] : = Dt[Tz[Ω], t]];

(*Rolling Bearing Friction Model
d = bore diameter of thrust bearing (mm)
D = outside diameter of thrust bearing (mm)
dm = pitch circle diameter of thrust bearing (mm)
fo = index for bearing type and lubrication type
type = a variable that defines type of bearing
type = 1 for Deep groove ball bearings
type = 2 for Tapered roller bearings
type = 3 for Needle roller bearings
type = 4 for Thrust ball bearings
T = oil operating temperature
ν = oil viscosity in mm^2/s
Mv = load independent component of frictional moment (N.m)
Fr = radial load component of bearing reaction
Fa = axial load component of bearing reaction
f1 = index taking into account magnitude of load
P1 = governs radial load-depending frictional moment Mm, takes into account that Mm changes with load angle
Mm = radial load dependent component of frictional moment (N.mm)
fa = index, depending on axial load Fa and lubricating condition*)

Friction[revx_, typex_, dx_, Dx_, Tempx_, Frx_, Fax_, Cox_] : = Module[{Friction, dm, Mv, Mm, Ma, fo, f1, P1},
 ν[Temp_] = 92.31*Exp[0.025Temp]; fo[type_] = Which[type = = 1, 2, type = = 2, 4.5, type = = 3, 5.25, type = = 4, 1.5];
 f1[type_, Fr_, Co_, Faxial_] = Which[type = = 1, 0.005 - 0.009 (0.6*Fr/Co)^0.5, type = = 2, 0.0004, type = = 3, 0.0005, type = = 4, 0.0012 (Faxial/Co)^0.33]; P1[type_, Fr_, Faxial_] = Which[type = = 1, Fr, type = = 2, 0.8*Cot[αo] Faxial, type = = 3, Fr, type = = 4, Faxial];

dm[diam_, DIAM_] = (diam + DIAM)/2;

Mv[rev_, type_, Temp_, diam_, DIAM_] = If[ν[Temp]*rev≥2000, 1*^ - 10*fo[type]*(ν[Temp]*rev)^(2/3)*dm[diam, DIAM]^3, 160*^ - 10*fo[type]*dm[diam, DIAM]^3];
Mm[type_, Fr_, Faxial_, diam_, DIAM_, Co_] = f1[type, Fr, Co, Faxial]*P1[type, Fr, Faxial]*dm[diam, DIAM]/1000;
```

```
Ma[type_, Faxial_, diam_, DIAM_] = Which[type==1, 0, type==2, (9*^ - 6)*Faxial*dm[diam, DIAM],
type==3, 0, type==4, (9*^ - 6)*Faxial*dm[diam, DIAM]];

Friction[rev_, type_, diam_, DIAM_, Temp_, Fr_, Faxial_, Co_] = Mv[rev, type, Temp, diam, DIAM] +
Mm[type, Fr, Faxial, diam, DIAM, Co] + Ma[type, Faxial, diam, DIAM] ; Friction[revx, typex, dx, Dx,
Tempx, Frx, Fax, Cox]]

SetDirectory["C:\\Users\\noor\\Documents\\ABH\\Dissertation\\Mahematica models"]
(*Orifice area*)
FileOrificeArea = OpenRead["AoRF.nb"];
ArFR[ϕ_] = Read[FileOrificeArea];
Close[FileOrificeArea];

(*Solid area between successive cylinders*)
FileSolidArea = OpenRead["Asolid.nb"];
Share[AsFR[ϕ_] = Read[FileSolidArea]];
Close[FileSolidArea];
Needs["PlotLegends`"]
Plot[AsFR[ϕ]*1000000, {ϕ, 0, 2Pi}, AxesOrigin→{0, 0}, AxesLabel→{"ϕ (rad)", "A_solid (mm^2)"},
BoundaryStyle→Thick, PlotStyle→Thick, LabelStyle→Directive[Bold], Ticks→{{0, Pi/2, Pi, 3Pi/2, 2Pi}}]

(*Constant Inputs*)
Ac : = Cylinder cross sectional area;
Ace : = Exit cross sectional area of the cylinder;
Ap : = Cross sectional area of the piston;
ARAM : = Cross sectional area of the ram;
AIAC : = Moment of inertia of actuating link around axis system attached to its CG and parallel to the
principal axes of the part;
ATinz : = Input torque to the main shaft;
A78 : = area of discharge/suction exit to HPA/LPA at yoke axis (Point 78 and 79);
B : = Oil bulk modulus;
Co1 : = The static load rating of the ball bearing of the main shaft;
Co2 : = The static load rating of the thrust roller bearing of the main shaft;
Co4 : = The static load rating of the thrust ball bearing at the barrel;
Cp = One half the radial clearance between the piston and the cylinder;
D1 : = Outside diameter of the ball bearing at the main shaft; (*mm*)
d11 : = Bore diameter of the ball bearing at the main shaft; (*mm*)
D2 : = Outside diameter of the thrust bearing at the main shaft; (*mm*)
d2 : = Bore diameter of the thrust bearing at the main shaft; (*mm*)
D3 : = Outside diameter of the needle bearing at the barrel; (*mm*)
d3 : = Bore diameter of the needle bearing at the barrel ; (*mm*)
D4 : = Outside diameter of the thrust ball bearing at the barrel; (*mm*)
d4 : = Bore diameter of the thrust ball bearing at the barrel; (*mm*)
DG : = Distance from upper end of actuating link (D) to its CG;
DF : = Distance from center of spherical joint between piston and connecting rod and the bottom end of the
cylindrical cavity for a zero yoke angle (Figure 3-15);
g : = Acceleration of gravity;
h : = Fluid film thickness between valve plate and the barrel;
Ims11 = Moment of inerital of main shaft along b_1 direction;
Ims12 = Product moment of inerital of main shaft (b_1- b_2);
Ims13 = Product moment of inerital of main shaft (b_1- b_3);
Ims22 = Moment of inerital of main shaft along b_2 direction;
Ims23 = Product moment of inerital of main shaft (b_2- b_3);
Ims33 = Moment of inerital of main shaft along b_3 direction;
```

Iim111 = Moment of inerital of 1st intermediate shaft along c_1 direction;
Iim113 = Product moment of inerital of 1st intermediate shaft (c_1- c_3);
Iim122 = Moment of inerital of 1st intermediate shaft along c_2 direction;
Iim133 = Moment of inerital of 1st intermediate shaft along c_3 direction;
Iim211 = Moment of inerital of 2nd intermediate shaft along c_1 direction;
Iim213 = Product moment of inerital of 2nd ntermediate shaft (c_1- c_3);
Iim222 = Moment of inerital of 2nd ntermediate shaft along c_2 direction;
Iim233 = Moment of inerital of 2nd intermediate shaft along c_3 direction;
Ios11 = Moment of inerital of barrel along d_1 direction;
Ios12 = Product moment of inerital of barrel (d_1- d_2);
Ios13 = Product moment of inerital of barrel (d_1- d_3);
Ios22 = Moment of inerital of barrel along d_2 direction;
Ios23 = Product moment of inerital of barrel (d_2- d_3);
Ios33 = Moment of inerital of barrel along d_3 direction;
Ip11 = Moment of inerital of piston along d_1 direction;
Ip33 = Moment of inerital of piston along d_3 direction;
Ic11 = Moment of inerital of 1st cross along f_1 direction;
Ic12 = Product moment of inerital of 1st cross (f_1- f_2);
Ic13 = Product moment of inerital of 1st cross (f_1- f_3);
Ivp11 : = Moment of inerital of yoke-valve plate along h_1 direction;
Ivp12 = Product moment of inerital of yoke-valve plate (h_1- h_2);
Ivp13 = Product moment of inerital of yoke-valve plate (h_1- h_3);
Ivp22 = Moment of inerital of yoke-valve plate along h_2 direction;
Ivp23 = Product moment of inerital of yoke-valve plate (h_2- h_3);
Ivp33 = Moment of inerital of yoke-valve plate along h_3 direction;
IP : = Distance from CG of second intermediate shaft to center of second cross;
Lac : = Length of actuating link;
LCo : = Length of oil cylindrical cavity at zero yoke angle (Figure 3-15);
LC2 : = Length of the convergent part of the cylindrical cavity (Figure 3-14);
LCIMo : = Contact length between first and second intermediate shafts at zero yoke angle;
LCR : = Length of the connecting rod;
LIM1 : = Distance from the center of the first cross to the far edge of the first intermediate shaft along the "c_3" direction;
Lis : = Length of input shaft of the CVJ (Figure 3-9);
Lp : = Length of piston that is in the cylinder when axial displacement is zero;
Lp1 = Distance from the spherical joint between the piston and the connecting rod to the piston's face;
LPtoCR : = Distance from the left face of the piston to the common point between the piston and the connecting rod;
LYtoVP : = Distance along the "d_3" direction from the yoke axis of rotation to the barrel valve plate interface;
L3 : = 55/1000;
L4 : = 51.67/1000;
MAC = Mass of the actuating link;
Mc1 : = Mass of the first cross;
Mc2 : = Mass of the second cross;
MCR : = Mass of the connecting rod;
MH : = Mass of gas in the HPA;
ML : = Mass of gas in the LPA;
Mim1 : = Mass of the first intermediate shaft;
Mim2 : = Mass of the second intermediate shaft;
MMS : = Mass of the main shaft;
Mos : = Mass of the barrel-output shaft assembly;
Mp : = Mass of piston;
MRAM : = Mass of the ram;
Mvp : = Mass of the valve plate-yoke assembly;

nrated : = Rated speed of pump, rpm;
PlossH : = Pressure losses between the discharge port and the HPA;
PlossL : = Pressure losses between the suction port and the LPA;
PmaxL = Maximum gas pressure in the LPA
PmaxH = Maximum gas pressure in the HPA;
PPH : = Pre-charge pressure in the HPA;
PPL : = Pre-charge pressure in the LPA;
r : = Pitch circle radius at the barrel side;
R : = Pitch circle radius at the main shaft side;
RN : = Gas constant of nitrogen, J/kg°K;
R1 : = Radius of the outer land of the port plate (Figure 2-5);
R2 : = Outside radius of the discharge/suction port (Figure 2-5);
R3 : = Inside radius of the discharge/suction port (Figure 2-5);
R4 : = Radius of the inner land of the port plate (Figure 2-5);
rAC : = Radius of pin between the yoke and the actuating link;
rC1 : = Distance from the center of the first or the center of the second cross to point 3 on the first cross or point 29 on the second cross;
rC2 : = Distance from the center of the first or second cross to point 23 on the first cross or point 27 on the second cross;
rCP1 : = Radius of the cross section of pin 3-4 that is attached to the input shaft at the first cross or the output shaft at the second cross;
rCP2 : = Radius of the cross section of pin 23-24 that is attached to the first or second intermediate shafts at point 23;
rCP3 : = Radius of the cross section of pin 23-24 that is attached to the first or second intermediate shafts at point 24;
RCRL : = Radius of the left end of the connecting rod;
RCRR : = Radius of the right end of the connecting rod;
rp : = The piston radius;
rY : = Radius of the yoke's pin at its axis of rotation;
Ry : = Distance from center of rotation of yoke to center of first or second cross;
r1z : = Distance from left end of main shaft to the ball bearing ;
r2z : Distance from left end of main shaft to the thrust bearing;
r3z : = Distance from left end of main shaft to the CG of the 1st cross along the a_3 direction;
r5z : = Distance from left end of main shaft to the ConRod spherical joint along the a_3 direction;
rCtoY67x = See nomenclature ;
rLPAtoY78x : = See nomenclature;
rim1z : = Distance from CG of 1st cross to CG of 1st intermediate shaft along c_3 direction;
rOSz : = Distance from yoke axis of rotation to CG of barrel along d_3 direction;
rWmsz : = Distance from left end of main shaft to its CG along the a_3 direction;
rWP : = Distance from ConRod spherical joint to CG of piston along d_3 direction;
rACtoY66x : = See nomenclature;
rACtoY66y : = See nomenclature;
rACtoY66z : = See nomenclature;
rB3FtoBz : = Distance from yoke axis of rotation to 1st needle bearing of the barrel along d_3 direction;
rB3StoBz : = Distance from yoke axis of rotation to 2nd needle bearing of the barrel along d_3 direction;
rB4toBz : = Distance from yoke axis of rotation to thrust ball bearing of the barrel along d_3 direction;
rvpx = Distance from yoke axis of rotation to CG of yoke-valve plate along h_1 direction;
rvpz = Distance from yoke axis of rotation to CG of yoke-valve plate along h_3 direction;
rCR : = See nomenclature;
T : = Operating oil temperature, ºC;
Tg : = Temperature of gas in the HPA or LPA at pre-charge, ºK;
Vfixed : = Volume of oil at end of the cylinder cavity (conical portion) (Figure 3-14);
αo : = Nominal contact angle of the thrust bearing at the main shaft;
ζ : = Kidney angle of the valve plate;
$\gamma 5$: = See nomenclature;

ϵ : = Inclination angle of the cylinder along which the ram slides;
μC1 = Friction coefficient at the pins of the first or second cross;
μim = Friction coefficient between the first and second intermediate shafts;
μY = Friction coefficient at the right/left pins of the yoke at its axis of rotation;
μACtoY = Friction coefficient at the pin between the yoke and the actuating link;
μCtoRAM90 = Friction coefficient between the ram and the cylinder walls at point 90;
θL = Angular rotation of the line of action of the reaction force from the LPA/HPA from the negative "a_3" direction;
ρ = Oil density;
ϕ = Angular rotation of the main shaft about its axis of rotation;
θ = Angular rotation of the yoke about its axis of rotation;

(*Main shaft - Kinematic*)

(*Transformation matrix of B frame wrt A frame)

```
MatrixForm[T1[ϕx_] = Tz[ϕx]];
```

(*Angular velocity of the rotating frame of reference expressed in B frame wrt to A frame*)

```
Simplify[MatrixForm[WABB[t_, ϕx_] = T1[ϕx].Dt[T1[ϕx]^T, t]]];
```

(*Angular velocity and angular acceleration of main shaft in vector form*)

```
Simplify[MatrixForm[BωMS = {WABB[t, ϕ][[3, 2]], WABB[t, ϕ][[1, 3]], WABB[t, ϕ][[2, 1]]}]];
Simplify[MatrixForm[BαMS = Dt[BωMS, t]]];
```

(*Position vectors of forces acting on main shaft*)

```
MatrixForm[Ar1 = {0, 0, r1z}]; (*Ball bearing at point 1*)
MatrixForm[Ar2 = {0, 0, r2z}]; (*Thrust bearing at point 2*)
MatrixForm[Br3 = {0, - rC1, r3z}]; (*pin 3 of 1st cross*)
MatrixForm[Br4 = {0, rC1, r3z}]; (*pin 4 of 1st cross*)

MatrixForm[ArCR1 = T1[ϕ]^T.{0, - R, r5z}]; (*1st ConRod*)
MatrixForm[ArCR2 = T1[ϕ + 2*Pi/9]^T.{0, - R, r5z}]; (*2nd ConRod*)
MatrixForm[ArCR3 = T1[ϕ + 4*Pi/9]^T.{0, - R, r5z}]; (*3rd ConRod*)
MatrixForm[ArCR4 = T1[ϕ + 6*Pi/9]^T.{0, - R, r5z}]; (*4th ConRod*)
MatrixForm[ArCR5 = T1[ϕ + 8*Pi/9]^T.{0, - R, r5z}]; (*5th ConRod*)
MatrixForm[ArCR6 = T1[ϕ + 10*Pi/9]^T.{0, - R, r5z}]; (*6th ConRod*)
MatrixForm[ArCR7 = T1[ϕ + 12*Pi/9]^T.{0, - R, r5z}]; (*7th ConRod*)
MatrixForm[ArCR8 = T1[ϕ + 14*Pi/9]^T.{0, - R, r5z}]; (*8th ConRod*)
MatrixForm[ArCR9 = T1[ϕ + 16*Pi/9]^T.{0, - R, r5z}]; (*9th ConRod*)

MatrixForm[ArWms = {0, 0, rWmsz}];
```

(*First Intermediate shaft angular rotation*)

```
(* Orthogonally constraint between the yoke axes*)
δ = ArcTan[Tan[ϕ]*Cos[θ/2]];
```

(*First Intermediate shaft transformation matrix*)

```
(*Attach coordinate system c1c2c3 to 1st intermediate shaft*)
(*c2 is aligned with axis of output yoke of 1st joint.*)
(*c3 is aligned with axis of intermediate shaft*)
MatrixForm[T2[σ_] = Tx[σ]];
MatrixForm[T3 = Simplify[Tz[δ]]]/.(1/Sqrt[Sec[ϕ]^2]→Cos[ϕ]);
```

(*Transformation matrix between A and C frames*)
MatrixForm[Tim1 = Simplify[T3.T2[θ/2]]]/.(1/Sqrt[Sec[ϕ]^2]→Cos[ϕ]);

(*Angular velocity of 1st intermediate shaft expressed in C frame in skew symmetric form*)

MatrixForm[WACC = Simplify[Tim1.Dt[Tim1, t]^T]];

(*Angular velocity of 1st intermediate shaft expressed in C frame in vector form*)
MatrixForm[Cωim1 = FullSimplify[{WACC[[3, 2]], WACC[[1, 3]], WACC[[2, 1]]}]];

MatrixForm[Aωim1 = Simplify[N[Tim1^T.Cωim1]]];

Aωim1ADAMS = Import["C:\\Users\\noor\\Documents\\ABH\\Dissertation\\Mahematica models\\Kinematic data from adams at 30 degrees\\Angular velocity\\AngVelFirstIntermediate.csv"];
Aωim1ADAMSmag = ListInterpolation[Aωim1ADAMS[[All, 5]], {Aωim1ADAMS[[All, 1]]}];

(*Angular acceleration of 1st intermediate shaft expressed in C frame in vector form*)
MatrixForm[Cαim1 = Simplify[Dt[Cωim1, t]]];

MatrixForm[Aαim1 = N[Tim1^T.Cαim1]];

Aαim1ADAMS = Import["C:\\Users\\noor\\Documents\\ABH\\Dissertation\\Mahematica models\\Kinematic data from adams at 30 degrees\\Angular acceleration\\AngAccFirstIntermediate.csv"];
Aαim1ADAMSz = ListInterpolation[Aαim1ADAMS[[All, 3]], {Aαim1ADAMS[[All, 1]]}];
Aαim1ADAMSy = ListInterpolation[Aαim1ADAMS[[All, 4]], {Aαim1ADAMS[[All, 1]]}];

(*First Intermediate shaft*)
(* Position vector of CG of 1st intermediate shaft expressed in C frame wrt center of 1st cross*)
MatrixForm[Crim1 = {0, 0, rim1z}];

(* Velocity of CG of 1st intermediate shaft expressed in C frame*)
MatrixForm[CVim1 = Cωim1×Crim1];
(*Acceleration of CG of 1st intermediate*)
Simplify[MatrixForm[Caim1 = Cωim1×(Cωim1×Crim1) + Cαim1×Crim1]];

Simplify[MatrixForm[Aaim1 = Simplify[Tim1^T.Caim1]]];

(*First Intermediate shaft*)
Lim = 2*Ry*Cos[θ/2]; (*Intermediate shaft length*)
(*Position vectors of the reaction forces wrt center of 1st cross*)
MatrixForm[Cr23 = { - rC2, 0, 0}];
MatrixForm[Cr24 = - Cr23];

(*First Cross coordinate system, $f_1f_2f_3$*)
(*1. f1 is parallel to b1*)
(*2. f2 is parallel to c2*)
MatrixForm[f1 = T1[ϕ][[1]]];
MatrixForm[f2 = Tim1[[2]]]/.(1/Sqrt[Sec[ϕ]^2]→Cos[ϕ]);
MatrixForm[f3 = Simplify[f1×f2]]/.Cos[ϕ] Sqrt[Sec[ϕ]^2]→1;

(*First Cross rotation matrix*)
MatrixForm[Tc1 = {f1, f2, f3}];

(*Angular velocity of 1st cross *)
MatrixForm[ωc1 = Tc1.Transpose[Dt[Tc1, t]]];
MatrixForm[Fωc1 = N[Simplify[{ωc1[[3, 2]], ωc1[[1, 3]], ωc1[[2, 1]]}/.(1/Sqrt[Sec[ϕ]^2]→Cos[ϕ])]]];

MatrixForm[Aωc1 = Simplify[N[Tc1^T.Fωc1]]];

Export["C:\\Users\\noor\\Documents\\ABH\\Dissertation\\Mahematica models\\Velocities and Accelerations\\Awc1.csv", Table[{t, Aωc1[[1]], Aωc1[[3]], - Aωc1[[2]]}, {t, 0, 0.04, 0.0001}]];

Aωc1ADAMS = Import["C:\\Users\\noor\\Documents\\ABH\\Dissertation\\Mahematica models\\Kinematic data from adams at 30 degrees\\Angular velocity\\AngVelFirstCross.csv"];
Aωc1ADAMSx = ListInterpolation[Aωc1ADAMS[[All, 2]], {Aωc1ADAMS[[All, 1]]}];
Aωc1ADAMSz = ListInterpolation[Aωc1ADAMS[[All, 3]], {Aωc1ADAMS[[All, 1]]}];
Aωc1ADAMSy = ListInterpolation[Aωc1ADAMS[[All, 4]], {Aωc1ADAMS[[All, 1]]}];

(*Angular acceleration of 1st cross in vector form expressed in F frame*)

MatrixForm[Fαc1 = Chop[Dt[Fωc1, t]]];

MatrixForm[Aαc1 = Chop[Tc1^T.Fαc1]];

Aαc1ADAMS = Import["C:\\Users\\noor\\Documents\\ABH\\Dissertation\\Mahematica models\\Kinematic data from adams at 30 degrees\\Angular acceleration\\AngAccFirstCross.csv"];

Aαc1ADAMSx = ListInterpolation[Aαc1ADAMS[[All, 2]], {Aαc1ADAMS[[All, 1]]}];
Aαc1ADAMSz = ListInterpolation[Aαc1ADAMS[[All, 3]], {Aαc1ADAMS[[All, 1]]}];
Aαc1ADAMSy = ListInterpolation[Aαc1ADAMS[[All, 4]], {Aαc1ADAMS[[All, 1]]}];

(*Position vectors of forces acting on FBD of 1st cross in terms of F frame wrt its origin*)

MatrixForm[Fr3 = {0, - rC1, 0}];
MatrixForm[Fr4 = - Fr3];
Fr23 = { - rC2, 0, 0};
Fr24 = - Fr23;

(*Second Intermediate Shaft*)

(*Relative velocity of 2nd intermediate shaft wrt 1st intermediate shaft expressed in C frame*)
SetAttributes[Ry, Constant]
MatrixForm[CVim2im1 = {0, 0, Dt[Lim, t]}];

(*Position vector of CG of 2nd intermediate shaft wrt center of 1st cross expressed in C frame*)
MatrixForm[Crim2 = {0, 0, Lim - IP}];

(*Velocity of CG of 2nd intermediate shaft expressed in C frame*)
MatrixForm[CVim2 = Simplify[CVim2im1 + Cωim1×Crim2]];

(*Acceleration of CG of 2nd intermediate shaft expressed in C frame*)
SetAttributes[{IP}, Constant]
MatrixForm[Caim2 = Simplify[Dt[CVim2im1, t] + Cωim1×(Cωim1×Crim2) + Cαim1×Crim2 + 2Cωim1×CVim2im1]];

(*Second Intermediate Shaft*)

(*Moment of inertia of 2nd intermediate shaft*)
MatrixForm[CIim2 = {{Iim211, 0, Iim213}, {0, Iim222, 0}, {Iim213, 0, Iim233}}];

(*Let origin of C frame be at center of 1st cross*)
(*Position vectors of forces acting on 2nd intermediate shaft*)
MatrixForm[Cr27 = { - rC2, 0, Lim}];
MatrixForm[Cr28 = {rC2, 0, Lim}];

(*Output Shaft coordinate system, d1d2d3*)

(*Attach coordinate system d1d2d3 to output shaft of 2nd joint*)
(* d1 is aligned with axis of output yoke of 2nd joint*)
(* d3 is aligned with axis of output shaft of 2nd joint*)
(*d1d2d3 and a1a2a3 are related by*)
MatrixForm[T4[ϕx_] = Tz[ϕx]];
MatrixForm[Dos = Simplify[T4[ϕ].T2[θ/2]]];

(*Output Shaft rotation matrix*)
(*coordinate frame e1e2e3*)
Simplify[MatrixForm[Tos[θx_, ϕx_] = T4[ϕx].T2[θx/2].T2[θx/2]]];

(*Angular velocity and angular acceleration of output shaft expressed in d frame*)

MatrixForm[WADD = Tos[θ, ϕ].Dt[Tos[θ, ϕ]^T, t]];

MatrixForm[Dωos = Simplify[{WADD[[3, 2]], WADD[[1, 3]], WADD[[2, 1]]}]];
MatrixForm[Dαos = Dt[Dωos, t]];

(*Second Cross coordinate system, i1i2i3*)

(* i1 is parallel to d1*)
(* i2 is parallel to c2*)
MatrixForm[i1 = Simplify[Tos[θ, ϕ][[1]]]];
MatrixForm[i2 = Tim1[[2]]]/.(1/Sqrt[Sec[ϕ]^2])→Cos[ϕ];
MatrixForm[i3 = Simplify[i1×i2]]/.Cos[ϕ] Sqrt[Sec[ϕ]^2]→1;

(*Rotation matrix of 2nd cross*)
MatrixForm[Tc2 = Simplify[{i1, i2, i3}]]/.{1/Sqrt[Sec[ϕ]^2]→Cos[ϕ], Cos[ϕ] Sqrt[Sec[ϕ]^2]→1};

(*Angular velocity and angular acceleration of 2nd cross expressed in I frame*)

MatrixForm[Wc2 = Tc2.Dt[Tc2^T, t]];

MatrixForm[Iωc2 = Simplify[{Wc2[[3, 2]], Wc2[[1, 3]], Wc2[[2, 1]]}/.(1/Sqrt[Sec[ϕ]^2])→Cos[ϕ]]];
MatrixForm[Iαc2 = Simplify[Dt[Iωc2, t]]];

MatrixForm[Aωc2 = N[Simplify[Tc2^T.Iωc2]]];

Aωc2ADAMS = Import["C:\\Users\\noor\\Documents\\ABH\\Dissertation\\Mahematica models\\Kinematic data from adams at 30 degrees\\Angular velocity\\AngVelSecondCross.csv"];

Aωc2ADAMSx = ListInterpolation[Aωc2ADAMS[[All, 2]], {Aωc2ADAMS[[All, 1]]}];
Aωc2ADAMSz = ListInterpolation[Aωc2ADAMS[[All, 3]], {Aωc2ADAMS[[All, 1]]}];
Aωc2ADAMSy = ListInterpolation[Aωc2ADAMS[[All, 4]], {Aωc2ADAMS[[All, 1]]}];

MatrixForm[Aαc2 = N[Simplify[Tc2^T.Iαc2]]];

Aαc2ADAMS = Import["C:\\Users\\noor\\Documents\\ABH\\Dissertation\\Mahematica models\\Kinematic data from adams at 30 degrees\\Angular acceleration\\AngAccSecondCross.csv"];

Aαc2ADAMSx = ListInterpolation[Aαc2ADAMS[[All, 2]], {Aαc2ADAMS[[All, 1]]}];
Aαc2ADAMSz = ListInterpolation[Aαc2ADAMS[[All, 3]], {Aαc2ADAMS[[All, 1]]}];
Aαc2ADAMSy = ListInterpolation[Aαc2ADAMS[[All, 4]], {Aαc2ADAMS[[All, 1]]}];

(*Second Cross*)

(*Position vector of point 27 of pin on 2nd cross wrt its CG expressed in I frame*)
MatrixForm[Ir27 = { - rC2, 0, 0}];

(*Position vector of CG of 2nd cross wrt center of 1st cross*)

MatrixForm[CrI = {0, 0, Lim}];

(*Velocity and acceleration of CG of 2nd cross expressed in C frame*)
MatrixForm[CVc2 = Simplify[CVim2im1 + Cωim1×CrI]];
SetAttributes[{rC2}, Constant]
MatrixForm[Cac2 = Simplify[Dt[CVim2im1, t] + Cωim1×(Cωim1×CrI) + Cαim1×CrI + 2Cωim1×CVim2im1]];
(*Moment of inertia of 2nd cross*)
MatrixForm[IIc2 = {{Ic11, 0, 0}, {0, Ic12, 0}, {0, 0, Ic13}}] ;

(*Position vectors of forces acting on 2nd cross wrt its CG*)
MatrixForm[Ir28 = - Ir27];
MatrixForm[Ir29 = {0, - rC1, 0}];
MatrixForm[Ir30 = - Ir29];

(*Barrel - Output Shaft Assembly*)

(*Attach coordinate frame D to center of rotation of yoke*)
MatrixForm[DrI = {0, 0, Ry}]; (*CG of 2nd cross wrt yoke axis of rotation*)
MatrixForm[DrOS = {0, 0, rOSz}]; (*Position vector of CG of barrel wrt point K*)

(*Velocity of CG of output shaft express wrt A frame*)

MatrixForm[AVos = Simplify[Chop[Tos[θ, ϕ]^T.(Dωos×DrOS)]]];

(*Acceleration of output shaft*)

MatrixForm[Aaos = Simplify[Chop[Tos[θ, ϕ]^T.(Dωos×(Dωos×DrOS) + Dαos×DrOS)]]];

(*Moment of inertia of output shaft*)
MatrixForm[DIos = {{Ios11, Ios12, Ios13}, {Ios12, Ios22, Ios23}, {Ios13, Ios23, Ios33}}];

(*Piston displacement*)

φo[θθ_] : = Module[{ φo}, φo[θ_] : = θ + ArcSin[(r - R Cos[θ] - (Ry + Lis) Sin[θ])/LCR]; φo[θθ]]
IF[θθ_, ϕϕ_] : = Module[{IF}, IF[θ_, ϕ_] : = - Ry - (Lis + Ry) Cos[θ] + R Cos[ϕ] Sin[θ] + Sqrt[LCR^2 - Sin[θ]^2 (Lis + Ry)^2 - r^2 + 2r R (1 - 2 Cos[ϕ]^2 Sin[θ/2]^2) + R^2 (Sin[θ]^2 Cos[ϕ]^2 - 1) + 2(Lis + Ry)Cos[ϕ]Sin[θ](r - R Cos[θ])]; IF[θθ, ϕϕ]];

Z[θθ_, ϕϕ_] : = Module[{Z, IH}, IH : = - Ry + LCR Cos[φo[θ] - θ] - (Lis + Ry) Cos[θ] + R Sin[θ]; Z[θ_, ϕ_] : = Chop[IH - IF[θ, ϕ]]; Z[θθ, ϕϕ]]

ZD[tt_, ii_] = Module[{ZD}, ZD[t_, i_] = Dt[Z[θ, ϕ + 2*Pi*(i - 1)/9], t, Constants→{r, R, Lis, Ry, LCR, i}]; ZD[tt, ii]];

ZDD[tt_, ii_] = Module[{ZDD}, ZDD[t_, i_] = Dt[Z[θ, ϕ + 2*Pi*(i - 1)/9], {t, 2}, Constants→{r, R, Lis, Ry, LCR, i}]; ZDD[tt, ii]];

(*Barrel - Output Shaft Assembly - Position vectors*)

(*Position vectors at points 29 and 30 wrt yoke center of rotation*)

Ar29 = (Tos[θ, ϕ]^T.DrI + Tc2^T.Ir29)/.(1/Sqrt[Sec[ϕ]^2])→Cos[ϕ];

Ar30 = (Tos[θ, ϕ]^T.DrI + Tc2^T.Ir30)/.(1/Sqrt[Sec[ϕ]^2])→Cos[ϕ];

(*Position vector of reaction force from thrust ball bearing at end of barrel*)
DrB4toB = {0, 0, rB4toBz};

```
(*Position vectors of reaction forces from piston and oil film between barrel and piston at points 31 to 39 (–DFBtoP, i) wrt yoke axes of rotation*)
Dr31 = Simplify[{0, - r, Ry + IF[θ, ϕ] + rWP}];
Dr32 = Simplify[{0, - r, Ry + IF[θ, ϕ + 2Pi/9] + rWP}];
Dr33 = Chop[Simplify[{0, - r, Ry + IF[θ, ϕ + 4Pi/9] + rWP}/.Cos[Pi/18 - ϕ]^2→(1 - Sin[Pi/18 - ϕ]^2)]];
Dr34 = Simplify[{0, - r, Ry + IF[θ, ϕ + 6Pi/9] + rWP}];
Dr35 = Simplify[{0, - r, Ry + IF[θ, ϕ + 8Pi/9] + rWP}];
Dr36 = Simplify[{0, - r, Ry + IF[θ, ϕ + 10Pi/9] + rWP}];
Dr37 = Simplify[{0, - r, Ry + IF[θ, ϕ + 12Pi/9] + rWP}];
Dr38 = Simplify[{0, - r, Ry + IF[θ, ϕ + 14Pi/9] + rWP}];
Dr39 = Simplify[{0, - r, Ry + IF[θ, ϕ + 16Pi/9] + rWP}];

(*Position vectors of reaction forces between discharge/suction port of valve plate and solid area located between each successive cylinder on barrel at points 69 to 77*)
DrBStoVP = {0, - r, LYtoVP};

(*Velocity & acceleration of piston wrt barrel expressed in D frame*)
SetAttributes[{ii1}, Constant]
MatrixForm[DVpb[t_, ii1_] = Simplify[Chop[{0, 0, - ZD[t, ii1]}]]];
MatrixForm[Dapb[t_, ii1_] = Simplify[Chop[{0, 0, - ZDD[t, ii1]}]]];

AVpb1ADAMS = Import["C:\\Users\\noor\\Documents\\ABH\\Dissertation\\Mahematica
models\\Kinematic data from adams at 30 degrees\\Velocity\\VelPistonToBarrel.csv"];

AVpb1ADAMSz = ListInterpolation[AVpb1ADAMS[[All, 2]], {AVpb1ADAMS[[All, 1]]}];
AVpb1ADAMSy = ListInterpolation[AVpb1ADAMS[[All, 3]], {AVpb1ADAMS[[All, 1]]}];
AVpb1ADAMSMag = ListInterpolation[AVpb1ADAMS[[All, 4]], {AVpb1ADAMS[[All, 1]]}];

(*Angular velocity of piston expressed in D frame*)
MatrixForm[Dωp = Dωos];

(*Position vector of CG of ball joint between piston and ConRod wrt center of yoke axis of rotation*)
MatrixForm[Drp[θ_, ϕ_, mm_] = {0, - r, IF[θ, ϕ + 2Pi*(mm - 1)/9] + Ry}];

(*Position vector of CG of piston wrt center of ball joint between piston and ConRod*)
DrWP = {0, 0, rWP};

(*Position vector of reaction force from barrel to piston*)
DrBtoP = {0, 0, rWP};

(*Velocity of CG of piston*)
MatrixForm[DVp[t_, jj_] = DVpb[t, jj] + Dωp×(Drp[θ, ϕ, jj] + DrWP)];

AVp[t_, j_] = Simplify[Tos[θ, ϕ + 2Pi*(j - 1)/9]^T.DVp[t, j]];

AVp1ADAMS = Import["C:\\Users\\noor\\Documents\\ABH\\Dissertation\\Mahematica models\\Kinematic
data from adams at 30 degrees\\Velocity\\VelPiston1.csv"];

AVp2ADAMS = Import["C:\\Users\\noor\\Documents\\ABH\\Dissertation\\Mahematica models\\Kinematic
data from adams at 30 degrees\\Velocity\\VelPiston2.csv"];
AVp3ADAMS = Import["C:\\Users\\noor\\Documents\\ABH\\Dissertation\\Mahematica models\\Kinematic
data from adams at 30 degrees\\Velocity\\VelPiston3.csv"];
AVp4ADAMS = Import["C:\\Users\\noor\\Documents\\ABH\\Dissertation\\Mahematica models\\Kinematic
data from adams at 30 degrees\\Velocity\\VelPiston4.csv"];
AVp5ADAMS = Import["C:\\Users\\noor\\Documents\\ABH\\Dissertation\\Mahematica models\\Kinematic
data from adams at 30 degrees\\Velocity\\VelPiston5.csv"];
```

```
AVp6ADAMS = Import["C:\\Users\\noor\\Documents\\ABH\\Dissertation\\Mahematica models\\Kinematic data from adams at 30 degrees\\Velocity\\VelPiston6.csv"];
AVp7ADAMS = Import["C:\\Users\\noor\\Documents\\ABH\\Dissertation\\Mahematica models\\Kinematic data from adams at 30 degrees\\Velocity\\VelPiston7.csv"];
AVp8ADAMS = Import["C:\\Users\\noor\\Documents\\ABH\\Dissertation\\Mahematica models\\Kinematic data from adams at 30 degrees\\Velocity\\VelPiston8.csv"];
AVp9ADAMS = Import["C:\\Users\\noor\\Documents\\ABH\\Dissertation\\Mahematica models\\Kinematic data from adams at 30 degrees\\Velocity\\VelPiston9.csv"];

AVp1ADAMSx = ListInterpolation[AVp1ADAMS[[All, 2]], {AVp1ADAMS[[All, 1]]}];
AVp1ADAMSz = ListInterpolation[AVp1ADAMS[[All, 3]], {AVp1ADAMS[[All, 1]]}];
AVp1ADAMSy = ListInterpolation[AVp1ADAMS[[All, 4]], {AVp1ADAMS[[All, 1]]}];
AVp1ADAMSMag = ListInterpolation[AVp1ADAMS[[All, 5]], {AVp1ADAMS[[All, 1]]}];
AVp2ADAMSx = ListInterpolation[AVp2ADAMS[[All, 2]], {AVp2ADAMS[[All, 1]]}];
AVp2ADAMSz = ListInterpolation[AVp2ADAMS[[All, 3]], {AVp2ADAMS[[All, 1]]}];
AVp2ADAMSy = ListInterpolation[AVp2ADAMS[[All, 4]], {AVp2ADAMS[[All, 1]]}];
AVp3ADAMSx = ListInterpolation[AVp3ADAMS[[All, 2]], {AVp3ADAMS[[All, 1]]}];
AVp3ADAMSz = ListInterpolation[AVp3ADAMS[[All, 3]], {AVp3ADAMS[[All, 1]]}];
AVp3ADAMSy = ListInterpolation[AVp3ADAMS[[All, 4]], {AVp3ADAMS[[All, 1]]}];
AVp4ADAMSx = ListInterpolation[AVp4ADAMS[[All, 2]], {AVp4ADAMS[[All, 1]]}];
AVp4ADAMSz = ListInterpolation[AVp4ADAMS[[All, 3]], {AVp4ADAMS[[All, 1]]}];
AVp4ADAMSy = ListInterpolation[AVp4ADAMS[[All, 4]], {AVp4ADAMS[[All, 1]]}];
AVp5ADAMSx = ListInterpolation[AVp5ADAMS[[All, 2]], {AVp5ADAMS[[All, 1]]}];
AVp5ADAMSz = ListInterpolation[AVp5ADAMS[[All, 3]], {AVp5ADAMS[[All, 1]]}];
AVp5ADAMSy = ListInterpolation[AVp5ADAMS[[All, 4]], {AVp5ADAMS[[All, 1]]}];

AVp6ADAMSx = ListInterpolation[AVp6ADAMS[[All, 2]], {AVp6ADAMS[[All, 1]]}];
AVp6ADAMSz = ListInterpolation[AVp6ADAMS[[All, 3]], {AVp6ADAMS[[All, 1]]}];
AVp6ADAMSy = ListInterpolation[AVp6ADAMS[[All, 4]], {AVp6ADAMS[[All, 1]]}];
AVp7ADAMSx = ListInterpolation[AVp7ADAMS[[All, 2]], {AVp7ADAMS[[All, 1]]}];
AVp7ADAMSz = ListInterpolation[AVp7ADAMS[[All, 3]], {AVp7ADAMS[[All, 1]]}];
AVp7ADAMSy = ListInterpolation[AVp7ADAMS[[All, 4]], {AVp7ADAMS[[All, 1]]}];
AVp8ADAMSx = ListInterpolation[AVp8ADAMS[[All, 2]], {AVp8ADAMS[[All, 1]]}];
AVp8ADAMSz = ListInterpolation[AVp8ADAMS[[All, 3]], {AVp8ADAMS[[All, 1]]}];
AVp8ADAMSy = ListInterpolation[AVp8ADAMS[[All, 4]], {AVp8ADAMS[[All, 1]]}];
AVp9ADAMSx = ListInterpolation[AVp9ADAMS[[All, 2]], {AVp9ADAMS[[All, 1]]}];
AVp9ADAMSz = ListInterpolation[AVp9ADAMS[[All, 3]], {AVp9ADAMS[[All, 1]]}];
AVp9ADAMSy = ListInterpolation[AVp9ADAMS[[All, 4]], {AVp9ADAMS[[All, 1]]}];
```

(*The Piston*)

```
(*Moment of inertia of piston*)
MatrixForm[DIp = {{Ip11, 0, 0}, {0, Ip11, 0}, {0, 0, Ip33}}];
```

(*Angular velocity and Acceleration of piston*)

```
MatrixForm[Dαp = Simplify[Dt[Dωos, t]]];
MatrixForm[Dap[θx_, ϕx_, kk_] = Chop[Dapb[t, kk] + Dωp×(Dωp×(Drp[θx, ϕx, kk] + DrWP)) + Dαp×(Drp[θx, ϕx, kk] + DrWP)]];

Aap[θ_, ϕ_, kk_] = Tos[θ, ϕ + 2Pi*(kk - 1)/9]^T.Dap[θ, ϕ, kk];

Aap1ADAMS = Import["C:\\Users\\noor\\Documents\\ABH\\Dissertation\\Mahematica models\\Kinematic data from adams at 30 degrees\\Acceleration\\AccPiston1.csv"];

Aap2ADAMS = Import["C:\\Users\\noor\\Documents\\ABH\\Dissertation\\Mahematica models\\Kinematic data from adams at 30 degrees\\Acceleration\\AccPiston2.csv"];
```

```
Aap3ADAMS = Import["C:\\Users\\noor\\Documents\\ABH\\Dissertation\\Mahematica models\\Kinematic
data from adams at 30 degrees\\Acceleration\\AccPiston3.csv"];
Aap4ADAMS = Import["C:\\Users\\noor\\Documents\\ABH\\Dissertation\\Mahematica models\\Kinematic
data from adams at 30 degrees\\Acceleration\\AccPiston4.csv"];
Aap5ADAMS = Import["C:\\Users\\noor\\Documents\\ABH\\Dissertation\\Mahematica models\\Kinematic
data from adams at 30 degrees\\Acceleration\\AccPiston5.csv"];
Aap6ADAMS = Import["C:\\Users\\noor\\Documents\\ABH\\Dissertation\\Mahematica models\\Kinematic
data from adams at 30 degrees\\Acceleration\\AccPiston6.csv"];
Aap7ADAMS = Import["C:\\Users\\noor\\Documents\\ABH\\Dissertation\\Mahematica models\\Kinematic
data from adams at 30 degrees\\Acceleration\\AccPiston7.csv"];
Aap8ADAMS = Import["C:\\Users\\noor\\Documents\\ABH\\Dissertation\\Mahematica models\\Kinematic
data from adams at 30 degrees\\Acceleration\\AccPiston8.csv"];
Aap9ADAMS = Import["C:\\Users\\noor\\Documents\\ABH\\Dissertation\\Mahematica models\\Kinematic
data from adams at 30 degrees\\Acceleration\\AccPiston9.csv"];

Aap1ADAMSx = ListInterpolation[Aap1ADAMS[[All, 2]], {Aap1ADAMS[[All, 1]]}];
Aap1ADAMSz = ListInterpolation[Aap1ADAMS[[All, 3]], {Aap1ADAMS[[All, 1]]}];
Aap1ADAMSy = ListInterpolation[Aap1ADAMS[[All, 4]], {Aap1ADAMS[[All, 1]]}];
Aap1ADAMSMag = ListInterpolation[Aap1ADAMS[[All, 5]], {Aap1ADAMS[[All, 1]]}];
Aap2ADAMSx = ListInterpolation[Aap2ADAMS[[All, 2]], {Aap2ADAMS[[All, 1]]}];
Aap2ADAMSz = ListInterpolation[Aap2ADAMS[[All, 3]], {Aap2ADAMS[[All, 1]]}];
Aap2ADAMSy = ListInterpolation[Aap2ADAMS[[All, 4]], {Aap2ADAMS[[All, 1]]}];
Aap2ADAMSMag = ListInterpolation[Aap2ADAMS[[All, 5]], {Aap2ADAMS[[All, 1]]}];
Aap3ADAMSx = ListInterpolation[Aap3ADAMS[[All, 2]], {Aap3ADAMS[[All, 1]]}];
Aap3ADAMSz = ListInterpolation[Aap3ADAMS[[All, 3]], {Aap3ADAMS[[All, 1]]}];
Aap3ADAMSy = ListInterpolation[Aap3ADAMS[[All, 4]], {Aap3ADAMS[[All, 1]]}];
Aap3ADAMSMag = ListInterpolation[Aap3ADAMS[[All, 5]], {Aap3ADAMS[[All, 1]]}];
Aap4ADAMSx = ListInterpolation[Aap4ADAMS[[All, 2]], {Aap4ADAMS[[All, 1]]}];
Aap4ADAMSz = ListInterpolation[Aap4ADAMS[[All, 3]], {Aap4ADAMS[[All, 1]]}];
Aap4ADAMSy = ListInterpolation[Aap4ADAMS[[All, 4]], {Aap4ADAMS[[All, 1]]}];
Aap4ADAMSMag = ListInterpolation[Aap4ADAMS[[All, 5]], {Aap4ADAMS[[All, 1]]}];
Aap5ADAMSx = ListInterpolation[Aap5ADAMS[[All, 2]], {Aap5ADAMS[[All, 1]]}];
Aap5ADAMSz = ListInterpolation[Aap5ADAMS[[All, 3]], {Aap5ADAMS[[All, 1]]}];
Aap5ADAMSy = ListInterpolation[Aap5ADAMS[[All, 4]], {Aap5ADAMS[[All, 1]]}];
Aap5ADAMSMag = ListInterpolation[Aap5ADAMS[[All, 5]], {Aap5ADAMS[[All, 1]]}];
Aap6ADAMSx = ListInterpolation[Aap6ADAMS[[All, 2]], {Aap6ADAMS[[All, 1]]}];
Aap6ADAMSz = ListInterpolation[Aap6ADAMS[[All, 3]], {Aap6ADAMS[[All, 1]]}];
Aap6ADAMSy = ListInterpolation[Aap6ADAMS[[All, 4]], {Aap6ADAMS[[All, 1]]}];
Aap6ADAMSMag = ListInterpolation[Aap6ADAMS[[All, 5]], {Aap6ADAMS[[All, 1]]}];
Aap7ADAMSx = ListInterpolation[Aap7ADAMS[[All, 2]], {Aap7ADAMS[[All, 1]]}];
Aap7ADAMSz = ListInterpolation[Aap7ADAMS[[All, 3]], {Aap7ADAMS[[All, 1]]}];
Aap7ADAMSy = ListInterpolation[Aap7ADAMS[[All, 4]], {Aap7ADAMS[[All, 1]]}];
Aap7ADAMSMag = ListInterpolation[Aap7ADAMS[[All, 5]], {Aap7ADAMS[[All, 1]]}];
Aap8ADAMSx = ListInterpolation[Aap8ADAMS[[All, 2]], {Aap8ADAMS[[All, 1]]}];
Aap8ADAMSz = ListInterpolation[Aap8ADAMS[[All, 3]], {Aap8ADAMS[[All, 1]]}];
Aap8ADAMSy = ListInterpolation[Aap8ADAMS[[All, 4]], {Aap8ADAMS[[All, 1]]}];
Aap8ADAMSMag = ListInterpolation[Aap8ADAMS[[All, 5]], {Aap8ADAMS[[All, 1]]}];
Aap9ADAMSx = ListInterpolation[Aap9ADAMS[[All, 2]], {Aap9ADAMS[[All, 1]]}];
Aap9ADAMSz = ListInterpolation[Aap9ADAMS[[All, 3]], {Aap9ADAMS[[All, 1]]}];
Aap9ADAMSy = ListInterpolation[Aap9ADAMS[[All, 4]], {Aap9ADAMS[[All, 1]]}];
Aap9ADAMSMag = ListInterpolation[Aap9ADAMS[[All, 5]], {Aap9ADAMS[[All, 1]]}];
```

(*Connecting Rod - Position vectors*)

```
(*position vector of point B wrt point A*)
MatrixForm[BrB = {0, - R, 0}];
```

(*Position vector of point E wrt point A*)

MatrixForm[ArE[θx_, ϕx_] = Simplify[Chop[{0, 0, Lis} + Tim1^T.{0, 0, Lim} + Tos[θx, ϕx]^T.{0, - r, IF[θx, ϕx]}]]];

(*Position vector of E wrt B*)

MatrixForm[ArEB[θx_, ϕx_] = Simplify[Chop[ArE[θx, ϕx] - T1[ϕx]^T.BrB]]];

(*Velocity of point B*)

MatrixForm[AVB[ϕx_] = Simplify[Chop[T1[ϕx]^T].(BωMS×BrB)]];

MatrixForm[AaB[ϕx_] = Simplify[Chop[T1[ϕx]^T.(BωMS×(BωMS×BrB) + BαMS×BrB)]]];

(*Connecting Rod - Velocity*)
(*Position vector of CG of ConRod wrt to its left end*)

ArCRG[θx_, ϕx_] = T1[ϕx]^T.BrB + rCR*ArEB[θx, ϕx]/LCR;

(*Velocity of CG of ConRod*)
AVCR[tt_, ii_] = Module[{AVCR}, AVCR[t_, i_] = Dt[ArCRG[θ, ϕ + 2Pi (i - 1)/9], t, Constants→{r, R, Lis, Ry, LCR, i}]; AVCR[tt, ii]];

AVCR1ADAMS = Import["C:\\Users\\noor\\Documents\\ABH\\Dissertation\\Mahematica models\\Kinematic data from adams at 30 degrees\\Velocity\\VelConRod1.csv"];

AVCR1ADAMSx = ListInterpolation[AVCR1ADAMS[[All, 2]], {AVCR1ADAMS[[All, 1]]}];
AVCR1ADAMSz = ListInterpolation[AVCR1ADAMS[[All, 3]], {AVCR1ADAMS[[All, 1]]}];
AVCR1ADAMSy = ListInterpolation[AVCR1ADAMS[[All, 4]], {AVCR1ADAMS[[All, 1]]}];
AVCR1ADAMSMag = ListInterpolation[AVCR1ADAMS[[All, 5]], {AVCR1ADAMS[[All, 1]]}];

(*Acceleration of ConRod*)
AaCR[tt_, ii_] = Module[{AaCR}, AaCR[t_, i_] = Dt[ArCRG[θ, ϕ + 2Pi (i - 1)/9], {t, 2}, Constants→{r, R, Lis, Ry, LCR, i}]; AaCR[tt, ii]];
AaCR1ADAMS = Import["C:\\Users\\noor\\Documents\\ABH\\Dissertation\\Mahematica models\\Kinematic data from adams at 30 degrees\\Acceleration\\AccConRod1.csv"];

AaCR1ADAMSx = ListInterpolation[AaCR1ADAMS[[All, 2]], {AaCR1ADAMS[[All, 1]]}];
AaCR1ADAMSz = ListInterpolation[AaCR1ADAMS[[All, 3]], {AaCR1ADAMS[[All, 1]]}];
AaCR1ADAMSy = ListInterpolation[AaCR1ADAMS[[All, 4]], {AaCR1ADAMS[[All, 1]]}];
AaCR1ADAMSMag = ListInterpolation[AaCR1ADAMS[[All, 5]], {AaCR1ADAMS[[All, 1]]}];

(*Valve Plate - Yoke assembly*)

(*Attach coordinate system h1h2h3 to valve plate*)
MatrixForm[Tvp = Tx[θ]];

(*Angular velocity (skew symmetric form) of valve plate*)
MatrixForm[ωvp = Simplify[Tvp.Transpose[Dt[Tvp, t]]]];
(*Angular velocity and angular acceleration (vector form) of valve plate*)
Simplify[MatrixForm[Hωvp = {ωvp[[3, 2]], ωvp[[1, 3]], ωvp[[2, 1]]}]];
MatrixForm[Hαvp = Dt[Hωvp, t]];

(*Position vector of CG of valve plate*)
MatrixForm[Hrvp = {rvpx, 0, rvpz}];

(*Velocity of CG of valve plate*)

MatrixForm[HVvp = Hωvp×Hrvp];

(*Acceleration of CG of valve plate*)
MatrixForm[Havp = Hωvp×(Hωvp×Hrvp) + Hαvp×Hrvp];

(*Moment of inertia of valve plate*)
MatrixForm[HIvp = {{Ivp11, Ivp12, Ivp13}, {Ivp12, Ivp22, Ivp23}, {Ivp13, Ivp23, Ivp33}}];

(*Displacement of ram (derivation based on displacement mechanism.nb)*)
x = L3(Cos[γ5 + ε] - Cos[γ5 + ε + θ]) + Sqrt[Lac^2 - (L4 - L3 Sin[γ5 + ε + θ])^2] - Sqrt[Lac^2 - (L4 - L3 Sin[γ5 + ε])^2];

(*Velocity of ram*)
SetAttributes[{L3, ε, Lac, γ5, L4}, Constant]
xD : = Simplify [Dt[x, t]];
AVram = Simplify[{0, - Sin[ε], - Cos[ε]}*xD] ;
AaRAM = Dt[AVram, t] ;
CD : = - (L4 - L3 Sin[γ5 + ε + θ]) - Sqrt[Lac^2 - (L4 - L3 Sin[γ5 + ε + θ])^2]Tan[γ5 + ε + θ];
AωAC = Simplify[(xD/CD)*{ - 1, 0, 0}];

(*Angular acceleration of actuating link*)
AαAC = Dt[AωAC, t];

(*Distance from CG of actuating link to instant center of rotation*)
γ8 = - ArcSin[(L4 - L3 Sin[γ5 + ε + θ])/Lac];
CG := Sqrt[DG^2 + CD^2 - 2*DG*CD*Sin[γ8]];
γ4 := ArcSin[DG*Cos[γ8]/CG];

(*Velocity of CG of actuating link*)
AVAC = Simplify[AωAC*CG]×{0, - Sin[ε - γ4], - Cos[ε - γ4]};
SetAttributes[{L3, ε, Lac, γ5, DG, EH}, Constant]
AaAC = Dt[AVAC, t];

(*Barrel - Output Shaft Assembly*)

LC1[θθ_] : = Module[{LC1, CG, GF}, γo = ArcSin[(r - R)/LCR]; γ1 : = ArcTan[r/EH]; EF : = Sqrt[r^2 + EH^2];
GF[θx_] : = 2*EF*Sin[θx/2]; CG[θx_] : = (DF - LCR Cos[φo[θx]] + LCR Cos[γo]) Cos[θx] - GF[θx] Sin[γ1 - θx/2] - (- r + R + LCR Sin[φo[θx]]) Sin[θx]; LC1[θx_] : = CG[θx] - LC2 - Lp1; LC1[θθ]]

Vmin[θθ_] : = Module[{Vmin},
Vmin[θx_] : = Chop[LC1[θx]*Ac + Vfixed]; Vmin[θθ]]

Lmin[θθ_] : = Module[{Lmin}, Dce : = Sqrt[4*Ace/Pi]; Dc : = Sqrt[4*Ac/Pi]; Le : = LC2*Dce/(Dc - Dce);
Lmin[θx_] : = ((2*Ac/9)*(LC2 + Le)^2 - (2*Ace/9)*Le^2 + Ac*LC1[θx]*(LC1[θx]/2 + LC2 + Le) - Vmin[θx]*Le)/Vmin[θx]; Lmin[θθ]]

Lv[θθ_, ϕϕ_] : = Module[{Lv}, Lv[θx_, ϕx_] : = (Vmin[θx]*Lmin[θx] + Ac*Z[θx, ϕx]*(Z[θx, ϕx]/2 + LC1[θx] + LC2))/(Vmin[θx] + Ac*Z[θx, ϕx]); Lv[θθ, ϕϕ]]

VOIL[θθ_, ϕϕ_] : = Module[{VOIL}, VOIL[θx_, ϕx_] : = Vmin[θx] + Ac*Z[θx, ϕx]; VOIL[θθ, ϕϕ]]
VOILD[tt_, ii_] = Module[{VOILD}, VOILD[t_, i_] = Dt[VOIL[θ, ϕ + 2*Pi*(i - 1)/9], t, Constants→{i}];
VOILD[tt, ii]];

(*Oil Control Volume*)

(*External forces acting on oil control volume*)
(*1. Force from piston to control volume at points 40 to 48 denoted as –DFOILtoPi with respective position vectors*)
DrOILtoP1 = Drp[θ, ϕ, 1] + {0, 0, Lp1};
DrOILtoP2 = Drp[θ, ϕ, 2] + {0, 0, Lp1};
DrOILtoP3 = Drp[θ, ϕ, 3] + {0, 0, Lp1};
DrOILtoP4 = Drp[θ, ϕ, 4] + {0, 0, Lp1};
DrOILtoP5 = Drp[θ, ϕ, 5] + {0, 0, Lp1};
DrOILtoP6 = Drp[θ, ϕ, 6] + {0, 0, Lp1};
DrOILtoP7 = Drp[θ, ϕ, 7] + {0, 0, Lp1};
DrOILtoP8 = Drp[θ, ϕ, 8] + {0, 0, Lp1};
DrOILtoP9 = Drp[θ, ϕ, 9] + {0, 0, Lp1};

(*2. Weight of oil column*)
MatrixForm[AWOIL1 = {0, ρ*g*VOIL[θ, ϕ], 0}];
MatrixForm[AWOIL2 = {0, ρ g VOIL[θ, ϕ + 2*Pi/9], 0}];
MatrixForm[AWOIL3 = {0, ρ g VOIL[θ, ϕ + 4*Pi/9], 0}];
MatrixForm[AWOIL4 = {0, ρ g VOIL[θ, ϕ + 6*Pi/9], 0}];
MatrixForm[AWOIL5 = {0, ρ g VOIL[θ, ϕ + 8*Pi/9], 0}];
MatrixForm[AWOIL6 = {0, ρ g VOIL[θ, ϕ + 10*Pi/9], 0}];
MatrixForm[AWOIL7 = {0, ρ g VOIL[θ, ϕ + 12*Pi/9], 0}];
MatrixForm[AWOIL8 = {0, ρ g VOIL[θ, ϕ + 14*Pi/9], 0}];
MatrixForm[AWOIL9 = {0, ρ g VOIL[θ, ϕ + 16*Pi/9], 0}];

(*3.Reaction forces from barrel to control volumes at points 49 to 57 denoted as –DFOILtoBi.*)
(*Position vectors of forces from oil control volume in the cylinder at points 49 to 57*)
DrOILtoB[θx_, ϕx_] : = {0, 0, Z[θx, ϕx] + LC1[θx] + LC2 - Lv[θx, ϕx] + Lp1};
DrOILtoB1 : = Dr31 + DrOILtoB[θ, ϕ] - DrWP;
DrOILtoB2 : = Dr32 + DrOILtoB[θ, ϕ + 2*Pi/9] - DrWP;
DrOILtoB3 : = Dr33 + DrOILtoB[θ, ϕ + 4*Pi/9] - DrWP;
DrOILtoB4 : = Dr34 + DrOILtoB[θ, ϕ + 6*Pi/9] - DrWP;
DrOILtoB5 : = Dr35 + DrOILtoB[θ, ϕ + 8*Pi/9] - DrWP;
DrOILtoB6 : = Dr36 + DrOILtoB[θ, ϕ + 10*Pi/9] - DrWP;
DrOILtoB7 : = Dr37 + DrOILtoB[θ, ϕ + 12*Pi/9] - DrWP;
DrOILtoB8 : = Dr38 + DrOILtoB[θ, ϕ + 14*Pi/9] - DrWP;
DrOILtoB9 : = Dr39 + DrOILtoB[θ, ϕ + 16*Pi/9] - DrWP;

(*4. Force due to pressure on discharge or suction orifice at points 80 to 88 denoted as - DFOILtoVPi. The corresponding position vector is DrOILtoVP*)

(*Linear momentum of the control volume*)
DLMcv1 = ρ*DVpb[t, 1]*VOILD[t, 1];
DLMcv2 = ρ*DVpb[t, 2]*VOILD[t, 2];
DLMcv3 = ρ*DVpb[t, 3]*VOILD[t, 3];
DLMcv4 = ρ*DVpb[t, 4]*VOILD[t, 4];
DLMcv5 = ρ*DVpb[t, 5]*VOILD[t, 5];
DLMcv6 = ρ*DVpb[t, 6]*VOILD[t, 6];
DLMcv7 = ρ*DVpb[t, 7]*VOILD[t, 7];
DLMcv8 = ρ*DVpb[t, 8]*VOILD[t, 8];
DLMcv9 = ρ*DVpb[t, 9]*VOILD[t, 9];

(*Net rate of linear momentum through the control surface of oil control volume*)
DLMcs1 = ρ*Ac*DVpb[t, 1]*(DVpb[t, 1].{0, 0, - 1} + (Ac/ArFR[ϕ])*(DVpb[t, 1].{0, 0, 1}));
DLMcs2 = ρ*Ac*DVpb[t, 2]*(DVpb[t, 2].{0, 0, - 1} + (Ac/ArFR[ϕ + 2*Pi/9])*(DVpb[t, 2].{0, 0, 1}));
DLMcs3 = ρ*Ac*DVpb[t, 3]*(DVpb[t, 3].{0, 0, - 1} + (Ac/ArFR[ϕ + 4*Pi/9])*(DVpb[t, 3].{0, 0, 1}));
DLMcs4 = ρ*Ac*DVpb[t, 4]*(DVpb[t, 4].{0, 0, - 1} + (Ac/ArFR[ϕ + 6*Pi/9])*(DVpb[t, 4].{0, 0, 1}));

```
DLMcs5 = ρ*Ac*DVpb[t, 5]*(DVpb[t, 5].{0, 0, - 1} + (Ac/ArFR[ϕ + 8*Pi/9])*(DVpb[t, 5].{0, 0, 1}));
DLMcs6 = ρ*Ac*DVpb[t, 6]*(DVpb[t, 6].{0, 0, - 1} + (Ac/ArFR[ϕ + 10*Pi/9])*(DVpb[t, 6].{0, 0, 1}));
DLMcs7 = ρ*Ac*DVpb[t, 7]*(DVpb[t, 7].{0, 0, - 1} + (Ac/ArFR[ϕ + 12*Pi/9])*(DVpb[t, 7].{0, 0, 1}));
DLMcs8 = ρ*Ac*DVpb[t, 8]*(DVpb[t, 8].{0, 0, - 1} + (Ac/ArFR[ϕ + 14*Pi/9])*(DVpb[t, 8].{0, 0, 1}));
DLMcs9 = ρ*Ac*DVpb[t, 9]*(DVpb[t, 9].{0, 0, - 1} + (Ac/ArFR[ϕ + 16*Pi/9])*(DVpb[t, 9].{0, 0, 1}));

DrOILtoVP = {0, - r, LYtoVP};

File1 = OpenRead["POIL.nb"];
PD = Read[File1];
PS = Read[File1];
POIL1[t_] = Read[File1];
POIL2[t_] = Read[File1];
POIL3[t_] = Read[File1];
POIL4[t_] = Read[File1];
POIL5[t_] = Read[File1];
POIL6[t_] = Read[File1];
POIL7[t_] = Read[File1];
POIL8[t_] = Read[File1];
POIL9[t_] = Read[File1];
Pb[ϕ_] = Read[File1];
Close[File1];
```

(*Barrel - Output Shaft Assembly*)

```
PD1 = PD[[1]];
PS1 = PS[[1]];
```

(*Point of application of hydraulic forces*)

```
RoutD = (5 PD1 (R1^2 + 2 R1 R2 + 3 R2^2) + (R1 - R2)^2 (3 R1^2 + 4 R1 R2 + 3 R2^2) ρ BωMS[[3]]^2)/(5 (2 PD1
(R1 + 2 R2) + (R1 - R2)^2 (R1 + R2) ρ BωMS[[3]]^2));

RoutS = (5 PS1 (R1^2 + 2 R1 R2 + 3 R2^2) + (R1 - R2)^2 (3 R1^2 + 4 R1 R2 + 3 R2^2) ρ BωMS[[3]]^2)/(5 (2 PS1
(R1 + 2 R2) + (R1 - R2)^2 (R1 + R2) ρ BωMS[[3]]^2));

RinD = (30 PD1 R3 (2 R3 + R4) - 2 (R3 - R4)^2 (4 R3^2 + 7 R3 R4 + 4 R4^2) ρ BωMS[[3]]^2)/(90 PD1 R3 - 15
(R3 - R4)^2 (R3 + R4) ρ BωMS[[3]]^2);

RinS = (30 PS1 R3 (2 R3 + R4) - 2 (R3 - R4)^2 (4 R3^2 + 7 R3 R4 + 4 R4^2) ρ BωMS[[3]]^2)/(90 PS1 R3 - 15
(R3 - R4)^2 (R3 + R4) ρ BωMS[[3]]^2);
```

(*Position vectors of hydrodynamic forces*)

```
HrIND = { - RinD, 0, LYtoVP};
HrINS = {RinS, 0, LYtoVP};
HrOUTD = { - RoutD, 0, LYtoVP};
HrOUTS = {RoutS, 0, LYtoVP};
```

(*Main Shaft - Frictional Moment at Ball bearing at point (1)*)

```
nms = Simplify[BωMS[[3]]];
```

(*Radial load component of bearing reaction*)

```
Fr1 = (AFB1toMSx^2 + AFB1toMSy^2)^0.5;
```

(*Total frictional moment of the bearing (N.m)*)

```
AMB1toMSz = Friction[nms, 1, d11, D1, 40, Fr1, 0, Co1] ;
```

(*Main Shaft - Frictional Moment at Thrust bearing, point (2)*)

(*Radial load component of bearing reaction*)

Fr2 = (AFB2toMSx^2 + AFB2toMSy^2)^0.5;
(*Axial load component of bearing reaction*)
Fa2 = AFB2toMSz;
AMB2toMSz = Friction[nms, 2, d2, D2, 40, Fr2, Fa2, Co2] ;
(*MBz = total frictional moment of bearing (N.m)*)

(*Main Shaft - Forces*)

ATin = {0, 0, ATinz}; (*input torque*)
AFB1toMS = {AFB1toMSx, AFB1toMSy, 0}; (*Ball bearing reaction*)
AMB1toMS = Simplify[- AMB1toMSz*Sign[BωMS]]; (*Ball bearing Frictional moment*)

AFB2toMS = {AFB2toMSx, AFB2toMSy, AFB2toMSz}; (*Thrust bearing reaction*)
AMB2toMS = Simplify[- AMB2toMSz*Sign[BωMS]]; (*Thrust bearing Frictional moment*)

AWms = {0, g*MMS, 0};

(*First Intermediate shaft - Forces*)

(*1. Reaction forces and moments from 1st cross at points (23) and (24)*)
(*2. Reaction force and torque from 2nd intermediate shaft at point (25)*)

MatrixForm[CFIM2toIM125 = {0, 0, FIM2toIM125z}] ; (*reaction from 2nd intermediate shaft to 1st intermediate at (25)*)

MatrixForm[CMIM2toIM125 = {0, 0, - MIM2toIM125z}] ; (*Reaction torque from 2nd intermediate shaft to 1st intermediate shaft*)

MatrixForm[AWim1 = {0, g Mim1, 0}];

(*First Cross - Forces*)

(*1. Reaction forces from main shaft at points (3) and (4)*)
FFMStoC13 = {FFMStoC13x, 0, FFMStoC13z};
FFMStoC14 = - FFMStoC13;

(*Frictional moments from main shaft at right and left pins of 1st cross at points (3) and (4)*)
MMStoC13 = μC1*rCP1*Sqrt[FFMStoC13x^2 + FFMStoC13z^2];
MMStoC14 = MMStoC13;
FMMStoC13 = Simplify[MMStoC13*{0, - Sign[Fωc1[[2]]], 0}];
FMMStoC14 = Simplify[MMStoC14*{0, - Sign[Fωc1[[2]]], 0}];

(*Reaction forces from 1st intermediate shaft at points (23) and (24)*)
FFIM1toC123 = {0, FIM1toC123y, FIM1toC123z};
FFIM1toC124 = - FFIM1toC123;

(*Frictional moments from 1st intermediate shaft at points (23) and (24)*)
MIM1toC123 : = μC1*rCP2*Sqrt[FIM1toC123y^2 + FIM1toC123z^2];
MIM1toC124 : = μC1*rCP3*Sqrt[FIM1toC124y^2 + FIM1toC124z^2];
FMIM1toC123 = - MIM1toC123*Sign[Fωc1[[1]]]*{1, 0, 0};
FMIM1toC124 = - MIM1toC124*Sign[Fωc1[[1]]]*{1, 0, 0};

AWc1 = {0, g Mc1, 0}; (*Weight of 1st cross*)

(*Second Intermediate Shaft - Forces*)

(*1. Reaction forces and torques from 1st intermediate shaft at point (25)*)
(*2. Reaction forces and moments from 2nd cross at points (27) and (28)*)

(* - CFIM2toIM125*)
(* - CMIM2toIM125*)
(* - IFIM2toC227*)
(* - IFIM2toC228*)
(* - IMIM2toC227*)
(* - IMIM2toC228*)
AWim2 = {0, g*Mim2, 0};

(*Second Cross - Forces*)

(*1. Reaction forces and moments from 2nd intermediate shaft at the pins (points 27 and 28)*)
(*2. Reaction forces and moments from output shaft at the pins (points 29 and 30)*)
(*3. Weight of 2nd cross*)

MatrixForm[IFIM2toC227 = {0, FIM2toC227y, FIM2toC227z}];
MIM2toC227 = μC1*rCP2*Sqrt[FIM2toC227y^2 + FIM2toC227z^2];
MatrixForm[IMIM2toC227 = MIM2toC227*{ - Sign[Iωc2[[1]]], 0, 0}];
MatrixForm[IFIM2toC228 = - IFIM2toC227];
MIM2toC228 = μC1*rCP2*Sqrt[FIM2toC228y^2 + FIM2toC228z^2];
MatrixForm[IMIM2toC228 = MIM2toC228*{ - Sign[Iωc2[[1]]], 0, 0}];
MatrixForm[IFOStoC229 = {FOStoC229x, 0, FOStoC229z}];
MOStoC229 = μC1*rCP1*Sqrt[FOStoC229x^2 + FOStoC229z^2];
MatrixForm[IMOStoC229 = MOStoC229*{0, - Sign[Iωc2[[2]]], 0}];
MatrixForm[IFOStoC230 = - IFOStoC229];
MOStoC230 = μC1*rCP1*Sqrt[FOStoC230x^2 + FOStoC230z^2];
MatrixForm[IMOStoC230 = MOStoC230*{0, - Sign[Iωc2[[2]]], 0}];
MatrixForm[AWC2 = {0, Mc2*g, 0}];

(*Barrel - Output Shaft Assembly - Forces*)

(*1.Reaction forces from 2nd cross at points 29 and 30 denoted as - IFOStoC229 and - IFOStoC230 with respective position vectors: Ir29 and Ir30*)
(*2.Frictional moment from 2nd cross at points 29 and 30 denoted as - IMOStoC229 and - IMOStoC230*)
(*3.Reaction forces from piston and oil film between barrel and piston at points 31 to 39 denoted by - DFBtoPi, i = 1, 2, …9*)
(*4.Weight of output shaft - barrel assembly*)

AWos = {0, Mos g, 0};

(*5.Force from oil column in cylinder at points 49 to 57 denoted as DFOILtoB, i*)
(*6.Frictional moment due to fluid film between barrel and valve plate*)
(*7.Hydrodynamic forces HFVPtoBoutD, HFVPtoBinD, HFVPtoBinS, HFVPtoBoutS due to oil film between VP & barrel at points 59, 60, 61, and 62*)
(*8.Frictional moment form journal bearing at point 58*)
(*9.Reaction force from thrust ball bearing at end of barrel at point 65 denoted by DFB4toB*)
(*10.Frictional moment from thrust ball bearing at end of barrel at point 65 denoted by DMB4toB*)
(*11.Reaction forces between discharge/suction port of VP & solid area located between each successive cylinder on barrel at points 69 to 77. These forces denoted as - DFBStoVP, ii = 1, 2, …9*)
(*Barrel - Output Shaft Assembly - Forces*)

(*Force from needle bearing (point 58) to barrel*)
DFB3FtoB = {FB3FtoBx, FB3FtoBy, 0};
DFB3StoB = {FB3StoBx, FB3StoBy, 0};
(*Position vector of journal bearing reaction*)
DrB3FtoB = {0, 0, rB3FtoBz};
DrB3StoB = {0, 0, rB3StoBz};

```
FB3FtoBr = Sqrt[FB3FtoBx^2 + FB3FtoBy^2];
FB3StoBr = Sqrt[FB3StoBx^2 + FB3StoBy^2];

MB3FtoBz = Friction[nms, 3, d3, D3, 40, FB3FtoBr, 0, 1];
MB3StoBz = Friction[nms, 3, d3, D3, 40, FB3StoBr, 0, 1];

(*Frictional moment component at end of barrel at point 58*)
DMB3FtoB = MB3FtoBz*{0, 0, - Sign[Dωos[[3]]]};
DMB3StoB = MB3StoBz*{0, 0, - Sign[Dωos[[3]]]};

 (*Frictional moment at thrust bearing at end of barrel (point 65)*)
Fa4 = FB4toBz;
(*Value of frictional moment of thrust ball bearing*)
MB4toBz = Friction[nms, 4, d4, D4, 40, 0, FB4toBz, Co4];
(*Frictional moment opposes direction of angular velocity component along d3 direction of barrel*)
DMB4toB = - Sign[Dωos[[3]]]*MB4toBz {0, 0, 1};

(*Hydrodynamic force normal to interface between valve plate and barrel*)
MatrixForm[HFVPtoBoutD = {0, 0, - (ζ*(R1 - R2)/12)*2*PD1*(R1 + 2 R2) + ρ*BωMS[[3]]^2(R1 +
R2)*(R1 - R2)^2}];

MatrixForm[HFVPtoBoutS = - (ζ*(R1 - R2)/12)
 {0, 0, 2*PS1*(R1 + 2 R2) + ρ*BωMS[[3]]^2(R1 + R2)*(R1 - R2)^2}];

MatrixForm[HFVPtoBinD = - (ζ*(R3 - R4)/12)
 {0, 0, 6*PD1*R3 - ρ*BωMS[[3]]^2(R3 + R4)*(R3 - R4)^2}];

MatrixForm[HFVPtoBinS = - (ζ*(R3 - R4)/12)
 {0, 0, 6*PS1*R3 - ρ*BωMS[[3]]^2(R3 + R4)*(R3 - R4)^2}];

Export["C:\\Users\\noor\\Documents\\ABH\\Dissertation\\Mahematica models\\Pressure Force on
Pistons\\HFVPtoBinS.csv", Table[{t, HFVPtoBinS[[3]]}, {t, 0, 1, 0.0001}]];
Export["C:\\Users\\noor\\Documents\\ABH\\Dissertation\\Mahematica models\\Pressure Force on
Pistons\\HFVPtoBinD.csv", Table[{t, HFVPtoBinD[[3]]}, {t, 0, 1, 0.0001}]];
Export["C:\\Users\\noor\\Documents\\ABH\\Dissertation\\Mahematica models\\Pressure Force on
Pistons\\HFVPtoBoutS.csv", Table[{t, HFVPtoBoutS[[3]]}, {t, 0, 1, 0.0001}]];
Export["C:\\Users\\noor\\Documents\\ABH\\Dissertation\\Mahematica models\\Pressure Force on
Pistons\\HFVPtoBoutD.csv", Table[{t, HFVPtoBoutD[[3]]}, {t, 0, 1, 0.0001}]];

(*Shear moment at outer land for both discharge and suction ports*)
shearout = 1/4 R1 (R1 + R2) h ζ ( - PD1 - PS1 + 2 (R1 - R2) R2 ρ BωMS[[3]]^2);
(*Shear moment at inner land for both discharge and suction ports*)
shearin = 1/12 (R3 + R4) h ζ (3 PD1 R3 + 3 PS1 R3 + 2 ( - R3^3 + R4^3) ρ BωMS[[3]]^2);
(*Total moment due to fluid film between barrel and valve plate*)
MatrixForm[DMVPtoB = - {0, 0, shearout + shearin}*Sign[Dωos[[3]]]];

Export["C:\\Users\\noor\\Documents\\ABH\\Dissertation\\Mahematica models\\Pressure Force on
Pistons\\DMVPtoB.csv", Table[{t, DMVPtoB[[3]]}, {t, 0, 1, 0.0001}]];
```

(*The Piston - Forces*)

```
(*1. Reaction forces from ConRod to piston denoted by: - AFPtoCRi, i = 1 to 9*)
(*2. Frictional moment from ConRod to piston denoted by - AMPtoCRi at points (14) to (22)*)
(*3. Pressure force from hydraulic oil*)

MatrixForm[DFOILtoP1 = {0, 0, - POIL1[t][[1]]*Ap}];
MatrixForm[DFOILtoP2 = {0, 0, - POIL2[t][[1]]*Ap}];
```

```
MatrixForm[DFOILtoP3 = {0, 0, - POIL3[t][[1]]*Ap}];
MatrixForm[DFOILtoP4 = {0, 0, - POIL4[t][[1]]*Ap}];
MatrixForm[DFOILtoP5 = {0, 0, - POIL5[t][[1]]*Ap}];
MatrixForm[DFOILtoP6 = {0, 0, - POIL6[t][[1]]*Ap}];
MatrixForm[DFOILtoP7 = {0, 0, - POIL7[t][[1]]*Ap}];
MatrixForm[DFOILtoP8 = {0, 0, - POIL8[t][[1]]*Ap}];
MatrixForm[DFOILtoP9 = {0, 0, - POIL9[t][[1]]*Ap}];

Export["C:\\Users\\noor\\Documents\\ABH\\Dissertation\\Mahematica models\\Pressure Force on
Pistons\\DFOILtoP1.csv", Table[{t, - POIL1[t][[1]]*Ap}, {t, 0, 1, 0.0001}]];
Export["C:\\Users\\noor\\Documents\\ABH\\Dissertation\\Mahematica models\\Pressure Force on
Pistons\\DFOILtoP2.csv", Table[{t, - POIL2[t][[1]]*Ap}, {t, 0, 1, 0.0001}]];
Export["C:\\Users\\noor\\Documents\\ABH\\Dissertation\\Mahematica models\\Pressure Force on
Pistons\\DFOILtoP3.csv", Table[{t, - POIL3[t][[1]]*Ap}, {t, 0, 1, 0.0001}]];
Export["C:\\Users\\noor\\Documents\\ABH\\Dissertation\\Mahematica models\\Pressure Force on
Pistons\\DFOILtoP4.csv", Table[{t, - POIL4[t][[1]]*Ap}, {t, 0, 1, 0.0001}]];
Export["C:\\Users\\noor\\Documents\\ABH\\Dissertation\\Mahematica models\\Pressure Force on
Pistons\\DFOILtoP5.csv", Table[{t, - POIL5[t][[1]]*Ap}, {t, 0, 1, 0.0001}]];
Export["C:\\Users\\noor\\Documents\\ABH\\Dissertation\\Mahematica models\\Pressure Force on
Pistons\\DFOILtoP6.csv", Table[{t, - POIL6[t][[1]]*Ap}, {t, 0, 1, 0.0001}]];
Export["C:\\Users\\noor\\Documents\\ABH\\Dissertation\\Mahematica models\\Pressure Force on
Pistons\\DFOILtoP7.csv", Table[{t, - POIL7[t][[1]]*Ap}, {t, 0, 1, 0.0001}]];
Export["C:\\Users\\noor\\Documents\\ABH\\Dissertation\\Mahematica models\\Pressure Force on
Pistons\\DFOILtoP8.csv", Table[{t, - POIL8[t][[1]]*Ap}, {t, 0, 1, 0.0001}]];
Export["C:\\Users\\noor\\Documents\\ABH\\Dissertation\\Mahematica models\\Pressure Force on
Pistons\\DFOILtoP9.csv", Table[{t, - POIL9[t][[1]]*Ap}, {t, 0, 1, 0.0001}]];

 (*Frictional force between barrel and piston*)
(*Viscous force on one piston*)
FBtoP1z = - Pi*ν[T]*rp*DVpb[t, 1][[3]]*Lp/Cp;
FBtoP2z = - Pi*ν[T]*rp*DVpb[t, 2][[3]]*Lp/Cp;
FBtoP3z = - Pi*ν[T]*rp*DVpb[t, 3][[3]]*Lp/Cp;
FBtoP4z = - Pi*ν[T]*rp*DVpb[t, 4][[3]]*Lp/Cp;
FBtoP5z = - Pi*ν[T]*rp*DVpb[t, 5][[3]]*Lp/Cp;
FBtoP6z = - Pi*ν[T]*rp*DVpb[t, 6][[3]]*Lp/Cp;
FBtoP7z = - Pi*ν[T]*rp*DVpb[t, 7][[3]]*Lp/Cp;
FBtoP8z = - Pi*ν[T]*rp*DVpb[t, 8][[3]]*Lp/Cp;
FBtoP9z = - Pi*ν[T]*rp*DVpb[t, 9][[3]]*Lp/Cp;

 (*3. Reaction force from barrel to piston*)
MatrixForm[DFBtoP1 = {FBtoP1x, FBtoP1y, FBtoP1z}];
MatrixForm[DFBtoP2 = {FBtoP2x, FBtoP2y, FBtoP2z}];
MatrixForm[DFBtoP3 = {FBtoP3x, FBtoP3y, FBtoP3z}];
MatrixForm[DFBtoP4 = {FBtoP4x, FBtoP4y, FBtoP4z}];
MatrixForm[DFBtoP5 = {FBtoP5x, FBtoP5y, FBtoP5z}];
MatrixForm[DFBtoP6 = {FBtoP6x, FBtoP6y, FBtoP6z}];
MatrixForm[DFBtoP7 = {FBtoP7x, FBtoP7y, FBtoP7z}];
MatrixForm[DFBtoP8 = {FBtoP8x, FBtoP8y, FBtoP8z}];
MatrixForm[DFBtoP9 = {FBtoP9x, FBtoP9y, FBtoP9z}];

(*4. Weight of piston*)
AWp = {0, g*Mp, 0};

## (*Connecting Rod - Forces*)
(*1. Weight of ConRod*)
AWCR = {0, MCR*g, 0};
```

(*2. Reaction force from cup at main shaft side at points (5) to (13)*)
AFMStoCR1 = {AFMStoCR1x, AFMStoCR1y, AFMStoCR1z};
AFMStoCR2 = {AFMStoCR2x, AFMStoCR2y, AFMStoCR2z};
AFMStoCR3 = {AFMStoCR3x, AFMStoCR3y, AFMStoCR3z};
AFMStoCR4 = {AFMStoCR4x, AFMStoCR4y, AFMStoCR4z};
AFMStoCR5 = {AFMStoCR5x, AFMStoCR5y, AFMStoCR5z};
AFMStoCR6 = {AFMStoCR6x, AFMStoCR6y, AFMStoCR6z};
AFMStoCR7 = {AFMStoCR7x, AFMStoCR7y, AFMStoCR7z};
AFMStoCR8 = {AFMStoCR8x, AFMStoCR8y, AFMStoCR8z};
AFMStoCR9 = {AFMStoCR9x, AFMStoCR9y, AFMStoCR9z};

(*3. Reaction from piston to ConRod at points (14) to (22)*)
AFPtoCR1 = {AFPtoCR1x, AFPtoCR1y, AFPtoCR1z};
AFPtoCR2 = {AFPtoCR2x, AFPtoCR2y, AFPtoCR2z};
AFPtoCR3 = {AFPtoCR3x, AFPtoCR3y, AFPtoCR3z};
AFPtoCR4 = {AFPtoCR4x, AFPtoCR4y, AFPtoCR4z};
AFPtoCR5 = {AFPtoCR5x, AFPtoCR5y, AFPtoCR5z};
AFPtoCR6 = {AFPtoCR6x, AFPtoCR6y, AFPtoCR6z};
AFPtoCR7 = {AFPtoCR7x, AFPtoCR7y, AFPtoCR7z};
AFPtoCR8 = {AFPtoCR8x, AFPtoCR8y, AFPtoCR8z};
AFPtoCR9 = {AFPtoCR9x, AFPtoCR9y, AFPtoCR9z};

(*Valve Plate - Yoke - Forces*)

(*1. Reaction forces at axis of rotation of yoke at points 67 and 68 and their respective position vectors*)
AFCtoY67 = {FCtoY67x, FCtoY67y, FCtoY67z};
ArCtoY67 = { - rCtoY67x, 0, 0};
AFCtoY68 = {0, FCtoY68y, FCtoY68z};
ArCtoY68 = - ArCtoY67;

(*Value of frictional moments at axis of yoke at points 67 and 68*)
(*MCtoY67x = μY*rY*Sqrt[FCtoY67y^2 + FCtoY67z^2]
MCtoY68x = μY*rY*Sqrt[FCtoY68y^2 + FCtoY68z^2]*)

(*2. Friction moment at axis of yoke at points 67 and 68*)
(*AMCtoY67 = MCtoY67x*{ - Sign[Hωvp[[1]]], 0, 0}
AMCtoY68 = MCtoY68x*{ - Sign[Hωvp[[1]]], 0, 0}*)
(*Valve Plate - Yoke - Forces*)

(*3.Reaction force from actuating link at point 66 and its respective position vector*)
AFACtoY66 = {0, FACtoY66P*Sin[ϵ - γ8] + FACtoY66N*Cos[ϵ - γ8], FACtoY66P*Cos[ϵ - γ8] - FACtoY66N*Sin[ϵ - γ8]};
(*HrACtoY66 = {rACtoY66x, rACtoY66y, rACtoY66z}; *)

(*Value of frictional moment component at common axis of yoke and actuating link at points 66*)
(*MACtoY66x = μACtoY*rAC*Sqrt[AFACtoY66[[2]]^2 + AFACtoY66[[3]]^2]*)
(*4. Frictional moment vector from actuating link at point 66*)
(*AMACtoY66 = MACtoY66x*{ - Sign[AωAC[[1]]], 0, 0}*)

(*5. Reaction force from needle bearing at end of barrel at point 58 denoted as - DFB3FtoB and - DFB3StoB*)

(*6. Frictional moment form needle bearings at point 58 denoted as - DMB3FtoB and - DMB3StoB*)

(*7. Weight of valve plate - yoke assembly*)

```
AWvp = {0, Mvp*g, 0};

(*8.Reaction force from thrust ball bearing at end of barrel at point 65, - DFB4toB*)
DFB4toB = {0, 0, FB4toBz};

(*9.Frictional moment at thrust ball bearing (point 65) denoted by –DMB4toB*)

(*10. Hydrodynamic forces : - HFVPtoBoutD, - HFVPtoBinD, - HFVPtoBinS, and - HFVPtoBoutS
due to oil film between valve plate and barrel at points 59, 60, 61, and 62 respectively.*)

(*11.Frictional moment due to fluid film between barrel and valve plate denoted as - DMVPtoB*)

(*12.Reaction forces between discharge/suction port of valve plate and solid area located between each
successive cylinder at points 69 to 77 respectively*)
DFBStoVP1 = {0, 0, Pb[ϕ][[1]]*AsFR[ϕ]};
DFBStoVP2 = {0, 0, Pb[ϕ + 2*Pi/9][[1]]*AsFR[ϕ + 2*Pi/9]};
DFBStoVP3 = {0, 0, Pb[ϕ + 4*Pi/9][[1]]*AsFR[ϕ + 4*Pi/9]};
DFBStoVP4 = {0, 0, Pb[ϕ + 6*Pi/9][[1]]*AsFR[ϕ + 6*Pi/9]};
DFBStoVP5 = {0, 0, Pb[ϕ + 8*Pi/9][[1]]*AsFR[ϕ + 8*Pi/9]};
DFBStoVP6 = {0, 0, Pb[ϕ + 10*Pi/9][[1]]*AsFR[ϕ + 10*Pi/9]};
DFBStoVP7 = {0, 0, Pb[ϕ + 12*Pi/9][[1]]*AsFR[ϕ + 12*Pi/9]};
DFBStoVP8 = {0, 0, Pb[ϕ + 14*Pi/9][[1]]*AsFR[ϕ + 14*Pi/9]};
DFBStoVP9 = {0, 0, Pb[ϕ + 16*Pi/9][[1]]*AsFR[ϕ + 16*Pi/9]};

Export["C:\\Users\\noor\\Documents\\ABH\\Dissertation\\Mahematica models\\Pressure Force on
Pistons\\DFBStoVP1.csv", Table[{t, DFBStoVP1[[3]]}, {t, 0, 1, 0.0001}]];
Export["C:\\Users\\noor\\Documents\\ABH\\Dissertation\\Mahematica models\\Pressure Force on
Pistons\\DFBStoVP2.csv", Table[{t, DFBStoVP2[[3]]}, {t, 0, 1, 0.0001}]];
Export["C:\\Users\\noor\\Documents\\ABH\\Dissertation\\Mahematica models\\Pressure Force on
Pistons\\DFBStoVP3.csv", Table[{t, DFBStoVP3[[3]]}, {t, 0, 1, 0.0001}]];
Export["C:\\Users\\noor\\Documents\\ABH\\Dissertation\\Mahematica models\\Pressure Force on
Pistons\\DFBStoVP4.csv", Table[{t, DFBStoVP4[[3]]}, {t, 0, 1, 0.0001}]];
Export["C:\\Users\\noor\\Documents\\ABH\\Dissertation\\Mahematica models\\Pressure Force on
Pistons\\DFBStoVP5.csv", Table[{t, DFBStoVP5[[3]]}, {t, 0, 1, 0.0001}]];
Export["C:\\Users\\noor\\Documents\\ABH\\Dissertation\\Mahematica models\\Pressure Force on
Pistons\\DFBStoVP6.csv", Table[{t, DFBStoVP6[[3]]}, {t, 0, 1, 0.0001}]];
Export["C:\\Users\\noor\\Documents\\ABH\\Dissertation\\Mahematica models\\Pressure Force on
Pistons\\DFBStoVP7.csv", Table[{t, DFBStoVP7[[3]]}, {t, 0, 1, 0.0001}]];
Export["C:\\Users\\noor\\Documents\\ABH\\Dissertation\\Mahematica models\\Pressure Force on
Pistons\\DFBStoVP8.csv", Table[{t, DFBStoVP8[[3]]}, {t, 0, 1, 0.0001}]];
Export["C:\\Users\\noor\\Documents\\ABH\\Dissertation\\Mahematica models\\Pressure Force on
Pistons\\DFBStoVP9.csv", Table[{t, DFBStoVP9[[3]]}, {t, 0, 1, 0.0001}]];

 (*13. Reaction force from fluid inside hose between LPA and suction exit at yoke axis of rotation at
point 78*)
AFLPAtoY78 = A78*PS1 {0, - Sin[θL], Cos[θL]};
ArLPAtoY78 = { - rLPAtoY78x, 0, 0};

(*14. Reaction force from fluid inside hose between HPA and discharge exit at yoke axis of rotation at
point 79*)
AFHPAtoY79 = PD1*A78*{0, - Sin[θL], Cos[θL]};
ArHPAtoY79 = - ArLPAtoY78;

Export["C:\\Users\\noor\\Documents\\ABH\\Dissertation\\Mahematica models\\Pressure Force on
Pistons\\AFLPAtoY78.csv", Table[{t, AFLPAtoY78[[2]], AFLPAtoY78[[3]]}, {t, 0, 1, 0.0001}]];
```

```
Export["C:\\Users\\noor\\Documents\\ABH\\Dissertation\\Mahematica models\\Pressure Force on
Pistons\\AFHPAtoY79.csv", Table[{t, AFHPAtoY79[[2]], AFHPAtoY79[[3]]}, {t, 0, 1, 0.0001}]];

 (*15. Force due to pressure on discharge or suction orifice at points 80 to 88 as well as its position
vector*)
DFOILtoVP1 = {0, 0, Pb[ϕ][[1]]}*ArFR[ϕ];
DFOILtoVP2 = {0, 0, Pb[ϕ + 2*Pi/9][[1]]*ArFR[ϕ + 2*Pi/9]};
DFOILtoVP3 = {0, 0, Pb[ϕ + 4*Pi/9][[1]]*ArFR[ϕ + 4*Pi/9]};
DFOILtoVP4 = {0, 0, Pb[ϕ + 6*Pi/9][[1]]*ArFR[ϕ + 6*Pi/9]};
DFOILtoVP5 = {0, 0, Pb[ϕ + 8*Pi/9][[1]]*ArFR[ϕ + 8*Pi/9]};
DFOILtoVP6 = {0, 0, Pb[ϕ + 10*Pi/9][[1]]*ArFR[ϕ + 10*Pi/9]};
DFOILtoVP7 = {0, 0, Pb[ϕ + 12*Pi/9][[1]]*ArFR[ϕ + 12*Pi/9]};
DFOILtoVP8 = {0, 0, Pb[ϕ + 14*Pi/9][[1]]*ArFR[ϕ + 14*Pi/9]};
DFOILtoVP9 = {0, 0, Pb[ϕ + 16*Pi/9][[1]]*ArFR[ϕ + 16*Pi/9]};
DFOILtoVP1z = Interpolation[Table[{t, DFOILtoVP1[[3]]}, {t, 0, 1, 0.0001}]];
DFOILtoVP1 = {0, 0, DFOILtoVP1z[t]};

DFOILtoVP2z = Interpolation[Table[{t, DFOILtoVP2[[3]]}, {t, 0, 1, 0.0001}]];
DFOILtoVP2 = {0, 0, DFOILtoVP2z[t]};

DFOILtoVP3z = Interpolation[Table[{t, DFOILtoVP3[[3]]}, {t, 0, 1, 0.0001}]];
DFOILtoVP3 = {0, 0, DFOILtoVP3z[t]};

DFOILtoVP4z = Interpolation[Table[{t, DFOILtoVP4[[3]]}, {t, 0, 1, 0.0001}]];
DFOILtoVP4 = {0, 0, DFOILtoVP4z[t]};

DFOILtoVP5z = Interpolation[Table[{t, DFOILtoVP5[[3]]}, {t, 0, 1, 0.0001}]];
DFOILtoVP5 = {0, 0, DFOILtoVP5z[t]};

DFOILtoVP6z = Interpolation[Table[{t, DFOILtoVP6[[3]]}, {t, 0, 1, 0.0001}]];
DFOILtoVP6 = {0, 0, DFOILtoVP6z[t]};

DFOILtoVP7z = Interpolation[Table[{t, DFOILtoVP7[[3]]}, {t, 0, 1, 0.0001}]];
DFOILtoVP7 = {0, 0, DFOILtoVP7z[t]};

DFOILtoVP8z = Interpolation[Table[{t, DFOILtoVP8[[3]]}, {t, 0, 1, 0.0001}]];
DFOILtoVP8 = {0, 0, DFOILtoVP8z[t]};

DFOILtoVP9z = Interpolation[Table[{t, DFOILtoVP9[[3]]}, {t, 0, 1, 0.0001}]];
DFOILtoVP9 = {0, 0, DFOILtoVP9z[t]};

Export["C:\\Users\\noor\\Documents\\ABH\\Dissertation\\Mahematica models\\Pressure Force on
Pistons\\DFOILtoVP1.csv", Table[{t, DFOILtoVP1[[3]]}, {t, 0, 1, 0.0001}]];
Export["C:\\Users\\noor\\Documents\\ABH\\Dissertation\\Mahematica models\\Pressure Force on
Pistons\\DFOILtoVP2.csv", Table[{t, DFOILtoVP2[[3]]}, {t, 0, 1, 0.0001}]];
Export["C:\\Users\\noor\\Documents\\ABH\\Dissertation\\Mahematica models\\Pressure Force on
Pistons\\DFOILtoVP3.csv", Table[{t, DFOILtoVP3[[3]]}, {t, 0, 1, 0.0001}]];
Export["C:\\Users\\noor\\Documents\\ABH\\Dissertation\\Mahematica models\\Pressure Force on
Pistons\\DFOILtoVP4.csv", Table[{t, DFOILtoVP4[[3]]}, {t, 0, 1, 0.0001}]];
Export["C:\\Users\\noor\\Documents\\ABH\\Dissertation\\Mahematica models\\Pressure Force on
Pistons\\DFOILtoVP5.csv", Table[{t, DFOILtoVP5[[3]]}, {t, 0, 1, 0.0001}]];
Export["C:\\Users\\noor\\Documents\\ABH\\Dissertation\\Mahematica models\\Pressure Force on
Pistons\\DFOILtoVP6.csv", Table[{t, DFOILtoVP6[[3]]}, {t, 0, 1, 0.0001}]];
Export["C:\\Users\\noor\\Documents\\ABH\\Dissertation\\Mahematica models\\Pressure Force on
Pistons\\DFOILtoVP7.csv", Table[{t, DFOILtoVP7[[3]]}, {t, 0, 1, 0.0001}]];
```

```
Export["C:\\Users\\noor\\Documents\\ABH\\Dissertation\\Mahematica models\\Pressure Force on
Pistons\\DFOILtoVP8.csv", Table[{t, DFOILtoVP8[[3]]}, {t, 0, 1, 0.0001}]];
Export["C:\\Users\\noor\\Documents\\ABH\\Dissertation\\Mahematica models\\Pressure Force on
Pistons\\DFOILtoVP9.csv", Table[{t, DFOILtoVP9[[3]]}, {t, 0, 1, 0.0001}]];

 (*Oil Control Volume - Sum of Forces*)
DFOILtoB1 = - DFOILtoP1 + Tos[θ, ϕ].AWOIL1 - DFOILtoVP1 - DLMcv1 - DLMcs1;
DFOILtoB2 : = - DFOILtoP2 + Tos[θ, ϕ + 2*Pi/9].AWOIL2 - DFOILtoVP2 - DLMcv2 - DLMcs2;
DFOILtoB3 : = - DFOILtoP3 + Tos[θ, ϕ + 4*Pi/9].AWOIL3 - DFOILtoVP3 - DLMcv3 - DLMcs3;
DFOILtoB4 : = - DFOILtoP4 + Tos[θ, ϕ + 6*Pi/9].AWOIL4 - DFOILtoVP4 - DLMcv4 - DLMcs4;
DFOILtoB5 : = - DFOILtoP5 + Tos[θ, ϕ + 8*Pi/9].AWOIL5 - DFOILtoVP5 - DLMcv5 - DLMcs5;
DFOILtoB6 : = - DFOILtoP6 + Tos[θ, ϕ + 10*Pi/9].AWOIL6 - DFOILtoVP6 - DLMcv6 - DLMcs6;
DFOILtoB7 : = - DFOILtoP7 + Tos[θ, ϕ + 12*Pi/9].AWOIL7 - DFOILtoVP7 - DLMcv7 - DLMcs7;
DFOILtoB8 : = - DFOILtoP8 + Tos[θ, ϕ + 14*Pi/9].AWOIL8 - DFOILtoVP8 - DLMcv8 - DLMcs8;
DFOILtoB9 : = - DFOILtoP9 + Tos[θ, ϕ + 16*Pi/9].AWOIL9 - DFOILtoVP9 - DLMcv9 - DLMcs9;
DFOILtoB1x = Interpolation[Table[{t, DFOILtoB1[[1]]}, {t, 0, 1, 0.0001}]];
DFOILtoB1y = Interpolation[Table[{t, DFOILtoB1[[2]]}, {t, 0, 1, 0.0001}]];
DFOILtoB1z = Interpolation[Table[{t, DFOILtoB1[[3]]}, {t, 0, 1, 0.0001}]];
DFOILtoB1 = {DFOILtoB1x[t], DFOILtoB1y[t], DFOILtoB1z[t]};

DFOILtoB2x = Interpolation[Table[{t, DFOILtoB2[[1]]}, {t, 0, 1, 0.0001}]];
DFOILtoB2y = Interpolation[Table[{t, DFOILtoB2[[2]]}, {t, 0, 1, 0.0001}]];
DFOILtoB2z = Interpolation[Table[{t, DFOILtoB2[[3]]}, {t, 0, 1, 0.0001}]];
DFOILtoB2 = {DFOILtoB2x[t], DFOILtoB2y[t], DFOILtoB2z[t]};

DFOILtoB3x = Interpolation[Table[{t, DFOILtoB3[[1]]}, {t, 0, 1, 0.0001}]];
DFOILtoB3y = Interpolation[Table[{t, DFOILtoB3[[2]]}, {t, 0, 1, 0.0001}]];
DFOILtoB3z = Interpolation[Table[{t, DFOILtoB3[[3]]}, {t, 0, 1, 0.0001}]];
DFOILtoB3 = {DFOILtoB3x[t], DFOILtoB3y[t], DFOILtoB3z[t]};

DFOILtoB4x = Interpolation[Table[{t, DFOILtoB4[[1]]}, {t, 0, 1, 0.0001}]];
DFOILtoB4y = Interpolation[Table[{t, DFOILtoB4[[2]]}, {t, 0, 1, 0.0001}]];
DFOILtoB4z = Interpolation[Table[{t, DFOILtoB4[[3]]}, {t, 0, 1, 0.0001}]];
DFOILtoB4 = {DFOILtoB4x[t], DFOILtoB4y[t], DFOILtoB4z[t]};

DFOILtoB5x = Interpolation[Table[{t, DFOILtoB5[[1]]}, {t, 0, 1, 0.0001}]];
DFOILtoB5y = Interpolation[Table[{t, DFOILtoB5[[2]]}, {t, 0, 1, 0.0001}]];
DFOILtoB5z = Interpolation[Table[{t, DFOILtoB5[[3]]}, {t, 0, 1, 0.0001}]];
DFOILtoB5 = {DFOILtoB5x[t], DFOILtoB5y[t], DFOILtoB5z[t]};

DFOILtoB6x = Interpolation[Table[{t, DFOILtoB6[[1]]}, {t, 0, 1, 0.0001}]];
DFOILtoB6y = Interpolation[Table[{t, DFOILtoB6[[2]]}, {t, 0, 1, 0.0001}]];
DFOILtoB6z = Interpolation[Table[{t, DFOILtoB6[[3]]}, {t, 0, 1, 0.0001}]];
DFOILtoB6 = {DFOILtoB6x[t], DFOILtoB6y[t], DFOILtoB6z[t]};

DFOILtoB7x = Interpolation[Table[{t, DFOILtoB7[[1]]}, {t, 0, 1, 0.0001}]];
DFOILtoB7y = Interpolation[Table[{t, DFOILtoB7[[2]]}, {t, 0, 1, 0.0001}]];
DFOILtoB7z = Interpolation[Table[{t, DFOILtoB7[[3]]}, {t, 0, 1, 0.0001}]];
DFOILtoB7 = {DFOILtoB7x[t], DFOILtoB7y[t], DFOILtoB7z[t]};

DFOILtoB8x = Interpolation[Table[{t, DFOILtoB8[[1]]}, {t, 0, 1, 0.0001}]];
DFOILtoB8y = Interpolation[Table[{t, DFOILtoB8[[2]]}, {t, 0, 1, 0.0001}]];
DFOILtoB8z = Interpolation[Table[{t, DFOILtoB8[[3]]}, {t, 0, 1, 0.0001}]];
DFOILtoB8 = {DFOILtoB8x[t], DFOILtoB8y[t], DFOILtoB8z[t]};

DFOILtoB9x = Interpolation[Table[{t, DFOILtoB9[[1]]}, {t, 0, 1, 0.0001}]];
```

```
DFOILtoB9y = Interpolation[Table[{t, DFOILtoB9[[2]]}, {t, 0, 1, 0.0001}]];
DFOILtoB9z = Interpolation[Table[{t, DFOILtoB9[[3]]}, {t, 0, 1, 0.0001}]];
DFOILtoB9 = {DFOILtoB9x[t], DFOILtoB9y[t], DFOILtoB9z[t]};

Export["C:\\Users\\noor\\Documents\\ABH\\Dissertation\\Mahematica models\\Pressure Force on
Pistons\\DFOILtoB1.csv", Table[{t, DFOILtoB1[[1]], DFOILtoB1[[2]], DFOILtoB1[[3]]}, {t, 0, 1,
0.0001}]];
Export["C:\\Users\\noor\\Documents\\ABH\\Dissertation\\Mahematica models\\Pressure Force on
Pistons\\DFOILtoB2.csv", Table[{t, DFOILtoB2[[1]], DFOILtoB2[[2]], DFOILtoB2[[3]]}, {t, 0, 1,
0.0001}]];
Export["C:\\Users\\noor\\Documents\\ABH\\Dissertation\\Mahematica models\\Pressure Force on
Pistons\\DFOILtoB3.csv", Table[{t, DFOILtoB3[[1]], DFOILtoB3[[2]], DFOILtoB3[[3]]}, {t, 0, 1,
0.0001}]];
Export["C:\\Users\\noor\\Documents\\ABH\\Dissertation\\Mahematica models\\Pressure Force on
Pistons\\DFOILtoB4.csv", Table[{t, DFOILtoB4[[1]], DFOILtoB4[[2]], DFOILtoB4[[3]]}, {t, 0, 1,
0.0001}]];
Export["C:\\Users\\noor\\Documents\\ABH\\Dissertation\\Mahematica models\\Pressure Force on
Pistons\\DFOILtoB5.csv", Table[{t, DFOILtoB5[[1]], DFOILtoB5[[2]], DFOILtoB5[[3]]}, {t, 0, 1,
0.0001}]];
Export["C:\\Users\\noor\\Documents\\ABH\\Dissertation\\Mahematica models\\Pressure Force on
Pistons\\DFOILtoB6.csv", Table[{t, DFOILtoB6[[1]], DFOILtoB6[[2]], DFOILtoB6[[3]]}, {t, 0, 1,
0.0001}]];
Export["C:\\Users\\noor\\Documents\\ABH\\Dissertation\\Mahematica models\\Pressure Force on
Pistons\\DFOILtoB7.csv", Table[{t, DFOILtoB7[[1]], DFOILtoB7[[2]], DFOILtoB7[[3]]}, {t, 0, 1,
0.0001}]];
Export["C:\\Users\\noor\\Documents\\ABH\\Dissertation\\Mahematica models\\Pressure Force on
Pistons\\DFOILtoB8.csv", Table[{t, DFOILtoB8[[1]], DFOILtoB8[[2]], DFOILtoB8[[3]]}, {t, 0, 1,
0.0001}]];
Export["C:\\Users\\noor\\Documents\\ABH\\Dissertation\\Mahematica models\\Pressure Force on
Pistons\\DFOILtoB9.csv", Table[{t, DFOILtoB9[[1]], DFOILtoB9[[2]], DFOILtoB9[[3]]}, {t, 0, 1,
0.0001}]];
```

(*Displacement Mechanism (Actuating Link)_Forces*)

(*1. Reaction force from the pin of ram at point 90 with its respective position vector as measured from yoke axis of rotation*)

```
AFRAMtoAC90 = {0, FRAMtoAC90z*Sin[ϵ - γ8] + FRAMtoAC90y*Cos[ϵ - γ8], FRAMtoAC90z*Cos[ϵ -
γ8] - FRAMtoAC90y*Sin[ϵ - γ8]};

ArRAMtoAC90 = {0, - L3*Sin[γ5 + θ] - Lac*Sin[ϵ - γ8], L3*Cos[γ5 + θ] - Lac*Cos[ϵ - γ8]};
```

(*2. Reaction force from yoke at point 66 denoted as - AFACtoY66*)

```
(*Position vector of AFACtoY66 as measured from yoke axis of rotation*)
ArACtoY66 = {rACtoY66x, - L3*Sin[γ5 + θ], L3*Cos[γ5 + θ]};
```

(*3. Weight of actuating link and corresponding position vector*)

```
AWAC = {0, MAC*g, 0};
ArWAC = {0, - L3*Sin[θ + γ5] - (Lac - DG)*Sin[ϵ - γ8], L3*Cos[θ + γ5] - (Lac - DG)*Cos[ϵ - γ8]};
```

(*The ram - Forces*)

(*1. Reaction force from the pin between ram and actuating link at point 90 denoted as - AFRAMtoAC90*)

(*2. Reaction force from the ram cylinder interface at point 90*)

```
AFCtoRAM90 = {0, μCtoRAM90*NCtoRAM90*Sin[ϵ] - NCtoRAM90*Cos[ϵ],
μCtoRAM90*NCtoRAM90*Cos[ϵ] + NCtoRAM90*Sin[ϵ]};
```

(*3. Weight of ram*)
AWRAM = {0, MRAM*g, 0};

(*4. Cylinder pressure force on ram*)
AFPtoRAM = PRAM*ARAM*{0, Sin[ϵ], Cos[ϵ]};

(*The Piston - Sum of forces*)

ForceP1 = - AFPtoCR1 + Tos[θ, ϕ]^T.(DFOILtoP1 + DFBtoP1) + AWp - Mp*(Tos[θ, ϕ]^T.Dap[θ, ϕ, 1]);

ForceP2 = - AFPtoCR2 + Tos[θ, ϕ + 2*Pi/9]^T.(DFOILtoP2 + DFBtoP2) + AWp - Mp*(Tos[θ, ϕ + 2*Pi/9]^T.Dap[θ, ϕ, 2]);

ForceP3 = - AFPtoCR3 + Tos[θ, ϕ + 4*Pi/9]^T.(DFOILtoP3 + DFBtoP3) + AWp - Mp*(Tos[θ, ϕ + 4*Pi/9]^T.Dap[θ, ϕ, 3]);

ForceP4 = - AFPtoCR4 + Tos[θ, ϕ + 6*Pi/9]^T.(DFOILtoP4 + DFBtoP4) + AWp - Mp*(Tos[θ, ϕ + 6*Pi/9]^T.Dap[θ, ϕ, 4]);

ForceP5 = - AFPtoCR5 + Tos[θ, ϕ + 8*Pi/9]^T.(DFOILtoP5 + DFBtoP5) + AWp - Mp*(Tos[θ, ϕ + 8*Pi/9]^T.Dap[θ, ϕ, 5]);

ForceP6 = - AFPtoCR6 + Tos[θ, ϕ + 10*Pi/9]^T.(DFOILtoP6 + DFBtoP6) + AWp - Mp*(Tos[θ, ϕ + 10*Pi/9]^T.Dap[θ, ϕ, 6]);

ForceP7 = - AFPtoCR7 + Tos[θ, ϕ + 12*Pi/9]^T.(DFOILtoP7 + DFBtoP7) + AWp - Mp*(Tos[θ, ϕ + 12*Pi/9]^T.Dap[θ, ϕ, 7]);

ForceP8 = - AFPtoCR8 + Tos[θ, ϕ + 14*Pi/9]^T.(DFOILtoP8 + DFBtoP8) + AWp - Mp*(Tos[θ, ϕ + 14*Pi/9]^T.Dap[θ, ϕ, 8]);

ForceP9 = - AFPtoCR9 + Tos[θ, ϕ + 16*Pi/9]^T.(DFOILtoP9 + DFBtoP9) + AWp - Mp*(Tos[θ, ϕ + 16*Pi/9]^T.Dap[θ, ϕ, 9]);

FxP1 = ForceP1[[1]];
FxP2 = ForceP2[[1]];
FxP3 = ForceP3[[1]];
FxP4 = ForceP4[[1]];
FxP5 = ForceP5[[1]];
FxP6 = ForceP6[[1]];
FxP7 = ForceP7[[1]];
FxP8 = ForceP8[[1]];
FxP9 = ForceP9[[1]];

FyP1 = ForceP1[[2]];
FyP2 = ForceP2[[2]];

```
FyP3 = ForceP3[[2]];
FyP4 = ForceP4[[2]];
FyP5 = ForceP5[[2]];
FyP6 = ForceP6[[2]];
FyP7 = ForceP7[[2]];
FyP8 = ForceP8[[2]];
FyP9 = ForceP9[[2]];

FzP1 = ForceP1[[3]];
FzP2 = ForceP2[[3]];
FzP3 = ForceP3[[3]];
FzP4 = ForceP4[[3]];
FzP5 = ForceP5[[3]];
FzP6 = ForceP6[[3]];
FzP7 = ForceP7[[3]];
FzP8 = ForceP8[[3]];
FzP9 = ForceP9[[3]];
```

(*The Piston - Sum of moments*)

```
(*Moments about the common point between ConRod and piston (points 14 to 22)*)
AMPtoCR1 = {0, 0, 0};
AMPtoCR2 = {0, 0, 0};
AMPtoCR3 = {0, 0, 0};
AMPtoCR4 = {0, 0, 0};
AMPtoCR5 = {0, 0, 0};
AMPtoCR6 = {0, 0, 0};
AMPtoCR7 = {0, 0, 0};
AMPtoCR8 = {0, 0, 0};
AMPtoCR9 = {0, 0, 0};

MomentP1 : = DrBtoP×DFBtoP1 + DrWP×(Tos[θ, ϕ].AWp) - DIp.Dαp - DrWP×(Mp*Dap[θ, ϕ, 1]) - Tos[θ,
ϕ].AMPtoCR1;
MomentP2 : = DrBtoP×DFBtoP2 + DrWP×(Tos[θ, ϕ + 2*Pi/9].AWp) - DIp.Dαp - DrWP×(Mp*Dap[θ, ϕ,
2]) - Tos[θ, ϕ + 2*Pi/9].AMPtoCR2;
MomentP3 : = DrBtoP×DFBtoP3 + DrWP×(Tos[θ, ϕ + 4*Pi/9].AWp) - DIp.Dαp - DrWP×(Mp*Dap[θ, ϕ,
3]) - Tos[θ, ϕ + 4*Pi/9].AMPtoCR3;
MomentP4 : = DrBtoP×DFBtoP4 + DrWP×(Tos[θ, ϕ + 6*Pi/9].AWp) - DIp.Dαp - DrWP×(Mp*Dap[θ, ϕ,
4]) - Tos[θ, ϕ + 6*Pi/9].AMPtoCR4;
MomentP5 : = DrBtoP×DFBtoP5 + DrWP×(Tos[θ, ϕ + 8*Pi/9].AWp) - DIp.Dαp - DrWP×(Mp*Dap[θ, ϕ,
5]) - Tos[θ, ϕ + 8*Pi/9].AMPtoCR5;
MomentP6 : = DrBtoP×DFBtoP6 + DrWP×(Tos[θ, ϕ + 10*Pi/9].AWp) - DIp.Dαp - DrWP×(Mp*Dap[θ, ϕ,
6]) - Tos[θ, ϕ + 10*Pi/9].AMPtoCR6;
MomentP7 : = DrBtoP×DFBtoP7 + DrWP×(Tos[θ, ϕ + 12*Pi/9].AWp) - DIp.Dαp - DrWP×(Mp*Dap[θ, ϕ,
7]) - Tos[θ, ϕ + 12*Pi/9].AMPtoCR7;
MomentP8 : = DrBtoP×DFBtoP8 + DrWP×(Tos[θ, ϕ + 14*Pi/9].AWp) - DIp.Dαp - DrWP×(Mp*Dap[θ, ϕ,
8]) - Tos[θ, ϕ + 14*Pi/9].AMPtoCR8;
MomentP9 : = DrBtoP×DFBtoP9 + DrWP×(Tos[θ, ϕ + 16*Pi/9].AWp) - DIp.Dαp - DrWP×(Mp*Dap[θ, ϕ,
9]) - Tos[θ, ϕ + 16*Pi/9].AMPtoCR9;

MxP1 = MomentP1[[1]];
MxP2 = MomentP2[[1]];
MxP3 = MomentP3[[1]];
MxP4 = MomentP4[[1]];
MxP5 = MomentP5[[1]];
MxP6 = MomentP6[[1]];
MxP7 = MomentP7[[1]];
```

```
MxP8 = MomentP8[[1]];
MxP9 = MomentP9[[1]];

MyP1 = MomentP1[[2]];
MyP2 = MomentP2[[2]];
MyP3 = MomentP3[[2]];
MyP4 = MomentP4[[2]];
MyP5 = MomentP5[[2]];
MyP6 = MomentP6[[2]];
MyP7 = MomentP7[[2]];
MyP8 = MomentP8[[2]];
MyP9 = MomentP9[[2]];

solP1 = NSolve[{FxP1 = = 0, FyP1 = = 0, FzP1 = = 0, MxP1 = = 0, MyP1 = = 0}, {AFPtoCR1x, FBtoP1x,
FBtoP1y, AFPtoCR1y, AFPtoCR1z }];
solP2 = NSolve[{FxP2==0, FyP2==0, FzP2==0, MxP2==0, MyP2==0}, {AFPtoCR2x, FBtoP2x, FBtoP2y,
AFPtoCR2y, AFPtoCR2z }];
solP3 = NSolve[{FxP3==0, FyP3==0, FzP3==0, MxP3==0, MyP3==0}, {AFPtoCR3x, FBtoP3x, FBtoP3y,
AFPtoCR3y, AFPtoCR3z }];
solP4 = NSolve[{FxP4==0, FyP4==0, FzP4==0, MxP4==0, MyP4==0}, {AFPtoCR4x, FBtoP4x, FBtoP4y,
AFPtoCR4y, AFPtoCR4z }];
solP5 = NSolve[{FxP5==0, FyP5==0, FzP5==0, MxP5==0, MyP5==0}, {AFPtoCR5x, FBtoP5x, FBtoP5y,
AFPtoCR5y, AFPtoCR5z }];
solP6 = NSolve[{FxP6==0, FyP6==0, FzP6==0, MxP6==0, MyP6==0}, {AFPtoCR6x, FBtoP6x, FBtoP6y,
AFPtoCR6y, AFPtoCR6z }];
solP7 = NSolve[{FxP7==0, FyP7==0, FzP7==0, MxP7==0, MyP7==0}, {AFPtoCR7x, FBtoP7x, FBtoP7y,
AFPtoCR7y, AFPtoCR7z }];
solP8 = NSolve[{FxP8==0, FyP8==0, FzP8==0, MxP8==0, MyP8==0}, {AFPtoCR8x, FBtoP8x, FBtoP8y,
AFPtoCR8y, AFPtoCR8z }];
solP9 = NSolve[{FxP9==0, FyP9==0, FzP9==0, MxP9==0, MyP9==0}, {AFPtoCR9x, FBtoP9x, FBtoP9y,
AFPtoCR9y, AFPtoCR9z }];

FBtoP1x = Evaluate[FBtoP1x]/.solP1[[1]];
FBtoP1y = Evaluate[FBtoP1y]/.solP1[[1]];
AFPtoCR1x = Chop[Evaluate[AFPtoCR1x]/.solP1[[1]]];
AFPtoCR1y = Evaluate[AFPtoCR1y]/.solP1[[1]];
AFPtoCR1z = Evaluate[AFPtoCR1z]/.solP1[[1]];

FBtoP2x = Evaluate[FBtoP2x]/.solP2[[1]];
FBtoP2y = Evaluate[FBtoP2y]/.solP2[[1]];
AFPtoCR2x = Chop[Evaluate[AFPtoCR2x]/.solP2[[1]]];
AFPtoCR2y = Evaluate[AFPtoCR2y]/.solP2[[1]];
AFPtoCR2z = Evaluate[AFPtoCR2z]/.solP2[[1]];

FBtoP3x = Evaluate[FBtoP3x]/.solP3[[1]];
FBtoP3y = Evaluate[FBtoP3y]/.solP3[[1]];
AFPtoCR3x = Chop[Evaluate[AFPtoCR3x]/.solP3[[1]]];
AFPtoCR3y = Evaluate[AFPtoCR3y]/.solP3[[1]];
AFPtoCR3z = Evaluate[AFPtoCR3z]/.solP3[[1]];

FBtoP4x = Evaluate[FBtoP4x]/.solP4[[1]];
FBtoP4y = Evaluate[FBtoP4y]/.solP4[[1]];
AFPtoCR4x = Chop[Evaluate[AFPtoCR4x]/.solP4[[1]]];
AFPtoCR4y = Evaluate[AFPtoCR4y]/.solP4[[1]];
AFPtoCR4z = Evaluate[AFPtoCR4z]/.solP4[[1]];
```

```
FBtoP5x = Evaluate[FBtoP5x]/.solP5[[1]];
FBtoP5y = Evaluate[FBtoP5y]/.solP5[[1]];
AFPtoCR5x = Chop[Evaluate[AFPtoCR5x]/.solP5[[1]]];
AFPtoCR5y = Evaluate[AFPtoCR5y]/.solP5[[1]];
AFPtoCR5z = Evaluate[AFPtoCR5z]/.solP5[[1]];

FBtoP6x = Evaluate[FBtoP6x]/.solP6[[1]];
FBtoP6y = Evaluate[FBtoP6y]/.solP6[[1]];
AFPtoCR6x = Chop[Evaluate[AFPtoCR6x]/.solP6[[1]]];
AFPtoCR6y = Evaluate[AFPtoCR6y]/.solP6[[1]];
AFPtoCR6z = Evaluate[AFPtoCR6z]/.solP6[[1]];

FBtoP7x = Evaluate[FBtoP7x]/.solP7[[1]];
FBtoP7y = Evaluate[FBtoP7y]/.solP7[[1]];
AFPtoCR7x = Chop[Evaluate[AFPtoCR7x]/.solP7[[1]]];
AFPtoCR7y = Evaluate[AFPtoCR7y]/.solP7[[1]];
AFPtoCR7z = Evaluate[AFPtoCR7z]/.solP7[[1]];

FBtoP8x = Evaluate[FBtoP8x]/.solP8[[1]];
FBtoP8y = Evaluate[FBtoP8y]/.solP8[[1]];
AFPtoCR8x = Chop[Evaluate[AFPtoCR8x]/.solP8[[1]]];
AFPtoCR8y = Evaluate[AFPtoCR8y]/.solP8[[1]];
AFPtoCR8z = Evaluate[AFPtoCR8z]/.solP8[[1]];

FBtoP9x = Evaluate[FBtoP9x]/.solP9[[1]];
FBtoP9y = Evaluate[FBtoP9y]/.solP9[[1]];
AFPtoCR9x = Chop[Evaluate[AFPtoCR9x]/.solP9[[1]]];
AFPtoCR9y = Evaluate[AFPtoCR9y]/.solP9[[1]];
AFPtoCR9z = Evaluate[AFPtoCR9z]/.solP9[[1]];
AFBtoP1 = Tos[θ, ϕ]^T.DFBtoP1;

AFBtoP2 = Tos[θ, ϕ]^T.DFBtoP2;

AFBtoP3 = Tos[θ, ϕ]^T.DFBtoP3;

AFBtoP4 = Tos[θ, ϕ]^T.DFBtoP4;

AFBtoP5 = Tos[θ, ϕ]^T.DFBtoP5;

AFBtoP6 = Tos[θ, ϕ]^T.DFBtoP6;

AFBtoP7 = Tos[θ, ϕ]^T.DFBtoP7;

AFBtoP8 = Tos[θ, ϕ]^T.DFBtoP8;

AFBtoP9 = Tos[θ, ϕ]^T.DFBtoP9;


Export["C:\\Users\\noor\\Documents\\ABH\\Dissertation\\Mahematica models\\Pressure Force on
Pistons\\DFBtoP1.csv", Table[{t, DFBtoP1[[1]], DFBtoP1[[2]], DFBtoP1[[3]]}, {t, 0, 1, 0.0001}]];
Export["C:\\Users\\noor\\Documents\\ABH\\Dissertation\\Mahematica models\\Pressure Force on
Pistons\\DFBtoP2.csv", Table[{t, DFBtoP2[[1]], DFBtoP2[[2]], DFBtoP2[[3]]}, {t, 0, 1, 0.0001}]];
Export["C:\\Users\\noor\\Documents\\ABH\\Dissertation\\Mahematica models\\Pressure Force on
Pistons\\DFBtoP3.csv", Table[{t, DFBtoP3[[1]], DFBtoP3[[2]], DFBtoP3[[3]]}, {t, 0, 1, 0.0001}]];
Export["C:\\Users\\noor\\Documents\\ABH\\Dissertation\\Mahematica models\\Pressure Force on
Pistons\\DFBtoP4.csv", Table[{t, DFBtoP4[[1]], DFBtoP4[[2]], DFBtoP4[[3]]}, {t, 0, 1, 0.0001}]];
```

```
Export["C:\\Users\\noor\\Documents\\ABH\\Dissertation\\Mahematica models\\Pressure Force on
Pistons\\DFBtoP5.csv", Table[{t, DFBtoP5[[1]], DFBtoP5[[2]], DFBtoP5[[3]]}, {t, 0, 1, 0.0001}]];
Export["C:\\Users\\noor\\Documents\\ABH\\Dissertation\\Mahematica models\\Pressure Force on
Pistons\\DFBtoP6.csv", Table[{t, DFBtoP6[[1]], DFBtoP6[[2]], DFBtoP6[[3]]}, {t, 0, 1, 0.0001}]];
Export["C:\\Users\\noor\\Documents\\ABH\\Dissertation\\Mahematica models\\Pressure Force on
Pistons\\DFBtoP7.csv", Table[{t, DFBtoP7[[1]], DFBtoP7[[2]], DFBtoP7[[3]]}, {t, 0, 1, 0.0001}]];
Export["C:\\Users\\noor\\Documents\\ABH\\Dissertation\\Mahematica models\\Pressure Force on
Pistons\\DFBtoP8.csv", Table[{t, DFBtoP8[[1]], DFBtoP8[[2]], DFBtoP8[[3]]}, {t, 0, 1, 0.0001}]];
Export["C:\\Users\\noor\\Documents\\ABH\\Dissertation\\Mahematica models\\Pressure Force on
Pistons\\DFBtoP9.csv", Table[{t, DFBtoP9[[1]], DFBtoP9[[2]], DFBtoP9[[3]]}, {t, 0, 1, 0.0001}]];
```

(*Connecting Rod - Sum of forces*)

```
ForceCR1 : = AWCR + AFMStoCR1 + AFPtoCR1 - MCR*AaCR[t, 1];
ForceCR2 : = AWCR + AFMStoCR2 + AFPtoCR2 - MCR*AaCR[t, 2];
ForceCR3 : = AWCR + AFMStoCR3 + AFPtoCR3 - MCR*AaCR[t, 3];
ForceCR4 : = AWCR + AFMStoCR4 + AFPtoCR4 - MCR*AaCR[t, 4];
ForceCR5 : = AWCR + AFMStoCR5 + AFPtoCR5 - MCR*AaCR[t, 5];
ForceCR6 : = AWCR + AFMStoCR6 + AFPtoCR6 - MCR*AaCR[t, 6];
ForceCR7 : = AWCR + AFMStoCR7 + AFPtoCR7 - MCR*AaCR[t, 7];
ForceCR8 : = AWCR + AFMStoCR8 + AFPtoCR8 - MCR*AaCR[t, 8];
ForceCR9 : = AWCR + AFMStoCR9 + AFPtoCR9 - MCR*AaCR[t, 9];

FxCR1 = ForceCR1[[1]];
FxCR2 = ForceCR2[[1]];
FxCR3 = ForceCR3[[1]];
FxCR4 = ForceCR4[[1]];
FxCR5 = ForceCR5[[1]];
FxCR6 = ForceCR6[[1]];
FxCR7 = ForceCR7[[1]];
FxCR8 = ForceCR8[[1]];
FxCR9 = ForceCR9[[1]];

FyCR1 = ForceCR1[[2]];
FyCR2 = ForceCR2[[2]];
FyCR3 = ForceCR3[[2]];
FyCR4 = ForceCR4[[2]];
FyCR5 = ForceCR5[[2]];
FyCR6 = ForceCR6[[2]];
FyCR7 = ForceCR7[[2]];
FyCR8 = ForceCR8[[2]];
FyCR9 = ForceCR9[[2]];

FzCR1 = ForceCR1[[3]];
FzCR2 = ForceCR2[[3]];
FzCR3 = ForceCR3[[3]];
FzCR4 = ForceCR4[[3]];
FzCR5 = ForceCR5[[3]];
FzCR6 = ForceCR6[[3]];
FzCR7 = ForceCR7[[3]];
FzCR8 = ForceCR8[[3]];
FzCR9 = ForceCR9[[3]];

solCR1 = NSolve[{FxCR1==0, FyCR1==0, FzCR1==0}, {AFMStoCR1x, AFMStoCR1y, AFMStoCR1z }];

solCR2 = NSolve[{FxCR2==0, FyCR2==0, FzCR2==0}, {AFMStoCR2x, AFMStoCR2y, AFMStoCR2z }];
```

```
solCR3 = NSolve[{FxCR3==0, FyCR3==0, FzCR3==0}, {AFMStoCR3x, AFMStoCR3y, AFMStoCR3z }];

solCR4 = NSolve[{FxCR4==0, FyCR4==0, FzCR4==0}, {AFMStoCR4x, AFMStoCR4y, AFMStoCR4z }];

solCR5 = NSolve[{FxCR5==0, FyCR5==0, FzCR5==0}, {AFMStoCR5x, AFMStoCR5y, AFMStoCR5z }];

solCR6 = NSolve[{FxCR6==0, FyCR6==0, FzCR6==0}, {AFMStoCR6x, AFMStoCR6y, AFMStoCR6z }];

solCR7 = NSolve[{FxCR7==0, FyCR7==0, FzCR7==0}, {AFMStoCR7x, AFMStoCR7y, AFMStoCR7z }];

solCR8 = NSolve[{FxCR8==0, FyCR8==0, FzCR8==0}, {AFMStoCR8x, AFMStoCR8y, AFMStoCR8z }];

solCR9 = NSolve[{FxCR9==0, FyCR9==0, FzCR9==0}, {AFMStoCR9x, AFMStoCR9y, AFMStoCR9z }];

AFMStoCR1x = Evaluate[AFMStoCR1x]/.solCR1[[1]];
AFMStoCR1y = Evaluate[AFMStoCR1y]/.solCR1[[1]];
AFMStoCR1z = Evaluate[AFMStoCR1z]/.solCR1[[1]];

AFMStoCR2x = Evaluate[AFMStoCR2x]/.solCR2[[1]];
AFMStoCR2y = Evaluate[AFMStoCR2y]/.solCR2[[1]];
AFMStoCR2z = Evaluate[AFMStoCR2z]/.solCR2[[1]];

AFMStoCR3x = Evaluate[AFMStoCR3x]/.solCR3[[1]];
AFMStoCR3y = Evaluate[AFMStoCR3y]/.solCR3[[1]];
AFMStoCR3z = Evaluate[AFMStoCR3z]/.solCR3[[1]];

AFMStoCR4x = Evaluate[AFMStoCR4x]/.solCR4[[1]];
AFMStoCR4y = Evaluate[AFMStoCR4y]/.solCR4[[1]];
AFMStoCR4z = Evaluate[AFMStoCR4z]/.solCR4[[1]];

AFMStoCR5x = Evaluate[AFMStoCR5x]/.solCR5[[1]];
AFMStoCR5y = Evaluate[AFMStoCR5y]/.solCR5[[1]];
AFMStoCR5z = Evaluate[AFMStoCR5z]/.solCR5[[1]];

AFMStoCR6x = Evaluate[AFMStoCR6x]/.solCR6[[1]];
AFMStoCR6y = Evaluate[AFMStoCR6y]/.solCR6[[1]];
AFMStoCR6z = Evaluate[AFMStoCR6z]/.solCR6[[1]];

AFMStoCR7x = Evaluate[AFMStoCR7x]/.solCR7[[1]];
AFMStoCR7y = Evaluate[AFMStoCR7y]/.solCR7[[1]];
AFMStoCR7z = Evaluate[AFMStoCR7z]/.solCR7[[1]];

AFMStoCR8x = Evaluate[AFMStoCR8x]/.solCR8[[1]];
AFMStoCR8y = Evaluate[AFMStoCR8y]/.solCR8[[1]];
AFMStoCR8z = Evaluate[AFMStoCR8z]/.solCR8[[1]];

AFMStoCR9x = Evaluate[AFMStoCR9x]/.solCR9[[1]];
AFMStoCR9y = Evaluate[AFMStoCR9y]/.solCR9[[1]];
AFMStoCR9z = Evaluate[AFMStoCR9z]/.solCR9[[1]];

AFMStoCR1x = Interpolation[Table[{t, AFMStoCR1x}, {t, 0, 1, 0.0001}]];
AFMStoCR1y = Interpolation[Table[{t, AFMStoCR1y}, {t, 0, 1, 0.0001}]];
AFMStoCR1z = Interpolation[Table[{t, AFMStoCR1z}, {t, 0, 1, 0.0001}]];

AFMStoCR2x = Interpolation[Table[{t, AFMStoCR2x}, {t, 0, 1, 0.0001}]];
AFMStoCR2y = Interpolation[Table[{t, AFMStoCR2y}, {t, 0, 1, 0.0001}]];
```

```
AFMStoCR2z = Interpolation[Table[{t, AFMStoCR2z}, {t, 0, 1, 0.0001}]];

AFMStoCR3x = Interpolation[Table[{t, AFMStoCR3x}, {t, 0, 1, 0.0001}]];
AFMStoCR3y = Interpolation[Table[{t, AFMStoCR3y}, {t, 0, 1, 0.0001}]];
AFMStoCR3z = Interpolation[Table[{t, AFMStoCR3z}, {t, 0, 1, 0.0001}]];

AFMStoCR4x = Interpolation[Table[{t, AFMStoCR4x}, {t, 0, 1, 0.0001}]];
AFMStoCR4y = Interpolation[Table[{t, AFMStoCR4y}, {t, 0, 1, 0.0001}]];
AFMStoCR4z = Interpolation[Table[{t, AFMStoCR4z}, {t, 0, 1, 0.0001}]];

AFMStoCR5x = Interpolation[Table[{t, AFMStoCR5x}, {t, 0, 1, 0.0001}]];
AFMStoCR5y = Interpolation[Table[{t, AFMStoCR5y}, {t, 0, 1, 0.0001}]];
AFMStoCR5z = Interpolation[Table[{t, AFMStoCR5z}, {t, 0, 1, 0.0001}]];

AFMStoCR6x = Interpolation[Table[{t, AFMStoCR6x}, {t, 0, 1, 0.0001}]];
AFMStoCR6y = Interpolation[Table[{t, AFMStoCR6y}, {t, 0, 1, 0.0001}]];
AFMStoCR6z = Interpolation[Table[{t, AFMStoCR6z}, {t, 0, 1, 0.0001}]];

AFMStoCR7x = Interpolation[Table[{t, AFMStoCR7x}, {t, 0, 1, 0.0001}]];
AFMStoCR7y = Interpolation[Table[{t, AFMStoCR7y}, {t, 0, 1, 0.0001}]];
AFMStoCR7z = Interpolation[Table[{t, AFMStoCR7z}, {t, 0, 1, 0.0001}]];

AFMStoCR8x = Interpolation[Table[{t, AFMStoCR8x}, {t, 0, 1, 0.0001}]];
AFMStoCR8y = Interpolation[Table[{t, AFMStoCR8y}, {t, 0, 1, 0.0001}]];
AFMStoCR8z = Interpolation[Table[{t, AFMStoCR8z}, {t, 0, 1, 0.0001}]];

AFMStoCR9x = Interpolation[Table[{t, AFMStoCR9x}, {t, 0, 1, 0.0001}]];
AFMStoCR9y = Interpolation[Table[{t, AFMStoCR9y}, {t, 0, 1, 0.0001}]];
AFMStoCR9z = Interpolation[Table[{t, AFMStoCR9z}, {t, 0, 1, 0.0001}]];

AFMStoCR1 = {AFMStoCR1x[t], AFMStoCR1y[t], AFMStoCR1z[t]};
AFMStoCR2 = {AFMStoCR2x[t], AFMStoCR2y[t], AFMStoCR2z[t]};
AFMStoCR3 = {AFMStoCR3x[t], AFMStoCR3y[t], AFMStoCR3z[t]};
AFMStoCR4 = {AFMStoCR4x[t], AFMStoCR4y[t], AFMStoCR4z[t]};
AFMStoCR5 = {AFMStoCR5x[t], AFMStoCR5y[t], AFMStoCR5z[t]};
AFMStoCR6 = {AFMStoCR6x[t], AFMStoCR6y[t], AFMStoCR6z[t]};
AFMStoCR7 = {AFMStoCR7x[t], AFMStoCR7y[t], AFMStoCR7z[t]};
AFMStoCR8 = {AFMStoCR8x[t], AFMStoCR8y[t], AFMStoCR8z[t]};
AFMStoCR9 = {AFMStoCR9x[t], AFMStoCR9y[t], AFMStoCR9z[t]};

s4 = OpenWrite["FConRod.nb"]
Write[s4, AFMStoCR1[[1]]]
Write[s4, AFMStoCR1[[2]]]
Write[s4, AFMStoCR1[[3]]]
Write[s4, Norm[AFMStoCR1]]
Write[s4, AFPtoCR1[[1]]]
Write[s4, AFPtoCR1[[2]]]
Write[s4, AFPtoCR1[[3]]]},
Write[s4, Norm[AFPtoCR1]]}
Close[s4]
```

(*Connecting Rod - moments*)

```
AMMStoCR1 = {0, 0, 0};
AMMStoCR2 = {0, 0, 0};
AMMStoCR3 = {0, 0, 0};
AMMStoCR4 = {0, 0, 0};
```

AMMStoCR5 = {0, 0, 0};
AMMStoCR6 = {0, 0, 0};
AMMStoCR7 = {0, 0, 0};
AMMStoCR8 = {0, 0, 0};
AMMStoCR9 = {0, 0, 0};

(*Second Intermediate Shaft - Sum of forces*)

AWim2 = {0, 0, 0};

(*MatrixForm[ForceIM2 : = - Tim1^{T}.CFIM2toIM125 + Tc2^{T}.(- IFIM2toC227 - IFIM2toC228) + AWim2 -

Tim1^{T}.(Mim2*Caim2)]; *)

CFIM2toIM125 = Tim1.AWim2 - Mim2*Caim2;
FIM2toIM125z = CFIM2toIM125[[3]]

(*Second Intermediate Shaft - Sum of moments*)

IMIM2toC227 = {0, 0, 0};
IMIM2toC228 = {0, 0, 0};
(*Sum of the moments of forces acting on 2nd intermediate shaft about center of 2nd cross*)

MomentIM2 = Chop[- CMIM2toIM125 - 2Cr27×(Tim1.(Tc2^{T}.IFIM2toC227)) + Crim2×(Tim1.AWim2) -

CIim2.Cαim1 - Crim2×(Mim2*Caim2)];

(*Second Cross - sum of moments about center of 2nd cross*)

IMOStoC229 = {0, 0, 0};
IMOStoC230 = {0, 0, 0};

MomentC2 = Ir27×IFIM2toC227 + IMIM2toC227 + Ir28×IFIM2toC228 + IMIM2toC228 +
Ir29×IFOStoC229 + IMOStoC229 + Ir30×IFOStoC230 + IMOStoC230 - IIc2.Iαc2;

FIM2toC227z = (- 0.5IMIM2toC227 - 0.5IMIM2toC228 - Ir29×IFOStoC229 - 0.5IMOStoC229 -
0.5IMOStoC230 + 0.5IIc2.Iαc2)[[2]]/Ir27[[1]];

FOStoC229z = (- Ir27×IFIM2toC227 - 0.5IMIM2toC227 - 0.5IMIM2toC228 - 0.5IMOStoC229 -
0.5IMOStoC230 + 0.5IIc2.Iαc2)[[1]]/Ir29[[2]];

(*Barrel - Output Shaft Assembly - sum of forces*)

ForceOS = Tos[θ, ϕ].(Tc2^{T}.(- IFOStoC229 - IFOStoC230)) + DFOILtoB1 + DFOILtoB2 + DFOILtoB3 +

DFOILtoB4 + DFOILtoB5 + DFOILtoB6 + DFOILtoB7 + DFOILtoB8 + DFOILtoB9 - DFBtoP1 -
DFBtoP2 - DFBtoP3 - DFBtoP4 - DFBtoP5 - DFBtoP6 - DFBtoP7 - DFBtoP8 - DFBtoP9 - DFBStoVP1 -
DFBStoVP2 - DFBStoVP3 - DFBStoVP4 - DFBStoVP5 - DFBStoVP6 - DFBStoVP7 - DFBStoVP8 -

DFBStoVP9 + Tos[θ,ϕ].Tvp^{T}.(HFVPtoBoutD + HFVPtoBinD + HFVPtoBinS + HFVPtoBoutS) +

DFB3FtoB + DFB3StoB + DFB4toB + Tos[θ, ϕ].AWos - Tos[θ, ϕ].(Mos*Aaos);

FB4toBz = (- DFOILtoB1 - DFOILtoB2 - DFOILtoB3 - DFOILtoB4 - DFOILtoB5 - DFOILtoB6 -
DFOILtoB7 - DFOILtoB8 - DFOILtoB9 + DFBtoP1 + DFBtoP2 + DFBtoP3 + DFBtoP4 + DFBtoP5 +
DFBtoP6 + DFBtoP7 + DFBtoP8 + DFBtoP9 + DFBStoVP1 + DFBStoVP2 + DFBStoVP3 + DFBStoVP4 +

DFBStoVP5 + DFBStoVP6 + DFBStoVP7 + DFBStoVP8 + DFBStoVP9 - Tos[θ, ϕ].Tvp^{T}.(HFVPtoBoutD

+ HFVPtoBinD + HFVPtoBinS + HFVPtoBoutS) - DFB3FtoB - DFB3StoB - Tos[θ, ϕ].AWos + Tos[θ,
ϕ].(Mos*Aaos))[[3]];
FB4toBz = Interpolation[Table[{t, FB4toBz}, {t, 0, 1, 0.0001}]];

(*Barrel - Output Shaft Assembly - sum of moments about axis of rotation of yoke*)

```
DMB3FtoB = {0, 0, 0};
DMB3StoB = {0, 0, 0};
DMB4toB = {0, 0, 0};

MomentOS = - Tos[θ, ϕ].(Ar29×(Tc2^T.IFOStoC229)) - Tos[θ, ϕ].(Ar30×(Tc2^T.IFOStoC230)) -

Dr31×DFBtoP1 - Dr32×DFBtoP2 - Dr33×DFBtoP3 - Dr34×DFBtoP4 - Dr35×DFBtoP5 - Dr36×DFBtoP6 -
Dr37×DFBtoP7 - Dr38×DFBtoP8 - Dr39×DFBtoP9 + DrOS×(Tos[θ, ϕ].AWos) + Tos[θ,

ϕ].Tvp^T.(HrOUTD×HFVPtoBoutD) + Tos[θ, ϕ].Tvp^T.(HrIND×HFVPtoBinD) + Tos[θ,

ϕ].Tvp^T.(HrINS×HFVPtoBinS) + Tos[θ, ϕ].Tvp^T.(HrOUTS×HFVPtoBoutS) + DMVPtoB +

DrB3FtoB×DFB3FtoB + DrB3StoB×DFB3StoB + DrB4toB×DFB4toB -
{DrBStoVP[[2]]*(DFBStoVP1[[3]] + DFBStoVP2[[3]] + DFBStoVP3[[3]] + DFBStoVP4[[3]] +
DFBStoVP5[[3]] + DFBStoVP6[[3]] + DFBStoVP7[[3]] + DFBStoVP8[[3]] + DFBStoVP9[[3]]), 0, 0} +
{DrOILtoB1[[2]]*DFOILtoB1[[3]] - DrOILtoB1[[3]]*DFOILtoB1[[2]], DrOILtoB1[[3]]*DFOILtoB1[[1]],
- DrOILtoB1[[2]]*DFOILtoB1[[1]]} + {DrOILtoB2[[2]]*DFOILtoB2[[3]] -
DrOILtoB2[[3]]*DFOILtoB2[[2]], DrOILtoB2[[3]]*DFOILtoB2[[1]], - DrOILtoB2[[2]]*DFOILtoB2[[1]]}
+ {DrOILtoB3[[2]]*DFOILtoB3[[3]] - DrOILtoB3[[3]]*DFOILtoB3[[2]],
DrOILtoB3[[3]]*DFOILtoB3[[1]], - DrOILtoB3[[2]]*DFOILtoB3[[1]]} +
{DrOILtoB4[[2]]*DFOILtoB4[[3]] - DrOILtoB4[[3]]*DFOILtoB4[[2]], DrOILtoB4[[3]]*DFOILtoB4[[1]],
- DrOILtoB4[[2]]*DFOILtoB4[[1]]} + {DrOILtoB5[[2]]*DFOILtoB5[[3]] -
DrOILtoB5[[3]]*DFOILtoB5[[2]], DrOILtoB5[[3]]*DFOILtoB5[[1]], - DrOILtoB5[[2]]*DFOILtoB5[[1]]}
+ {DrOILtoB6[[2]]*DFOILtoB6[[3]] - DrOILtoB6[[3]]*DFOILtoB6[[2]],
DrOILtoB6[[3]]*DFOILtoB6[[1]], - DrOILtoB6[[2]]*DFOILtoB6[[1]]} +
{DrOILtoB7[[2]]*DFOILtoB7[[3]] - DrOILtoB7[[3]]*DFOILtoB7[[2]], DrOILtoB7[[3]]*DFOILtoB7[[1]],
- DrOILtoB7[[2]]*DFOILtoB7[[1]]} + {DrOILtoB8[[2]]*DFOILtoB8[[3]] -
DrOILtoB8[[3]]*DFOILtoB8[[2]], DrOILtoB8[[3]]*DFOILtoB8[[1]], - DrOILtoB8[[2]]*DFOILtoB8[[1]]}
+ {DrOILtoB9[[2]]*DFOILtoB9[[3]] - DrOILtoB9[[3]]*DFOILtoB9[[2]],
DrOILtoB9[[3]]*DFOILtoB9[[1]], - DrOILtoB9[[2]]*DFOILtoB9[[1]]} - Mos*(DrOS×(Tos[θ, ϕ].Aaos)) -
DIos.Dαos;

MzOS = MomentOS[[3]];

solBarrelMz = Solve[{MzOS==0}, {FOStoC229x}];

FOStoC229x = Evaluate[FOStoC229x]/.solBarrelMz[[1]];
FOStoC229x = Interpolation[Table[{t, FOStoC229x}, {t, 0, 1, 0.0001}]];

IFOStoC229 = {FOStoC229x[t], 0, FOStoC229z};
IFOStoC230 = - IFOStoC229;

MomentC2 = Ir27×IFIM2toC227 + IMIM2toC227 + Ir28×IFIM2toC228 + IMIM2toC228 +
Ir29×IFOStoC229 + IMOStoC229 + Ir30×IFOStoC230 + IMOStoC230 - IIc2.Iαc2;

MzC2 = MomentC2[[3]];

solIC2Mz = NSolve[{MzC2==0}, {FIM2toC227y}];

FIM2toC227y = Evaluate[FIM2toC227y]/.solIC2Mz[[1]];

MomentIM2 = Chop[ - CMIM2toIM125 - 2Cr27×(Tim1.(Tc2^T.IFIM2toC227)) + Crim2×(Tim1.AWim2) -

CIim2.Cαim1 - Crim2×(Mim2*Caim2)];
```

MzIM2 = MomentIM2[[3]];

solIM2Mz = Solve[{MzIM2==0}, {MIM2toIM125z}];

ByteCount[MIM2toIM125z = Evaluate[MIM2toIM125z]/.solIM2Mz[[1]]]

(*First Intermediate shaft - Sum of moments about CG of 1st cross*)

FMIM1toC123 = {0, 0, 0};
FMIM1toC124 = {0, 0, 0};

(*Moment of inertita of 1st intermediate shaft*)
MatrixForm[CIim1 = {{Iim111, 0, Iim113}, {0, Iim122, 0}, {Iim113, 0, Iim133}}];

MomentIM1 = ($Tim1^T$.Cr23)×(- $Tc1^T$.FFIM1toC123) + ($Tim1^T$.Cr24)×(- $Tc1^T$.FFIM1toC124) +

$Tim1^T$.CMIM2toIM125 - ($Tim1^T$.Crim1)×AWim1 - $Tim1^T$.(CIim1.Cαim1) -$Tim1^T$.Crim1)×(Mim1*Aaim1);

MyIM1 = MomentIM1[[2]];
MzIM1 = MomentIM1[[3]];

solMyMzIM1 = NSolve[{MyIM1==0, MzIM1==0}, {FIM1toC123z, FIM1toC123y}];

FIM1toC123z = Evaluate[FIM1toC123z]/.solMyMzIM1[[1]];
FIM1toC123y = Evaluate[FIM1toC123y]/.solMyMzIM1[[1]];

(*First Cross - Sum of moments about center of 1st cross*)

FMMStoC13 = 0;
FMMStoC14 = 0;

(*Moment of inertia of 1st cross*)
MatrixForm[FIc1 : = {{Ic11, 0, 0}, {0, Ic11, 0}, {0, 0, Ic13}}]

MomentC1 : = Fr3×FFMStoC13 + Fr4×FFMStoC14 + FMMStoC13 + FMMStoC14 + Fr23×FFIM1toC123 + FMIM1toC123 + Fr24×FFIM1toC124 + FMIM1toC124 - FIc1.Fαc1;
MxC1 = MomentC1[[1]];
MzC1 = MomentC1[[3]];

solMxMzC1 = NSolve[{MxC1==0, MzC1==0}, {FFMStoC13x, FFMStoC13z}];

FFMStoC13x = Evaluate[FFMStoC13x]/.solMxMzC1[[1]];
FFMStoC13z = Evaluate[FFMStoC13z]/.solMxMzC1[[1]];

(*Main Shaft - Sum of Moments about center of 2nd bearing*)

AMB1toMS = {0, 0, 0};
AMB2toMS = {0, 0, 0};

(*Moment of inertia of main shaft*)
BIms = {{Ims11, Ims12, Ims13}, {Ims12, Ims22, Ims23}, {Ims13, Ims23, Ims33}};

MomentMS = ATin + (Ar1 - Ar2)×AFB1toMS - (T1[ϕ]^T.Br3 - Ar2)×($Tc1^T$.FFMStoC13) - (T1[ϕ]^T.Br4 -

Ar2)×($Tc1^T$.FFMStoC14) - (ArCR1 - Ar2)×AFMStoCR1 - (ArCR2 - Ar2)×AFMStoCR2 - (ArCR3 -

Ar2)×AFMStoCR3 - (ArCR4 - Ar2)×AFMStoCR4 - (ArCR5 - Ar2)×AFMStoCR5 - (ArCR6 -

Ar2)×AFMStoCR6 - (ArCR7 - Ar2)×AFMStoCR7 - (ArCR8 - Ar2)×AFMStoCR8 - (ArCR9 - Ar2)×AFMStoCR9 + (ArWms - Ar2)×AWms - T1[ϕ]^{T}.(BIms.BαMS);

MxMS = MomentMS[[1]];
MyMS = MomentMS[[2]];

SolMxMyMS = NSolve[{MxMS==0, MyMS==0}, {AFB1toMSx, AFB1toMSy}]

AFB1toMSx = Evaluate[AFB1toMSx]/.SolMxMyMS[[1]];
AFB1toMSy = Evaluate[AFB1toMSy]/.SolMxMyMS[[1]];

(*Main Shaft - Sum of Forces*)

AFB2toMS = - AFB1toMS + Tc1^{T}.FFMStoC13 + Tc1^{T}.FFMStoC14 + AFMStoCR1 + AFMStoCR2 + AFMStoCR3 + AFMStoCR4 + AFMStoCR5 + AFMStoCR6 + AFMStoCR7 + AFMStoCR8 + AFMStoCR9 - AWms;

AFB2toMSx = Interpolation[Table[{t, AFB2toMS[[1]]}, {t, 0, 1, 0.0001}]];

AFB2toMSy = Interpolation[Table[{t, AFB2toMS[[2]]}, {t, 0, 1, 0.0001}]];

AFB2toMSz = Interpolation[Table[{t, AFB2toMS[[3]]}, {t, 0, 1, 0.0001}]];
AFB2toMS = {AFB2toMSx[t], AFB2toMSy[t], AFB2toMSz[t]};

(*Displacement Mechanism (Actuating Link) - Sum of moments about point 90*)

MomentAC90 = Chop[- (ArACtoY66 - ArRAMtoAC90)×AFACtoY66 + (ArWAC - ArRAMtoAC90)×AWAC - (ArWAC - ArRAMtoAC90)×(MAC*AaAC) - AIAC.AαAC];

MxAC90 = Simplify[MomentAC90[[1]]]
solMxAC90 = Solve[{MxAC90==0}, {FACtoY66N}]
FACtoY66N = Evaluate[FACtoY66N]/.solMxAC90[[1]];

(*Displacement Mechanism (Actuating Link) - Sum of moments about point 66*)

MomentAC66 = Chop[(ArRAMtoAC90 - ArACtoY66)×AFRAMtoAC90 + (ArWAC - ArACtoY66)×AWAC - (ArWAC - ArACtoY66)×(MAC*AaAC) - AIAC.AαAC];

MxAC66 = Simplify[MomentAC66[[1]]]
solMxAC66 = Solve[{MxAC66==0}, {FRAMtoAC90y}]
FRAMtoAC90y = Evaluate[FRAMtoAC90y]/.solMxAC66[[1]];

AMCtoY67 = {0, 0, 0};
AMCtoY68 = {0, 0, 0};
AMACtoY66 = {0, 0, 0};

MomentVPplusOS = Tos[θ, ϕ].((ArCtoY68 - ArCtoY67)×AFCtoY68) + Tos[θ, ϕ].((ArACtoY66 - ArCtoY67)×AFACtoY66) + Tos[θ, ϕ].((Tvp^{T}.Hrvp - ArCtoY67)×AWvp) + Tos[θ, ϕ].((ArHPAtoY79 - ArCtoY67)×AFHPAtoY79) + Tos[θ, ϕ].((ArLPAtoY78 - ArCtoY67)×AFLPAtoY78) + (DrOILtoVP - Tos[θ, ϕ].ArCtoY67)×(DFOILtoVP1 + DFOILtoVP2 + DFOILtoVP3 + DFOILtoVP4 + DFOILtoVP5 + DFOILtoVP6 + DFOILtoVP7 + DFOILtoVP8 + DFOILtoVP9) - Tos[θ, ϕ].((Tvp^{T}.Hrvp - ArCtoY67)×(Tvp^{T}.(Mvp*Havp))) - Tos[θ, ϕ].(Tvp^{T}.(HIvp.Hαvp)) - Tos[θ, ϕ].((Ar29 -

ArCtoY67)×(Tc2^T.IFOStoC229)) - Tos[θ, ϕ].((Ar30 - ArCtoY67)×(Tc2^T.IFOStoC230)) - (Dr31 - Tos[θ, ϕ].ArCtoY67)×DFBtoP1 - (Dr32 - Tos[θ, ϕ].ArCtoY67)×DFBtoP2 - (Dr33 - Tos[θ, ϕ].ArCtoY67)×DFBtoP3 - (Dr34 - Tos[θ, ϕ].ArCtoY67)×DFBtoP4 - (Dr35 - Tos[θ, ϕ].ArCtoY67)×DFBtoP5 - (Dr36 - Tos[θ, ϕ].ArCtoY67)×DFBtoP6 - (Dr37 - Tos[θ, ϕ].ArCtoY67)×DFBtoP7 - (Dr38 - Tos[θ, ϕ].ArCtoY67)×DFBtoP8 - (Dr39 - Tos[θ, ϕ].ArCtoY67)×DFBtoP9 + (DrOS - Tos[θ, ϕ].ArCtoY67)×(Tos[θ, ϕ].AWos) + (DrOILtoB1 - Tos[θ, ϕ].ArCtoY67)×DFOILtoB1 + (DrOILtoB2 - Tos[θ, ϕ].ArCtoY67)×DFOILtoB2 + (DrOILtoB3 - Tos[θ, ϕ].ArCtoY67)×DFOILtoB3 + (DrOILtoB4 - Tos[θ, ϕ].ArCtoY67)×DFOILtoB4 + (DrOILtoB5 - Tos[θ, ϕ].ArCtoY67)×DFOILtoB5 + (DrOILtoB6 - Tos[θ, ϕ].ArCtoY67)×DFOILtoB6 + (DrOILtoB7 - Tos[θ, ϕ].ArCtoY67)×DFOILtoB7 + (DrOILtoB8 - Tos[θ, ϕ].ArCtoY67)×DFOILtoB8 + (DrOILtoB9 - Tos[θ, ϕ].ArCtoY67)×DFOILtoB9 - Mos*((DrOS - Tos[θ, ϕ].ArCtoY67)×(Tos[θ, ϕ].Aaos)) - DIos.Dαos;

MxVPplusOS = MomentVPplusOS[[1]];

MyVPplusOS = MomentVPplusOS[[2]];

MzVPplusOS = MomentVPplusOS[[3]];
solMomentVPplusOS = NSolve[{MxVPplusOS==0, MyVPplusOS==0, MzVPplusOS==0}, {FCtoY68y, FCtoY68z, FACtoY66P}];

FCtoY68y = Evaluate[FCtoY68y]/.solMomentVPplusOS[[1]];
FCtoY68z = Evaluate[FCtoY68z]/.solMomentVPplusOS[[1]];
FACtoY66P = Evaluate[FACtoY66P]/.solMomentVPplusOS[[1]];

FCtoY68y = Interpolation[Table[{t, FCtoY68y}, {t, 0, 1, 0.0001}]]
FCtoY68z = Interpolation[Table[{t, FCtoY68z}, {t, 0, 1, 0.0001}]]
FACtoY66P = Interpolation[Table[{t, FACtoY66P}, {t, 0, 1, 0.0001}]]

AFCtoY68 = {0, FCtoY68y[t], FCtoY68z[t]}
AFACtoY66 = {0, FACtoY66P[t]*Sin[ϵ - γ8] + FACtoY66N*Cos[ϵ - γ8], FACtoY66P[t]*Cos[ϵ - γ8] - FACtoY66N*Sin[ϵ - γ8]}

ForceVPplusOS = Tos[θ, ϕ].(AFCtoY67 + AFCtoY68 + AFACtoY66 + AWvp + AFLPAtoY78 + AFHPAtoY79 - Tvp^T.(Mvp*Havp) + AWos - Mos*Aaos - Tc2^T.(IFOStoC229 + IFOStoC230)) + DFOILtoVP1 + DFOILtoVP2 + DFOILtoVP3 + DFOILtoVP4 + DFOILtoVP5 + DFOILtoVP6 + DFOILtoVP7 + DFOILtoVP8 + DFOILtoVP9 + DFOILtoB1 + DFOILtoB2 + DFOILtoB3 + DFOILtoB4 + DFOILtoB5 + DFOILtoB6 + DFOILtoB7 + DFOILtoB8 + DFOILtoB9 - DFBtoP1 - DFBtoP2 - DFBtoP3 - DFBtoP4 - DFBtoP5 - DFBtoP6 - DFBtoP7 - DFBtoP8 - DFBtoP9;

AFCtoY67 = - AFCtoY68 - AFACtoY66 - AWvp - AFLPAtoY78 - AFHPAtoY79 + Tvp^T.(Mvp*Havp) - AWos + Mos*Aaos + Tc2^T.(IFOStoC229 + IFOStoC230) - Tos[θ, ϕ]^T.(DFOILtoVP1 + DFOILtoVP2 + DFOILtoVP3 + DFOILtoVP4 + DFOILtoVP5 + DFOILtoVP6 + DFOILtoVP7 + DFOILtoVP8 + DFOILtoVP9 + DFOILtoB1 + DFOILtoB2 + DFOILtoB3 + DFOILtoB4 + DFOILtoB5 + DFOILtoB6 + DFOILtoB7 + DFOILtoB8 + DFOILtoB9 - DFBtoP1 - DFBtoP2 - DFBtoP3 - DFBtoP4 - DFBtoP5 - DFBtoP6 - DFBtoP7 - DFBtoP8 - DFBtoP9);
FCtoY67x = Interpolation[Table[{t, AFCtoY67[[1]]}, {t, 0, 1, 0.0001}]];
FCtoY67y = Interpolation[Table[{t, AFCtoY67[[2]]}, {t, 0, 1, 0.0001}]];
FCtoY67z = Interpolation[Table[{t, AFCtoY67[[3]]}, {t, 0, 1, 0.0001}]];
AFCtoY67 = {FCtoY67x[t], FCtoY67y[t], FCtoY67z[t]};

(*Displacement Mechanism (Actuating Link) - Sum of forces*)
ForceAC = AFRAMtoAC90 - AFACtoY66 + AWAC - MAC*AaAC;

```
FzAC = ForceAC[[3]]
FyAC = ForceAC[[2]]

solFzAC = Solve[{FyAC==0}, {FRAMtoAC90z}]
FRAMtoAC90z = Evaluate[FRAMtoAC90z]/.solFzAC[[1]];
```

(*Ram - Sum of Forces*)

```
ForceRam = - AFRAMtoAC90 + AFCtoRAM90 + AWRAM + AFPtoRAM - MRAM*AaRAM;

FyRam = ForceRam[[2]]
FzRam = ForceRam[[3]]

solForceRam = NSolve[{FyRam==0, FzRam==0}, {NCtoRAM90, PRAM}];
NCtoRAM90 = Evaluate[NCtoRAM90]/.solForceRam[[1]];
PRAM = Evaluate[PRAM]/.solForceRam[[1]];

Export["C:\\Users\\noor\\Documents\\ABH\\Dissertation\\Mahematica models\\AFB1toMSx.xls",
Chop[Table[{t, - AFB1toMS[[1]]}, {t, 0, 0.12, 0.0001}]]];
Export["C:\\Users\\noor\\Documents\\ABH\\Dissertation\\Mahematica models\\AFB1toMSy.xls",
Chop[Table[{t, - AFB1toMS[[2]]}, {t, 0, 0.12, 0.0001}]]];
Export["C:\\Users\\noor\\Documents\\ABH\\Dissertation\\Mahematica models\\AFB1toMSmag.xls",
Chop[Table[{t, Norm[AFB1toMS]}, {t, 0, 0.12, 0.0001}]]];
Export["C:\\Users\\noor\\Documents\\ABH\\Dissertation\\Mahematica models\\AFB2toMSx.xls",
Chop[Table[{t, - AFB2toMS[[1]]}, {t, 0, 0.12, 0.0001}]]];

Export["C:\\Users\\noor\\Documents\\ABH\\Dissertation\\Mahematica models\\AFB2toMSy.xls",
Chop[Table[{t, - AFB2toMS[[2]]}, {t, 0, 0.12, 0.0001}]]];
Export["C:\\Users\\noor\\Documents\\ABH\\Dissertation\\Mahematica models\\AFB2toMSz.xls",
Chop[Table[{t, - AFB2toMS[[3]]}, {t, 0, 0.12, 0.0001}]]];
Export["C:\\Users\\noor\\Documents\\ABH\\Dissertation\\Mahematica models\\AFB2toMSmag.xls",
Chop[Table[{t, Norm[AFB2toMS]}, {t, 0, 0.12, 0.0001}]]];

Export["C:\\Users\\noor\\Documents\\ABH\\Dissertation\\Mahematica models\\AFCtoY67x.xls",
Chop[Table[{t, - AFCtoY67[[1]]}, {t, 0, 0.12, 0.0001}]]]
Export["C:\\Users\\noor\\Documents\\ABH\\Dissertation\\Mahematica models\\AFCtoY67y.xls",
Chop[Table[{t, - AFCtoY67[[2]]}, {t, 0, 0.12, 0.0001}]]]
Export["C:\\Users\\noor\\Documents\\ABH\\Dissertation\\Mahematica models\\AFCtoY67z.xls",
Chop[Table[{t, - AFCtoY67[[3]]}, {t, 0, 0.12, 0.0001}]]]
Export["C:\\Users\\noor\\Documents\\ABH\\Dissertation\\Mahematica models\\AFCtoY67mag.xls",
Chop[Table[{t, Norm[AFCtoY67]}, {t, 0, 0.12, 0.0001}]]]

Export["C:\\Users\\noor\\Documents\\ABH\\Dissertation\\Mahematica models\\AFCtoY68y.xls",
Chop[Table[{t, - AFCtoY68[[2]]}, {t, 0, 0.12, 0.0001}]]]
Export["C:\\Users\\noor\\Documents\\ABH\\Dissertation\\Mahematica models\\AFCtoY68z.xls",
Chop[Table[{t, - AFCtoY68[[3]]}, {t, 0, 0.12, 0.0001}]]]
Export["C:\\Users\\noor\\Documents\\ABH\\Dissertation\\Mahematica models\\AFCtoY68mag.xls",
Chop[Table[{t, Norm[AFCtoY68]}, {t, 0, 0.12, 0.0001}]]]
Export["C:\\Users\\noor\\Documents\\ABH\\Dissertation\\Mahematica models\\AFCtoRAM90y.xls",
Chop[Table[{t, - AFCtoRAM90[[2]]}, {t, 0, 0.12, 0.0001}]]]
Export["C:\\Users\\noor\\Documents\\ABH\\Dissertation\\Mahematica models\\AFCtoRAM90z.xls",
Chop[Table[{t, - AFCtoRAM90[[3]]}, {t, 0, 0.12, 0.0001}]]]
Export["C:\\Users\\noor\\Documents\\ABH\\Dissertation\\Mahematica models\\AFCtoRAM90mag.xls",
Chop[Table[{t, Norm[AFCtoRAM90]}, {t, 0, 0.12, 0.0001}]]]

DFTofAFB1toMSx = Take[Abs[Fourier[Table[AFB1toMS[[1]], {t, 0, 1, 1/(1024)}], FourierParameters→{ -
1, 1}]], {1, 256}];
```

```
ListLinePlot[DFTofAFB1toMSx, PlotRange→All, AxesLabel→{"Frequency (Hz)", "AFB1toMSx (N)"},
LabelStyle→Directive[Bold], PlotStyle→Thick]

Export["C:\\Users\\noor\\Documents\\ABH\\Dissertation\\Mahematica models\\DFTofAFB1toMSx.xls",
DFTofAFB1toMSx];

s3 = OpenWrite["Fcase.nb"]
Write[s3, AFB1toMS[[1]]]
Write[s3, AFB1toMS[[2]]]
Write[s3, Norm[AFB1toMS]]
Write[s3, AFB2toMS[[1]]]
Write[s3, AFB2toMS[[2]]]
Write[s3, AFB2toMS[[3]]]
Write[s3, Norm[AFB2toMS]]
Write[s3, AFCtoY67[[1]]]
Write[s3, AFCtoY67[[2]]]
Write[s3, AFCtoY67[[3]]]
Write[s3, Norm[AFCtoY67]]
Write[s3, AFCtoY68[[2]]]
Write[s3, AFCtoY68[[3]]]
Write[s3, Norm[AFCtoY68]]
Write[s3, AFCtoRAM90[[2]]]
Write[s3, AFCtoRAM90[[3]]]
Write[s3, Norm[AFCtoRAM90]]
Close[s3]
```

APPENDIX C: MATHEMATICA NOTEBOOK TO SOLVE FOR THE ORIFICE AREA AND THE SOLID AREA BETWEEN SUCCESSIVE CYLINDERS

(*Constant Inputs*)
SetDirectory["C :\\Users\\noor\\Documents\\ABH\\Dissertation\\Mahematica models"]

L45 = Length of notch groove base (Figure 3-20);
R2 : = Outside radius of the discharge/suction port (Figure 2-5);
R3 : = Inside radius of the discharge/suction port (Figure 2-5);

ϕ1 : = See Figure 3-17;
ϕ2 : = See Figure 3-17;
ϕ3 : = See Figure 3-17;
ϕ4 : = See Figure 3-17;
ϕ5 : = See Figure 3-17;
ϕ6 = See Figure 3-17;
ϕ7 : = See Figure 3-17;
ϕ8 : = See Figure 3-17;
ϕ9 : = See Figure 3-17;

λ1 : = See Figure 3-29;
λ2 : = See Figure 3-29;
λ3 : = See Figure 3-29;
λ4 : = See Figure 3-29;
λ5 : = See Figure 3-29;
λ6 : = See Figure 3-29;
λ7 : = See Figure 3-29;
λ8 : = See Figure 3-29;
λ9 : = See Figure 3-29;
λ10 : = See Figure 3-29;
λ11 : = See Figure 3-29;
λ12 : = See Figure 3-29;
λ13 : = See Figure 3-29;

ζD : = Angle between two successive cylinders;
ζc : = Angle between center lines of the circular ends of the bottom of the cylindrical cavity (Figure **3-32**);
ζ1 : = Angular position of center line of circular end of discharge port with respect to the TDC (Figure **3-32**);
ζ : = Kidney angle of the valve plate;

(*Orifice area*)

Rk = (R2 - R3)/2;
Aor1 = 0.00002*(2Pi*Rk + R2*ζc + R3*ζc);

C1 = ($R2^2$ + 6 R2 R3 + $R3^2$);
C2 = Sqrt[(3 R2 + R3)(R2 + 3 R3)]

```
L16 = Sqrt[(1/(8(R2 + R3)^2) Sin[(ϕ - ϕ2)/2]^2 (2 C1^2 + C2^2 (R2 - R3)^2 + C2 (R2 - R3) (C2 (R2 - R3) Cos[ζc + ϕ + ϕ2] + 2 C1 Sin[ζc + ϕ + ϕ2])))];

L17 = Sqrt[ 1/(16(R2 + R3)^2) (( C1 (Cos[ζ1] - Cos[ζc/2 + ϕ2]) + (R2 - R3)C2( Sin[ζ1] + Sin[ζc/2 + ϕ2]))^2
+ C1 (Sin[ζc/2 + ϕ2] - Sin[ζ1]) + 2 (R2 - R3)C2)^2];

Aor2[ϕ_] = (L45*L16/L17)^2/4 + Aor1;
```

(*Coordinates of point (5)*)

```
Aor3[ϕϕ_] : = Module[{Aor3, L12, δ1}, L12 = \[Sqrt](0.5(R2^2 - 6 R2 R3 + R3^2 + (R2 + R3)^2 Cos[ϕ - ζ1 +
ζc/2])); δ1 = 2*ArcSin[L12/(2*Rk)]; Aor3[ϕ_] = Simplify[Rk^2 (δ1 - Sin[δ1]) + Aor2[ϕ3]]; Aor3[ϕϕ]];

Aor3F : = ReadList["C :\\Users\\noor\\Documents\\ABH\\Dissertation\\Mahematica models\\Aor3.txt",
Number, RecordLists→True];

func3 : = ao + a1 xx + a2 xx^2 + a3 xx^3;
FindFit[Aor3F, func3, {ao, a1, a2, a3}, {xx}];
fit3 = func3/.%;
Aor3fit[ϕ_] = 0.0000323178 - 0.000379348 ϕ + 0.00132973 ϕ2 - 0.000954045 ϕ3;

Aor4[ϕ_] = Aor3fit[ϕ];

Aor5[ϕϕ_] : = Module[{Aor5, δ2}, δ2 = ϕ + ζc/2 - ζ1; Aor5[ϕ_] = Pi*Rk^2 + 0.5*(R2^2 - R3^2)*δ2 + Aor1
+ L45^2/4; Aor5[ϕϕ]]

Aor5F[ϕ_] = 0.0000570751 + 0.000242107 ( - 0.506844 + ϕ)

δ2P = ϕ6 + ζc/2 - ζ1;
Aor6[ϕ_] = Pi*Rk^2 + 0.5*(R2^2 - R3^2)*δ2P + Aor1 + L45^2/4 + Aor1

Aor7[ϕϕ_] : = Module[{Aor7, δ3}, δ3 = Pi - (ζ1 - ζc/2 + ϕ); Aor7[ϕ_] : = Aor1 + L45^2/4 + Pi*Rk^2 +
0.5*(R2^2 - R3^2)*δ3; Aor7[ϕϕ]]

Aor7F[ϕ_] = 0.0000570751 + 0.000242107 (2.634749 - ϕ)

Aor8[ϕϕ_] : = Module[{Aor8, L12, δ1}, L12 = \[Sqrt](0.5*(R2^2 - 6 R2 R3 + R3^2 - (R2 + R3)^2 Cos[ζ1 - ζc/2
+ ϕ])); Rk = (R2 - R3)/2; δ1 = 2*ArcSin[L12/(2*Rk)]; Aor8[ϕ_] = Simplify[Rk^2 (δ1 - Sin[δ1]) + Aor1];
Aor8[ϕϕ]]

Aor8F : = ReadList["C :\\Users\\noor\\Documents\\ABH\\Dissertation\\Mahematica models\\Aor8.txt",
Number, RecordLists→True]

func8 : = aoo + a11 x1 + a22 x1^2 + a33 x1^3;
FindFit[Aor8F, func8, {aoo, a11, a22, a33}, {x1}];
fit8 = func8/.%;

Aor8fit[ϕ_] = - 0.0176193 + 0.020274 ϕ - 0.00766259 ϕ2 + 0.000954142 ϕ3;

Ar[ϕ_] = Piecewise[{{Aor1, ϕ1 - Pi< = ϕ<ϕ2 - Pi}, {Aor2[ϕ + Pi], ϕ2 - Pi< = ϕ<ϕ3 - Pi}, {Aor3fit[ϕ + Pi],
ϕ3 - Pi< = ϕ<ϕ5 - Pi}, {Aor5F[ϕ + Pi], ϕ5 - Pi< = ϕ<ϕ6 - Pi}, {Aor6[ϕ + Pi], ϕ6 - Pi< = ϕ<ϕ7 - Pi},
{Aor7F[ϕ + Pi], ϕ7 - Pi< = ϕ<ϕ8 - Pi}, {Aor8fit[ϕ + Pi], ϕ8 - Pi< = ϕ<ϕ9 - Pi}, {Aor1, ϕ1< = ϕ<ϕ2},
{Aor2[ϕ], ϕ2< = ϕ<ϕ3}, {Aor3fit[ϕ], ϕ3< = ϕ<ϕ5}, {Aor5F[ϕ], ϕ5< = ϕ<ϕ6}, {Aor6[ϕ], ϕ6< = ϕ<ϕ7},
{Aor7F[ϕ], ϕ7< = ϕ<ϕ8}, {Aor8fit[ϕ], ϕ8< = ϕ<ϕ9}, {Aor1, ϕ9< = ϕ<Pi}}];

Needs["FourierSeries`"]
```

```
s = OpenWrite["AoRF.nb"]
Write[s, ArFR[ϕ_] = NFourierTrigSeries[Ar[ϕ], ϕ, 40, AccuracyGoal→3, PrecisionGoal→3]]
Close[s]
```

(*Solid area between succesive cylinders*)

```
Ass2[ϕϕ_] = Module[{Ass2, δ4}, δ4 = - ζ1 - ζc/2 + ζD + ϕ; Ass2[ϕ_] : = 0.5*δ4*(R2^2 - R3^2); Ass2[ϕϕ]];

As1 = 0.5*(R2^2 - R3^2)*( - ζ1 - ζc/2 + ζD + λ2);

As3[ϕϕ_] : = Module[{As3, δ1, δ4}, δ1 : = 2*ArcSin[Sqrt[0.5*(R2^2 - 6 R2 R3 + R3^2 + (R2 + R3)^2 Cos[ζ1 -
ζc/2 - ϕ])]/(R2 - R3)]; δ4 : = - ζ1 - ζc/2 + ζD + ϕ; As3[ϕ_] : = 0.5*δ4*(R2^2 - R3^2) - 0.25*(R2 - R3)^2*(δ1 -
Sin[δ1]); As3[ϕϕ]]

Rk = (R2 - R3)/2;
As4 : = 0.5*(ζD - ζc)*(R2^2 - R3^2) - Pi*Rk^2;

As5[ϕϕ_] : = Module[{As5, δ1, δ4}, δ1 : = δ1 = 2 ArcSin[Sqrt[R2^2 - 6 R2 R3 + R3^2 - (R2 + R3)^2 Cos[ζ1 -
ζc/2 + ζD + ϕ]]/(Sqrt[2] (R2 - R3))]; δ4 = - ζ1 - ζc/2 - ϕ + Pi; As5[ϕ_] : = 0.5*δ4*(R2^2 - R3^2) - 0.25*(R2
- R3)^2*(δ1 - Sin[δ1]); As5[ϕϕ]]

As6[ϕϕ_] : = Module[{As6, δ4}, δ4 : = Pi - (ζ1 + ζc/2 + ϕ); As6[ϕ_] : = 0.5*δ4*(R2^2 - R3^2); As6[ϕϕ]]

AsHalf[ϕ_] = Piecewise[{{As1, 0≤ϕ<λ2}, {Ass2[ϕ], λ2≤ϕ<λ3}, {As3[ϕ], λ3≤ϕ<λ4}, {As4, λ4≤ϕ<λ5},
{As5[ϕ], λ5≤ϕ<λ6}, {As6[ϕ], λ6< = ϕ<λ7}, {As1, λ7≤ϕ<Pi}}];

As[ϕ_] : = AsHalf[ϕ] + AsHalf[ϕ + Pi];

s1 = OpenWrite["Asolid.nb"];
Write[s1, Chop[NFourierTrigSeries[As[ϕ], ϕ, 40, AccuracyGoal→3, PrecisionGoal→3]]];
Close[s1];
```

APPENDIX D: MATHEMATICA NOTEBOOK TO SOLVE FOR THE PISTON PRESSURE

```
SetDirectory["C :\\Users\\noor\\Documents\\ABH\\Dissertation\\Mahematica models"]
```

(*Orifice area*)

```
FileOrificeArea = OpenRead["AoRF.nb"];
ArFR[ϕ_] = Read[FileOrificeArea];
Close[FileOrificeArea];
```

Ac : = Cylinder cross sectional area;
Ace : = Exit cross sectional area of the cylinder;

B : = Oil bulk modulus;
DF : = Distance from center of spherical joint between piston and connecting rod and the bottom end of the cylindrical cavity for a zero yoke angle (Figure 3-15);

LC2 : = Length of the convergent part of the cylindrical cavity (Figure 3-14);
LCR : = Length of the connecting rod;
Lis : = Length of input shaft of the CVJ (Figure 3-9);
Lp : = Length of piston that is in the cylinder when axial displacement is zero;
LPtoCR : = Distance from the left face of the piston to the common point between the piston and the connecting rod;

MH : = Mass of gas in the HPA;
ML : = Mass of gas in the LPA;

nrated : = Rated speed of pump, rpm;
PlossH : = Pressure losses between the discharge port and the HPA;
PlossL : = Pressure losses between the suction port and the LPA;
PmaxL = Maximum gas pressure in the LPA
PmaxH = Maximum gas pressure in the HPA;
PPH : = Pre-charge pressure in the HPA;
PPL : = Pre-charge pressure in the LPA;

r : = Pitch circle radius at the barrel side;
R : = Pitch circle radius at the main shaft side;
RN : = Gas constant of nitrogen, J/kg°K;

Ry : = Distance from center of rotation of yoke to center of first or second cross;
Tg : = Temperature of gas in the HPA or LPA at pre-charge, ºK;
Vfixed : = Volume of oil at end of the cylinder cavity (conical portion) (Figure 3-14);

ρ = Oil density;
g = Acceleration of gravity;

$\phi 1$: = See Figure 3-17;
$\phi 2$: = See Figure 3-17;
$\phi 3$: = See Figure 3-17;

ϕ4 : = See Figure 3-17;
ϕ5 : = See Figure 3-17;
ϕ6 = See Figure 3-17;
ϕ7 : = See Figure 3-17;
ϕ8 : = See Figure 3-17;
ϕ9 : = See Figure 3-17;

ϕ = Angular rotation of the main shaft about its axis of rotation;
θ = Angular rotation of the yoke about its axis of rotation;

(*The Piston displacement*)

φo[$\theta\theta$_] : = Module[{ φo}, φo[θ_] : = θ + ArcSin[(r - R Cos[θ] - (Ry + Lis) Sin[θ])/LCR]; φo[$\theta\theta$]]

IF[$\theta\theta$_,$\phi\phi$_] : = Module[{IF},IF[θ_,ϕ_] : = - Ry - (Lis + Ry) Cos[θ] + R Cos[ϕ] Sin[θ] + Sqrt[LCR^2 - Sin[θ]^2 (Lis + Ry)^2 - r^2 + 2r R (1 - 2 Cos[ϕ]^2 Sin[θ/2]^2) + R^2 (Sin[θ]^2 Cos[ϕ]^2 - 1) + 2(Lis + Ry)Cos[ϕ]Sin[θ](r - R Cos[θ])]; IF[$\theta\theta$,$\phi\phi$]];

Z[$\theta\theta$_,$\phi\phi$_] : = Module[{Z,IH},IH : = - Ry + LCR Cos[φo[θ] - θ] - (Lis + Ry) Cos[θ] + R Sin[θ]; Z[θ_,ϕ_] : = Chop[IH - IF[θ,ϕ]]; Z[$\theta\theta$,$\phi\phi$]]

LC1[$\theta\theta$_] : = Module[{LC1,CG,GF},γo = ArcSin[(r - R)/LCR]; γ1 : = ArcTan[r/EH]; EF : = Sqrt[r^2 + EH^2];
GF[θx_] : = 2*EF*Sin[θx/2]; CG[θx_] : = (DF - LCR Cos[φo[θx]] + LCR Cos[γo]) Cos[θx] - GF[θx] Sin[γ1 - θx/2] - (- r + R + LCR Sin[φo[θx]]) Sin[θx]; LC1[θx_] : = CG[θx] - LC2 - Lp1; LC1[$\theta\theta$]]

Vmin[$\theta\theta$_] : = Module[{Vmin},Vmin[θx_] : = Chop[LC1[θx]*Ac + Vfixed]; Vmin[$\theta\theta$]]

Lmin[$\theta\theta$_] : = Module[{Lmin},Dce : = Sqrt[4*Ace/Pi]; Dc : = Sqrt[4*Ac/Pi]; Le : = LC2*Dce/(Dc - Dce); Lmin[θx_] : = ((2*Ac/9)*(LC2 + Le)^2 - (2*Ace/9)*Le^2 + Ac*LC1[θx]*(LC1[θx]/2 + LC2 + Le) - Vmin[θx]*Le)/Vmin[θx]; Lmin[$\theta\theta$]]

Lv[$\theta\theta$_,$\phi\phi$_] : = Module[{Lv},Lv[θx_,ϕx_] : = (Vmin[θx]*Lmin[θx] + Ac*Z[θx,ϕx]*(Z[θx,ϕx]/2 + LC1[θx] + LC2))/(Vmin[θx] + Ac*Z[θx,ϕx]); Lv[$\theta\theta$,$\phi\phi$]]

VOIL[$\theta\theta$_,$\phi\phi$_] : = Module[{VOIL},VOIL[θx_,ϕx_] : = Vmin[θx] + Ac*Z[θx,ϕx]; VOIL[$\theta\theta$,$\phi\phi$]]

VOILD[tt_,ii_] = Module[{VOILD},VOILD[t_,i_] = Simplify[Dt[VOIL[θ,ϕ + 2*Pi*(i - 1)/9],t,Constants→{i}]]; VOILD[tt,ii]];

VPH = MH*RN*Tg/PPH; (*precharge volume of HPA*)
VPL = ML*RN*Tg/PPL; (*precharge volume of LPA*)

PminL = PPL/0.9; (*minimum pressure of LPA*)
PminH = PPH/0.9; (*minimum pressure of HPA*)

(*Gas volume at tmin operating pressure*)
VmaxH = ((PPH/PminH)*VPH^1.4)^(1/1.4); (*HPA*)
VmaxL = ((PPL/PminL)*VPL^1.4)^(1/1.4); (*LPA*)

(*Gas volume at max operating pressure*)
VminH = ((PPH/PmaxH)*VPH^1.4)^(1/1.4); (*HPA*)
VminL = ((PPL/PmaxL)*VPL^1.4)^(1/1.4); (*LPA*)

(*Boundary pressure*)

```
Unit11[x_] = (1 - Clip[(1/(ϕ2 - ϕ1))Sin[x - (ϕ1 + ϕ2)/2]])/2;
Unit22[x_] = (1 + Clip[(1/(ϕ2 - ϕ1))Sin[x - (ϕ1 + ϕ2)/2]])/2;

PH[t_] = PminH*(VmaxH/VH[t])^1.4;
VL[t_] = VmaxH + VminL - VH[t];
PL[t_] = PminL*(VmaxL/VL[t])^1.4;
PD = PH[t] + PlossH + 101325;
PS = PL[t] - PlossL + 101325;

Pb[xx_] = Unit11[xx]*PD + Unit22[xx]*PS;

Cd = 0.62

QDS1[t_] = - Cd*ArFR[ϕ]*Sign[POIL1[t] - Pb[ϕ]]*Sqrt[2*Abs[POIL1[t] - Pb[ϕ]]/ρ];
QDS2[t_] = - Cd*ArFR[ϕ + 2*Pi/9]*Sign[POIL2[t] - Pb[ϕ + 2*Pi/9]]*Sqrt[2*Abs[POIL2[t] - Pb[ϕ +
2*Pi/9]]/ρ];
QDS3[t_] = - Cd*ArFR[ϕ + 4*Pi/9]*Sign[POIL3[t] - Pb[ϕ + 4*Pi/9]]*Sqrt[2*Abs[POIL3[t] - Pb[ϕ +
4*Pi/9]]/ρ];
QDS4[t_] = - Cd*ArFR[ϕ + 6*Pi/9]*Sign[POIL4[t] - Pb[ϕ + 6*Pi/9]]*Sqrt[2*Abs[POIL4[t] - Pb[ϕ +
6*Pi/9]]/ρ];
QDS5[t_] = - Cd*ArFR[ϕ + 8*Pi/9]*Sign[POIL5[t] - Pb[ϕ + 8*Pi/9]]*Sqrt[2*Abs[POIL5[t] - Pb[ϕ +
8*Pi/9]]/ρ]; QDS6[t_] = - Cd*ArFR[ϕ + 10*Pi/9]*Sign[POIL6[t] - Pb[ϕ + 10*Pi/9]]*Sqrt[2*Abs[POIL6[t] -
Pb[ϕ + 10*Pi/9]]/ρ];
QDS7[t_] = - Cd*ArFR[ϕ + 12*Pi/9]*Sign[POIL7[t] - Pb[ϕ + 12*Pi/9]]*Sqrt[2*Abs[POIL7[t] - Pb[ϕ +
12*Pi/9]]/ρ];
QDS8[t_] = - Cd*ArFR[ϕ + 14*Pi/9]*Sign[POIL8[t] - Pb[ϕ + 14*Pi/9]]*Sqrt[2*Abs[POIL8[t] - Pb[ϕ +
14*Pi/9]]/ρ];
QDS9[t_] = - Cd*ArFR[ϕ + 16*Pi/9]*Sign[POIL9[t] - Pb[ϕ + 16*Pi/9]]*Sqrt[2*Abs[POIL9[t] - Pb[ϕ +
16*Pi/9]]/ρ];

nms = 60D[ϕ,t]/(2Pi);

ηv1[t_] = (89.10 + 39.0242 (nms/nrated) - 27.725 (nms/nrated)^2)*Exp[ - 0.003403 Abs[POIL1[t] -
Pb[ϕ]]/1000000]/100;
ηv2[t_] = (89.10 + 39.0242 (nms/nrated) - 27.725 (nms/nrated)^2)*Exp[ - 0.003403 Abs[POIL2[t] - Pb[ϕ +
2Pi/9]]/1000000]/100;
ηv3[t_] = (89.10 + 39.0242 (nms/nrated) - 27.725 (nms/nrated)^2)*Exp[ - 0.003403 Abs[POIL3[t] - Pb[ϕ +
4Pi/9]]/1000000]/100;
ηv4[t_] = (89.10 + 39.0242 (nms/nrated) - 27.725 (nms/nrated)^2)*Exp[ - 0.003403 Abs[POIL4[t] - Pb[ϕ +
6Pi/9]]/1000000]/100;
ηv5[t_] = (89.10 + 39.0242 (nms/nrated) - 27.725 (nms/nrated)^2)*Exp[ - 0.003403 Abs[POIL5[t] - Pb[ϕ +
8Pi/9]]/1000000]/100;
ηv6[t_] = (89.10 + 39.0242 (nms/nrated) - 27.725 (nms/nrated)^2)*Exp[ - 0.003403 Abs[POIL6[t] - Pb[ϕ +
10Pi/9]]/1000000]/100;
ηv7[t_] = (89.10 + 39.0242 (nms/nrated) - 27.725 (nms/nrated)^2)*Exp[ - 0.003403 Abs[POIL7[t] - Pb[ϕ +
12Pi/9]]/1000000]/100;
ηv8[t_] = (89.10 + 39.0242 (nms/nrated) - 27.725 (nms/nrated)^2)*Exp[ - 0.003403 Abs[POIL8[t] - Pb[ϕ +
14Pi/9]]/1000000]/100;
ηv9[t_] = (89.10 + 39.0242 (nms/nrated) - 27.725 (nms/nrated)^2)*Exp[ - 0.003403 Abs[POIL9[t] - Pb[ϕ +
16Pi/9]]/1000000]/100;

Q1[t_] = QDS1[t]*ηv1[t];
Q2[t_] = QDS2[t]*ηv2[t];
Q3[t_] = QDS3[t]*ηv3[t];
Q4[t_] = QDS4[t]*ηv4[t];
Q5[t_] = QDS5[t]*ηv5[t];
```

```
Q6[t_] = QDS6[t]*ηv6[t];
Q7[t_] = QDS7[t]*ηv7[t];
Q8[t_] = QDS8[t]*ηv8[t];
Q9[t_] = QDS9[t]*ηv9[t];

QTTD[t_] = (Abs[Q1[t]] + Abs[Q2[t]] + Abs[Q3[t]] + Abs[Q4[t]] + Abs[Q5[t]] + Abs[Q6[t]] + Abs[Q7[t]]
+ Abs[Q8[t]] + Abs[Q9[t]])/2;
```

(*Solve the differential equation of the oil pressure in the ith cylinder*)

```
eqs = {POIL1'[t] = = (B/VOIL[θ,ϕ])*(Q1[t] - VOILD[t,1]),POIL2'[t] = = (B/VOIL[θ,ϕ + 2*Pi/9])*(Q2[t] -
VOILD[t,2]),POIL3'[t] = = (B/VOIL[θ,ϕ + 4*Pi/9])*(Q3[t] - VOILD[t,3]),POIL4'[t] = = (B/VOIL[θ,ϕ +
6*Pi/9])*(Q4[t] - VOILD[t,4]),POIL5'[t] = = (B/VOIL[θ,ϕ + 8*Pi/9])*(Q5[t] - VOILD[t,5]),POIL6'[t] = =
(B/VOIL[θ,ϕ + 10*Pi/9])*(Q6[t] - VOILD[t,6]),POIL7'[t] = = (B/VOIL[θ,ϕ + 12*Pi/9])*(Q7[t] -
VOILD[t,7]),POIL8'[t] = = (B/VOIL[θ,ϕ + 14*Pi/9])*(Q8[t] - VOILD[t,8]),POIL9'[t] = = (B/VOIL[θ,ϕ +
16*Pi/9])*(Q9[t] - VOILD[t,9]),VH'[t]== - QTTD[t]};

bcs1 = {POIL1[0] = = PmaxL,POIL2[0] = = PmaxL,POIL3[0] = = PmaxL,POIL4[0] = = PmaxL,POIL5[0]
= = PmaxL,POIL6[0] = = PminH,POIL7[0] = = PminH,POIL8[0] = = PminH,POIL9[0] = = PminH,VH[0] =
= VmaxH};

sol =
NDSolve[{eqs,bcs1},{POIL1,POIL2,POIL3,POIL4,POIL5,POIL6,POIL7,POIL8,POIL9,VH},{t,0,1},MaxS
teps→Infinity,AccuracyGoal→5,PrecisionGoal→5];


Needs["PlotLegends`"]
DFTPallPistons = Take[Abs[Fourier[Table[PallPistons[[1]]/1000000,{t,0,1,1/1024}],FourierParameters→{ -
1,1}]],{1,256}];

ListLinePlot[DFTPallPistons,PlotRange→All,AxesLabel→{"Frequency (Hz)","Pressure of all pistons
(MPa)"},LabelStyle→Directive[Bold],PlotStyle→Thick]

Export["C :\\Users\\noor\\Documents\\ABH\\Dissertation\\Mahematica
models\\PressureAllPistonsHarmonics10.xls",DFTPallPistons];

Q1 = Interpolation[Table[{t,Evaluate[Q1[t]/.sol]*60000},{t,0,1,0.0001}]];
Q2 = Interpolation[Table[{t,Evaluate[Q2[t]/.sol]*60000},{t,0,1,0.0001}]];
Q3 = Interpolation[Table[{t,Evaluate[Q3[t]/.sol]*60000},{t,0,1,0.0001}]];
Q4 = Interpolation[Table[{t,Evaluate[Q4[t]/.sol]*60000},{t,0,1,0.0001}]];
Q5 = Interpolation[Table[{t,Evaluate[Q5[t]/.sol]*60000},{t,0,1,0.0001}]];
Q6 = Interpolation[Table[{t,Evaluate[Q6[t]/.sol]*60000},{t,0,1,0.0001}]];
Q7 = Interpolation[Table[{t,Evaluate[Q7[t]/.sol]*60000},{t,0,1,0.0001}]];
Q8 = Interpolation[Table[{t,Evaluate[Q8[t]/.sol]*60000},{t,0,1,0.0001}]];
Q9 = Interpolation[Table[{t,Evaluate[Q9[t]/.sol]*60000},{t,0,1,0.0001}]];

s = OpenWrite["POIL.nb"]
Write[s,Evaluate[PD/.sol]]
Write[s,Evaluate[PS/.sol]]
Write[s,Evaluate[POIL1[t]/.sol]]
Write[s,Evaluate[POIL2[t]/.sol]]
Write[s,Evaluate[POIL3[t]/.sol]]
Write[s,Evaluate[POIL4[t]/.sol]]
Write[s,Evaluate[POIL5[t]/.sol]]
Write[s,Evaluate[POIL6[t]/.sol]]
Write[s,Evaluate[POIL7[t]/.sol]]
```

```
Write[s,Evaluate[POIL8[t]/.sol]]
Write[s,Evaluate[POIL9[t]/.sol]]
Write[s,Evaluate[Pb[ϕ]/.sol]]
Close[s]

s2 = OpenWrite["QOIL.nb"]
Write[s2,Q1[t]]
Write[s2,Q2[t]]
Write[s2,Q3[t]]
Write[s2,Q4[t]]
Write[s2,Q5[t]]
Write[s2,Q6[t]]
Write[s2,Q7[t]]
Write[s2,Q8[t]]
Write[s2,Q9[t]]
Close[s2]
```